Measurement of the mixing parameters of neutral charm mesons and search for indirect CP violation with $D^0 \rightarrow K_S^0\pi^+\pi^-$ decays at LHCb

Martha Hilton

Supervisor: Mark Williams

A thesis presented for the degree of
Doctor of Philosophy

Department of Physics and Astronomy
University of Manchester
UK
October 7, 2021

Contents

List of Figures

List of Tables

Abstract

Mixing is the time-dependent phenomenon of a neutral meson (in this case charm meson D^0) changing into its anti-particle ($\bar{D}^0$) and vice versa. This occurs because the mass eigenstates, denoted D_1 and D_2 are linear combinations of the flavour eigenstates D^0 and $\bar{D}^0$. Mixing is governed by two parameters x and y defined as: $x \equiv (m_1 - m_2)/\Gamma$ and $y \equiv (\Gamma_1 - \Gamma_2)/(2\Gamma)$ where Γ is the average decay width. *CP*-violation can occur in mixing or in the interference between mixing and decay. The *CP*-violation parameters $|q/p|$ and ϕ describe the superposition of the flavour eigenstates and the mass eigenstates: $|D_{1,2}\rangle = p\,|D^0\rangle \pm q\,\left|\bar{D}^0\right\rangle$. The self-conjugate decay $D^0 \to K^0_S\pi^+\pi^-$ offers direct access to the mixing and *CP*-violation parameters through a time and phase-space dependent fit to the Dalitz variables and decay-time of this decay. This thesis reports a measurement of the mixing and *CP*-violation parameters using data collected at the LHCb experiment in the Run 2 data-taking period in 2016-2018, corresponding to an integrated luminosity of 6 fb^{-1}. This analysis uses D^0 mesons originating from semi-leptonic B meson decays. The $D^0 \to K^0_S\pi^+\pi^-$ decay is modelled by expressing the three-body decay as the superposition of successive two-body decays through intermediate resonances. The blinded mixing parameters are found to be:

$$x = (x.xx \pm 0.86_{\text{stat}} \pm 0.39_{\text{syst}} \pm 0.24_{\text{model}}) \times 10^{-3}$$

$$y = (y.yy \pm 0.76_{\text{stat}} \pm 0.59_{\text{syst}} \pm 0.26_{\text{model}}) \times 10^{-3}$$

where the uncertainties are statistical, systematic and from the choice of amplitude model. The *CP*-violation parameters are expressed in terms of Δx and Δy which

are defined as the difference in mixing parameters measured for D^0 and $\bar{D}^0$:

$$\Delta x = (0.00 \pm 0.59) \times 10^{-3}$$
$$\Delta y = (0.00 \pm 0.51) \times 10^{-3}$$

the uncertainties are currently statistical only and the results are blind.

Lay Summary

The fundamental particles that make up the universe and the interactions between them are described, to our best knowledge, by the Standard Model of particle physics. The Standard Model is experimentally verified to an extremely high precision but it has some significant theoretical shortcomings and cannot fully explain all the phenomena observed in nature. Therefore physicists are searching for a new theory beyond the Standard Model which can explain these anomalies.

The fundamental particles consist of six quarks, three pairs of leptons and corresponding neutrino (as well as the anti-particles) and the force carriers which mediate the forces between the particles. A meson is a type of particle made from a quark - antiquark pair. The D^0 meson which is the subject of this thesis is made from a charm quark and an up antiquark, it is neutrally charged. A neutral (zero charge) meson can oscillate over time between particle and anti-particle states (in this case a $\bar{D}^0$ consisting of a charm antiquark and an up quark) through a time-dependent phenomenon called mixing. New virtual particles can change the oscillation rate, so any discrepancy from the Standard Model predictions may be a hint of new physics.

One of the shortcomings of the Standard Model is that it does not account for enough *CP* (charge parity) violation to explain the matter - antimatter asymmetry we see in the universe today. *CP*-violation refers to differences in which a particle and its antiparticle behave, these can be observed directly in a particle decay or in mixing. *CP*-violation can arise both through differences in overall decay probabilities (*CP*-violation in decay) which are constant as a function of decay time, and also through asymmetric mixing effects, which are time dependent. *CP*-violation in decay was discovered in charm mesons in 2019 but at the time of writing there is no evidence for *CP*-violation in mixing or in the interference between mixing and decay of particles containing charm quarks. Therefore precision measurements of *CP*-violation and mixing in charm are important tools to understand potential new physics beyond the Standard Model.

At the Large Hadron Collider at CERN, protons (made from two up and one down quarks) are accelerated to extremely high speeds and collided. The LHCb detector collects the data from these proton collisions. It is a special detector that was built to study heavy flavour (beauty and charm quarks) physics measurements. The research presented in this thesis uses data collected at the LHCb detector from 2016 to 2018 to perform a measurement of the charm mixing parameters and search for indirect *CP*-violation.

Glossary

AUC	Area Under ROC Curve. 124
BDT	Boosted Decision Tree. 113
CERN	European Organisation for Nuclear Research (Organisation européenne pour la recherche nucléaire). 73
CF	Cabibbo favoured. 53
CKM	Cabibbo-Kobayashi-Maskawa (matrix). 52
CPU	Central Processing Unit. 90
DCS	Doubly Cabibbo suppressed. 53
DIRA	Direction angle. 121
DTF	Decay Tree Fitter. 112
ECAL	Electromagnetic Calorimeter. 79
FPR	False Positive Rate. 124
GEM	Gas Electron Multiplier chambers. 89
GIM	Glashow–Iliopoulos–Maiani mechanism. 53
HCAL	Hadronic Calorimeter. 79
HLT	High Level Trigger. 90

HPD	Hybrid Photon Detectors. 85
IP	Impact Parameter. 81
IT	Inner Tracker. 78
KS	Kolmogorov-Smirnov test. 123
LHC	Large Hadron Collider. 73
LHCb	Large Hadron Collider Beauty experiment. 73
MC	Monte Carlo. 131
MVA	Multivariate Analysis. 120
MWPC	Multi-Wire Proportional Chambers. 88
OT	Outer Tracker. 79
PDF	Probability Density Function. 114
PDG	Particle Data Group. 110
PID	Particle identification. 103
PMNS	Pontecorvo–Maki–Nakagawa–Sakata (matrix). 64
PS	Pre-Shower. 86
PV	Primary Vertex. 80
QCD	Quantum Chromodynamics. 59
QED	Quantum Electrodynamics. 55
RICH	Ring Imaging Cherenkov detectors. 78
ROC	Receiver operating characteristic curve. 123
SCS	Singly Cabibbo suppressed. 53
SM	The Standard Model of particle physics. 51

SPD	Scintillator Pad Detector. 86
SPS	Super Proton Synchrotron. 74
SV	Secondary vertex. 103
TCKs	Trigger Configuration Keys. 105
TIS	Triggered independently of signal. 105
TOS	Triggered on signal. 105
TPR	True Positive Rate. 124
TT	Tracker Turicenis. 78
VELO	Vertex Locator. 78
WLS	Wavelength-shifting fibres. 87

Declaration

This work represents the combined efforts of the LHCb collaboration. Hence, parts of the content has been published elsewhere and/or presented to several audiences. I hereby declare that, subject to the above comment, the submission is my own original work undertaken while being at the University of Manchester and that no portion of the work referred to in this thesis has been submitted in support of an application for another degree or qualification of this or any other university or other institute of learning.

Copyright Statement

1. The author of this thesis (including any appendices and/or schedules to this thesis) owns certain copyright or related rights in it (the "Copyright") and s/he has given the University of Manchester certain rights to use such Copyright, including for administrative purposes.
2. Copies of this thesis, either in full or in extracts and whether in hard or electronic copy, may be made only in accordance with the Copyright, Designs and Patents Act 1988 (as amended) and regulations issued under it or, where appropriate, in accordance with licensing agreements which the University has from time to time. This page must form part of any such copies made.
3. The ownership of certain Copyright, patents, designs, trademarks and other intellectual property (the "Intellectual Property") and any reproductions of copyright works in the thesis, for example graphs and tables ("Reproductions"), which may be described in this thesis, may not be owned by the author and may be owned by third parties. Such Intellectual Property and Reproductions cannot and must not be made available for use without the prior written permission of the owner(s) of the relevant Intellectual Property and/or Reproductions.
4. Further information on the conditions under which disclosure, publication and commercialisation of this thesis, the Copyright and any Intellectual Property and/or Reproductions described in it may take place is available in the University IP Policy (see http://documents.manchester.ac.uk/DocuInfo.aspx?DocID=24420), in any relevant Thesis restriction declarations deposited in the University Library, the University Library's regulations (see http://www.library.manchester.ac.uk/about/regulations/) and in the University's policy on Presentation of Theses.

Acknowledgements

Thank you to my supervisor Mark Williams for the weekly meetings, constant feedback and for believing in me and supporting me throughout this process. Also to my co-supervisor Marco Gersabeck.

Chris Burr - I would not have been able to do this without your support, help and lessons in physics and computing. If I turn out to be half of the physicist and computer scientist that you are I will be extremely proud.

To my friends at the University of Manchester and CERN, Dònal, Owen, Krishan, Srishti for Friday beers at Sandbar or R1, two amazing ski seasons and summers in Geneva. To Bruno and David for all the cycles and for making the lockdown summer of 2020 one of the best summers I've had.

Thank you to my girl friends since Day 1, Rosa, Faith, Philippa, Edie, Anna, Jodie, Rachael, Matilda, Charlotte. I could not have asked for a better group of best friends.

To my family: India my cousin and best friend, Sophie for cooking me many dinners and bringing love and food and Tipu to every Christmas.

Mum and Dad. You are the strongest people I know. I owe everything to you.

To Mum and Dad.

Preface

Education

Imperial College London

- MSci. Physics with Theoretical Physics
  September 2012 - June 2016
  MSci. Dissertation: *Rare decays at LHCb*
  Supervisor: Dr. Mitesh Patel

University of Manchester

- Doctor of Philosophy (PhD)
  September 2017 - July 2021
  School of Physics and Astronomy
  Thesis: *Measurement of the mixing parameters of neutral charm mesons and search for indirect CP violation with* $D^0 \to K^0_S\pi^+\pi^-$ *decays at LHCb*
  Supervisor: Dr. Mark Williams

Preface

The work presented in this thesis was undertaken by me on behalf of the LHCb collaboration. The work represents the combined efforts of the LHCb collaboration, and the analysis relies on the work of many other members of the collaboration. However, the physics analysis which I present in this thesis is my work. I produced all results, plots and histograms in the thesis, unless clearly stated. The $D^0 \to K^0_S\pi^+\pi^-$

analysis was the core part of my PhD studies and is the main topic of this thesis. However I also have worked on several other projects and contributions during my PhD studies, some of which are listed here:

- **Charm Monte Carlo Liaison:** I was appointed the role of the Charm (physics working group) Monte Carlo liaison from October 2018 - January 2021. This involved planning, coordinating and documenting all aspects of simulation generation for the working group members, consisting of approximately 40 active analyses.
- **Starterkit and Early Career Initiatives:** I took a leading role in early career initiatives within the LHCb collaboration. This included being the main organiser of the Starterkit workshop for approximately 80 PhD students, organising LHCb UK student meetings and being on the organising panel of the YETI (Young Experimentalist and Theorist Institute) 2020 conference.
- **VELO:** (Vertex Locator) I had a minor role in some of the activities on the upgraded LHCb Vertex Locator. This included, taking part in some Test Beam shifts in October 2018 for testing the modules for the detector upgrade, and the inspection of several hundred front end hybrids which are to be used on the LHCb VELO Upgrade modules for experiment control and data propagation.

CHAPTER 1

Introduction

The Standard Model (SM) of particle physics is the theory governing the fundamental particles and their interactions. The theory classifies the elementary particles. There are 12 spin-1/2 fermions consisting of six quarks: up, down, top, bottom, strange, charm and six leptons: the electron, muon and tau and corresponding neutrinos. Each of the 12 particles have a corresponding antiparticle. The fundamental strong, weak and electromagnetic forces are mediated by the gauge bosons; the gluon, W and Z bosons and the photon. Finally the spin-0 scalar Higgs boson provides the mechanism by which the gauge bosons gain their masses through the Higgs mechanism and spontaneous symmetry breaking.

The quarks carry colour charge and interact under the strong interaction. The strong force is responsible for the phenomena of colour confinement which binds quarks into hadrons, either a meson consisting of a quark-antiquark pair or a baryon consisting of three quarks. The quarks and three leptons (electron, muon, tau) are charged under the electromagnetic force and all fermions are subject to the weak interaction.

The photon is a massless particle which is the mediator of the electromagnetic force between electrically charged particles. The W and Z bosons are the mediators of the weak interaction between all fermions. The gluons are the force carriers of the strong force and mediate strong interactions between particles carrying colour charge (the quarks).

The Standard Model is experimentally verified to a remarkable degree of precision but does not explain all the phenomena observed in nature. The Standard Model has predicted the existence of a number of fundamental particles before their discoveries; including the W and Z bosons, the charm, bottom and top quarks and the Higgs boson. However the current theory has some significant theoretical shortcomings such as: the amount of charge-parity (*CP*) violation in the Standard Model is not sufficient to account for the asymmetry we observe in the universe today; there is no mechanism by which the neutrinos have mass, in other words whether they are Dirac or Majorana particles; there is no dark matter candidate despite compelling astronomical evidence that dark matter exists.

The Standard Model is based on a number of symmetries. Charge symmetry is the symmetry under the transformation of charge (electric charge). Parity symmetry is symmetry under the transformation of spatial coordinate(s). *CP* (charge-parity) symmetry states that the laws of physics should be the same if the particle is interchanged with its antiparticle (charge symmetry) while its spatial coordinates are inverted (parity symmetry). *CP*-violation has been well established in the kaon [37] and beauty [31] sectors and was observed in the charm sector in 2019 [10]. *CP*-violation in the charm sector is predicted to be small $O(10^{-3} - 10^{-4})$ [33] and is difficult to compute reliably due to low energy strong interactions. Any enhancement of *CP*-violation may therefore be a hint of new physics. *CP*-violation occurs in the SM in three ways: in direct decay, in mixing and in the interference between mixing and decay.

In the case of neutral mesons, the mass eigenstates are quantum superpositions of the flavour eigenstates. When the particle decays (as a mass state) it does so as a mixture of flavour states. This time-dependent phenomena results in a neutral meson oscillating into its antiparticle and vice versa, i.e. over time there is an oscillating probability of appearing as a given flavour state.

Mixing between a neutral meson and its antiparticle occurs through the weak interaction of neutral mesons, via the exchange of W bosons and heavy quarks (short-distance). For long-distance processes the main propagator is a stable *CP*-conjugate state eg. $\pi^+\pi^-$. Mixing occurs via both long-distance and short-distance contributions; in charm, long-distance contributions are thought to dominate, making theoretical predictions more challenging. In addition, due to the GIM mechanism [48] and CKM suppression [35], mixing is highly suppressed in the charm sector, making experimental measurements more difficult. New virtual particles may contribute to the amplitude, changing the oscillation rate, so any deviation from Standard Model predictions would constitute evidence for new physics effects. The parameters describing the time-dependent oscillations between a D^0 and a $\bar{D}^0$ are defined as $x \equiv (m_1 - m_2)/\Gamma$ and $y \equiv (\Gamma_1 - \Gamma_2)/2\Gamma$, where m_1 and m_2 and Γ_1 and Γ_2 are the masses and widths of the mass eigenstates and Γ is the average width. *CP*-violation in mixing is governed by a complex number q/p (described in more detail in Chapter 2) conventionally split into two real numbers $|q/p|$ and $\phi = arg(q/p)$. *CP*-symmetry corresponds to $|q/p| = 1$ and $\phi = 0$.

Mixing was postulated by Gell-Mann and Pais in 1955 [47] and was discovered in kaons by Lederman and others in 1957 [46]. Mixing in B mesons was discovered by the ARGUS collaboration in 1987 [23]. Evidence for mixing in the charm sector was reported by the B factories Belle [76] and BaBar [32] in 2007. Recently a model-independent method to measure the mixing parameters was performed by LHCb [9] and reported the first observation of a non-zero mass difference of neutral charm mesons by a single experiment [13].

The self-conjugate decay $D^0 \to K^0_S\pi^+\pi^-$ offers direct access to both the Cabibbo-favoured and doubly Cabibbo-suppressed decays in the same mode. Due to the rich resonant structure of the Dalitz plane of this decay, the Cabibbo-favoured and mixed decays can be separated. This allows direct access to the mixing parameters x and y through and time and phase-dependent amplitude fit to the Dalitz plane and decay-time of this decay.

The LHCb detector at the Large Hadron Collider (LHC) at CERN is a forward detector which was specifically designed for the study of hadrons containing a b quark and for measurements of *CP*-violation and rare decays. It has since expanded its physics program to charm physics. Due to the large cross section of $c\bar{c}$ at the LHC and the dedicated detector and Trigger at the LHCb experiment, LHCb is able to test Standard Model predictions of mixing and *CP*-violation in charm to unprecedented precision.

In this analysis the analysed LHCb data corresponds to a luminosity of 6 fb^{-1} collected during the Run 2 data-taking period from 2016-2018. This analysis uses D^0 mesons from semi-leptonic B meson decays, for example $B \to D^0\mu^-\bar{\nu}X$ where the B meson is charged or neutral, in which the initial flavour of the neutral D meson is tagged by the charge of the muon. The Run 1 data-taking period from 2011-2012 collected 3 fb^{-1} of data has been prepared and a combined Run 1 and Run 2 result is in preparation. For the purpose of this thesis, we present the Run 2 data and results.

1.1 World Averages

The world averages as of June 2021 for the mixing parameters for the no *CP*-violation case are:

$$\begin{aligned} x &= \left(0.51^{+0.12}_{-0.14}\right) \times 10^{-2} \\ y &= (0.63 \pm 0.07) \times 10^{-2} \end{aligned} \tag{1.1}$$

and for the CP violation allowed case:

$$\begin{aligned} x &= (0.37 \pm 0.12) \times 10^{-2} \\ y &= \left(0.68^{+0.06}_{-0.07}\right) \times 10^{-2} \\ |q/p| &= 0.951^{+0.053}_{-0.042} \\ \phi &= \left(-5.3^{+4.9}_{-4.5}\right)^{\circ} \end{aligned} \tag{1.2}$$

The world averages for the mixing and *CP*-violation parameters can be seen in Figure 1.1. It is also instructive to look at the world averages with the latest result included as of July 2021 which will be discussed in more detail in the following section. These are shown in Figure 1.2. Note the significant improvement from Figure 1.1 to Figure 1.2, almost exclusively due to the result described in the next section and in Ref. [13].

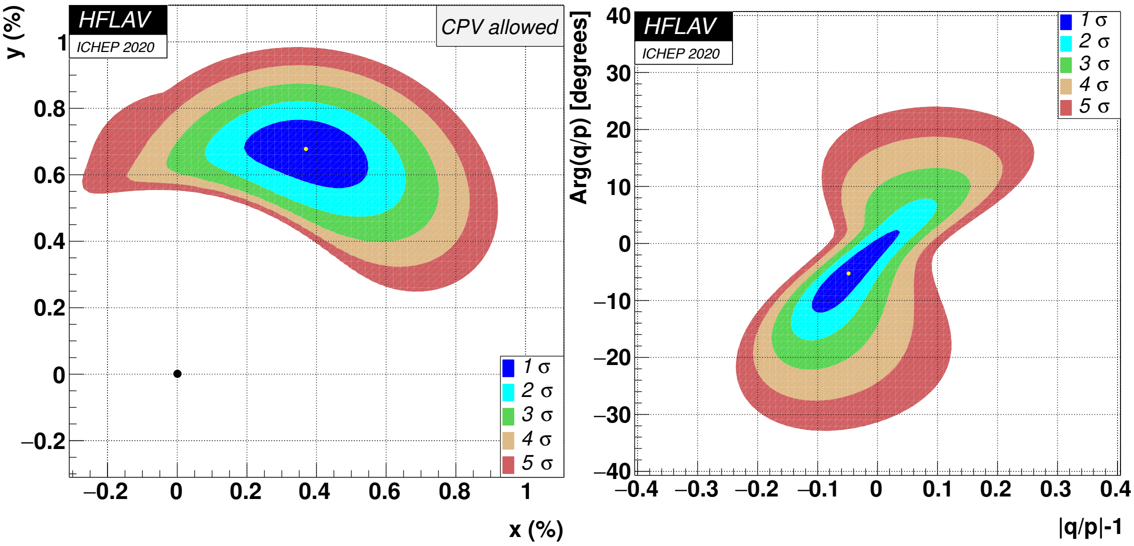

Figure 1.1: World averages June 2021 of the mixing and CP-violation parameters x, y, $|q/p|$ and ϕ from the Heavy Flavour Averaging Group [27].

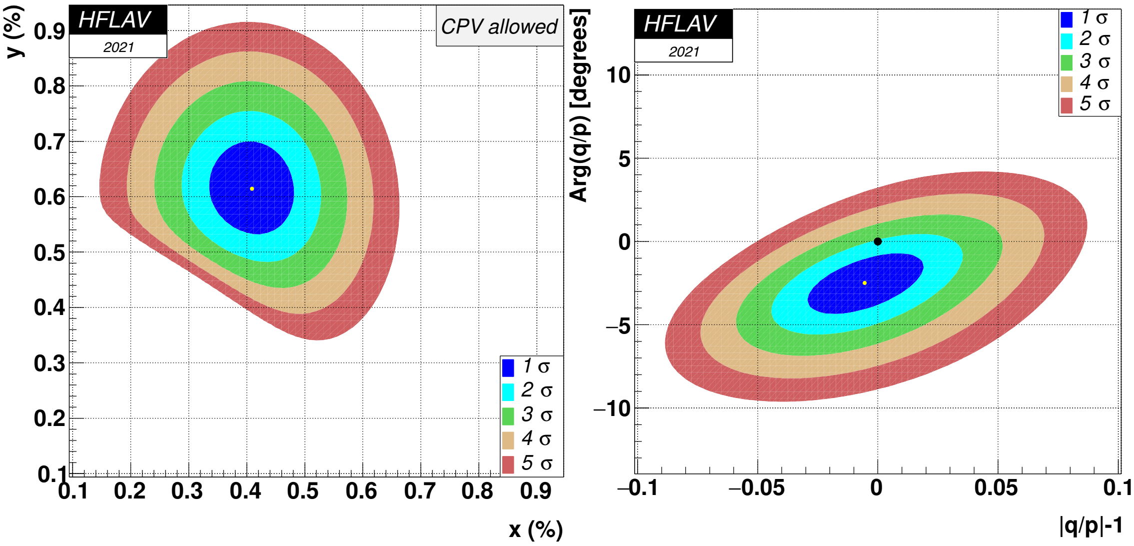

Figure 1.2: World averages July 2021 of the mixing and CP-violation parameters x, y, $|q/p|$ and ϕ from the Heavy Flavour Averaging Group [27]. Note the scale of the axis is significantly smaller than Figure 1.1.

1.2 Model-independent method

The mixing parameters x and y can be measured with LHCb data using a model-dependent or model-independent approach. The model-independent approach is based on the bin-flip method, which is optimised for the measurement of the parameter x [44]. This avoids the need for an accurate modelling of the efficiency across the phase-space and decay-time.

The self-conjugate $D^0 \to K^0_S\pi^+\pi^-$ decay is unique as it offers direct access to the mixing and *CP*-violation parameters. This decay gives access to the Cabibbo favoured and doubly Cabibbo-suppressed decays in the same channel. Due to the rich resonant substructure of the Dalitz plane of this decay, it is possible to separate regions in phase space which are dominated by direct Cabibbo-favoured decays from regions influenced by mixing. One can achieve this by splitting the Dalitz plane along the leading diagonal, where one half would correspond to Cabibbo-favoured decay and the opposite would correspond to mixing + Cabibbo-favoured decay. So the ratio of candidates in the upper half compared to the lower half gives a measure of the influence of mixing on the decay. More useful, and experimentally robust, is to examine the time-dependence of this ratio, from which the mixing and *CP*-violation parameters can be directly extracted. The sensitivity can be further improved by subdividing the Dalitz plane into several bin-pairs mirrored about the Dalitz diagonal. Hence the term ‘bin-flip’.

The Dalitz plot is divided into symmetric bins of approximately equal strong-phase differences between the D^0 and $\bar{D}^0$ amplitudes. The bins are symmetric with respect to the $m^2_- = m^2_+$ bisector, the bins are labelled $\pm b$ referring to the upper and lower regions of the Dalitz plane as shown in Figure 1.3. The strong-phase represents the interference between the Caibibbo-favoured and the doubly Cabibbo-suppressed decay modes. This can be measured at e^+e^- colliders such as CLEO [61] and BES-III [19] since quantum correlated D-$\bar{D}$ are produced. These can decay (not independently) into the same final state ($K^0_S\pi^+\pi^-$) giving access to the strong-phase between the Cabibbo-favoured and doubly Cabibbo-suppressed decay modes. Consequently this cannot be measured at LHCb so any measurements

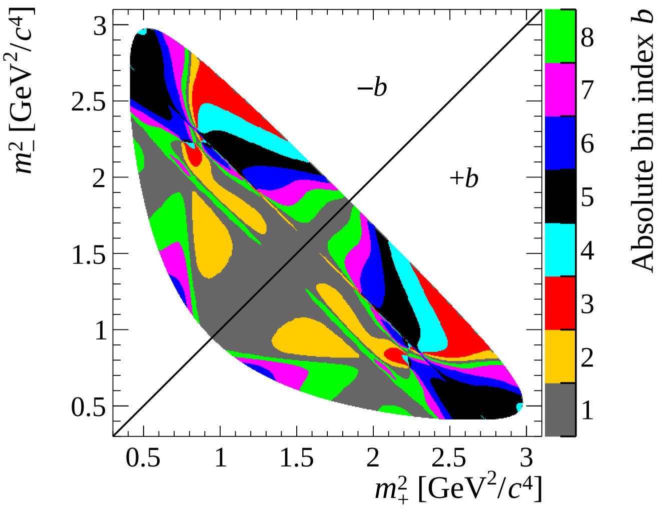

Figure 1.3: Binning of the $D^0 \rightarrow K_S^0\pi^+\pi^-$ Dalitz plot taken from the CLEO collaboration and used for the model-independent bin-flip analysis. The bins are symmetric across the bisector and are labelled ±b.

performed rely on these external inputs.

The data are further split into bins of decay-time labelled by the index j. For each bin in phase-space and decay-time, the ratio between initially produced D^0 and $\bar{D}^0$ is measured, given by R_{bj}^+ and R_{bj}^-:

$$R_{bj}^{\pm} \approx \frac{r_b + \frac{1}{4}r_b\langle t^2\rangle_j Re(z_{cp}^2 - \Delta z^2) + \frac{1}{4}\langle t^2\rangle_j |z_{cp} \pm \Delta z|^2 + \sqrt{r_b}\langle t\rangle_j Re[X_b^*(z_{CP} \pm \Delta z)]}{1 + \frac{1}{4}\langle t^2\rangle_j Re(z_{CP}^2 - \Delta z^2) + r_b\frac{1}{4}\langle t^2\rangle_j |z_{CP} \pm \Delta z|^2 + \sqrt{r_b}\langle t\rangle_j Re[X_b(z_{CP} \pm \Delta z)]} \tag{1.3}$$

In this equation $\langle t\rangle_j$ is the average decay-time of unmixed decays in bins of decay-time indexed j. The parameter r_b is the ratio of signal yields in the symmetric Dalitz plot bins $\pm b$ at $t = 0$. The parameter $X_b \equiv c_b - is_b$ is taken from external inputs and is the average strong-phase difference in the bins in phase-space indexed b, in this case this is taken from the most recent measurement of the strong-phase differences from BES-III [19]. The free parameters of the fit are r_b, z_{CP} and Δz defined by:

$$z_{CP} \pm \Delta z \equiv -(q/p)^{\pm 1}(y + ix) \tag{1.4}$$

Two analyses using this method have been published by LHCb. The first used

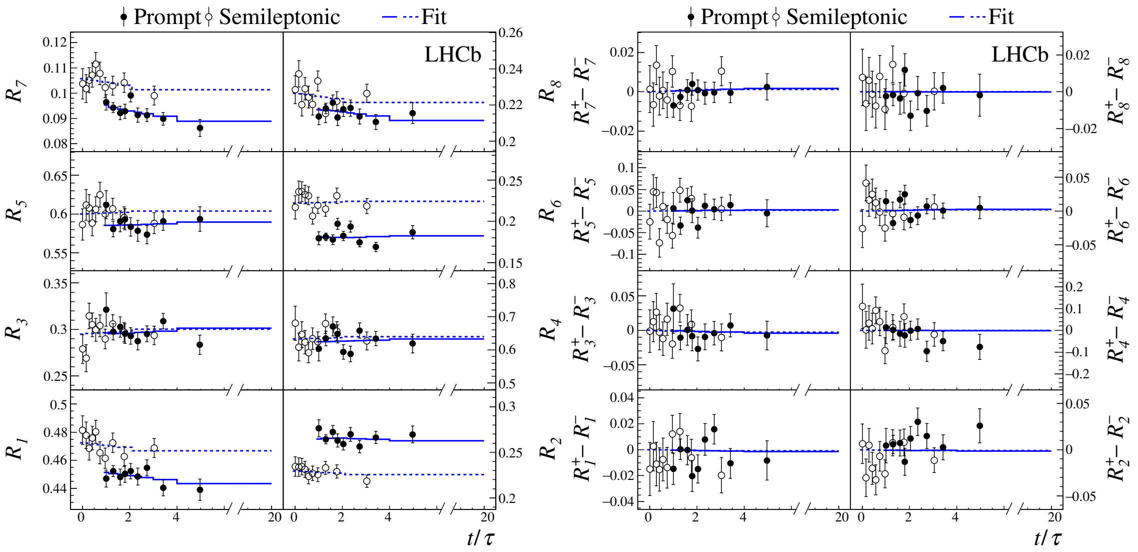

Figure 1.4: Ratios (left) and differences (right) of the D^0 and $\bar{D}^0$ yield ratios as a function of decay-time for each Dalitz bin. Prompt data are given by closed points, semi-leptonic data by open points. Fit projections for prompt is given by the solid line and for semi-leptonic by the dashed line [9].

prompt $D^{*+} \to D^0(\to K_S^0\pi^+\pi^-)\pi^+$ and semi-leptonic $B^- \to D^0(\to K_S^0\pi^+\pi^-)\mu^- X$ decays where the initial flavour of the neutral D meson is tagged by the charge of the pion in the prompt sample and the charge of the muon in the semi-leptonic sample. This used Run 1 data corresponding to 3 fb^{-1} [9]. The fit results are shown in Figure 1.4. The ratios of the D^0 and $\bar{D}^0$ yield ratios in each Dalitz bin as a function of decay-time are shown on the left where any time-dependence is a sign of mixing. The differences are shown on the right where any time-dependence is a sign of *CP*-violation.

The results are:

$$\begin{aligned} y_{CP} &= [0.74 \pm 0.36 \pm 0.11]\% \\ \Delta y &= [-0.06 \pm 0.16 \pm 0.03]\% \\ x_{CP} &= [0.27 \pm 0.16 \pm 0.04]\% \\ \Delta x &= [-0.053 \pm 0.070 \pm 0.022]\% \end{aligned} \tag{1.5}$$

where the uncertainties are statistical and systematic respectively [9]. The mixing and *CP*-violation parameters x and y and $|q/p|$ and ϕ can then be derived from the results.

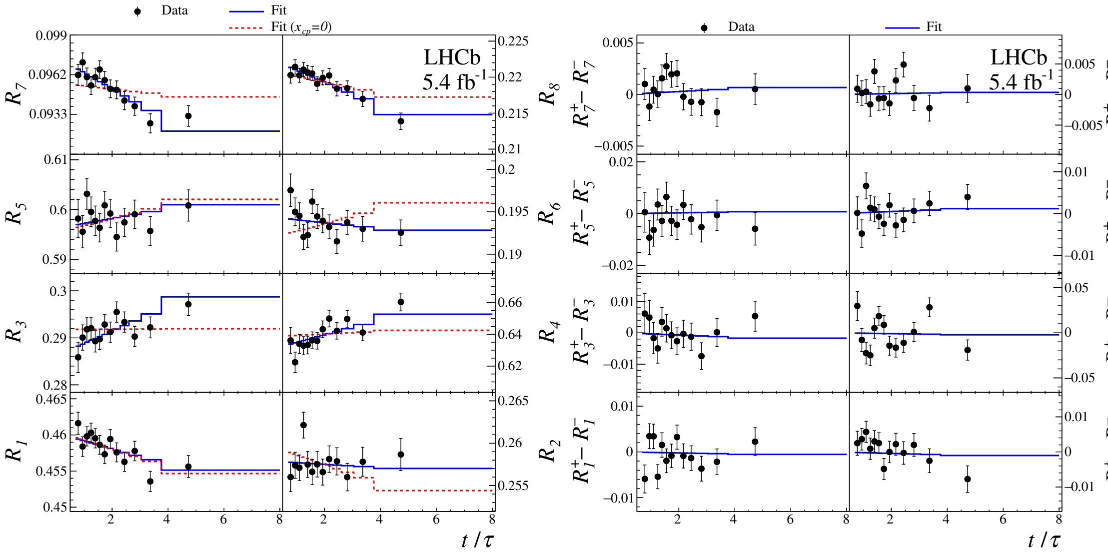

Figure 1.5: Ratios (left) and differences (right) of the D^0 and $\bar{D}^0$ yield ratios as a function of decay-time for each Dalitz bin. Prompt data are given by black points. Fit projections is given by the solid blue line and the $x_{CP} = 0$ is the red dashed line for comparison [13].

An updated result with the Run 2 dataset using prompt decays was published in 2021 [13] and constitutes the first observation of a non-zero mass difference (x) in neutral charm mesons by a single experiment. The results are:

$$\begin{aligned} y_{CP} &= [0.459 \pm 0.120_{\text{stat}} \pm 0.085_{\text{syst}}]\% \\ \Delta y &= [0.020 \pm 0.036_{\text{stat}} \pm 0.013_{\text{syst}}]\% \\ x_{CP} &= [0.397 \pm 0.046_{\text{stat}} \pm 0.029_{\text{syst}}]\% \\ \Delta x &= [-0.027 \pm 0.018_{\text{stat}} \pm 0.001_{\text{syst}}]\% \end{aligned} \tag{1.6}$$

The results are shown in Figure 1.5 where the slope of the blue line in the left hand plot indicates mixing. The red dashed line is the no mixing $x_{CP} = 0$ case for comparison.

1.3 Other existing measurements

Other previous measurements using $D^0 \to K_S^0\pi^+\pi^-$ decays have been published by the CLEO, BaBar, Belle and CDF collaborations. A measurement of the time-integrated *CP* asymmetry was published by CDF in 2012, which is consistent with no direct *CP* violation [14]. The measurements of the $D^0 - \bar{D}^0$ mixing parameters and search for indirect *CP* violation have followed a model-dependent approach, with the exception of the model-independent method described in the previous section. The most recent determination of the amplitude model of $D^0 \to K^0_S\pi^+\pi^-$ decays was from the Belle and BaBar collaborations in 2018 [20]. The Belle data sample corresponds to 924 fb^{-1} recorded at or near the $\Upsilon(4S)$ and $\Upsilon(5S)$ resonances. This dataset provides a high statistics sample of $e^+e^- \to c\bar{c}$ events that is used to determine the $D^0 \to K^0_S\pi^+\pi^-$ decay amplitudes, collected at the Belle detector [15]. The combined Belle and BaBar data samples correspond to data collected at the $\Upsilon(4S)$ resonance and contains $(471 \pm 3) \times 10^6$ $B\bar{B}$ pairs from the BaBar detector and $(772 \pm 11) \times 10^6$ from Belle. The amplitude model reported in this analysis is used as the baseline for this work when developing the amplitude model as discussed in Chapter 8.

1.4 Analysis method

Alternatively to the model-independent approach, the parameters of interest x and y (and the *CP*-violation parameters) can be extracted from a time and phase-space dependent fit of an amplitude model to the Dalitz variables and decay time of the $D^0 \to K^0_S\pi^+\pi^-$ decay. The model consists of resonant and non-resonant components and describes the $D^0 \to K^0_S\pi^+\pi^-$ decay as a superposition of decays through intermediate resonances and their interferences. The initial resonant and non-resonant components are taken from a published analysis of this channel by the Belle and Babar collaborations based on a large fraction of their collected data [20]. The background model is derived from a data-driven approach.

The event-selection and reconstruction may distort the kinematics of the final state particles in the decay, leading to a non-uniform acceptance across the Dalitz plane. Similarly, there may be variations in acceptance as a function of decay-time. The phase-space and decay-time acceptance is derived from simulation and accounted for in the final amplitude fit model. The LHCb detector also has a finite decay-time resolution which also needs to be accounted for in the fit. The background distribution for the final amplitude fit is derived from data by extracting the background sWeights from the events which have passed all the selection criteria. For each candidate, a signal probability is also derived and used in the fit to assign the appropriate combination of signal and background PDFs for each candidate. An unbinned time-dependent maximum-likelihood fit to data is performed to extract the parameters of interest x and y.

This thesis presents the measurement of the mixing parameters of neutral charm mesons and a search for indirect *CP*-violation using semi-leptonic $D^0 \to K^0_S\pi^+\pi^-$ decays collected at the LHCb detector during the Run 2 data-taking period. The theory is described in Chapter 2, the LHCb detector in Chapter 3. The analysis method is described in more detail in Chapter 4. The data selection is described in Chapter 5. The simulated Monte Carlo data used in this analysis is described in Chapters 6 and 7. The amplitude fit model is described in Chapter 8, toy studies in Chapter 9 and the systematic uncertainties in Chapter 10. The final results and conclusion are presented in Chapter 11.

CHAPTER 2

Theory

2.1 The Standard Model

The measurement described in this thesis is interpreted in the context of the Standard Model of particle physics (SM). The SM is a theoretical framework used to describe three of the four fundamental forces in the universe, as well as classifying all known elementary particles and their interactions. The three fundamental forces described by this model are the electromagnetic force, as well as the weak and the strong force. The gravitational force, which is negligible on the scale of fundamental particle physics, is not included in the SM. The fundamental particles are classified as twelve spin-1/2 fermions, the spin-1 gauge bosons which are the mediators of the fundamental forces, and the spin-0 Higgs boson. The fermions are further classified into six quarks (up, down, charm, strange, top, bottom) and six leptons (electron, muon, tau and corresponding neutrinos). Each fermion has a corresponding antiparticle partner of the same mass but opposite physical charges (such as electric charge). The leptons and quarks are charged under the weak interaction which is mediated by the $W^{\pm}$ and Z bosons, the three charged leptons electron, muon and tau are also charged under the electromagnetic force which is mediated by the photon. The quarks are charged under the electromagnetic force and have a color charge of the strong force, this is mediated by eight gluons. The Higgs boson provides the

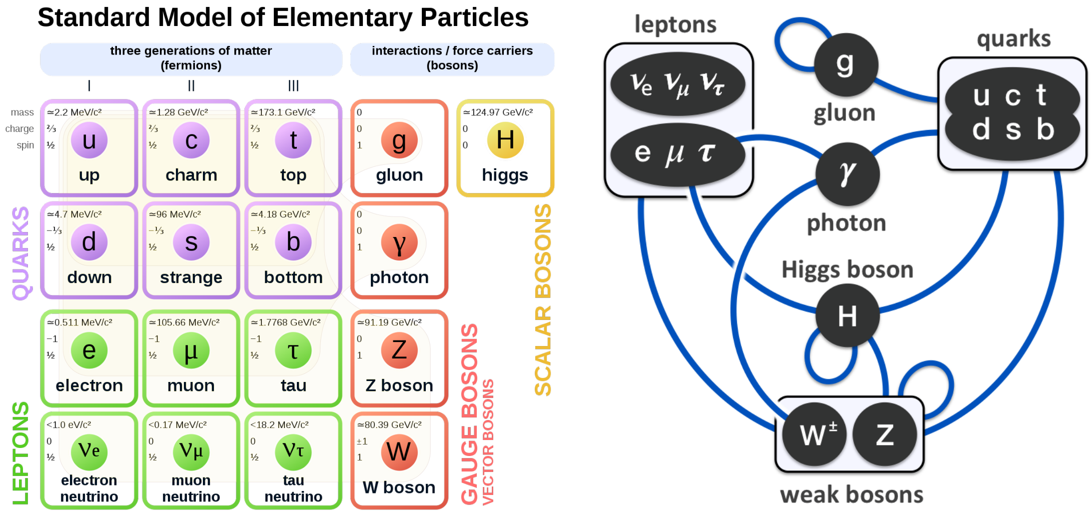

Figure 2.1: The elementary particles of the Standard Model including the matter particles (fermions) and force carriers (bosons); the diagram on the left shows the charge, mass and spin of the particles and the diagram on the right shows the interactions between the different particles. Images taken from Ref. [83].

mechanism by which the fundamental particles gain their masses, through the Higgs mechanism and spontaneous symmetry breaking. Hadronisation is the process of the formation of hadrons out of quarks and gluons. Hadrons are formed due to that fact that quarks can only exist in colorless combinations, which is in turn caused by the fact that gluons are non-Abelian and therefore self-interact. The most common of the bound states of quarks are the meson $q\bar{q}$ and the baryon formed of qqq or $\bar{q}\bar{q}\bar{q}$. More complex states consisting of more quarks are possible; such as pentaquarks formed of $q\bar{q}qqq$ which have been observed at the LHCb detector [1].

Quarks and leptons are categorised in terms of three generations. Each quark generation contains an u-type quark with electric charge $Q = +2/3$ and a d-type quark with charge $Q = -1/3$. Due to the fact that the quark mass eigenstates are linear combinations of the flavour eigenstates, they can mix (change flavour) under the weak force. Quark mixing is governed by the Cabbibo-Kobayashi-Maskawa (CKM) matrix [35, 56]:

$$V_{CKM} = \begin{pmatrix} V_{ud} & V_{us} & V_{ub} \\ V_{cd} & V_{cs} & V_{cb} \\ V_{td} & V_{ts} & V_{tb} \end{pmatrix} \tag{2.1}$$

The elements of the CKM matrix V_{ij} describe the coupling strength of the flavour-changing weak current between u and d-type quarks, which is mediated by the $W^{\pm}$ bosons. The CKM matrix has a hierarchical structure where off-diagonal elements are smaller and therefore the quarks are more likely to interact with those of the same generation.

In particular, tree-level decays of particles containing a charm quark depend on the matrix elements V_{ud}, V_{us}, V_{cd} and V_{cs}. The hierarchy of the CKM matrix elements becomes evident using the Wolfenstein parametrisation, which is based on the expansion in powers of the small parameter λ where $|V_{ud}| \approx |V_{cs}| \approx 1 - \lambda$ and $|V_{us}| \approx |V_{cd}| \approx \lambda$ [84]. Tree-level transitions $u \to s$ and $c \to d$ depend on the V_{us} and V_{cd} matrix elements respectively and are known as doubly Cabibbo suppressed (DCS) decays. They have small branching fractions compared to $c \to s$ Cabibbo-favoured (CF) transitions and singly Cabibbo-suppressed (SCS) decays. In the SM, any weak interactions mediated by the neutral Z boson conserve quark flavour. Processes which change quark flavour without changing the charge (flavour-changing neutral currents) are only allowed in the SM in higher order processes involving multiple W bosons and are highly suppressed by the Glashow–Iliopoulos–Maiani (GIM) mechanism [48].

The SM is parametrised under the gauge symmetry group $\mathrm{SU}(3)_C \times \mathrm{SU}(2)_L \times \mathrm{U}(1)_Y$. The theory of strong interaction between quarks carrying the quantum number colour is described by the $\mathrm{SU}(3)_C$ gauge group and the $\mathrm{SU}(2)_L \times$ $\mathrm{U}(1)_Y$ describes the unification of electromagnetic and weak interactions. The labels of the gauge groups correspond to the quantum number associated with the interaction: $\mathrm{SU}(3)_C$ denotes the color charge carried by quarks and gluons, $\mathrm{SU}(2)_L$ denotes that the weak interaction only couples to left-handed fermions, and $\mathrm{U}(1)_Y$ denotes weak hypercharge, $Y = 2(Q - T_3)$ where Q is the charge of the electromagnetic force and T_3 is the weak isospin. The gauge groups of degree n have $n^2 - 1$ generators; for example the gauge group $\mathrm{SU}(2)_L$ is of degree $n = 2$ and therefore has three generators. The generators of the gauge group lead to the existence of the gauge bosons. Therefore the $\mathrm{SU}(3)_C$ group has $n = 3$ and eight generators which correspond to the eight gluons. The $\mathrm{SU}(2)_L \times \mathrm{U}(1)_Y$ electroweak symmetry group has four generators $W_{1,2,3}$ and B; the generators $W_{1,2}$ correspond to the gauge bosons $W^{\pm}$ and the generators W_3 and B mix to form the neutral Z boson and the photon.

As mentioned the SM has some significant shortcomings. For example, the amount of *CP*-violation allowed in the SM does not account for the matter-antimatter symmetry seen in the universe today. Numerous cosmological observations provide evidence for the existence of dark matter; for example galaxy rotation curves [42], gravitational lensing [79] and the angular power spectrum of the cosmic microwave background [21]. However the SM does not provide a dark matter candidate.

2.1.1 Electroweak theory

The electroweak theory is the unification of the electromagnetic and weak forces [49, 81] and is described by the $\mathrm{SU}(2)_L \times \mathrm{U}(1)_Y$ gauge symmetry group. The fields of the SM are classified as quark and lepton fields with quark doublets Q^i_L and singlets u^i_R and d^i_R and lepton doublets L^i_L and singlets e^i_R where:

$$Q^i_L = \begin{pmatrix} u \\ d \end{pmatrix}_L \quad L^i_L = \begin{pmatrix} \nu_e \\ e \end{pmatrix} \tag{2.2}$$

are quark and lepton doublets respectively, u and d represent the u-type and d-type quarks, e represents the three leptons e, μ, τ, and ν_e represents the corresponding neutrinos. We introduce left and right-handed chiral spinor fields, e_L and e_R for the electron:

$$\begin{aligned} e_L &\equiv P_L\psi = \frac{1-\gamma^5}{2}\psi \\ e_R &\equiv P_R\psi = \frac{1+\gamma^5}{2}\psi \end{aligned} \tag{2.3}$$

where these are eigenstates of the helecity operator, ψ denotes the spinor field and $\gamma^5 = i\gamma^0\gamma^1\gamma^2\gamma^3$ and $\{\gamma^0, \gamma^1, \gamma^2, \gamma^3\}$ are the gamma or Dirac matrices.

The dynamics of elementary particles under the influence of the electroweak interaction can be derived from the electromagnetic Lagrangian of a free fermion field $\mathcal{L}_0$ by considering the effects of local phase transformations and accounting for weak currents:

$$\mathcal{L}_0 = i\bar{\psi}\gamma_\mu\partial^\mu\psi - m\bar{\psi}\psi \tag{2.4}$$

Consider a local gauge transformation

$$\psi(x) \rightarrow \psi'(x) = e^{i\alpha(x)}\psi(x) \tag{2.5}$$

and replace ∂^μ with the covariant derivative

$$D_\mu \equiv \partial_\mu - ieA_\mu \tag{2.6}$$

where

$$A_\mu \rightarrow A'_\mu = A_\mu + \frac{1}{e}\partial_\mu \alpha \tag{2.7}$$

then the free fermion Lagrangian is invariant under the local gauge transformation:

$$\begin{aligned} \mathcal{L}_0 \rightarrow \mathcal{L}'_0 &= i\bar{\psi}\gamma_\mu D^\mu \psi - m\bar{\psi}\psi \\ &= \bar{\psi}(i\gamma_\mu \partial^\mu - m)\psi + e\bar{\psi}\gamma^\mu A_\mu \psi \end{aligned} \tag{2.8}$$

The demand of local gauge invariance introduces the gauge field A_μ, which can be interpreted physically as the field of the photon. Now consider the Lagrangian of Quantum Electrodynamics (QED):

$$\mathcal{L}_{QED} = \bar{\psi}(i\gamma_\mu \partial^\mu - m)\psi + e\bar{\psi}\gamma^\mu A_\mu \psi - \frac{1}{4}F_{\mu\nu}F^{\mu\nu} \tag{2.9}$$

where $F_{\mu\nu} = \partial_\mu A_\nu - \partial_\nu A_\mu$ is the field strength tensor and the last term is the kinetic term for the photon field A_μ. The Lagrangian for the electroweak theory is given by:

$$\begin{aligned} \mathcal{L}_{EW} =& \bar{L}^i_L \gamma^\mu \left[i\partial_\mu - g\frac{\vec{\tau}}{2}\vec{W}_\mu - g'\frac{Y}{2}B_\mu \right] L^i_L \\ &+ \bar{e}^i_R \gamma^\mu \left[i\partial_\mu - g'\frac{Y}{2}B_\mu \right] e^i_R - \frac{1}{4}B_{\mu\nu}B^{\mu\nu} - \frac{1}{4}\vec{W}_{\mu\nu}\vec{W}^{\mu\nu} \end{aligned} \tag{2.10}$$

where

- L^i_L and e^i_L are the doublet and singlet fields for the leptons as described in Equations 2.3 and 2.2,
- $\vec{\tau} = (\tau_1, \tau_2, \tau_3)$ are the Pauli matrices,
- $\vec{W}_\mu = (W^1_\mu, W^2_\mu, W^3_\mu)$ and B_μ are vector fields,

- Y is the weak hypercharge, the generator associated with the U$(1)_Y$ symmetry group,
- $B_{\mu\nu} = \partial_\mu B_\nu - \partial_\nu B_\mu$ and $\vec{W}_{\mu\nu} = \partial_\mu \vec{W}_\nu - \partial_\nu \vec{W}_\mu$ are the antisymmetric field strength tensors,
- g and g' are the coupling strengths for $\vec{W}_\mu$ and B_μ respectively.

The linear combination of the vector fields W^1_μ and W^2_μ leads to the physical fields $W^\pm_\mu = \frac{1}{\sqrt{2}}(W^1_\mu \mp iW^2_\mu)$ and describe the massive $W^\pm$ bosons. The B_μ and W^3_μ fields mix:

$$\begin{aligned} A_\mu &= B_\mu \cos\theta_W + W^3_\mu \sin\theta_W \\ Z_\mu &= -B_\mu \sin\theta_W + W^3_\mu \cos\theta_W \end{aligned} \tag{2.11}$$

where the fields A_μ and Z_μ correspond to the massless photon and massive Z boson respectively and θ_W is the Weinberg angle. The Weinberg angle can be expressed by the mixing of the B and W_3 gauge bosons to form the Z boson and the photon through spontaneous symmetry breaking:

$$\begin{pmatrix} \gamma \\ Z \end{pmatrix} = \begin{pmatrix} \cos\theta_W & \sin\theta_W \\ -\sin\theta_W & \cos\theta_W \end{pmatrix} \begin{pmatrix} B \\ W_3 \end{pmatrix} \tag{2.12}$$

It also gives the relationship between the mass of the Z and W bosons at leading order:

$$m_Z = \frac{m_W}{\cos\theta_W} \tag{2.13}$$

2.1.2 Higgs mechanism

In the Salam-Weinberg model of electroweak unification, the Higgs mechanism is embedded in the U$(1)_Y\times$SU$(2)_L$ local gauge symmetry of the electroweak sector of the SM. This brief example will show the key concepts of how the Higgs mechanism leads to the generation of the masses of the gauge bosons. The simplest Higgs model consists of two complex scalar fields:

$$\phi = \begin{pmatrix} \phi^+ \\ \phi^0 \end{pmatrix} = \frac{1}{\sqrt{2}} \begin{pmatrix} \phi_1 + i\phi_2 \\ \phi_3 + i\phi_4 \end{pmatrix} \tag{2.14}$$

The Lagrangian for this doublet scalar field is:

$$\mathcal{L} = (\partial_\mu \phi)^\dagger (\partial^\mu \phi) - V(\phi) \tag{2.15}$$

where the Higgs potential is given by:

$$V(\phi) = \mu^2 \phi^\dagger \phi + \lambda (\phi^\dagger \phi)^2 \tag{2.16}$$

We minimise $V(\phi)$ to obtain the set of degenerate minima for $\mu^2 < 0$ satisfying:

$$\phi^\dagger \phi = -\frac{\mu^2}{2\lambda} \tag{2.17}$$

In order to ensure that the photon is massless after symmetry breaking, the minimum of the potential must correspond to a non-zero vacuum expectation value of the scalar field ϕ^0. We chose the ground state:

$$\phi_G = \frac{1}{\sqrt{2}} \begin{pmatrix} 0 \\ v \end{pmatrix} \tag{2.18}$$

We expand the field about its minimum, this is called the unitary gauge:

$$\phi(x) = \frac{1}{\sqrt{2}} \begin{pmatrix} 0 \\ v + \eta(x) \end{pmatrix} \tag{2.19}$$

The mass terms of the gauge bosons can be identified by writing the Lagrangian in Equation 2.15 such that it is invariant under local SU(2)$_L$×U(1)$_Y$ gauge symmetry and replacing the derivatives with the appropriate covariant derivatives. The mass terms are identified by the relevant term of the Lagrangian:

$$\mathcal{L} \supset \frac{1}{8} v^2 g^2 (W^1_\mu W^{1\mu} + W^2_\mu W^{2\mu}) + \frac{1}{8} v^2 (g W^3_\mu + g' B_\mu)(g W^{3\mu} + g' B^\mu) \tag{2.20}$$

by comparison with the mass terms:

$$\frac{1}{2}m_W^2 W_\mu^1 W^{1\mu} \quad \text{and} \quad \frac{1}{2}m_W^2 W_\mu^2 W^{2\mu} \tag{2.21}$$

Therefore the mass of the $W^\pm$ bosons is given by:

$$m_W = \frac{1}{2}gv \tag{2.22}$$

To identify the masses of the Z boson and the photon we compare the last term in Equation 2.15 to the mass terms:

$$\frac{1}{2}m_Z^2 Z_\mu Z^\mu \quad \text{and} \quad \frac{1}{2}m_A^2 A_\mu A^\mu \tag{2.23}$$

which leads to:

$$A_\mu = \frac{g' W_\mu^3 + g B_\mu}{\sqrt{g^2 + g'^2}} \quad \text{and} \quad Z_\mu = \frac{g W_\mu^3 - g' B_\mu}{\sqrt{q^2 + g'^2}} \tag{2.24}$$

and

$$m_A = 0 \quad \text{and} \quad m_Z = \frac{1}{2}v\sqrt{g^2 + g'^2} \tag{2.25}$$

By using the relationship between the physical fields and underlying fields in Equation 2.11 the mass of the Z boson can be expressed as:

$$m_Z = \frac{1}{2}\frac{g}{\cos\theta_W}v \tag{2.26}$$

and combining Equations 2.22 and 2.26 one gets the relation with the Weinberg angle θ_W given in Equation 2.13. The Higgs mechanism for the spontaneous symmetry breaking of the $\mathrm{SU}(2)_L \times \mathrm{U}(1)_Y$ gauge group generates the masses of the $W^\pm$ and Z bosons. Similarly it is also responsible for the generation of the fermion masses. The relevant terms in the Lagrangian for the electron doublet is:

$$\mathcal{L}_e \supset -\frac{g_e}{\sqrt{2}}v(\bar{e}_L e_R + \bar{e}_R e_L) - \frac{g_e}{\sqrt{2}}h(\bar{e}_L e_R + \bar{e}_R e_L) \tag{2.27}$$

The Yukawa coupling g_e is chosen to be consistent with the observed electron mass:

$$m_e = \frac{g_e v}{\sqrt{2}} \tag{2.28}$$

Similarly for an u quark the Lagrangian is given by:

$$\mathcal{L}_u \supset -\frac{g_u}{\sqrt{2}} v(\bar{u}_L u_R + \bar{u}_R u_L) - \frac{g_u}{\sqrt{2}} h(\bar{u}_L u_R + \bar{u}_R u_L) \tag{2.29}$$

and hence the masses of the quarks are given by:

$$m_u = \frac{g_u v}{\sqrt{2}} \quad \text{and} \quad m_d = \frac{g_d v}{\sqrt{2}} \tag{2.30}$$

where g_u and g_d are the Yukawa couplings for the u and d quarks respectively and the vacuum expectation value of the Higgs field is $v = 246$ GeV.

2.1.3 Quantum chromodynamics

The theory of the strong interaction is governed by Quantum Chromodynamics (QCD) and is described by the non-abelian gauge symmetry group SU$(3)_C$. The generators of the gauge group SU$(3)_C$ are the Gell-Mann matrices which are defined by $[T_a, T_b] = i f_{abc} T_c$ where f_{abc} are the antisymmetric structure constants. Similarly to the QED Lagrangian, a gauge invariant QCD Lagrangian can be written by introducing the covariant derivative:

$$D_\mu \equiv \partial_\mu + i g T_a G^a_\mu \tag{2.31}$$

where G^a_μ transforms as follows under a local gauge transformation:

$$G^a_\mu \to G^a_\mu - \frac{1}{g}\partial_\mu \alpha^a - f_{abc}\alpha_b G^c_\mu \tag{2.32}$$

The gauge invariant QCD Lagrangian for a colour field q is then given by:

$$\mathcal{L}_{QCD} = \bar{q}(i\gamma^\mu \partial_\mu - m)q - g(\bar{q}\gamma^\mu T^a q)G^a_\mu - \frac{1}{4}G^a_{\mu\nu}G^{\mu\nu}_a \tag{2.33}$$

which is invariant under the local gauge transformation:

$$q(x) \rightarrow e^{i\alpha_a(x)T^a} q(x) \tag{2.34}$$

where $a = 1, ..., 8$ and $G^a_{\mu\nu} \equiv \partial_\mu G^a_\nu - \partial_\nu G^a_\nu - g f_{abc} G^b_\mu G^c_\nu$. The generators of $\mathrm{SU}(3)_C$, T^a give rise to the eight gluons, the mediators of the strong force. In contrast to the electroweak interaction, no experimental evidence for the violation of the symmetry under charge parity transformations in the strong interaction has been observed. QCD does allow a violation of *CP* symmetry and it is not understood why *CP* should be conserved in QCD; this is known as the strong *CP* problem.

2.2 Neutral meson mixing

Neutral meson mixing is the time-dependent phenomena of a particle changing into its antiparticle and vice versa. This occurs because the mass eigenstates are linear combinations of the flavour eigenstates. Mixing in the charm sector is complimentary to studies in the beauty and kaon sectors. Charm mixing is highly suppressed so is the least experimentally constrained of the three sectors. In addition the charm system is the only one which comprises up-type quarks, so it has unique sensitivity to new physics coupling preferentially to the up sector.

Mixing occurs in the charm sector when a D^0 transitions into a $\bar{D}^0$ or vice versa. This occurs via a flavour-changing current which changes the flavour quantum number by $|\Delta F| = 2$. In the charm sector, mixing has contributions from the d and s transitions in the box diagram in Figure 2.2. Due to the GIM mechanism, these contribute with approximately equal magnitude and opposite sign where the sign change comes from the CKM matrix. The GIM mechanism is an efficient cancellation of two amplitudes of similar magnitude and opposite sign, one corresponding to a down quark exchange and one to a strange quark exchange. Therefore weak interactions which change strangeness by $|\Delta S| = 2$ are highly suppressed. In the box diagram in Figure 2.2, the vertex factors from the d and s transitions nearly cancel, and the amplitude of the b transition is small due to the off-diagonal elements of the CKM matrix $V^*_{ci} V_{ui}$.

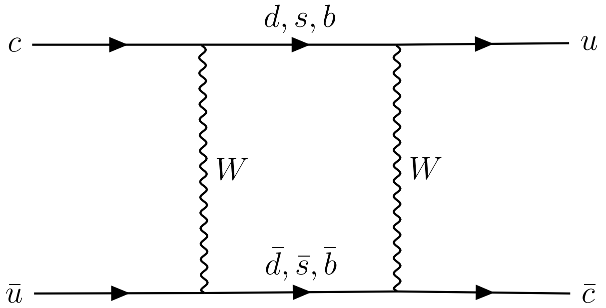

Figure 2.2: Feynman box diagram for the $D^0 - \bar{D}^0$ transition via the exchange of intermediate quarks

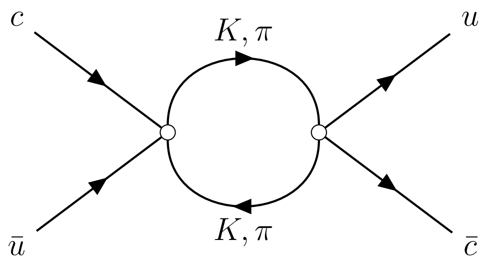

Figure 2.3: Diagram of a $D^0 - \bar{D}^0$ transition through long-distance hadronic interactions.

Mixing can occur through long-distance and short-distance contributions; in charm long-distance effects are expected to dominate due to the suppression mechanisms described above, making theoretical predictions challenging [68]. A Feynman diagram of a short-distance $D^0 - \bar{D}^0$ transition can be seen in Figure 2.2 and for the long-distance hadronic contribution in Figure 2.3.

Neutral meson mixing can be characterised by epxressing the mass eigenstates as linear combinations of the flavour eigenstates:

$$|D_{1,2}\rangle = p\left|D^0\right\rangle \pm q\left|\bar{D}^0\right\rangle \tag{2.35}$$

where p and q satisfy $|p^2| + |q^2| = 1$. The effective Hamiltonian describing D^0 mixing is given by $\mathcal{H} = \mathbf{M} - i\mathbf{\Gamma}$ where $\mathbf{M}$ and $\mathbf{\Gamma}$ and the Hermitian mass and decay matrices. The eigenstates of this Hamiltonian are:

$$\mathcal{H}\,|D_{1,2}\rangle = \lambda_{1,2}\,|D_{1,2}\rangle \tag{2.36}$$

where the eigenvalues are $\lambda_{1,2} \equiv m_{1,2} - i\Gamma_{1,2}/2$ and $m_{1,2}$ and $\Gamma_{1,2}$ are the masses and decay widths respectively. The time evolution of the eigenstates is then given by:

$$\begin{aligned}|D_{1,2}(t)\rangle &= e^{-i\lambda_{1,2}t}\,|D_{1,2}(0)\rangle \\ &= e^{-im_{1,2}t}e^{-\frac{\Gamma_{1,2}}{2}t}\,|D_{1,2}(0)\rangle\end{aligned} \tag{2.37}$$

We can introduce the mixing parameters x and y:

$$x = \frac{m_1 - m_2}{\Gamma} \quad \text{and} \quad y = \frac{\Gamma_1 - \Gamma_2}{2\Gamma} \tag{2.38}$$

where $m = (m_1 + m_2)/2$ and $\Gamma = (\Gamma_1 + \Gamma_2)/2$ are the average mass and decay widths respectively. The time evolution of the mass eigenstates in Equation 2.37 can then be written as:

$$\begin{aligned}|D_{1,2}(t)\rangle &= e^{-imt}e^{-\frac{\Gamma}{2}t}e^{\mp(y+ix)\frac{\Gamma}{2}t}\,|D_{1,2}(0)\rangle \\ &\equiv e_{1,2}(t)\,|D_{1,2}(0)\rangle\end{aligned} \tag{2.39}$$

We use Equation 2.35 to derive the time evolution of the flavour eigenstates which are given by:

$$\begin{aligned}\left|D^0(t)\right\rangle &= \frac{e_1(t)+e_2(t)}{2}\left|D^0\right\rangle + \frac{q}{p}\frac{e_1(t)-e_2(t)}{2}\left|\bar{D}^0\right\rangle \\ \left|\bar{D}^0(t)\right\rangle &= \frac{e_1(t)+e_2(t)}{2}\left|\bar{D}^0\right\rangle + \frac{p}{q}\frac{e_1(t)-e_2(t)}{2}\left|D^0\right\rangle\end{aligned} \tag{2.40}$$

The time-dependent amplitudes for D^0 and $\bar{D}^0$ decaying into a final state f, $\mathcal{A}_f(t)$ and $\bar{\mathcal{A}}_f(t)$ are therefore defined as:

$$\begin{aligned}\mathcal{A}_f(t) \equiv \langle f|\,\mathcal{H}\left|D^0(t)\right\rangle &= \langle f|\,\mathcal{H}\frac{e_1(t)+e_2(t)}{2}\left|D^0\right\rangle + \langle f|\,\mathcal{H}\frac{q}{p}\frac{e_1(t)-e_2(t)}{2}\left|\bar{D}^0\right\rangle \\ \bar{\mathcal{A}}_f(t) \equiv \langle f|\,\mathcal{H}\left|\bar{D}^0(t)\right\rangle &= \langle f|\,\mathcal{H}\frac{e_1(t)+e_2(t)}{2}\left|\bar{D}^0\right\rangle + \langle f|\,\mathcal{H}\frac{p}{q}\frac{e_1(t)-e_2(t)}{2}\left|D^0\right\rangle\end{aligned} \tag{2.41}$$

This can be rewritten as:

$$
\begin{aligned}
\mathcal{A}_f(t) &= \frac{e_1(t)+e_2(t)}{2}\mathcal{A}_f + \frac{q}{p}\frac{e_1(t)-e_2(t)}{2}\bar{\mathcal{A}}_f \\
&= \frac{1}{2}e_1(t)\left(A+\frac{q}{p}B\right) + \frac{1}{2}\left(A-\frac{q}{p}B\right) \\
\bar{\mathcal{A}}_f(t) &= \frac{e_1(t)+e_2(t)}{2}\bar{\mathcal{A}}_f + \frac{p}{q}\frac{e_1(t)-e_2(t)}{2}\mathcal{A}_f \\
&= \frac{1}{2}e_1(t)\left(B+\frac{p}{q}A\right) + \frac{1}{2}e_2(t)\left(B-\frac{p}{q}A\right)
\end{aligned}
\tag{2.42}
$$

where the notation $A \equiv \mathcal{A}_f$ and $B \equiv \bar{\mathcal{A}}_f$ is used. Substitute $e_{1,2}(t)$ in Equation 2.39 into the above Equation 2.42. The square of the time-dependent amplitude is then given by:

$$
\begin{aligned}
\mid \mathcal{A}_f(t) \mid^2 = \frac{1}{2}e^{-\Gamma t} \Bigg[&\left(\mid A \mid^2 - \mid \frac{q}{p}B \mid^2 \right)\cos(x\Gamma t) - 2\,\mathrm{Im}\left(AB^* \left[\frac{q}{p}\right]^* \right)\sin(x\Gamma t) \\
&+ \left(\mid A \mid^2 + \mid \frac{q}{p}B \mid^2 \right)\cosh(y\Gamma t) - 2\,\mathrm{Re}\left(AB^* \left[\frac{q}{p}\right]^* \right)\sinh(y\Gamma t) \Bigg]
\end{aligned}
\tag{2.43}
$$

as well as a similar equation for $\left|\bar{\mathcal{A}}_f(t)\right|^2$.

Here A and B represent the amplitudes of a D^0 and $\bar{D}^0$ respectively decaying into some final state f. For a multi-body decay such as $D^0 \to K^0_S\pi^+\pi^-$ the amplitudes A and B depend on the multidimensional phase-space which in this case is defined by the Dalitz variables $m^2(K^0_s\pi^+)$ and $m^2(K^0_s\pi^-)$; this is discussed in more detail in Section 2.4. The time-dependent amplitude is a function of the amplitudes A and B as well as the mixing parameters x and y. The neutral meson oscillations effect the phase-space and decay-time distributions of this decay. Therefore the mixing parameters x and y can be extracted from a time-dependent amplitude fit in the Dalitz variables and decay-time of this decay.

As an analogous example, consider the two-body wrong-sign decay $D^0 \to K^+\pi^-$. Here there are two ways the decay can proceed; by direct DCS decay or by mixing followed by CF decay. It is the interference between these processes that gives the sensitivity to *CP*-violation. In order to extract the mixing parameters, one also needs to measure the direct right-sign CF decay $D^0 \to K^-\pi^+$. At LHCb there is no way to measure the absolute value of the strong phase between the CF and DCS decays; instead we measure x' and y', the mixing parameters x and y rotated by this unknown phase with respect to the true values. The three-body self-conjugate decay $D^0 \to K_S^0\pi^+\pi^-$ is unique as it offers access to the direct wrong-sign DCS decay, mixed followed by CF, and the right-sign CF decay in the same final state. Therefore we can identify different regions of phase-space with right-sign and wrong-sign decays which allows us direct access to the mixing parameters x and y.

2.3 *CP*-violation

CP-violation is the violation of *CP*-symmetry or the combination of charge symmetry and parity symmetry. Under *CP*-symmetry, the laws of physics would be the same if a particle was interchanged with its antiparticle (charge symmetry) and its spatial coordinates are inverted (parity symmetry). *CP*-violation was discovered in the kaon sector in 1964 [37] and in the beauty sector by Belle and BaBar in 2001 [16, 30]. Studies of *CP*-violation play an important role in cosmology to explain the dominance of matter over antimatter in the universe, as well as in the study of weak interactions in particle physics. In order to account for the inbalance of matter and antimatter in the universe, the Sakharov conditions were proposed: baryon number violation, charge symmetry and *CP*-symmetry violation, and interactions out of thermal equalibrium [72].

In the SM, *CP*-violation is introduced through an irreducible complex phase in the CKM mixing matrix. *CP*-violation is not allowed in the strong interaction. In the lepton sector *CP*-violation can enter in the SM via the Pontecorvo–Maki–Nakagawa–Sakata (PMNS) matrix [70, 63]. However the amount of *CP*-violation allowed in the SM is too small to account for the matter-antimatter asymmetry observed in the universe. Therefore physics beyond the SM associated with large energy scales (such as the energy scale of the early universe) are needed to explain the matter-antimatter asymmetry observed in the universe. *CP*-violation can be introduced by new particles or interactions, motivating searches and precision measurements at high energy physics experiments such as the LHC.

Measurements of *CP*-violation have been performed in the kaon and beauty sectors [37, 31] but until 2019 *CP*-violation had not been discovered in charm [10]. Measurements of *CP*-violation in charm are complimentary to those in kaon and beauty and provide a unique opportunity to measure *CP*-violation in particles containing only up-type quarks. Theoretical predictions of *CP*-violation in the charm sector are $\mathcal{O}(10^{-3} - 10^{-4})$ [52], but due to low-energy strong interactions they are difficult to compute reliably. Contributions of physics beyond the SM may alter the size of *CP*-violation in charm, therefore making searches for *CP*-asymmetries a potentially sensitive probe of new physics.

The CKM matrix can be written in terms of three rotation angles and a complex phase:

$$V_{CKM} = \begin{pmatrix} c_{12}c_{13} & s_{12}s_{13} & s_{13}e^{-i\delta} \\ -s_{12}c_{23} - c_{12}s_{23}s_{13}e^{i\delta} & -c_{12}c_{23} - s_{12}s_{23}s_{13}e^{i\delta} & s_{23}c_{13} \\ s_{12}s_{23} - c_{12}c_{23}s_{13}e^{i\delta} & -c_{12}s_{23} - s_{12}c_{23}s_{13}e^{i\delta} & c_{23}c_{13} \end{pmatrix} \tag{2.44}$$

where $s_{ij} = \sin\theta_{ij}$ and $c_{ij} = \cos\theta_{ij}$, where *CP*-violation enters in the complex phase δ. The hierarchical structure of the CKM matrix also allows us to write it in terms of the Wolfenstein parametrisation:

$$V_{CKM} = \begin{pmatrix} 1 - \lambda^2/2 & \lambda & A\lambda^3(\rho - i\eta) \\ -\lambda & 1 - \lambda^2/2 & A\lambda^2 \\ A\lambda^3(1 - \rho - i\eta) & -A\lambda^2 & 1 \end{pmatrix} + \mathcal{O}(\lambda^4) \tag{2.45}$$

where the parameters A, λ, ρ, η are all $\mathcal{O}(1)$. It can be seen that *CP*-violation only enters in terms of $\mathcal{O}(\lambda^3)$ hence it is small in the SM.

CP-violation can occur in the SM in three ways: *CP*-violation in decay (direct *CP*-violation), *CP*-violation in mixing and *CP*-violation in the interference between mixing and decay (indirect *CP*-violation). *CP*-violation in decay occurs when the amplitude of a process is different to that from the *CP*-conjugate:

$$\Gamma(D^0 \to f) \neq \Gamma(\bar{D}^0 \to \bar{f}) \tag{2.46}$$

or alternatively:

$$|A_f| \neq \ |\bar{A}_{\bar{f}}| \tag{2.47}$$

This type of *CP*-violation can occur for any type of particle, including both charged and neutral mesons and baryons. *CP*-violation in mixing occurs when the rate of the D^0 mixing into a $\bar{D}^0$ is different to that of the opposite process:

$$\Gamma(D^0 \to \bar{D}^0) \neq \Gamma(\bar{D}^0 \to D^0) \tag{2.48}$$

This occurs when $|q| \neq |p|$. A D^0 meson can decay into a self-conjugate final state $f = \bar{f}$ directly $D^0 \to f$ or by first mixing into a $\bar{D}^0$ and then decaying, $D^0 \to \bar{D}^0 \to f$. Then *CP*-violation in the interference between mixing and decay occurs when:

$$\Gamma(D^0 \to \bar{D}^0 \to f, t) \neq \Gamma(\bar{D}^0 \to D^0 \to f, t) \tag{2.49}$$

The decay paths can interfere with each other and the relative phases between the two amplitudes is relevant. *CP*-violation in the interference between mixing and decay is present for a non-vanishing phase:

$$\phi = arg\left(\frac{q\bar{A}_f}{pA_f}\right) \neq 0 \tag{2.50}$$

CP-violation in mixing and in the interference between mixing and decay are therefore characterised by the parameters $|q/p|$ and ϕ. This can also be expressed in an alternative formalism where the mixing parameters are different for D^0 and $\bar{D}^0$ and are expressed as $x_{CP} \pm \Delta x$ and $y_{CP} \pm \Delta y$. These parameters are measured in previous model-independent analyses at LHCb including the bin-flip analysis [9]. The parameters are related to the *CP*-violation parameters $|q/p|$ and ϕ as follows:

$$x_{CP} = \frac{1}{2}\left[x\cos\phi\left(\left|\frac{q}{p}\right| + \left|\frac{p}{q}\right|\right) + y\sin\phi\left(\left|\frac{q}{p}\right| - \left|\frac{p}{q}\right|\right)\right] \tag{2.51}$$

$$\Delta x = \frac{1}{2}\left[x\cos\phi\left(\left|\frac{q}{p}\right| - \left|\frac{p}{q}\right|\right) + y\sin\phi\left(\left|\frac{q}{p}\right| + \left|\frac{p}{q}\right|\right)\right] \tag{2.52}$$

$$y_{CP} = \frac{1}{2}\left[y\cos\phi\left(\left|\frac{q}{p}\right| + \left|\frac{p}{q}\right|\right) - x\sin\phi\left(\left|\frac{q}{p}\right| - \left|\frac{p}{q}\right|\right)\right] \tag{2.53}$$

$$\Delta y = \frac{1}{2}\left[y\cos\phi\left(\left|\frac{q}{p}\right| - \left|\frac{p}{q}\right|\right) - x\sin\phi\left(\left|\frac{q}{p}\right| + \left|\frac{p}{q}\right|\right)\right] \tag{2.54}$$

Conservation of *CP*-symmetry in mixing ($|q/p| = 1$) and in the interference of mixing and decay ($\phi = 0$) implies $x_{CP} = x$, $y_{CP} = y$ and $\Delta x = \Delta y = 0$. *CP*-violation in mixing and in the interference of mixing and decay may be referred to as time-dependent *CP*-violation. *CP*-violation in decay may be measured by performing a time-integrated amplitude fit separately on datasets where the flavour of the neutral D meson at production was D^0 or $\bar{D}^0$. The complex coefficients of the amplitudes may be compared, and in the case of *CP*-symmetry the amplitudes of the $D^0 \to K^0_S\pi^-\pi^+$ and the charge conjugate would agree.

The observable Δy is frequently denoted as A_Γ and is measured in several LHCb analyses [8]. The model-independent bin-flip method [44] introduces the parameters x_{CP} and Δx as defined above. This allows for a conveniently symmetric notation and the parameters are optimally suited for use in measurements and combinations of results.

Theoretical predictions of *CP*-violation in the charm sector have large uncertainties due to contributions from QCD which are difficult to calculate precisely. Although direct *CP*-violation in the charm sector has been discovered at LHCb, indirect *CP*-violation in mixing or in the interference between mixing and decay has yet to be discovered at the time of writing.

2.4 Amplitude Analysis

The term amplitude analysis refers to the study of a variety of scattering and decay processes. This thesis focuses on the study of multi-body decays of particles that decay via the weak interaction to short-lived resonances that in turn decay via the strong force. The three-body decay $D^0 \to K^0_S\pi^+\pi^-$ can proceed through many possible intermediate states such as $K^{*\pm}$, K^{*0} and ρ^0. In order to perform such analyses we need a model that encapsulates the various possible intermediate states and their shapes and which has enough freedom to adapt to give the best description of the data.

The dynamics of a three-body decay $D^0 \to abc$ where D^0, a, b, c are all pseudoscalar mesons, can be completely described by the Dalitz variables which are a pair of squared invariant masses m^2_{ab} and m^2_{ac}. In the absence of contributions from intermediate resonances, the two-dimensional distribution of candidates would be uniform over the Dalitz plane, within the physically allowed region dictated by the masses of the four particles. Figure 2.4 shows an example Dalitz plot with the kinematic limits from momentum and energy conservation in the three-body decay. Decay processes with higher-multiplicity final states, or final state particles with nonzero spin, have substantially more Lorentz-invariant degrees of freedom. A description of the complex amplitude variation across the phase space defined by these degrees of freedom is known as an amplitude model [62]. Such models allow the contributions of various intermediate resonances to be disentangled, providing a full description of the decay process which can be used in *CP*-violation and mixing studies. The amplitude model consists of the wrong-sign (DCS and mixed followed by CF) processes such as $D^0 \to K^{*+}\pi^-$ where $K^{*+} \to K^0_S\pi^+$ and right-sign (CF) processes such as $D^0 \to K^{*-}\pi^+$ where $K^{*-} \to K^0_S\pi^-$, and singly-Cabibbo supressed processes such as $D^0 \to K^0_S\rho^0$ where $\rho^0 \to \pi^+\pi^-$. Fitting the amplitude model to data allows us to disentangle these processes; and it is the time evolution of these processes which gives the sensitivity to mixing and *CP*-violation in mixing and the interference between mixing and decay.

2.4.1 Isobar model

The isobar model is a widely used formalism for the construction of amplitude models. In this formalism the three-body decay is modelled as a linear superposition of quasi two-body amplitudes where the D^0 decays through intermediate resonances r: $D^0 \to (r \to ab)c$. The matrix elements for a three-body decay are expressed as the sum of matrix elements of a quasi two-body decay through the intermediate resonance r, each multiplied by a complex coefficient, which encodes relative differences in amplitudes and phases, including also strong phase differences:

$$\mathcal{M}_{K^0_S\pi^+\pi^-}(m^2_{ab}, m^2_{ac}) = \sum_r a_r e^{i\phi_r}\mathcal{M}_r(m^2_{ab}, m^2_{ac}) \tag{2.55}$$

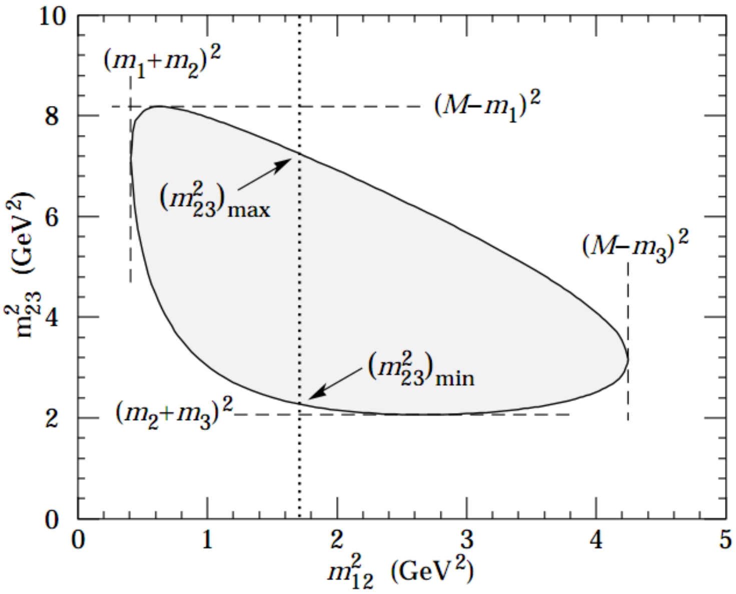

Figure 2.4: Example of a Dalitz plot showing the kinematic limits for a three-body decay.

where $a_r e^{i\phi_r}$ is the complex amplitude for the resonance r and the contributions from each intermediate state is given by:

$$\mathcal{M}_r(m^2_{ab}, m^2_{ac}) = B^{D^0}_J(p, |p_0|, d_{D^0})\Omega_J(m^2_{ab}, m^2_{ac})T_r(m^2_{ab})B^r_J(q, |q_0|, d_r) \tag{2.56}$$

where $B^{D^0}_J(p, |p_0|, d_{D^0})$ and $B^r_J(q, |q_0|, d_r)$ are the Blatt-Weisskopf centrifugal barrier factors for the production and decay, respectively, of the resonance r. p (q) is the momentum of c (a or b) in the r rest frame and p_0 (q_0) is the quantity using the mass m_r as opposed to the reconstructed mass m_{ab}. In this analysis, the Blatt-Weisskopf effective radius is fixed to $d_r = 1.5$ GeV^{-1} for intermediate resonances and to $d_{D^0} = 5.0$ GeV^{-1} for the D^0 meson. Finally, $\Omega_J(m^2_{ab}, m^2_{ac})$ is the spin factor for a resonance with spin J and T_r is the dynamical function describing the resonance r. The phase-space dependence of the amplitude is contained in the spin factor as well as the dynamical function T_r, where different parametrisations of T_r are discussed in Chapter 8 which depend on the resonance in question. The model-dependence of the analysis method enters through the choice of resonances contributing to the sum in Equation 2.55 and the chosen parameterisation of $\mathcal{M}_r$.

The Blatt-Weisskopf form factors are given by:

$$\begin{aligned}
L = 0 &: F^{(0)}(z, z_0) = 1 \\
L = 1 &: F^{(1)}(z, z_0) = \sqrt{\frac{1 + z_0}{1 + z}} \\
L = 2 &: F^{(2)}(z, z_0) = \sqrt{\frac{(z^0 - 3)^2 + 9z_0}{(z - 3)^2 + 9z}}
\end{aligned} \tag{2.57}$$

where $z = (\mid q \mid d)^2$ and $z_0 = (\mid q_0 \mid d)^2$. The spin factors are given by:

$$\begin{aligned}
\Omega_0(m^2_{ab}, m^2_{ac}) &= 1 \\
\Omega_1(m^2_{ab}, m^2_{ac}) &= m^2_{ac} - m^2_{bc} - \frac{(m^2_{D^0} - m^2_c)(m^2_a - m^2_b)}{m^2_{ab}} \\
\Omega_2(m^2_{ab}, m^2_{ac}) &= \left[m^2_{ac} - m^2_{bc} - \frac{(m^2_{D^0} - m^2_c)(m^2_a - m^2_b)}{m^2_{ab}} \right]^2 \\
&\quad - \frac{1}{3} \left[m^2_{ab} - 2(m^2_{D^0} + m^2_c) + \frac{(m^2_{D^0} + m^2_c)^2}{m^2_{ab}} \right] \\
&\quad \times \left[m^2_{ab} - 2(m^2_a + m^2_b) + \frac{(m^2_a + m^2_b)^2}{m^2_{ab}} \right]
\end{aligned} \tag{2.58}$$

Resonances with spin J produce characteristic Dalitz plot distributions with J nodes. The intermediate resonances can interfere with each other, creating constructive and destructive regions in the Dalitz plot. Figure 2.5 shows Dalitz plots with different spin contributions: Figure 2.5a shows the broad structure of the $K^0_S\pi^+$ S-wave contribution, Figure 2.5b shows a peaking structure of the $K^0_S\pi^-$ vector resonance, Figure 2.5c shows a $K^0_S\pi^+$ tensor resonance and Figure 2.5d shows the interference between two vector resonances. An amplitude model may also contain non-resonant quasi-two-body components which are included in the model. A further description of the fit model is given in Chapter 8 with the other parametrisations of T_r which are specifically used for this analysis.

In summary the self-conjugate three-body decay $D^0 \to K^0_S\pi^+\pi^-$ offers direct access to the mixing parameters x and y as well as the *CP*-violation parameters $|q/p|$ and ϕ. The amplitude of the decay can be described by the superposition of two-body decays through intermediate resonances. The amplitude is described by the Dalitz variables $m^2(K^0_S\pi^+)$ and $m^2(K^0_S\pi^-)$. The time-dependence of the amplitude model

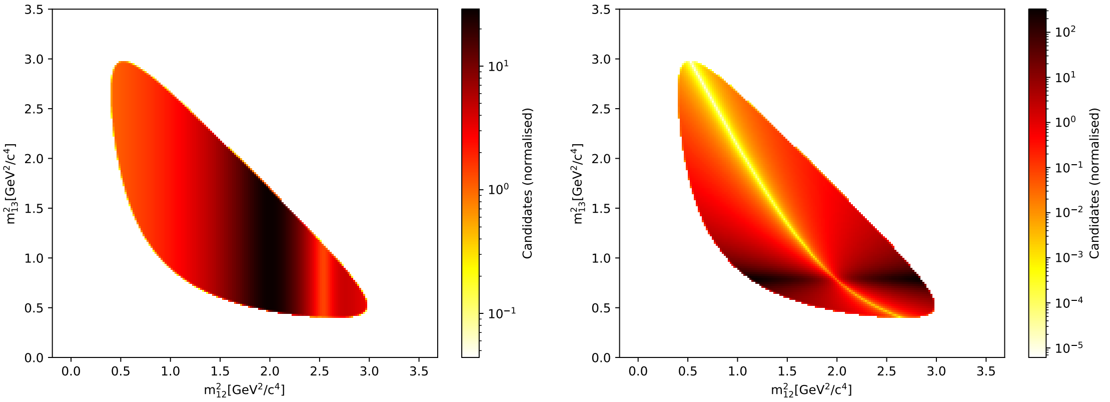

(a) $K_S^0\pi^+$ S-wave contribution (b) $K_S^0\pi^-$ vector resonance

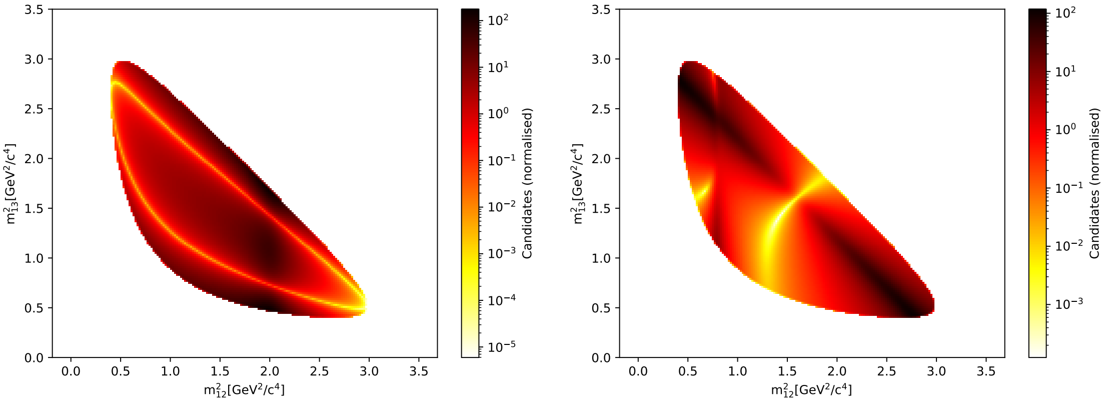

(c) $K_S^0\pi^+$ tensor resonance (d) Interference between $\pi^+\pi^-$ and $K_S^0\pi^+$ vector resonances

Figure 2.5: Illustrations of Dalitz plot distributions produced by resonances with different spins; spin $J = 0, 1, 2$ contributions and an interference between two vector resonances are shown. The decay process is $D^0 \to K_S^0\pi^+\pi^-$ for illustrative purposes.

gives sensitivity to mixing and *CP*-violation. Therefore the mixing and *CP*-violation parameters of interest can be extracted from a time and phase-space dependent fit of the amplitude model to the Dalitz variables and decay-time of this decay using the time-dependent formalism in Equation 2.43. The amplitudes of a D^0 and $\bar{D}^0$ decaying to the final state A and B are expressed in the formalism given in Equation 2.55.

CHAPTER 3

Detector

The data analysed in this measurement have been collected at the LHCb experiment at the Large Hadron Collider (LHC). The LHC is a proton-proton (*pp*) collider, which was designed to run at a luminosity of 10^{34} cm^{-2}s^{-1} and achieve centre-of-mass energies of 14 TeV for *pp* collisions. The particle accelerator is built in a tunnel of 27 km circumference built $\sim$100m underground at the Centre for European Nuclear Research (CERN) near the French-Swiss border. At the LHC, the ATLAS and CMS experiments are general-purpose detectors focusing particularly on precision tests of the Standard Model, Higgs physics and direct new physics searches whereas ALICE aims at the investigation of the quark-gluon plasma. The LHCb detector is a forward-arm detector which is primarily designed for the study of beauty and charm decays and with a physics program focusing on measurements of *CP*-violation and rare decays.

3.1 The Large Hadron Collider

The LHC accelerator complex consists of a succession of machines that accelerate particles to increasingly higher energies. The source of protons for the beam is hydrogen gas where the atoms are stripped of the electrons by an electric field. LINAC 2 accelerates the protons to energies of 50 MeV before they are injected into the Proton Synchrotron Booster. The injection occurs every 100 ms providing

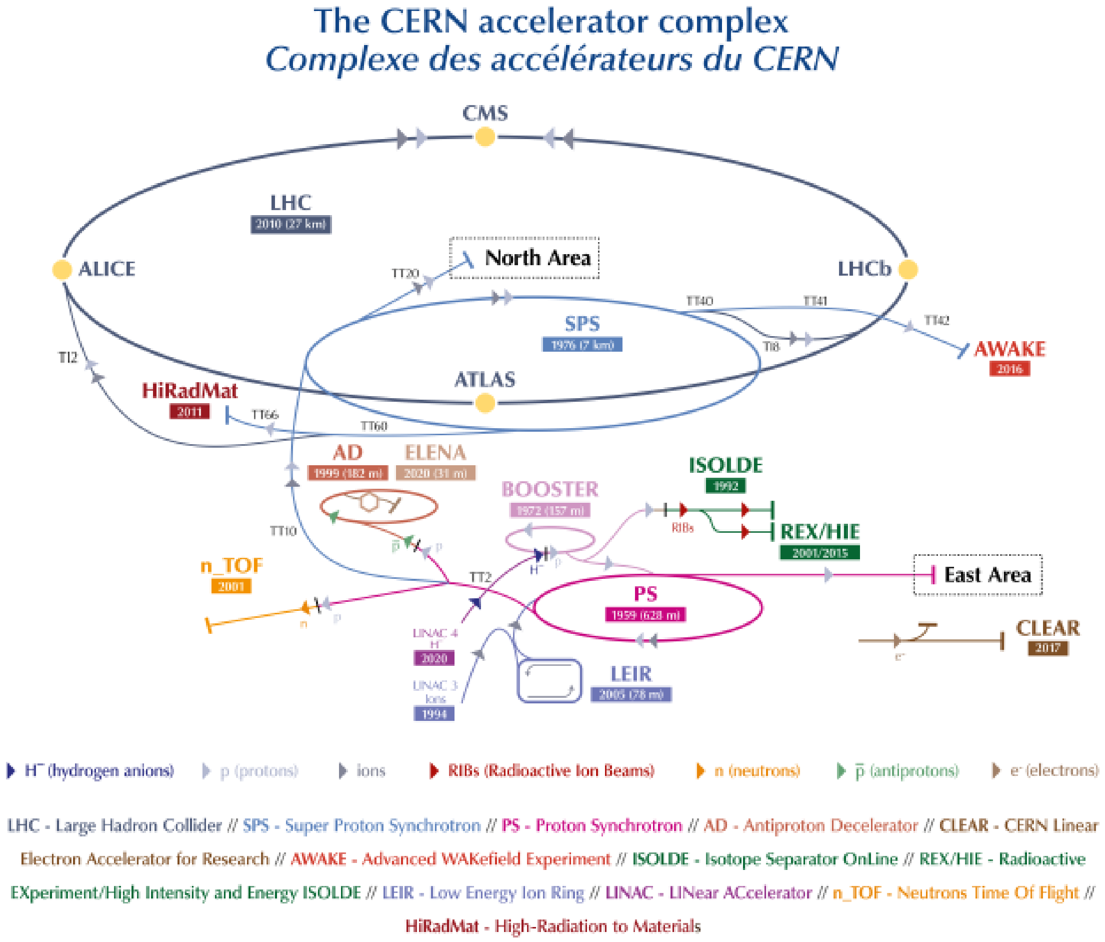

Figure 3.1: Illustration of the CERN accelerator complex displaying the accelerators and detectors at CERN and the LHC [65].

bunches of $\sim 10^{11}$ protons. Here the protons are accelerated to energies of 1.4 GeV. The beam is then injected into the Proton Synchrotron which accelerates the protons to 25 GeV and the Super Proton Synchrotron (SPS) with a circumference of 7 km. The SPS accelerates the beam to 450 GeV, which is the injection energy for the LHC. The bunch spacing of the proton bunches is now 25 ns. Before injection into the LHC the particles are split into two beams travelling in opposite directions. The beams collide at four interaction points where the four experiments are situated; ATLAS, CMS, ALICE and LHCb. An illustration of the CERN accelerator complex is shown in Figure 3.1.

In order to maximise the luminosity delivered to the experiments, the LHC machine operates in a sequence of fills during which *pp* bunches circulate for several hours (typically $\sim$ 10 hours) and generate collisions. During this time, the bunch intensities drop due to beam-beam interactions and other effects; the beams are then dumped before a new fill is started.

Instantaneous luminosity corresponds to the potential number of collisions per second. The LHC is designed to run at an instantaneous luminosity of 10^{34} cm^{-2}s^{-1}. During the Run 2 data-taking period the machine and beam performance allowed nearly every fill to run with a peak luminosity of $\sim 2 \times 10^{34}$ cm^{-2} s^{-1}, which is around twice the design luminosity. Integrated luminosity refers to the total luminosity collected over a given period of time. The total integrated luminosity since the beginning of LHC operation in 2010 and until the end of Run 2 in 2018 is 189.3 fb^{-1} for ATLAS and CMS, of which 160 fb^{-1} were accumulated during Run 2. The higher the luminosity, the more rare physics events are observed; so one may want to maximise this quantity when designing a particle accelerator. However, in the case of very high luminosity the high event rate per bunch crossing can make events difficult for the detectors to resolve individual events. Therefore, the LHCb detector does not run at the LHC peak luminosity but aims for a lower number of collisions per bunch crossing through a process called luminosity levelling which will be discussed in Section 3.2. The luminous region is the region in space across which the collisions are distributed, and this also needs to be optimised to the acceptance of the detector. The luminous region can change between fills due to the crossing angle of the beams and other beam parameters and configurations.

The LHCb uses a right-handed cartesian coordinate system and the convention is as follows: the z axis is along the beam line as it passes through the detector, the y axis is perpendicular to the z axis in the vertical plane where the positive direction is upwards and the x axis is perpendicular in the horizontal plane where the positive direction points towards the centre of the LHC ring. Pseudorapidity is the spatial coordinate describing the angle of a particle relative to the beam axis. It is defined as:

$$\eta \equiv -\ln\left[\tan\left(\frac{\theta}{2}\right)\right] \tag{3.1}$$

where θ is the angle subtended with respect to the positive direction of the beam axis, in the case of the LHC coordinate system this is the positive z direction. The LHCb detector has the pseudorapidity range $1.9 < \eta < 4.9$.

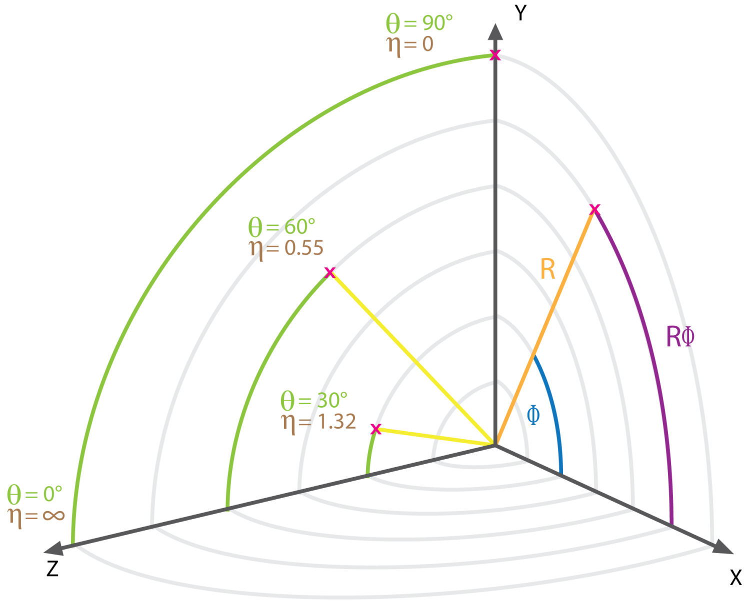

Figure 3.2: Coordinate system used in this thesis; pseudorapidity η is shown in the polar coordinates with the corresponding values of θ, z is along the beam axis and the (x, y) plane is transverse to the beam.

The LHC operated at a centre-of-mass energy of 7 TeV for pp collisions in 2010-2011 and 8 TeV in 2012 in the Run 1 data-taking period; the centre-of-mass energy was 13 TeV in 2015-2018 (Run 2 data-taking period). The LHC is also able to collide heavy nuclei such as lead (Pb) either in ion-ion collisions or in proton-ion collisions. This allows studies of the quark-gluon plasma, a state of matter in which quarks and gluons exist in thermal and chemical equilibrium. This is the primary purpose of the ALICE experiment but the other LHC experiments, ATLAS, CMS and LHCb now each have a heavy ion program.

3.2 The LHCb Detector

The LHCb detector [26] is a forward-arm detector situated at one of the interaction points on the LHC ring. The detector was specifically designed for the study of hadrons containing b and c quarks and focuses on measurements of CP-violation and rare decays such as $B_s^0 \to \mu^+\mu^-$ [4]. The LHCb physics program has since expanded to include measurements of lepton universality [5, 12], and searches for new conventional and exotic hadron states (for example the pentaquark discovery [1]). In addition LHCb has also performed BSM (beyond SM) searches for dark photons [6]

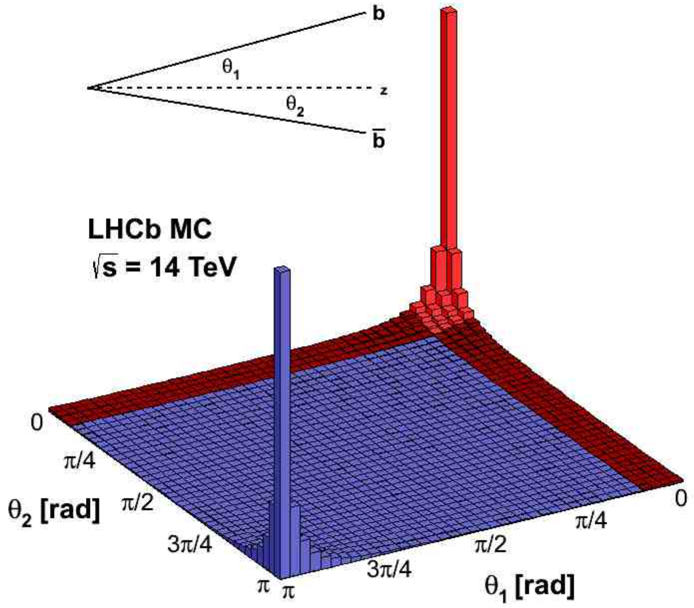

Figure 3.3: Angular distribution of $b\bar{b}$ production at $\sqrt{s} = 14$ TeV in the LHCb detector, where the detector acceptance is shown by the red shaded area [26].

and studies of QCD and electroweak interactions such as measurements of the forward production of vector bosons [2].

When $b\bar{b}$ pairs are produced at the LHC, the primary production method is gluon-gluon fusion, which occurs when two gluons collide in a pp interaction. The gluons have highly asymmetric momenta and in gluon-gluon fusion at the LHC, the most likely occurrence is that one gluon carries the majority of the momentum. Hence the $b\bar{b}$ pair is boosted in the direction of the gluon momentum, which is along one of the two beam directions. The LHCb acceptance is in the psuedorapidity range $2 < \eta < 5$, motivated by the fact that $b\bar{b}$ pairs are produced at angles close to the beam pipe. Figure 3.3 shows the angular distribution of the production of $b\bar{b}$ at LHCb where the LHCb acceptance is shown by the red shaded area. This shows the highly forward and correlated production of the $b\bar{b}$ pair. The acceptance in terms of the angle θ is $10 < \theta < 300$ (250) mrad in the bending (non-bending) plane.

The LHCb detector is designed to collect data at a luminosity of $\mathcal{L} = 2 \times 10^{32}$ cm^{-2}s^{-1}. In practice the LHCb detector exceeded this design goal, operating

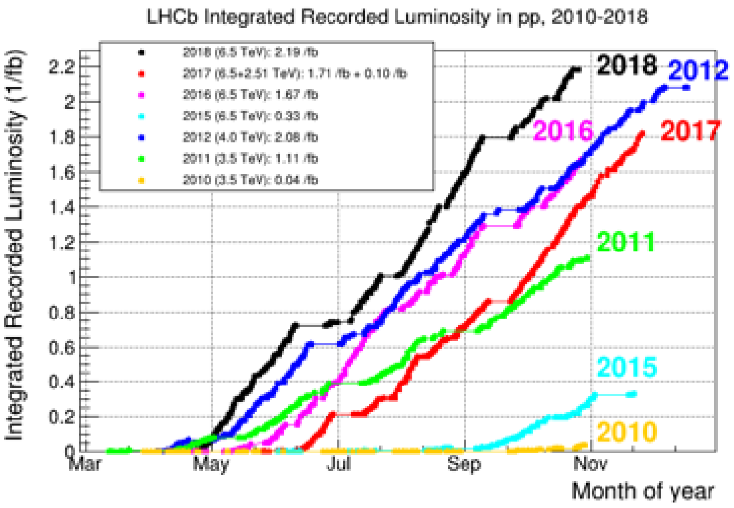

Figure 3.4: LHCb recorded luminosity in *pp* collisions from 2012-2018 [26].

at 5×10^{32} cm^{-2}s^{-1} for much of Run 2. The detector collected data during the Run 1 data-taking period at centre-of-mass energies of 7 TeV in 2010 and 2011 and 8 TeV in 2012 corresponding to a total integrated luminosity of 3 fb^{-1}. The Run 2 data-taking period was between 2015 and 2018 and collected data at a centre-of-mass energy of 13 TeV, corresponding to a total integrated luminosity of 6.1 fb^{-1}. The recorded luminosity at the LHCb detector is shown in Figure 3.4, the total recorded luminosity is 9.1 fb^{-1}. The design luminosity of LHCb is significantly lower than the general purpose detectors ATLAS and CMS; this is in order to prevent ageing of the detectors and to keep the number of *pp* interactions per bunch crossing close to one. Through the procedure of luminosity levelling, the beams are not focused as strongly as for ATLAS and CMS and the transverse beam overlap is adjusted by changing the offset between the proton beams.

A cross section of the LHCb detector is shown in Figure 3.5. The interaction point is located at the centre of the Vertex Locator (VELO), a silicon strip detector providing high precision measurements of the track and vertex coordinates. The Ring Imaging Cherenkov (RICH) detectors provide particle identification for pions, kaons and protons. The tracking system consists of the Tracker Turicenis (TT), located upstream from the magnet and tracking stations T1-T3, located downstream from the magnet. The tracking stations comprise two types of technology split into inner and outer regions. The Silicon Tracker (ST) consists of the inner regions of the tracking stations T1-T3 closest to the beam line (inner tracker IT), along with

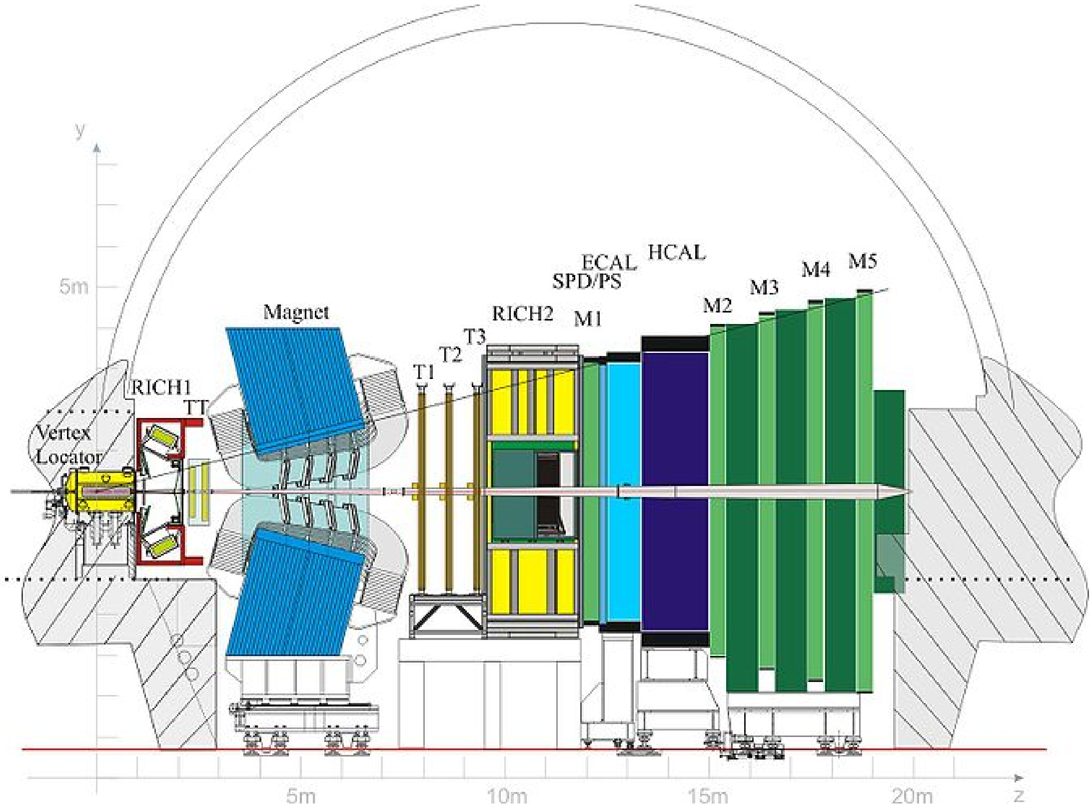

Figure 3.5: Cross-section of the LHCb detector [26].

the TT, and comprises silicon microstrip detectors. The signals in a silicon strip detector are formed when charged particles liberate electrons and holes within the semiconducting silicon. These charges drift under the influence of a bias voltage to be collected at the sensor surface as currents. The silicon is segmented into strips so that the signals can be identified with a particular region of the detector, where the size of the strip is dictated by the physics performance requirements and the number of channels which can be accommodated within resource limits. The Outer Tracker (OT) consists of the outer regions of the tracking stations T1-T3. The OT consists of straw tube drift chambers and measure the track coordinates of the particles. The calorimeter system consists of the electromagnetic calorimeter (ECAL) and hadronic calorimeter (HCAL) and provides particle identification and energy measurements of electrons, photons and hadrons. Finally the muon system (M1-M5) provides identification of muons.

3.2.1 Vertex Locator

The VELO lies closest to the beam line; the information from the VELO is used to reconstruct the trajectories of charged particles produced in the initial *pp* collision. Using the information from the VELO we can identify and locate both the primary vertices (PV) at the *pp* interaction point in the bunch crossing, and the secondary vertices caused by the decays of long-lived particles such as those containing b quarks. The displaced secondary vertex is a distinctive feature of b and c-hadron decays and is used to trigger on events in the high level trigger (discussed in Section 3.2.6). For a PV with 25 tracks, the vertex position is measured with a precision of 13 μm in the transverse plane and with 71 μm along the z axis.

Silicon detectors are widely used in tracking systems in particle physics to measure the position of charged particles. Track reconstruction software can then deduce several parameters including the flight path, the vertex of the interaction and the secondary vertex of particles with long lifetimes such as a hadron containing a b-quark. The VELO consists of 21 silicon modules which are placed close to the *pp* interaction point. The silicon microstrip modules contain R and ϕ sensors where R measures the radial distance to the beam axis and ϕ measures the azimuthal coordinate around the beam. Charged particles produced by the *pp* collisions traverse the silicon and generate electron-hole pairs; the electrons and holes drift under the influence of a bias voltage to be collected at the sensor surface. The electrons and holes produce currents at the surface and are detected using application specific electronics. These ‘hits’ in the VELO modules are used in track reconstruction software in the high level trigger to deduce the track parameters of a charged particle traversing the detector.

During data-taking the silicon modules are at a distance of 7 mm to the beam line (the closest active part of the module is 8.2 mm from the beam line); they then retract to a distance of 35 mm, preventing damage to the VELO during beam fill and beam dump. When the VELO closes it does so in such a way to ensure the detector is centred in the transverse plane on the luminous region, which differs between fills; this allows a measurement of the luminous region in real time.

The design of the VELO is optimised for the LHCb physics program and detector

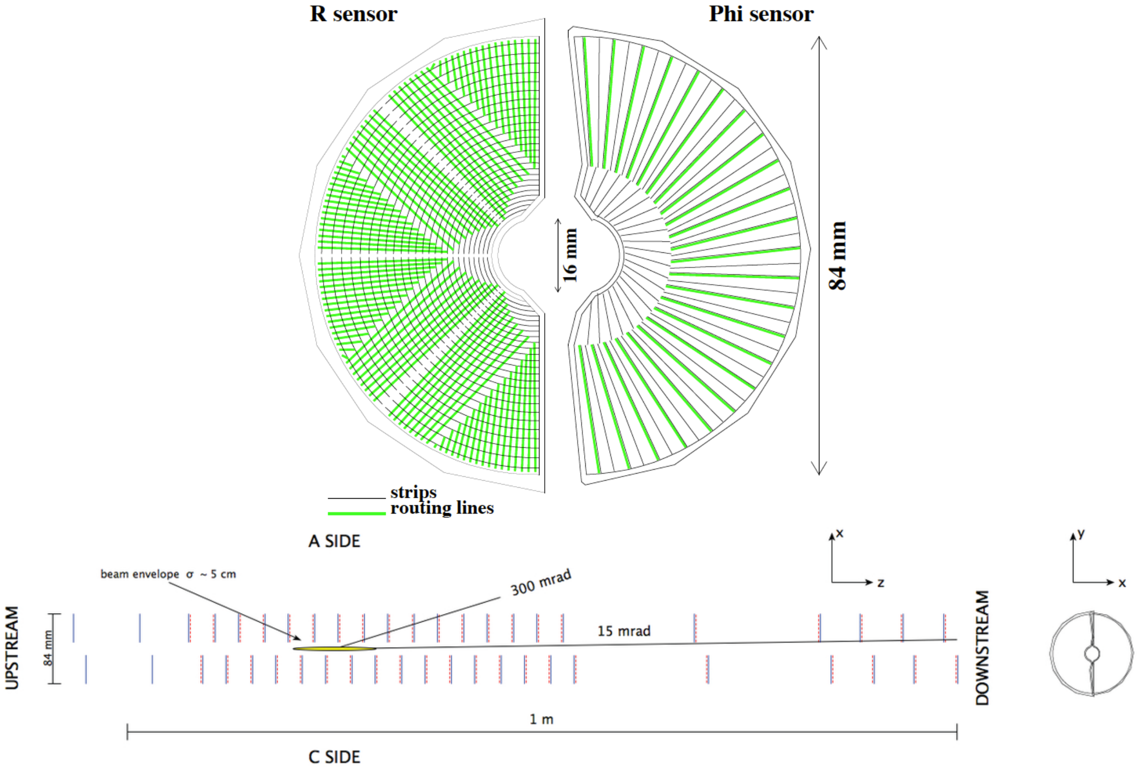

Figure 3.6: A schematic of the LHCb vertex locator; R and ϕ sensors and dimensions are shown in the top and the positions of the modules with respect to the beam axis are shown in the bottom [24].

performance in several ways. Firstly, it is designed to cover the forward direction and tracks in LHCb acceptance. The VELO also provides excellent vertex and impact parameter (IP) resolution which is crucial to many LHCb physics analyses. The impact parameter is defined as the distance of closest approach between a track and the PV. The IP is measured with a resolution of $(15 + 29/\mathrm{p}_T)$ µm, where p_T is expressed in GeV/c. In addition the reconstruction of the PV and the displaced secondary decay vertex of is used in the high level trigger which reduces the event rate from a 1 MHz event rate to a few kHz. The decay time of a particle is measured from the flight distance in the VELO, which provides a resolution of ∼50 fs and is crucial to many LHCb analyses.

3.2.2 Tracking

The primary purpose of the tracking system is to allow the trajectories of charged particles to be measured as they pass through the LHCb detector. Charged particle trajectories are bent by the magnetic field from the large dipole magnet of field strength 4 Tm located between the TT and the T1-T3 tracking stations. This allows the tracking system to determine the curvature and hence momentum of the particle. During data taking, the magnet polarity is periodically reversed in two configurations in order to account for detection asymmetries: magnet up where the magnetic field is in the positive y direction and magnet down where the field is in the negative y direction. This mitigates the majority of detector asymmetries. The information from the tracking system can also be matched to the corresponding signals in the VELO and other subdetectors to determine measurements of the track trajectory and parameters. The tracking system provides a measurement of the momentum of charged particles with a relative uncertainty that varies from 0.5% at low momentum to 1.0% at 200 GeV/c.

Silicon Tracker

The silicon tracker consists of the TT and the Inner Tracker. The TT consists of 500 μm thick silicon microstrip detectors with a strip pitch of $\sim$ 200 μm. The TT is a planar tracking station that is located upstream of the LHCb dipole magnet and covers the full acceptance of the experiment. The TT consists of four detection layers, where each layer is rotated in the x direction to overlap to avoid acceptance gaps and maximise spatial resolution. Each layer consists of 30 'half-modules' which in turn consist of seven silicon strip sensors, where a higher occupancy is accounted for closer to the beam line. Each TT sensor has 512 readout strips, and a spatial resolution of 50 μm is achieved. A schematic diagram of the TT can be seen in Figure 3.7. To account for a higher occupancy near the beam line, the different tones of brown in the figure indicate a difference in readout systems.

The IT covers a cross shaped region in the inner region of the tracking stations (T1-T3) downstream of the magnet and close to the beam pipe. The IT consists of two single-sensor modules of 320 μm thickness and two two-sensor modules with a thickness of 410 μm. This can be seen in Figure 3.7 by the yellow cross in the centre of the layer; the single-sensor modules are in the vertical direction and the two-sensor modules are in the horizontal direction. The cross shape is optimised for the stretching of the highest occupancy region due to the bending of charged

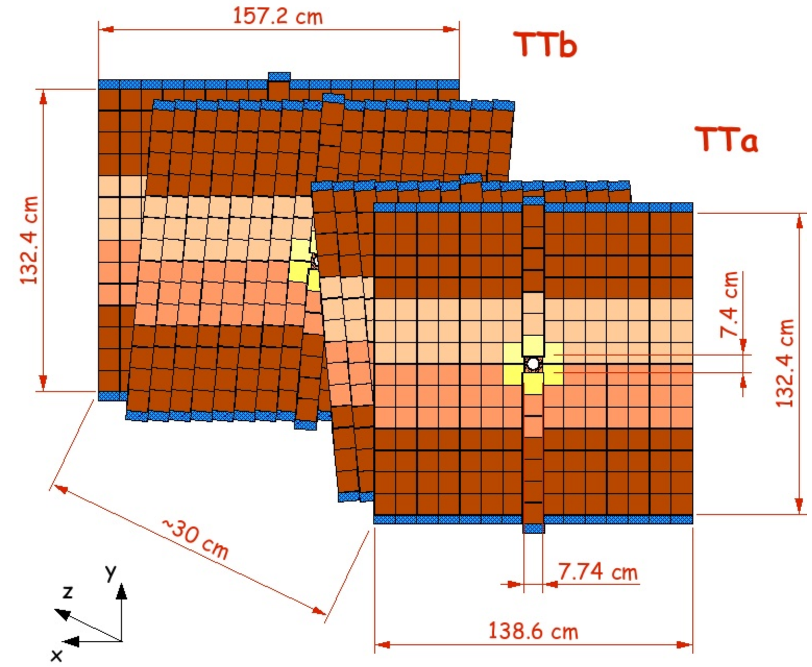

Figure 3.7: Layout of the Tracker Turicensis; the sensor placement is indicated by the different shades of brown. The Inner Tracker is indicated by the sensors in yellow [60].

particles by the magnet. The IT consists of four detection layers which overlap in the x direction to minimise acceptance gaps and improve the alignment. The sensors consists of 384 microstrips and have a strip pitch of 198 µm.

Outer Tracker

The Outer Tracker (OT) consists of the outer sections of the tracking stations T1-T3. It consists of straw-tube drift chambers with 5 mm cell diameter and filled with a mixture of argon and carbon dioxide. A charged particle passes through the gas tubes, ionising the gas molecules and producing elections. The position of the charged particle's trajectory can be determined from the drift time of the electron to the anode wire in the centre of each tube.

Each tracker is comprised of four layers, which are rotated in the same configuration as the TT. The outer boundaries of the OT correspond to a 300 mrad acceptance horizontally, and a 250 mrad acceptance vertically. Each tracking station is built from 72 modules; each module contains two layers of drift tubes. The OT has a drift

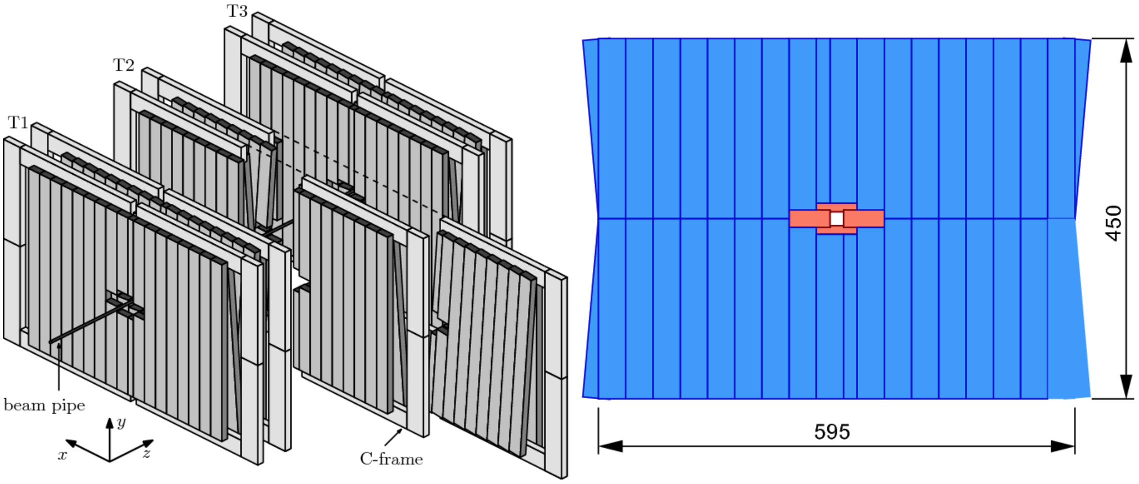

Figure 3.8: Layout of the LHCb Outer Tracker system on the right and a schematic diagram of one layer including dimensions in cm on the left.

time resolution of 2.6 ns and a spatial drift resolution of 179 μm. A diagram of the OT system can be seen in Figure 3.8.

3.2.3 Ring Imaging Cherenkov Detectors

The RICH detectors provide particle identification of kaons, pions and protons with momenta 2 - 100 GeV/c. The RICH detectors consist of two detectors; RICH1 upstream from the magnet and RICH2 downstream from the magnet. RICH1 has good performance in the low momentum range 1 - 60 GeV/c whereas RICH2 gives good separation of particles with higher momenta. RICH1 uses C_4F_{10} gas and RICH2 uses CF_4. During Run 1 RICH1 also included an aerogel radiator; this was removed for Run 2 as its ability to provide particle identification for particles with low momentum was compromised by the low number of photons in RICH1 in such a high track multiplicity environment. Removing it also contributed significantly to the speed of the RICH reconstruction as it reduced by more than half the number of photon candidates (combinations of photon-detector hits with tracks) for which a Cherenkov angle is calculated [67].

When a charged particle travels through a medium faster than the speed of light in that medium, Cherenkov radiation is emitted. Cherenkov radiation is emitted in a cone shape with opening angle θ_c with respect to the direction of the particles

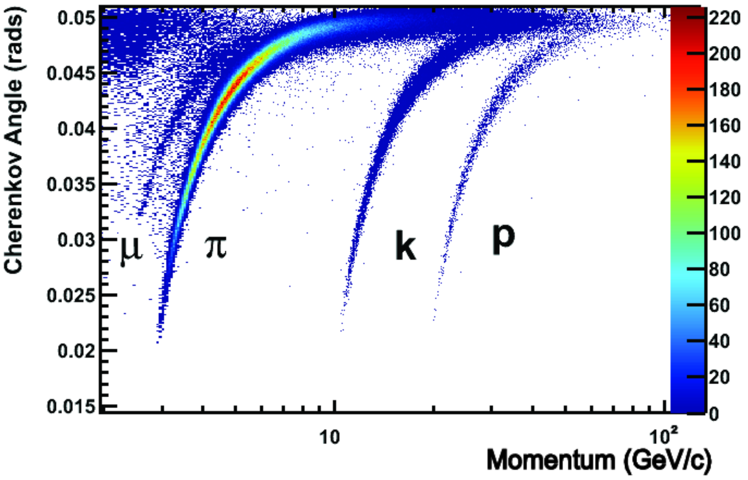

Figure 3.9: Reconstructed Cherenkov angle as a function of track momentum in RICH1 where the mass hypotheses for different particles are indicated.

momentum:

$$\cos\theta_c = \frac{1}{n\beta} \tag{3.2}$$

where n is the refractive index of the material and $\beta = v/c$ and v is the velocity of the particle. If the momentum of the particle is known, this provides a measurement of the mass of the particle. The mass hypotheses of different particles can be seen in Figure 3.9 in the plot of Cherenkov angle against the particle's momentum.

Through a combination of spherical and flat mirrors, the Cherenkov light is focused and reflected out of the acceptance onto an array of Hybrid Photon Detectors (HPD). To reduce the amount of scattering, RICH1 uses four lightweight spherical mirrors constructed from a carbon-fibre reinforced polymer. An incident Cherenkov photon releases a photoelectron from the conversion in a photocathode. The photoelectron is then accelerated by a high voltage field onto a silicon detector. The Cherenkov angle is reconstructed from the impact points of the Cherenkov photons on the HPDs. The resolution of the Cherenkov angle is determined to be 1.6 mrad for C_4F_{10} and 0.7 mrad for CF_4 [45]. A schematic diagram of the RICH detectors can be seen in Figure 3.10.

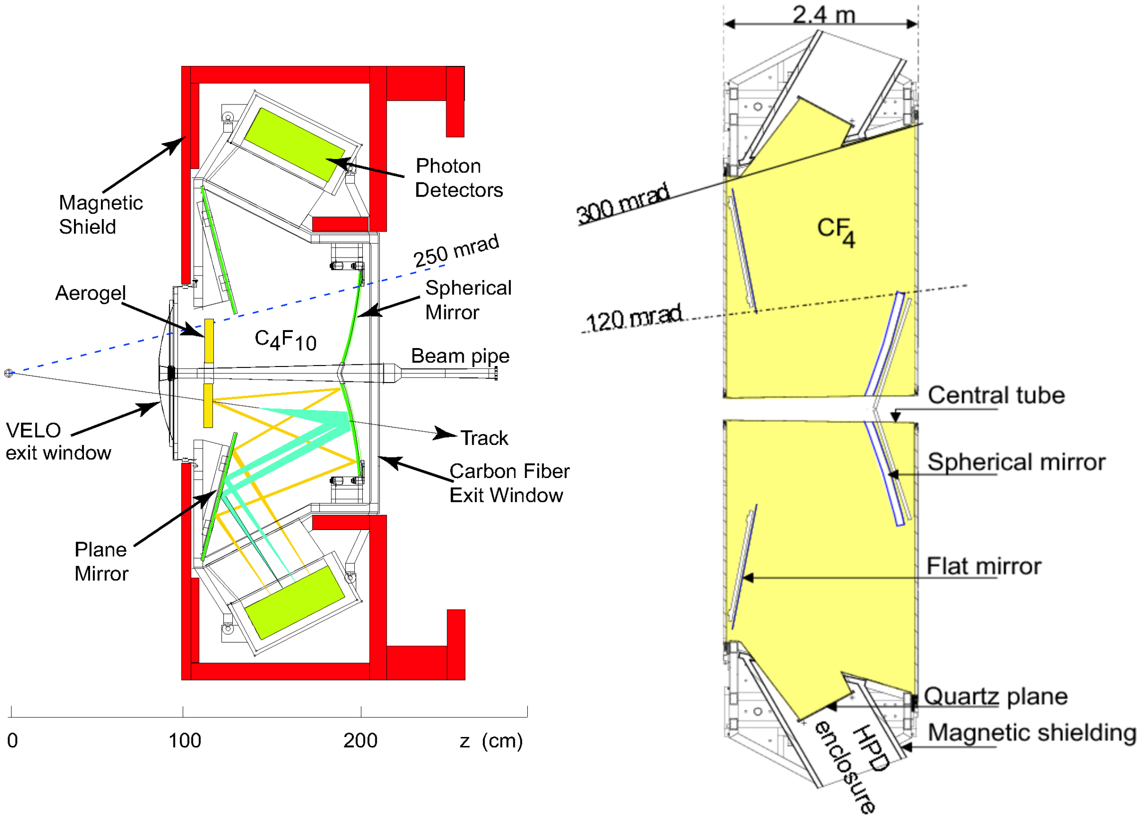

Figure 3.10: Schematic diagrams of the RICH1 on the left and RICH2 on the right including the dimensions of the detectors [26].

3.2.4 Calorimeter system

The LHCb calorimetry system consists of: the Pre-Shower (PS), the Scintillator Pad Detector (SPD), the Electromagnetic Calorimeter (ECAL) and the Hadronic Calorimeter (HCAL). The system is designed to stop most types of particles (electrons, photons, neutrons and other hadrons) and measure their energy loss in the process as they come to a halt. This provides particle identification for electrons and photons in the ECAL and protons, neutrons and other hadrons in the HCAL. The SPD determines whether particles hitting the calorimeter system are charged or neutral, while the PS indicates the electromagnetic character of the particle. The LHCb calorimeters are sampling calorimeters; they only measure a certain fraction of the energy deposited, which then needs to be calibrated to obtain the full energy. A sampling calorimeter typically has interleaved layers of a very dense material (for example lead or tungsten) designed to stop particles and initiate electromagnetic or hadronic showers and the ‘active’ material where the energy deposits are measured.

The SPD and PS consist of scintillating pads with a thickness of 15 mm, interspaced with a lead converter. Light is collected using wavelength-shifting fibres (WLS). The ends of the fibre are used to transmit the light to photomultipliers located at the edge of the detector. The SPD and PS are used, along with the ECAL, to trigger on electrons, photons and neutral pions.

The ECAL consists of alternating scintillating tiles and lead plates. The cell size varies from 4 × 4 cm in the inner part of the detector, to 6 × 6 cm and 12 × 12 cm in the middle and outer parts. An electromagnetic shower is produced in the 4 mm thick scintillation material and the 2 mm thick lead layer stops the particle since the kinetic energy is converted to other forms. Similarly to the SPD and PS the light is generated in the scintillation pads which are read out by the WLS fibres. The photons can then be read out by the photomultipliers. The overall detector dimensions are 7.76 × 6.30 m, covering an acceptance of 25 - 300 mrad in the horizontal plane and 25 - 250 mrad in the vertical.

The HCAL provides measurements of the position and energy of protons, neutrons and other hadrons. The HCAL is positioned behind the ECAL and consists of thin iron plates interspaced with scintillating tiles arranged parallel to the beam pipe. The cell dimensions of the calorimeter are 13 × 13 cm for the inner part and 26 × 26 cm for the outer. The scintillating tiles are 3 mm thick and are interspaced with 1 cm thick iron absorber. Similarly to the other calorimeter systems, the light is collected by optical fibres and read out using photomultipliers. The HCAL is not used for most LHCb analyses, but it plays a crucial role in the hardware trigger, providing information in a very short time on the level of hadronic activity in a bunch crossing (the ‘L0Hadron’ trigger). This subdetector will be completely removed for Run 3, since the hardware trigger will no longer be used. A diagram of the calorimetery system can be seen in Figure 3.11.

3.2.5 Muon system

The muon system provides particle identification and triggering of muons; the information is used in the Level-0 muon triggers as well as in the high-level trigger and offline analysis. Due to the fact that muons are heavy particles and lose less

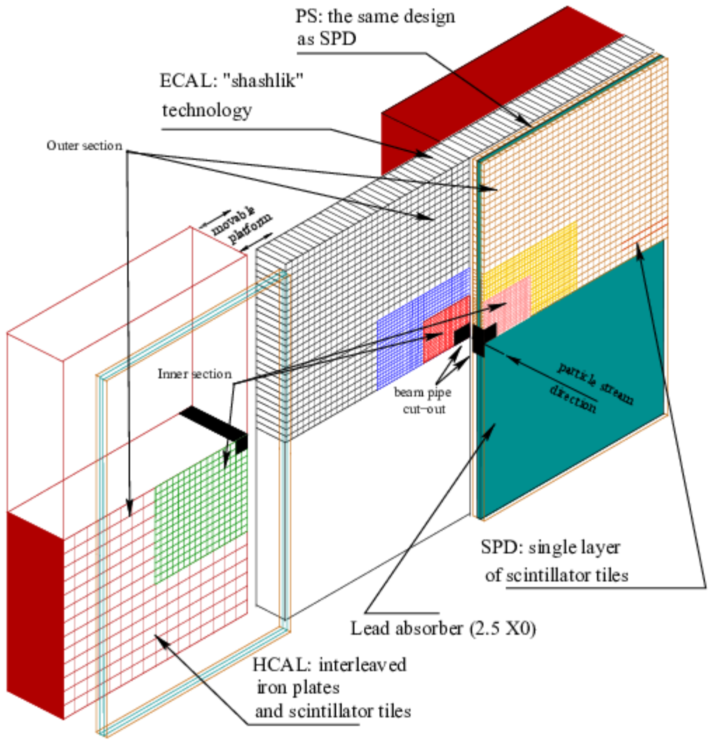

Figure 3.11: A diagram of the LHCb calorimeter system including the PS, SPD, ECAL and HCAL [18].

energy due to Bremsstrahlung compared to electrons, they are likely to travel through the full detector; this motivates the position of the muon stations at the end of the detector. The muon system is comprised of five stations: M1 is situated before the calorimeter system and M2-M5 are placed after. The muon system has an acceptance of ±300 mrad in the horizontal axis and ±250 mrad in the vertical. Each station is divided into four regions, R1 to R4, with increasing distance from the beam axis. The granularity increases as the regions are further removed from the beam line, such that the occupancy along the detector is comparable. The penetrating power of muons increases with their momentum, so the number of hits will depend on the muon kinematics. Muons of momenta $3 < p < 6$ GeV/c are expected to provide hits in M2 and M3; muons of momenta $6 < p < 10$ GeV/c, are expected to produce hits in M2, M3 and either M4 or M5. Muons with a momentum larger than 10 GeV/c should provide hits in all muon stations [45]. A diagram of the muon system can be seen in Figure 3.12.

The muon system contains multi-wire proportional chambers (MWPC) filled

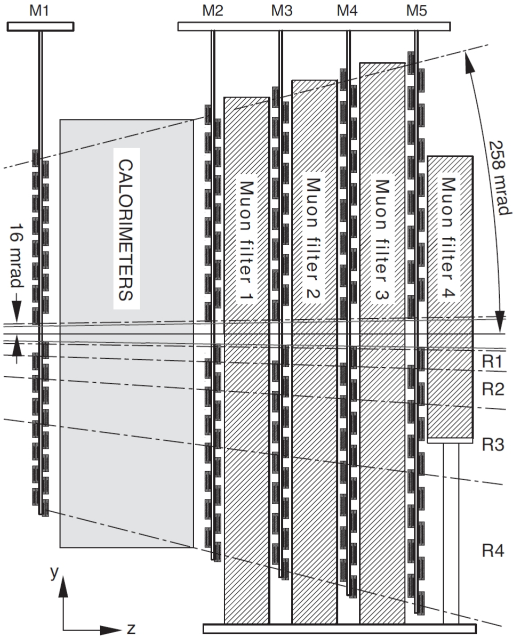

Figure 3.12: The LHCb muon system consisting of muon stations M1-M5 split into regions R1-R4 [39].

with a gas mixture of carbon dioxide, argon and CF_4. The muon traverses through the detector and ionizes the gas producing electrons; the electrons are collected on a tungsten wire of diameter 30 μm. A drift time resolution of 5 ns is achieved [45]. In the region closest to the beam line in M1, 12 Gas Electron Multiplier (GEM) chambers are used which were chosen since they are more radiation-hard. The GEM chambers consist of a cathode, and electrode and three GEM foils, and is filled with the same gases as in the MWPCs. A drift time resolution of 3 ns is achieved in the GEMs.

3.2.6 The LHCb Trigger

At the LHC the proton bunch crossing rate is 40 MHz; the LHCb trigger system is designed to reduce the data rate to 5 kHz which can be saved to storage for offline analysis [11]. The trigger system consists of the Level-0 (L0) hardware trigger and two high-level software triggers, HLT1 and HLT2. This can be seen in the diagram in Figure 3.13.

The L0 trigger reduces the rate of events considered for further processing from the *pp* bunch crossing rate of 40 MHz to 1 MHz using real-time information from

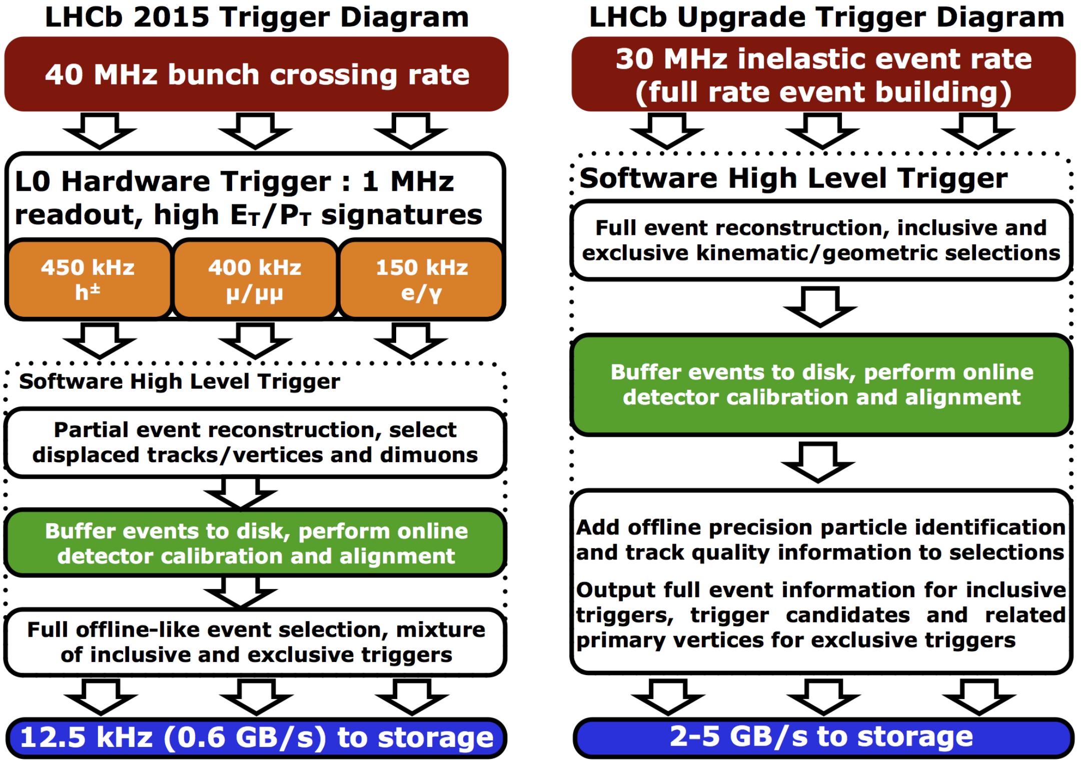

Figure 3.13: LHCb trigger system for the Run 2 data taking period on the left and Run 3 on the right [59].

the VELO, calorimeter and muon systems. The L0 uses signatures of high p_T tracks and high energy calorimeter deposits to identify potential heavy flavour events. In addition, it uses two dedicated silicon layers of the VELO to perform a simplified vertex reconstruction, which allows events with multiple *pp* interactions to be rejected.

The HLT software trigger is run on a CPU farm. HLT1 performs a partial reconstruction using information from the tracking stations and identifies tracks of $p_T > 500$ MeV. The information from the tracking system is also used to identify events with a high IP which is a signature of particles from b and c-hadron decays. The trigger also uses the output of multivariate algorithms to classify events with one or two tracks which are consistent with coming from a heavy and long-lived hadron. The information from the muon system is used to select single and dimuon events. This further reduces the readout rate to 100 kHz.

The second stage HLT2 performs a full event reconstruction using information from the entire detector. All charged tracks are reconstructed and particle identification information is available. For example reconstructed displaced vertices are used as a signature of b hadron decays. The HLT2 consists of a mixture of inclusive and exclusive triggers and results in an output rate of 12.5 kHz which is sent to storage for offline analysis. Inclusive triggers select events with resonances such as J/ψ which can be used for calibration. Exclusive triggers use information such as the mass, vertex quality and separation for a B candidate to provide a high efficiency for fully reconstructed B decays.

Before HLT2 is run, a real-time calibration and alignment takes place in which time the data is buffered to disk while waiting for them to become available. The tracking detectors including the tracking system and the VELO are aligned using a Kalman filter. In addition the RICH detectors are aligned at every LHC fill and the calorimeters are calibrated in order to counteract changes and ageing of the detector material.

In Run 3 we will need to achieve the same reconstruction performance with a harsher environment and increased pile-up. This will be achieved by recording all bunch crossings with a fully software-based trigger. The hardware (L0) trigger will be completely removed. The HLT1 reconstruction will be run on Graphics Processing Units (GPUs), including partial and fast reconstruction and selections. The difference between the trigger schemes in Run 2 and Run 3 is seen in Figure 3.13.

CHAPTER 4

Analysis Method

The mixing parameters x and y and the *CP*-violation parameters $|q/p|$ and ϕ (alternatively defined in terms of Δx and Δy) can be extracted from a time and phase-space dependent fit to the Dalitz variables and decay time of the $D^0 \to K_S^0\pi^+\pi^-$ decay. The time-dependent amplitudes of a neutral D meson decaying to some final state f are given by the following, repeated from Equation 2.42:

$$\mathcal{A}_f(t) \equiv \langle f|\, \mathcal{H}\, \big|D^0(t)\big\rangle = \frac{e_1(t)+e_2(t)}{2}\mathcal{A}_f + \frac{q}{p}\frac{e_1(t)-e_2(t)}{2}\bar{\mathcal{A}}_f \tag{4.1}$$

$$\bar{\mathcal{A}}_f(t) \equiv \langle f|\, \mathcal{H}\, \big|\bar{D}^0(t)\big\rangle = \frac{e_1(t)+e_2(t)}{2}\bar{\mathcal{A}}_f + \frac{p}{q}\frac{e_1(t)-e_2(t)}{2}\mathcal{A}_f \tag{4.2}$$

where $\mathcal{A}_f$ and $\bar{\mathcal{A}}_f$ are time and phase-space dependent amplitudes and

$$e_{1,2}(t) = e^{-imt}e^{-\frac{\Gamma}{2}t}e^{\mp(y+ix)\frac{\Gamma}{2}t}. \tag{4.3}$$

Since $\mathcal{A}_f$ and $\bar{\mathcal{A}}_f$ are functions of the phase space $m^2(K_S^0\pi^+)$ and $m^2(K_S^0\pi^-)$, the amplitude dependence on decay time and phase space is directly influenced by neutral meson oscillations and matter-antimatter asymmetries. Thus the mixing and *CP*-violation parameters can be extracted from the time and phase-space dependent fit to data. The mixing parameters are given as: $x \equiv (m_1 - m_2)/\Gamma$ and $y \equiv (\Gamma_1 - \Gamma_2)/(2\Gamma)$

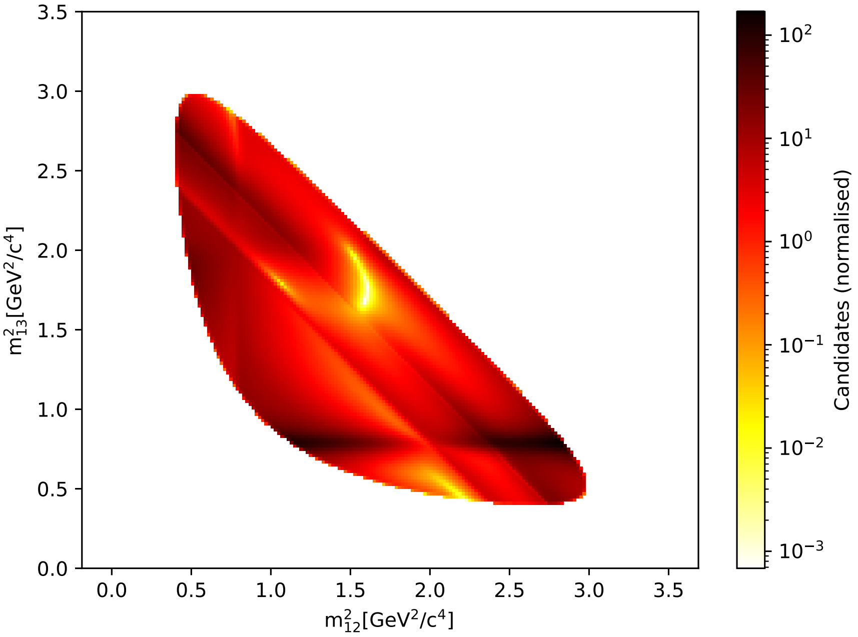

Figure 4.1: Dalitz plot of the $D^0 \to K^0_S\pi^+\pi^-$ decay illustrating the intermediate resonances and their interferences.

where x is the mass difference between the mass eigenstates of the neutral D meson and y is the width difference.

The phase-space distribution of the $D^0 \to K^0_S\pi^+\pi^-$ decay is modelled by expressing the decay as the sum of intermediate resonances and their interferences. The neutral D meson decays into one stable final state particle and a resonance followed by the decay of the resonance into the other two final state particles. The decay amplitude is then modelled by the resonant and non-resonant contributions and their interferences across the phase-space spanned by the Dalitz variables $m^2(K^0_S\pi^+)$ and $m^2(K^0_S\pi^-)$. Due to the different masses and widths of the resonances, they manifest themselves in different phase-space regions. Scalar resonances appear as a band in the Dalitz plot whereas vector resonances exhibit one node and tensor resonances show two nodes as can be seen in Figure 4.1 and Figure 2.4. The amplitudes at a given point in phase-space are given by:

$$\mathcal{A}_f \equiv \mathcal{A}(m^2(K^0_S\pi^+), m^2(K^0_S\pi^-)) = \sum_r c_r A_r(m^2(K^0_S\pi^+), m^2(K^0_S\pi^-)) \tag{4.4}$$

$$\bar{\mathcal{A}}_f \equiv \bar{\mathcal{A}}(m^2(K^0_S\pi^+), m^2(K^0_S\pi^-)) = \sum_r \bar{c}_r \bar{A}_r(m^2(K^0_S\pi^+), m^2(K^0_S\pi^-)) \tag{4.5}$$

where the sum is evaluated over all intermediate resonances r with complex amplitude A_r contributing to the decay with complex coefficients c_r.

If the decays $D^0 \to f$ and $\bar{D}^0 \to f$ are *CP*-symmetric, in the absence of mixing then $\mathcal{A}(m^2(K^0_S\pi^+), m^2(K^0_S\pi^-)) = \bar{\mathcal{A}}(m^2(K^0_S\pi^-), m^2(K^0_S\pi^+))$. As such, the Dalitz coordinates are defined such that the D^0 and $\bar{D}^0$ phase space is mirrored so that these two samples can be simultaneously visualised and compared. This leads to the definition of the Dalitz variables in terms of the final state particles and the D^0 flavour: $m^2_{12} = m^2(K^0_S\pi^+)$ and $m^2_{13} = m^2(K^0_S\pi^-)$ for D^0 and $m^2_{12} = m^2(K^0_S\pi^-)$ and $m^2_{13} = m^2(K^0_S\pi^+)$ for $\bar{D}^0$; in both cases $m^2_{23} = m^2(\pi^+\pi^-)$. Then using this definition we obtain $\mathcal{A}(m^2_{12}, m^2_{13}) = \bar{\mathcal{A}}(m^2_{12}, m^2_{13})$ under *CP*-symmetry.

The parameters of interest, the mixing parameters x and y and *CP*-violation parameters $|q/p|$ and ϕ, can be extracted from a fit in D^0 decay-time and the Dalitz variables to data; this is hereby referred to as the mixing fit. The amplitude model describes the amplitude of the $D^0 \to K^0_S\pi^+\pi^-$ decay as a superposition of intermediate resonances and their interferences. There is no way, a priori, to know which resonances enter the model and their shapes, which have associated uncertainties. This requires a data-driven treatment whereby the state-of-the-art models from previous analyses are used as starting points, but the final model is determined from the LHCb data itself. The preliminary model is taken from Ref. [20] from the Belle and BaBar collaborations. In addition to narrow (Breit-Wigner) resonances for L=1 (P-wave) and L=2 (D-wave) resonances, there can be non-resonant L=0 (S-wave) components. These are modelled using data-driven parameterisations based on previous scattering experiments, as described in Chapter 8. The parameters of the fit are the real and imaginary components of the amplitudes of the resonances, the masses and widths, the S-wave components and the mixing and *CP*-violation parameters x, y, $|q/p|$ and ϕ. The masses and widths of the resonances and the S-wave shape parameters are fixed from initial time-integrated fit studies as discussed in Chapter 8 or to the world averages in the case of some of the masses and widths. The fit can be run with the assumption of no *CP*-violation in which the *CP*-violation parameters are fixed to $|q/p| = 1$ and $\phi = 0$, or with *CP*-violation allowed in which case they are allowed to float. The time-dependent amplitude fit is developed and ran using the GooFit framework [73], a massively parallel maximum likelihood fitting framework which allows time-dependent amplitude fits to be ran on GPUs.

As well as theoretical knowledge of the amplitude model, there are several experimental effects such as acceptance and detector resolution, as well as background contamination which need to be accounted for in the mixing fit. For example, the detector geometry and reconstruction and event selection can distort the kinematic distributions of the final state particles, leading to a non-uniform acceptance across the Dalitz plane of the decay. There are also known variations in acceptance as a function of decay-time as well as a finite decay-time and phase-space resolution. In addition there is a non-negligible amount of combinatorial background remaining after the event selection, which contaminates the sample and must be modelled in the mixing fit. Out ability to tag the initial flavour of the neutral D meson as a D^0 or $\bar{D}^0$ is also imperfect in reality. The rest of this chapter briefly describes these experimental features, which are covered in more detail in Chapter 7.

The data used in this analysis were taken during the Run 2 data-taking period in years 2016-2018. This analysis uses D mesons which originate from semi-leptonic B meson decays and distinguishes between two decay chains; single-tagged and double-tagged:

- $B \to D^0(\to K^0_S\pi^+\pi^-)\mu^-\bar{\nu}_\mu X$ (single-tagged)
- $B \to D^{*+}(\to D^0(\to K^0_S\pi^+\pi^-)\pi^+)\mu^-\bar{\nu}_\mu X$ (double-tagged).

This is an inclusive selection in which if there are additional particles in the decay, X, we still collect it as signal. The distinction between the single and double-tagged decay chains is made since the additional information added by the pion from the $D^*(2010)^\pm$ decay can be exploited to have a cleaner sample with less background. The initial flavour of the neutral D meson is tagged by the charge of the muon in the single-tagged sample and the charge of the so-called ‘soft pion’ in the double-tagged sample. It is possible that the D^0 meson is assigned the wrong flavour due to the $B \to D\mu X$ decay being reconstructed with a muon with the wrong charge. This can happen when the D^0 is paired with a random muon with the wrong charge. For the double-tagged case, the charge of the soft pion is used to tag the initial flavour of the D^0 but for the single-tagged case, the D^0 would be assigned the wrong flavour. The mistagged candidates would have the Dalitz coordinates m^2_{12} and m^2_{13} swapped and the decay time can be mismeasured. It is therefore necessary to determine the mistag fraction by use of a control sample so this can be accounted for in the final amplitude fit. This can be done by exploiting the two-body decay $D^0 \to K\pi$ and is discussed in more detail in Section 8.6.

In addition the data are split into subsamples by K^0_S type: K^0_S (LL) or K^0_S (DD) where L and D refer to long and downstream tracks. The K^0_S is reconstructed through its decay to two pions $K^0_S \to \pi^+\pi^-$. The K^0_S (LL) type refers to K^0_S which decay within the VELO acceptances such that both pions leave tracks in the VELO and tracking system. For K^0_S (DD) candidates, the decay occurs outside the VELO and the two pions only leave hits in the tracking stations. Note that it is possible to reconstruct K^0_S (LD) decays, where only one pion leaves hits in the VELO. However, these are dominated by background and not used in this analysis. Due to the long lifetime of the K^0_S, $(8.954\pm0.004)\times10^{-11}$ s roughly a third of K^0_S reconstructed in the LHCb detector decay inside the VELO acceptance. A schematic of the LHCb tracking system with the five different types of track categories is shown in Figure 4.2. The different K^0_S types have different kinematics and are subject to different detector effects; they are therefore considered as separate subsamples for the fit. In particular the K^0_S (LL) has better momentum resolution so the two types are subject to different selection requirements.

The data used in this analysis are selected as follows; events are selected from those which have passed the LHCb trigger system, a loose offline preselection called stripping is then applied to these events. Specific trigger requirements and tighter offline preselection cuts are then applied before performing a multivariate analysis to further suppress combinatorial background. The distinction between signal and background used in the multivariate analysis is achieved by using so-called sWeights [69] from data, calculated from a fit to the D^0 mass for the single-tagged sample and $\delta m \equiv m(D^*) - m(D^0)$ for the double-tagged sample. The sWeights are calculated using the sPlot technique [69] which can statistically disentangle the

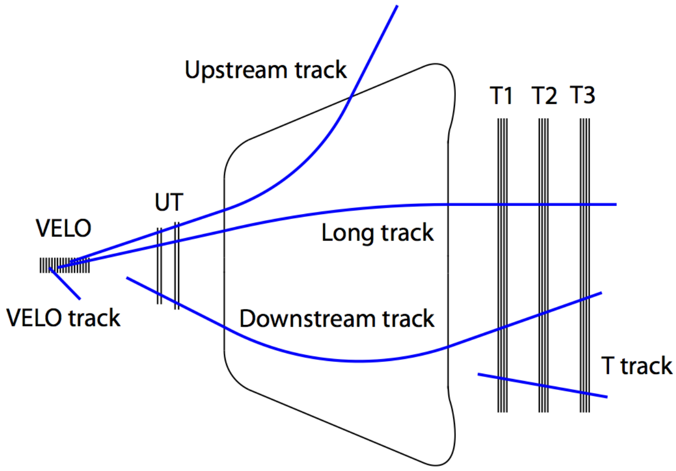

Figure 4.2: Schematic layout of the LHCb tracking system with different track types: VELO, Upstream, Long, Downstream and T tracks are shown. UT refers to the Upper Tracker also known as the TT [75].

signal and background distributions given a discriminating variable (this will be discussed in more detail in Section 5.4). Finally multiple candidates are removed and the double-tagged events are removed from the single-tagged samples. The data selection is discussed in detail in Chapter 5.

In the mixing fit, the background distribution for the D^0 decay-time and Dalitz variables is derived from a data-driven approach. The background distribution is obtained by extracting the sWeights using a similar approach as described above, but after all selection criteria have been applied. By extracting the per-candidate sWeights, the data can be split into signal and background distributions, which are used as inputs to the amplitude fit model. A per-event signal probability is derived from the $m(D^0)$ and δm mass fits; this is used as an input in the amplitude fit in order to assign the appropriate combination of signal and background PDF for each candidate.

The detector's forward geometry leads to a limited angular acceptance and the design of the detector and the applied selection criteria lead to a limited acceptance for characteristics such as particle momenta or decay times. The detector and reconstruction effects can lead to a non-uniform acceptance in phase-space and decay-time. This is accounted for in the mixing fit model by deriving the phase-space and decay-time acceptance from simulation. The simulation has imperfect agreement with data; it is therefore reweighted in certain kinematic variables in order to provide a better description of data. The simulated samples and the kinematic reweighting are discussed in detail in Chapter 6. In addition we know that the detector has some finite decay-time resolution. This is also derived from simulation and accounted for in the mixing fit model. In addition realistic toy pseudo-experiments are generated in order to asses the bias and coverage of the mixing fit, and to provide information for assessing systematic uncertainties on the reported parameter measurements.

In summary, the signal amplitude model is built from resonant and non-resonant contributions and their interferences. The background model is derived from a data-driven approach and the signal probabilities are derived from data and assigned as a per-event weight in the fit. The phase-space resolution and decay-time acceptance and resolution are derived from simulation and included in the fit model. The inputs required for the mixing fit are as follows:

- The amplitude model consisting of resonant and non-resonant components and their shapes (Chapter 8),
- Per-event signal and background probabilities which are taken from the D^0 (δm) fits for single-tagged (double-tagged) candidates (Chapter 5),
- Background distributions for the Dalitz variables and decay time, derived using a data-driven approach using background sWeights from the mass fits (Chapter 5),
- Description of the phase-space and decay-time acceptance, derived from simulation (Chapter 7),
- The decay-time resolution also derived from simulation (Chapter 7),
- The mistag fraction of wrongly tagged muons derived from $D^0 \to K\pi$ decays (Chapter 8).

The parameters of interest x and y (and Δx and Δy for the *CP*-violation allowed fit) are extracted from an unbinned maximum likelihood fit in D^0 decay-time and Dalitz variables to data.

CHAPTER 5

Data Selection

The data used in this analysis were collected at the LHCb detector during the Run 2 data-taking period. The D^0 candidates used in this analysis are from semi-leptonic B meson decays where the B meson is produced in the initial pp interaction and decays to a D^0 via the decay channels: $B \to D^0\mu^-X$ (single-tagged) and $B \to D^{*+}\mu^-X$ where $D^{*+} \to D^0\pi^+$ (double-tagged). Here the B meson is charged or neutral. The LHCb detector also has a high cross-section of prompt charm production where a D^{*+} meson is produced directly in the pp interaction [3], and the D^0 is produced in the decay $D^{*+} \to D^0\pi^+$. These samples can be used for analysis where the flavour of the D^0 is tagged by the pion. In principle prompt D^0 mesons are also produced, these are not used for analysis but can contribute to background. The prompt samples have higher yields due to the larger production cross-section, but requires tighter trigger requirements to suppress background rates. This leads to acceptance effects which are hard to model, in particular large correlations between decay-time and phase-space acceptance. The model-independent bin-flip analysis mentioned previously in Chapter 1 can take advantage of the larger prompt sample, since the model-independent analysis does not rely on the accurate description of the phase-space and decay-time acceptance effects. For the reasons described, the prompt sample is not considered in this analysis, which uses the semi-leptonic sample. This analysis uses the Run 2 dataset from 2016-2018, corresponding to an integrated luminosity of 6 fb^{-1}. The Run 1 dataset from 2011-2012 corresponds to an integrated luminosity of 3 fb^{-1}. This thesis reports a measurement using the Run 2 dataset only. However, we also perform the full event selection described in this chapter, as well as the assessment of the detector effects described in Chapter 7 for the Run 1 data, with the ultimate aim to add this independent sample to this analysis.

In order to select the candidates of interest from the large amounts of data collected at the LHC, a multi-stage event selection is performed. A typical event recorded at LHCb contains many particles, resulting in an enormous amount of data which cannot all be saved. It is therefore essential to: firstly reduce the full amount of data from a *pp* collision to a more manageable size which can be saved to disk, then further reduce background contamination to improve the analysis precision and reliability. The kinematic and topological characteristics of the decay can be exploited in the selection process to achieve this. This chapter describes the selection process which consists of the following stages:

- Events are required to pass the (hardware and software) LHCb trigger,
- Loose centralised offline preselection called stripping,
- Further analysis-specific, loose cut-based offline preselection,
- Multivariate selection to further maximise signal significance,
- Removal of multiple candidates.

Each of these stages will be described in detail below.

This analysis requires a sample of $D^0 \to K^0_S\pi^+\pi^-$ candidates where the D^0 originates from a semi-leptonic B meson decay and the B meson is produced in the primary *pp* interaction point (the PV). The B meson then decays into a D meson and a muon, the D^0 decays to $K^0_S\pi^+\pi^-$ and the K^0_S decays to two pions.

At the LHCb experiment, there are several decay properties which are typically exploited when events are selected. Due to the long lifetime of the B meson ((1.64 ± 0.004) ps for a charged B meson and (1.52 ± 0.004) ps for a neutral B meson), it travels a distance of several mm in the lab frame before decaying. This gives a distinct separation between the PV and the B meson decay vertex or secondary vertex

(SV). This is a characteristic signature of B meson decays which allows us to select events of interest. The impact parameter (IP) is defined at the transverse distance of closest approach between a particle's trajectory and a vertex, most commonly the PV. Charm mesons which originate from the PV (prompt) have an impact parameter of zero; therefore this quantity can be used to distinguish between prompt D mesons (background) and D mesons from semi-leptonic B meson decays. The χ^2_{IP} is defined as the difference in the vertex-fit χ^2 of a given PV reconstructed with and without the particle under consideration being included in the vertex fit. In addition, as a consequence of the heavy mass of b hadrons, the decay of a heavy hadron usually leads to final state particles with a relatively large transverse momentum p_T compared to background events. The LHCb detector also provides excellent particle identification (PID) using information from the RICH detectors which is exploited to identify protons, kaons and pions.

Several of these quantities which can be exploited in the event selection are defined in terms of χ^2 variables. This is effectively a way to simultaneously account for the value of the quantity and the uncertainty of the measurement, providing a more stable performance for selection criteria. For example the flight distance is defined as the displacement between a particle's PV and SV, ie. the distance travelled before the b or c hadron decays. This quantity can be used to separate long-lived from prompt particles; however the corresponding χ^2 variable gives a measure of the significance of the flight distance so is therefore a better choice as a discriminating variable in the event selection.

Firstly, events are required to pass the hardware (L0) trigger which selects events with a momentum above a certain threshold, consistent with those containing high momentum hadrons. There is then a software based trigger selection where a partial event reconstruction is performed in HLT1 using information from the VELO and tracking stations, which identifies tracks with a momentum above a certain threshold. In Run 2, a real-time calibration and alignment takes place between HLT1 and HLT2, so the reconstruction run at HLT2 uses the final fully-optimised algorithms. The HLT2 trigger performs a full event reconstruction using information from the entire detector. These events are then saved to disk for offline analysis. The data are then required to pass a loose offline preselection called stripping. $D^0 \to K^0_S\pi^+\pi^-$ candidates are required to pass dedicated stripping lines:

- Strippingb2D0MuXKsPiPiLLCharmFromBSemiLine
- Strippingb2D0MuXKsPiPiDDCharmFromBSemiLine
- Strippingb2DstarMuXKsPiPiLLCharmFromBSemiLine
- Strippingb2DstarMuXKsPiPiDDCharmFromBSemiLine

These are for single and double-tagged and K^0_S (LL) and K^0_S (DD) types. The stripping requirements are described in detail later in this chapter. Further loose offline preselection can then be applied to the data from stripping after which a multivariate technique is used to further reduce combinatorial background. The stripping, preselection and multivariate analysis selection is the same for both Run 1 and Run 2 data.

At the LHCb detector, for some events it is possible to have more than one genuine $D^0 \to K^0_S\pi^+\pi^-$ candidate. An 'event' is LHCb convention to describe the whole outcome of a given bunch-crossing and is identified by a unique event and run number. A candidate is a top level reconstructed object, for example a *b*-hadron, whose properties are to be measured, for example a mass or lifetime. An event with multiple candidates is an event in which there is more than one candidate passing the final selection. Multiple candidates need to be removed in order to avoid double-counting the events in the Dalitz plot and creating biases in the Dalitz variables of the decay. These are removed by randomly rejecting all but one of the candidates with the same event number. Due to the inclusive reconstruction in the preselection, the double-tagged dataset is a subset of the single-tagged dataset. To ensure that all analysed samples are statistically independent, double-tagged candidates have to be separated from the single-tagged sample. Double-tagged candidates are removed from the single-tagged dataset if the candidate's event number and the D^0 mass are the same. In this analysis, we select a sample of double-tagged candidates where the muon and pion tags agree (ie. they are of the opposite charge), the pion tag is used to tag the initial flavour of the neutral D meson. In addition to selecting a double-tagged sample of $D^{*+}\mu^-$ candidates, the same selection requirements are also applied to a sample of $D^{*+}\mu^+$ events. This is the so-called wrong-sign (WS) sample where the muon and pion tags do not agree; this independent sample is used for studies of the mistag component for the single-tagged sample for which the initial flavour is tagged by the charge of the muon. In addition a sample of two-body $D^0 \to K^-\pi^+$ decays have been selected using our selection criteria for the evaluation of the mistag fraction.

5.1 Trigger

The LHCb trigger comprises an offline L0 hardware trigger and the software High Level Trigger (HLT), consisting of HLT1 and HLT2. The trigger requirements are identified by a prefix indicating which candidate has passed the selection criteria of the specific trigger line. In this analysis, trigger requirements are imposed on the B candidate and the muon candidate. We do not impose trigger requirements on the D^0 candidate in order to reduce trigger-induced biases for the D^0 decay; since trigger requirements may be correlated to the decay-time and final state phase-space. This helps to simplify the analysis. The trigger lines used are listed in Table 5.1. In addition, trigger decisions are classified depending on whether the candidate's signal final state tracks were involved in the decision that the event passed the trigger. Hence, the events may be classified as triggered on signal (TOS) or triggered independently of signal (TIS). The general selection algorithm behind the listed trigger requirements does not change within the Run 1 or Run 2 data-taking periods, although there are differences between Run 1 and Run 2. However, the thresholds of the selection variables are subject to change in a given data-taking period; these thresholds are stored in so-called Trigger Configuration Keys (TCKs).

The L0 trigger is an online hardware trigger which decides which events to keep in real time. The L0 trigger can be subdivided into Muon, Dimuon, Electron, Hadron and Photon lines. Due to the fast timing requirement, it only uses information from the VELO, calorimeters and muon chambers and looks for simple signatures of large transverse energy and high-momentum tracks which are signatures of heavy flavour interactions. The L0 trigger condition mu_L0MuonDecision_TOS indicates that the Muon line was activated by a particle assumed to be a muon in the event, which is

Trigger level	Trigger line
Run 2	
L0	mu L0MuonDecision TOS
Hlt1	mu Hlt1TrackMuonDecision TOS
	Hlt1TrackMuonMVADecision TOS
Hlt2	B TopoMu{2,3,4}BodyDecision TOS
Run 1	
L0	mu L0MuonDecision TOS
Hlt1	mu Hlt1TrackAllL0Decision TOS
Hlt2	B TopoMu{2,3,4}BodyBBDTDecision TOS

Table 5.1: Summary of the Trigger requirements used in this analysis.

part of the signal decay (TOS). This decision is based on the transverse momentum of the muon and the number of hits in the SPD. The number of hits in the SPD provides a measure of the multiplicity of the event and hence low-multiplicity events are rejected.

The HLT1 and HLT2 triggers consist of several trigger lines comprising selections of decay channels or classes of decay channels such as three-body decays with a high energy muon. In the first stage of the offline hardware trigger, HLT1, a partial event reconstruction is performed using information from the VELO and tracking stations. The decisions of the HLT1 trigger lines rely on the properties of individual tracks and not on information of the complete event. For example an HLT1 decision may require thresholds on the momentum, transverse momentum and IP of a partially reconstructed track. These thresholds can also vary with time over a given data-taking period. HLT1 triggers with ‘MVA’ in the name use multivariate algorithms to classify events with one or two tracks which are consistent with coming from a heavy and long-lived hadron.

The second offline high-level trigger, HLT2, performs full event reconstruction using information from the entire detector performing additional pattern recognition which is not possible in HLT1 due to strict time constraints. This results in high quality long and downstream tracks. In addition HLT2 exploits the full PID from the RICH detectors and calorimeter system. HLT2 track reconstruction uses multivariate algorithms to classify events while rejecting fake tracks and maximising efficiency [11].

5.2 The LHCb selection framework

The data which passes the LHCb trigger requirements is saved to disk for further offline analysis. The selection framework used in LHCb relies on combining reconstructed tracks under some physical hypothesis. Some charged and neutral particles are created in the reconstruction in the HLT, including electrons, protons, charged kaons and pions, photons and neutral pions. These particles can then be combined to form composite particles such as B and D mesons.

In order to perform a physics analysis we need to build a decay chain with reconstructed particles that represents the physics process we want to study. For example consider the decay $B^- \to D^0\mu^- X$ where $D^0 \to K^0_S\pi^+\pi^-$ and $K^0_S \to \pi^+\pi^-$, the X denotes one or more unreconstructed decay products (at least one neutrino). We build the decay chain as follows:

- Get the four input pions and filter according to our physics needs,
- Combine two oppositely charged pions to form a K^0_S and apply selection cuts as necessary,
- Combine the K^0_S with the remaining two oppositely charged pions to build a D^0 meson and apply selection cuts,
- Combine the D^0 with a muon to build a partially reconstructed B^- meson candidate, again applying cuts as necessary.

LHCb provides central packages which allows analysts to access pre-made particles with reasonable reconstruction and selections; in this case four pions. These particles can then be combined in the steps above to form composite particles such as the K^0_S and the D^0 meson; applying selection criteria at each stage. This selection process is called stripping. The reconstruction and selection criteria for events used in this analysis is described in detail in the following sections and in Table 5.2.

Variable	Cut
K_S^0 daughter $\pi^{\pm}$ track ghost probability	< 0.5 (LL)
K_S^0 p	> 2 GeV (LL), > 3 GeV (DD)
K_S^0 p_T	> 250 MeV
K_S^0 mass after vertex fit - PDG value	< 30 MeV
K_S^0 χ^2 distance between PV and decay vertex	> 100
K_S^0 decay vertex χ^2/ndf	< 6
K_S^0 $\cos\theta_{DIRA}$	> 0.99
D^0 mass before vertex fit - PDG value	< 100 MeV
D^0 p_T before vertex fit	> 2 GeV
D^0 scalar sum of daughter p_T	> 1.4 GeV
D^0 χ^2 distance of closest approach	< 20
D^0 mass after vertex fit	< 80 MeV
D^0 vertex χ^2/ndf	< 6
D^0 scalar sum of daughter $\pi^{\pm}$ p_T	> 1.4 GeV
D^0 p_T after vertex fit	> 2 GeV
D^0 $v_z^{K_S^0} - v_z^{D^0}$	< 10 mm
$\pi^{\pm}$ p	> 2 GeV
$\pi^{\pm}$ p_T	> 250 MeV
$\pi^{\pm}$ track χ^2/ndf	< 4
$\pi^{\pm}$ track ghost probability	< 0.5
$\pi^{\pm}$ χ^2_{IP}	≥ 4
D^* δm before vertex fit	(-5,175) MeV
D^* vertex χ^2/ndf	< 8
D^* δm after vertex fit	(0,170) MeV
$\mu^{\pm}$ p_T	> 800 MeV
$\mu^{\pm}$ p	> 3 GeV
$\mu^{\pm}$ track ghost probability	< 0.5
$\mu^{\pm}$ track χ^2/ndf	< 4
$\mu^{\pm}$ PIDmu	> 0
B mass before vertex fit	< 6.2 GeV
B mass after vertex fit	(2.5,6) GeV
B vertex χ^2/ndf	< 6
B $\cos\theta_{DIRA}$	> 0.999

Table 5.2: Summary of the cuts in the stripping lines used in this analysis The cuts and variables are described in more detail in the text.

5.2.1 Pion reconstruction

In this analysis K_S^0 are reconstructed by combining two oppositely charged pions. Both K_S^0 (LL) and K_S^0 (DD) candidates and the pions are taken from so-called 'Particle Containers' which contain the information on the pre-made particles with a reasonable reconstruction and initial selection. Pion candidates are required to have p $>$ 2 GeV and $\mathrm{p}_T > 250$ MeV. Tracks are fit using a Kalman filter. A Kalman filter is an algorithm that provides estimates of some unknown variables given some measurements observed over time. To ensure a good quality of fit, the pions are required to have a track-fit $\chi^2/ndf < 4$.

Fake (or ghost) tracks are defined as reconstructed tracks which do not correspond to the trajectory of a true particle but are due to a mis-reconstruction of hits from separate tracks or from detector noise. A neural network based algorithm is used in order to identify fake tracks in the LHCb pattern recognition [43] and hence identify the so-called ghost probability. The ghost probability of the pion tracks is required to be less than 0.5. Finally, all pions are required to be inconsistent with originating from the PV via the criterion $\chi^2_{IP} > 4$, where χ^2_{IP} is the χ^2 of the IP of the pion track with respect to the PV; pions which are combined to form a K_S^0 (LL) candidate are required to have $\chi^2_{IP} > 9$, since these are not expected to point back towards the PV.

5.2.2 K_S^0 reconstruction

A K_S^0 candidate is reconstructed by combining two oppositely charged pions originating from a common vertex. With the selected oppositely charged pion pairs, we can fit a $K_S^0 \to \pi^+\pi^-$ vertex. This is done by expressing the hypothesis that there is a common origin vertex of both tracks as an optimisation problem, and then varying the measured π^+ and π^- four-momenta within their measured uncertainties to best fit that hypothesis. The result is a vertex object which has a fit χ^2 associated to it. The quality of the fit can then be used in the event selection. The K_S^0 decay vertex χ^2/ndf is required to be less than 6 in order to ensure a good quality of the vertex fit.

With the fitted pion four-vectors, one can form the four-vector of the K_S^0 as their sum, creating the K_S^0 candidate. The K_S^0 is required to have transverse momentum $\mathrm{p}_T > 250$ MeV and $\mathrm{p} > 2$ GeV for LL and $\mathrm{p} > 3$ GeV for DD candidates. In addition the invariant mass of the $\pi^+\pi^-$ system is required to lie within 30 MeV of the known PDG value of the K_S^0 mass (497.611±0.013 MeV). The χ^2 distance between the K_S^0 candidate's best PV and decay vertex must be greater than 100; this selects K_S^0 candidates with a sufficiently long lifetime. The best PV is chosen as the primary vertex with the smallest χ^2_{IP}, which corresponds to the closest PV. The θ_{DIRA} is defined as the angle between the K_S^0 momentum and the K_S^0 flight direction from the best PV to the decay vertex. The cosine of this angle is required to satisfy $\cos\theta_{DIRA} > 0.99$, meaning that the momentum and the flight direction of the K_S^0 candidate agree. The K_S^0 (LL) track ghost probability is required to be less than 0.5.

5.2.3 D^0 reconstruction

A D^0 candidate is reconstructed by combining a K_S^0 with two oppositely charged pions originating from a common vertex. The χ^2 of the D^0 decay vertex must satisfy $\chi^2/ndf < 6$ to ensure a good quality of fit. Prior to the vertex fit, the invariant mass of the $K_S^0\pi^+\pi^-$ system is is required to lie within 100 MeV of the known D^0 mass (1864.84±0.17 MeV from the PDG), since these quantities should be close for signal candidates. In order to ensure the K_S^0 and two pions come from a common vertex, all sub-combinations of two daughter particles must be compatible with originating at a common point, quantified by the χ^2 of the track positions at the point of closest approach. This variable must be less than 20 for all combinations.

The daughter particles' (K_S^0 and two oppositely charged pions) four-vectors are used to form the D^0 four vector as their sum. The invariant mass of the $K_S^0\pi^+\pi^-$ system after the vertex fit must be within 80 MeV of the PDG reference value of the D^0 mass. The scalar sum of the transverse momenta of the daughter particles (four pions from the D^0 and K_S^0) is required to be greater than 1.4 GeV and the transverse momentum of the D^0 candidate must be $\mathrm{p}_T > 2$ GeV. In addition the restriction of $v_z^{K_s^0} - v_z^{D^0} > 10$ mm on the position of the D^0 along the z axis is used to ensure the K_S^0 decay vertex lies downstream from the D^0 decay vertex; thus requiring that the

K_S^0 daughters can be reconstructed in the tracking stations.

5.2.4 D^* reconstruction

For double-tagged candidates, a D^* candidate is formed by combining a D^0 candidate and a soft pion in the decay $D^{*+} \to D^0\pi^+$. Here the pion is referred to as 'soft' since it has low momentum, being produced in a decay with little available energy ($m(D^*) - m(D^0) - m(\pi) < 6$ MeV). If no D^* candidate is reconstructed which fulfills the criteria, the candidate enters the single-tagged sample.

The delta mass is defined as $\delta m \equiv m(D^*) - m(D^0)$ and is required to satisfy -5 $< \delta m <$ 175 MeV. This reduces background from combinations of D^0 candidates with soft pions, which are not associated with the signal tracks, due to the D candidates δm distribution exhibiting a peak around 145 MeV. After the vertex fit $0 < \delta m <$ 170 MeV is required.

5.2.5 Muon reconstruction

Muon candidates are required to have $\mathrm{p}_T > 800$ MeV and $\mathrm{p} > 3$ GeV. In addition the muon track's ghost probability must be less than 0.5. The muon must have a signature in the detector consistent with the expectations of a muon, encapsulated by the LHCb requirement PIDmu > 0. The track-fit χ^2 is required to satisfy $\chi^2/ndf <$ 4 to ensure a good quality of fit. The χ^2 of the IP of the muon track with respect to the PV is required to be $\chi^2_{IP} \geq 4$.

5.2.6 B reconstruction

A D^0 (single-tagged) or D^* (double-tagged) candidate is combined with a muon to form a B candidate. The B candidate's decay vertex must have $\chi^2/ndf < 6$ in order to ensure good quality of the vertex fit. The invariant mass of the combined daughter particles (muon and D^0 or D^*) must be less than 6.2 GeV. The mass of the B candidate after the vertex fit must satisfy $2.5 < m_B < 6$ GeV; this wide range accounts for the fact that there are missing B decay products such as the neutrino, which are not reconstructed. The constraint $\cos\theta_{DIRA} > 0.999$ is used, where θ_{DIRA} is the angle between the direction of flight of the B meson from the primary vertex to the decay vertex and the B momentum. This ensures good agreement between the flight direction and the momentum.

5.3 Preselection

In addition to the stripping and trigger requirements, the candidates are made to pass some loose preselection cuts and a multivariate analysis to further reduce background. Once the $D^0 \to K_S^0\pi^+\pi^-$ decay has been reconstructed, the final state particle kinematics can be updated based on the additional knowledge of the decay topology and particle masses. In turn this affects other quantities which are calculated form the final state four-vectors, such as invariant masses and particle momenta. For example one can assume that the two K_S^0 daughter pions originate from the K_S^0 with a specific mass; this is called a mass constraint. Applying kinematic constraints leads to new best estimates for the track parameters of the final-state particles. This process is called a kinematic refit and is performed by the DecayTreeFitter (DTF) algorithm [53].

This analysis uses two instances of DTF with different mass constraints. For each instance, the refitted variables are saved for later use. In the first instance, the $D^0 \to K_S^0\pi^+\pi^-$ decay is refitted constraining the mass of the K_S^0 candidate to 497.614 MeV. In the second instance the mass of the K_S^0 candidate is constrained as well as the mass of the D^0 candidate to 1864.86 MeV. Variables computed using both the K_S^0 and D^0 mass constraints are: the reconstructed D^0 decay-time and Dalitz variables and the δm for the double-tagged sample. This restricts the Dalitz variables of all candidates to the phase space consistent with energy and momentum conservation. The reconstructed D^0 mass is computed using only the K_S^0 mass constraint; this improves the D^0 mass resolution compared to that without the constraint. After the $D^0 \to K_S^0\pi^+\pi^-$ decay has been refitted with DTF, we ensure that the fit has converged for both instances, which is technically enforced by requiring that the number of degrees of freedom is greater than zero. To ensure a good quality of the DTF fit, the decay tree refit with the K_S^0 mass constraint is required to have $\chi^2 < 25$.

A signal D^0 mass window of $1805 \leq m(D^0) \leq 1925$ MeV is chosen for the single-

Variable	Cut	Description
$m(B)$	$<$ 4900 MeV	B meson visible mass
DTF VCHI2NDOF	> 0	DTF status must converge
DTFD0KS VCHI2NDOF	> 0	DTF status with D^0 and K_S^0 mass constraints must converge
$\tau(D^0)$	$>$ -1 ps	D^0 decay-time

Table 5.3: Summary of preselection cuts used in this analysis.

tagged sample; this broad range allows the study of background contributions in the lowest and highest mass regions where no signal is expected. For the double-tagged sample a tighter cut of $1844 \leq m(D^0) \leq 1884$ MeV is applied. A cut on the visible mass of the B meson is set to $<$ 4900 MeV. The decay time resolution at LHCb causes the D^0 decay-time to extend into a negative decay-time range. However, the D^0 decay-time range below -1 ps is populated solely by background candidates. Thus, requiring $t(D^0) >$ -1 ps leads to a significant background reduction. All preselection requirements are listed in Table 5.3.

5.4 sPlot

The D^0 mass distribution for the single-tagged sample (δm distribution for the double-tagged sample), is fitted with a model which comprises the sum of signal and background components, using an unbinned extended maximum-likelihood fit. From the fit, sWeights are extracted which allow the signal and background contributions to be separated and used as training samples for a Boosted Decision Tree (BDT).

The sPlot formalism [69] takes the signal and background distributions for a discriminating variable, in this case the D^0 mass, and computes the sWeight for a given event. The sample of events are assumed to be characterised by a set of variables which can be split into two components. The first is a set of variables for which the distributions of the events are known (in this case the D^0 mass or δm); this is referred to as the discriminating variable. The second is a set of variables for which the distributions are considered to be unknown, these variables are referred to as the control variables. The sPlot technique allows the signal and background distributions for the control variables to be statistically disentangled and reconstructed independently, without making use of any a priori knowledge on this variable. This is done by using the known signal and background distributions for the discriminating variable in order to infer the behaviour of the signal and background events with respect to the control variables. The sPlot technique relies on the assumption that the control variable is uncorrelated with the discriminating variable. In this case the sWeight is an event weight for each event in the sample which can be applied in order to reconstruct the signal and background distributions for the control variable.

The extended log-likelihood is given by:

$$\mathcal{L} = \sum_{e=1}^{N} \ln \left\{ \sum_{i=1}^{N_s} N_i f_i(y_e) \right\} - \sum_{i=1}^{N_s} N_i \tag{5.1}$$

where

- N is the total number of events in the data sample,
- N_s is the number of species of event populating the data sample (signal and background),
- N_i is the average number of events expected for the i^{th} species,
- y is the set of discriminating variables (D^0 mass or δm),
- f_i is the value of the probability density function (PDF) for the i^{th} species,
- $f_i(y_e)$ is the value of the PDFs f_i for event e, associated with a set of values y_e for the set of discriminating variables,
- x is the set of control variables which, by definition, do not appear in the above expression for $\mathcal{L}$.

The log-likelihood is maximised for each event and an sWeight is calculated for both signal and background. The sWeight is defined by:

$${}_sP_n(y_e) = \frac{\sum_{j=1}^{N_s} \mathbf{V}_{nj} f_j(y_e)}{\sum_{k=1}^{N_s} N_k f_k(y_e)} \tag{5.2}$$

where $\mathbf{V}_{nj}$ is the covariance matrix which can be derived from the second derivative of $-\mathcal{L}$.

A summary of the different steps to implement the sPlot technique are the following:

1. Consider we are dealing with a data sample in which several species of event are present (in our case signal and background).
2. A maximum likelihood fit is performed to obtain the signal and background yields N_i. The fit relies on a discriminating variable y (D^0 mass or δm) uncorrelated with a control variable x; the latter is therefore totally absent from the fit.
3. The sWeights ${}_sP$ are calculated using Equation 5.2, where the covariance matrix can be derived from the log likelihood in Equation 5.1.
4. Histograms of x can be filled by weighting the events with the sWeights ${}_sP$ where the sum of the entries are equal to the yields of each species N_i provided by the fit.

The sPlots reproduce the true distributions of the species in the control variable x, within the statistical uncertainties. The sWeights are extracted separately for each year and K^0_S type (LL, DD) and for single and double-tagged candidates.

For single-tagged samples, the signal is modelled by the sum of a Bifurcated Gaussian distribution and a Johnson SU distribution. The Bifurcated Gaussian distribution is given by:

$$f_{BiG}(x|\mu,\sigma_R,\sigma_L) = \begin{cases} \frac{1}{\sigma_L\sqrt{2\pi}} e^{-\frac{1}{2}\left(\frac{x-\mu}{\sigma_L}\right)^2} & x \leq \mu \\ \frac{1}{\sigma_R\sqrt{2\pi}} e^{-\frac{1}{2}\left(\frac{x-\mu}{\sigma_R}\right)^2} & x > \mu \end{cases} \tag{5.3}$$

where x is the measured variable (in the following cases m_{D^0} or δm, note this is different to the variable x in the sPlot formalism) and μ and $\sigma_{L,R}$ are the mean and standard deviation of the distribution and are free parameters of the fit. The Johnson SU distribution [54] is defined as:

$$f_{SU}(x|\gamma,\delta,\xi,\lambda) = \gamma + \delta\sinh^{-1}\left(\frac{x-\xi}{\lambda}\right) \tag{5.4}$$

where x is similarly the measured varibale m_{D^0} or δm and γ, δ, ξ and λ are free parameters of the fit. The background is modelled by a first order Chebychev polynomial for the K^0_S (LL) sample and second order for the K^0_S (DD) sample. For the K^0_S (LL) sample the full PDF is given by:

$$F_{LL} = n_{sig} \times (cf_{BiG}(m_{D^0}) + (1-c)f_{SU}(m_{D^0})) + n_{bkg} \times (1 + a_1 m_{D^0}) \tag{5.5}$$

where c is the fraction of f_{BiG} in the signal PDF, and n_{sig} and n_{bkg} are the number of signal and background events respectively. For the K^0_S (DD) sample:

$$F_{DD} = n_{sig} \times (cf_{BiG}(m_{D^0}) + (1-c)f_{SU}(m_{D^0})) + n_{bkg} \times \left(1 + a_1 m_{D^0} + a_2(2m^2_{D^0} - 1)\right) \tag{5.6}$$

where a_1 and a_2 are the coefficients of the polynomial and free parameters of the fit. The sWeights are extracted from the double-tagged sample by a fit to the δm distribution where $\delta m = m(D^*) - m(D^0)$. The signal is described by a Johnson SU distribution and a Gaussian and the background is modelled by a special PDF shape that can be used to model the background of $D^* - D^0$ mass difference distributions. The background PDF is given by:

$$f_{bkg}(\delta m | m_0, A, B, C) = \left(1 - e^{-\frac{\delta m - m_0}{C}}\right)\left(\frac{\delta m}{m_0}\right)^A + B\left(\frac{\delta m}{m_0} - 1\right) \tag{5.7}$$

where m_0, A, B and C are free parameters of the fit. The combined signal and background PDF for the double-tagged sample is then given by:

$$F = n_{sig} \times \left(cf_{SU}(\delta m) + \frac{1}{\sqrt{2\pi}\sigma}(1-c)e^{-\frac{1}{2}\left(\frac{\delta m - \mu}{\sigma}\right)^2}\right) + n_{bkg} \times f_{bkg}(\delta m) \tag{5.8}$$

where c is the fraction of the Johnson in the signal PDF. Plots of the D^0 mass fits for the Run 2 single-tagged samples can be seen in Figure 5.1 and δm distributions for the double-tagged samples in Figure 5.2. The fit parameters are displayed on the plots; the parameters of interest are the number of signal and background events and these are shown along with the signal purity in Table 5.4.

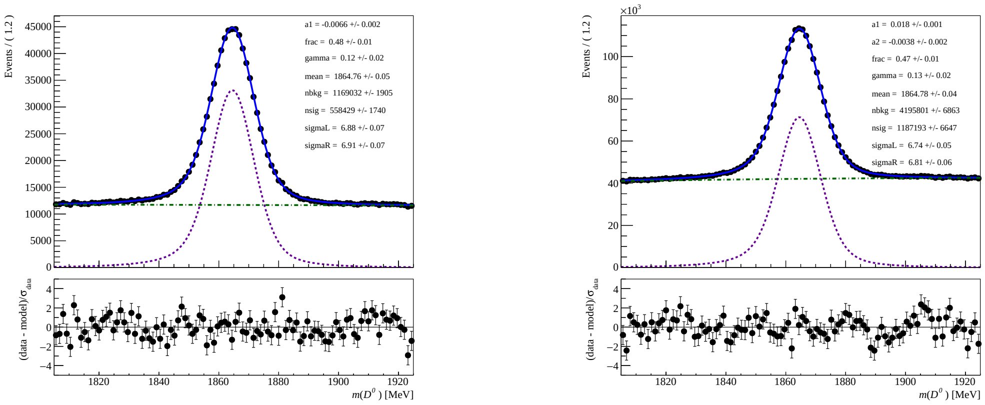

(a) K_S^0 (LL) 2016 (b) K_S^0 (DD) 2016

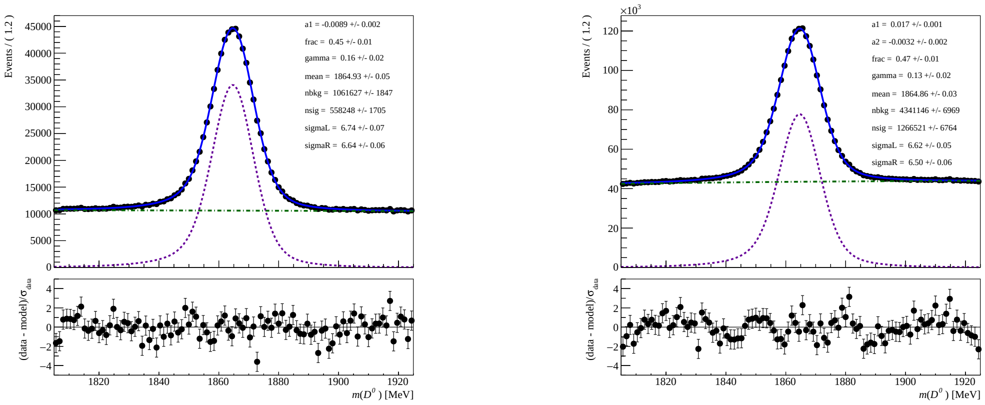

(c) K_S^0 (LL) 2017 (d) K_S^0 (DD) 2017

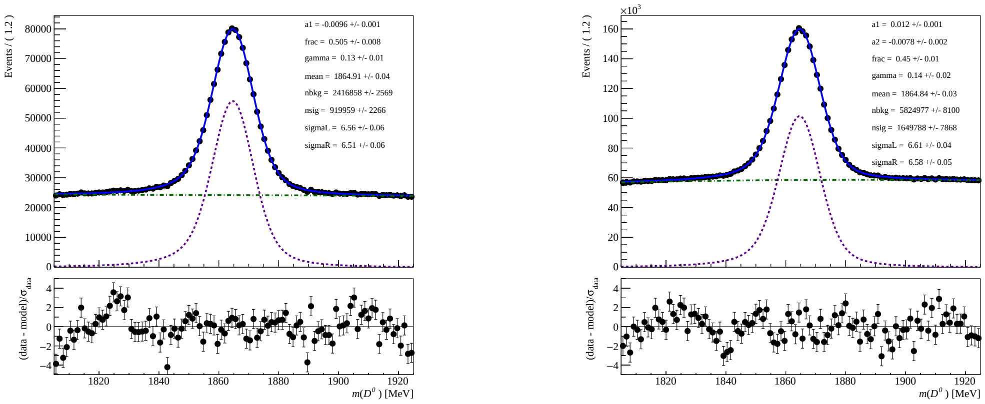

(e) K_S^0 (LL) 2018 (f) K_S^0 (DD) 2018

Figure 5.1: D^0 mass distributions for the single-tagged samples 2016-2018: data (black points), signal model comprised of a Bifurcated Gaussian and a Johnson SU (purple dashed line) background model (green dashed line), total model (blue line).

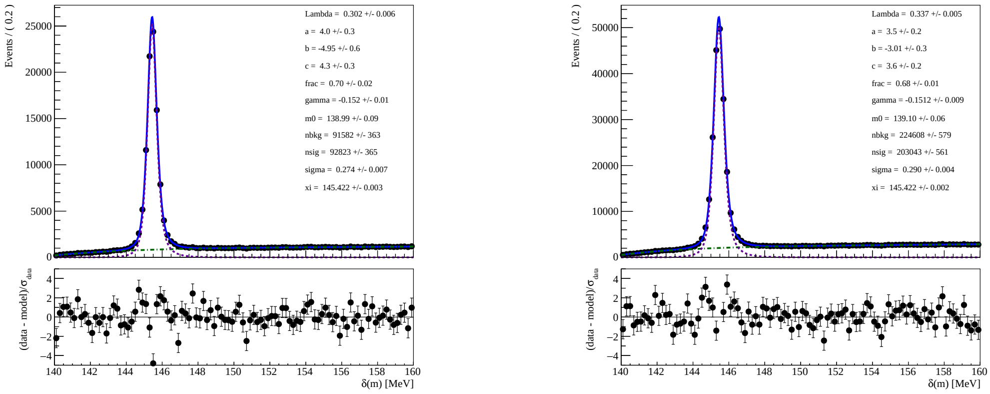

(a) K_S^0 (LL) 2016 (b) K_S^0 (DD) 2016

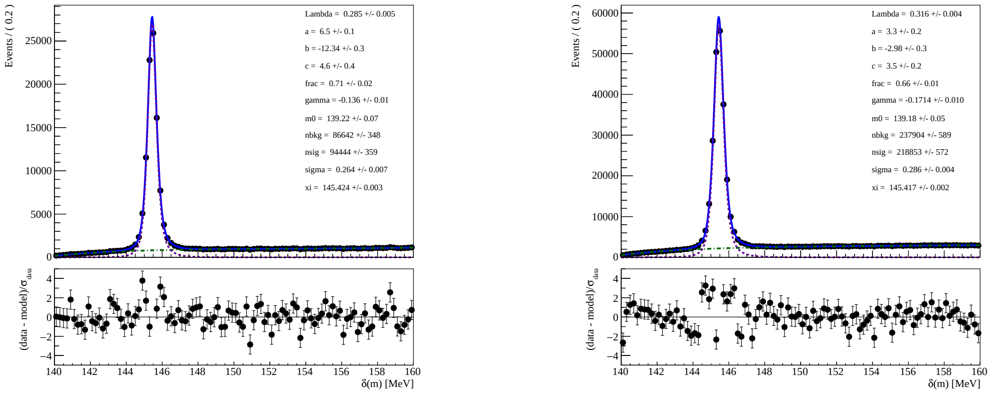

(c) K_S^0 (LL) 2017 (d) K_S^0 (DD) 2017

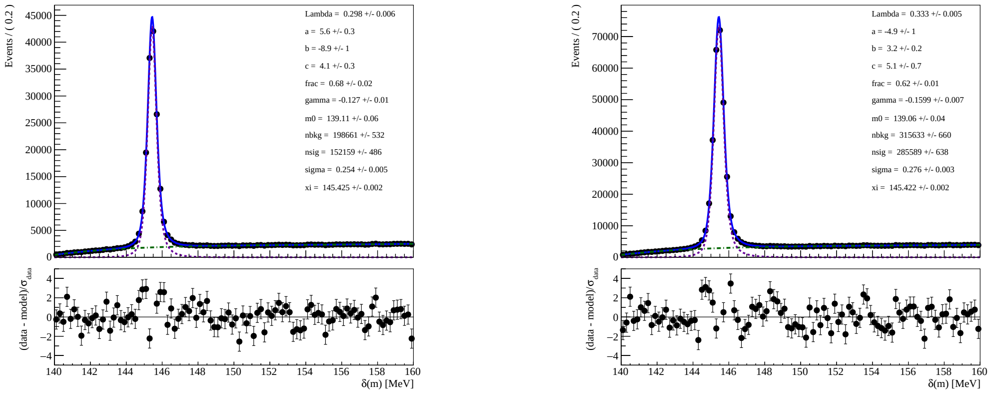

(e) K_S^0 (LL) 2018 (f) K_S^0 (DD) 2018

Figure 5.2: δm distributions for the double-tagged samples 2016-2018: data (black points), signal model comprised of a Johnson SU distribution and a Gaussian (purple dashed line) background model (green dashed line), total model (blue line).

	Single-tagged		Double-tagged	
	K^0_S (LL)	K^0_S (DD)	K^0_S (LL)	K^0_S (DD)
	2016			
Signal yield	558,429	1,187,193	92,823	203,043
Background yield	1,169,032	4,195,801	91,582	224,608
Signal purity	32.33%	22.05%	50.34%	47.48%
	2017			
Signal yield	558,248	1,266,521	94,444	218,853
Background yield	1,061,627	4,341,146	86,642	237,904
Signal purity	34.46%	22.59%	52.15%	47.91%
	2018			
Signal yield	919,959	1,649,788	152,159	285,589
Background yield	2,416,858	5,824,977	198,661	315,633
Signal purity	27.57%	22.07%	43.37%	47.50%

Table 5.4: Signal and background yields computed from the maximum likelihood fit, and signal purity $n_{sig}/(n_{sig}+n_{bkg})$ of the samples after the cut-based offline preselection describe but before the MVA. The mass range is $1805 < m(D^0) < 1925$ MeV for single-tagged candidates and $1844 < m(D^0) < 1844$ MeV for double-tagged candidates. These correspond to the fits in Figures 5.1 and 5.2.

5.5 Multivariate analysis

After the trigger and preselection requirements are applied, a Boosted Decision Tree (BDT) is used to further reduce the remaining background. The BDT uses distributions of variables that differ for $D^0 \to K^0_s\pi^+\pi^-$ events and background processes and gives an output which distinguishes between signal and background events by giving a ‘score’ of an event being signal-like or background-like. The BDT response is a single observable in the range [-1, 1] and indicates whether the candidate is more signal-like or background-like. In order to develop the BDT algorithm, a training process is first performed, which requires dedicated input samples of signal and background candidates. The separation of the input variables into signal and background components is sometimes achieved by using Monte Carlo simulation of signal and background processes. Alternatively one can use Monte Carlo for the signal distribution and sidebands from data for the background distribution, where no signal contribution should be present. Since we have a large signal yield in the data, and good ability to separate using the mass fits, we can use an entirely data-driven approach which overcomes several limitations of simulation; for example it provides a perfectly accurate model of detector effects and backgrounds by construction, and has no problems with low statistics. The sPlot formalism allows us to separate the signal and background distributions of the BDT input variables. Therefore in this analysis, the multivariate algorithm (MVA) is trained using data separated into sWeighted signal and background distributions.

The uBoost classifier is used for the multivariate analysis [77]. This is a gradient boosted decision tree with a loss function which penalises for non-uniformity across the Dalitz variables and decay-time. This provides a method of boosting with a uniform selection efficiency in a selected phase-space; hence reducing systematic uncertainties. The gradient boosting is a method of assigning incorrectly classified events larger weights in order to increase their importance. Each successive classifier should then improve the overall performance of the ensemble of classifiers. The ensemble of classifiers should perform better than a single classifier.

The input variables are chosen based on the discriminating power between signal and background; it is ensured that there are no correlations between the input variables and the D^0 mass or decay-time. This is demonstrated in Figure 5.4 which shows the correlation matrix for the BDT input variables and $m(D^0)$ and $\tau(D^0)$. For the former this is a requirement of the sPlot method to ensure the training sample distributions are reliable; for the latter, this helps to suppress large decay time sculpting effects and hence reduce potential systematic uncertainties on the final measurement. K-folding [82] is used in order to access an unbiased BDT score for the whole dataset. The sample is split into two which are referred to as even and odd, although note this is just a naming convention and the samples are split with a random seed. The even and odd samples are in turn split into training and testing samples; the BDT is trained using the training dataset. A check for overtraining is performed using the training and testing samples. The trained BDT from the even sample is applied to the odd sample and vice versa. This avoids biases from applying a BDT to the same dataset with which it was trained. The BDT input variables are as follows and described below:

- DTF vertex χ^2 per number of degrees of freedom
- B meson corrected mass

- arccos($DIRA$) where DIRA is the angle between the particle's momentum and line of flight
- χ^2_{IP} impact parameter χ^2, this is the difference in χ^2 between the primary vertex fits when the B candidate is included and excluded
- B meson flight distance
- χ^2_{FD} flight distance χ^2
- $\chi^2_{DV}/ndof$ decay vertex χ^2 of the B candidate per number of degrees of freedom
- χ^2_{PV} primary vertex χ^2 of the B candidate
- μ transverse momentum
- D^0 transverse momentum

The χ^2_{FD} is the flight distance χ^2 of the B candidate with respect to the PV. This discriminating variable has good separation between signal and B candidates originating from prompt D^* decays which are produced directly in the pp collision. The B meson flight distance also helps separate background from prompt D^* decays. The corrected mass of the B meson candidate accounts for the non-reconstructed neutrino in the semi-leptonic B meson decay, whereas the measured mass does not; this is therefore a better approximation of the invariant mass. The corrected mass is defined as:

$$m_{corr} = \sqrt{m^2 + \left|\vec{p_T^{miss}}\right|^2} + \left|\vec{p_T^{miss}}\right| \tag{5.9}$$

where m is the invariant mass of the B meson and $\vec{p_T^{miss}}$ is the missing transverse momentum relative to the direction of flight with respect to the PV, where the PV with the smallest χ^2_{IP} is taken. The χ^2 of the B meson candidate's PV also has good discriminating power as it is connected to the multiplicity of the event. Figure 5.3 shows sWeighted signal and background distributions of the BDT input variables, where good separation between signal and background can be seen. In addition we check the correlation between the BDT variables shown in Figure 5.4, from this we can see no significant correlations between each pair of variables.

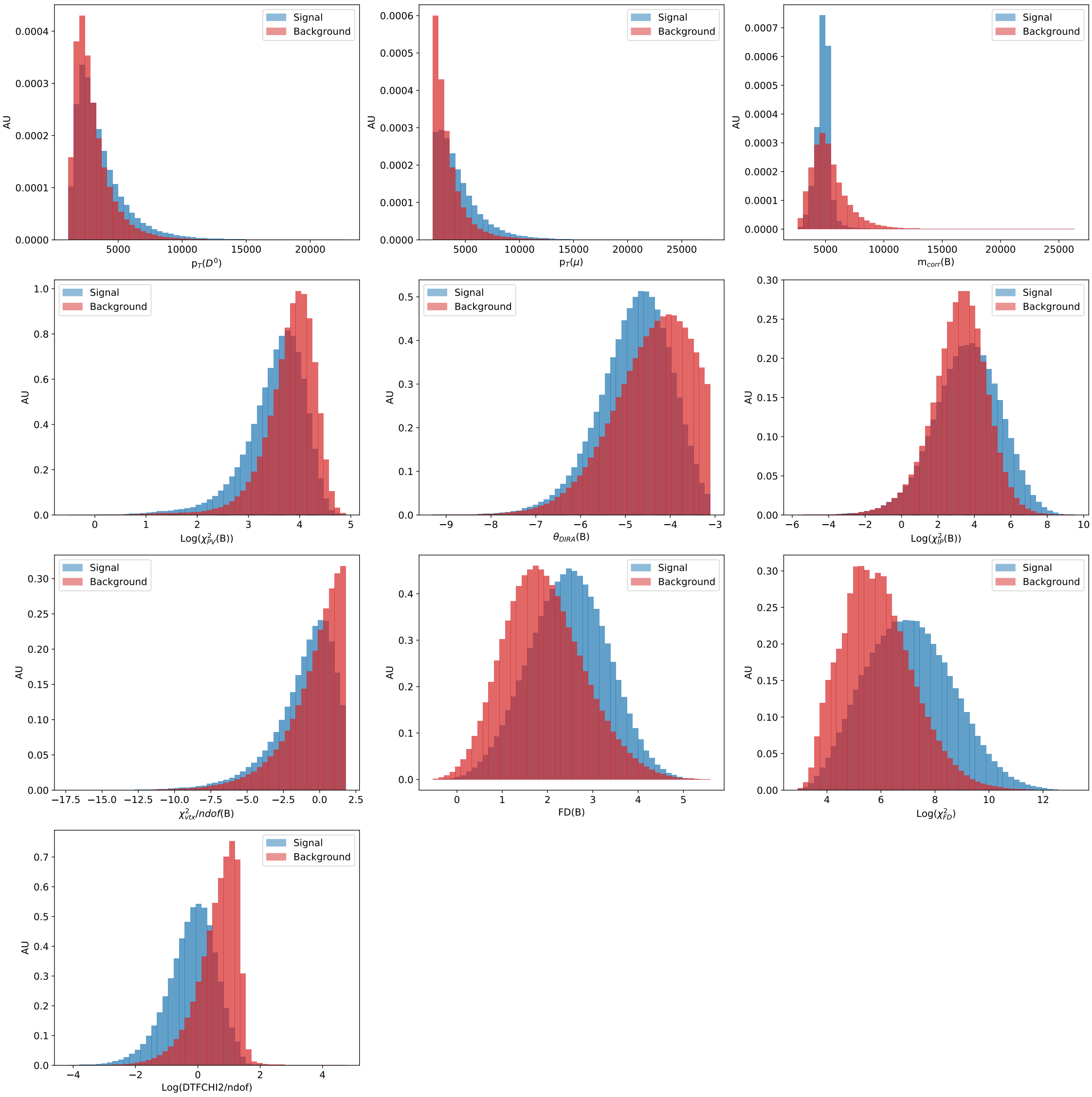

Figure 5.3: Distributions of the BDT input variables for signal (blue) and background (red) training samples: single-tagged K^0_S (LL) 2018 sample.

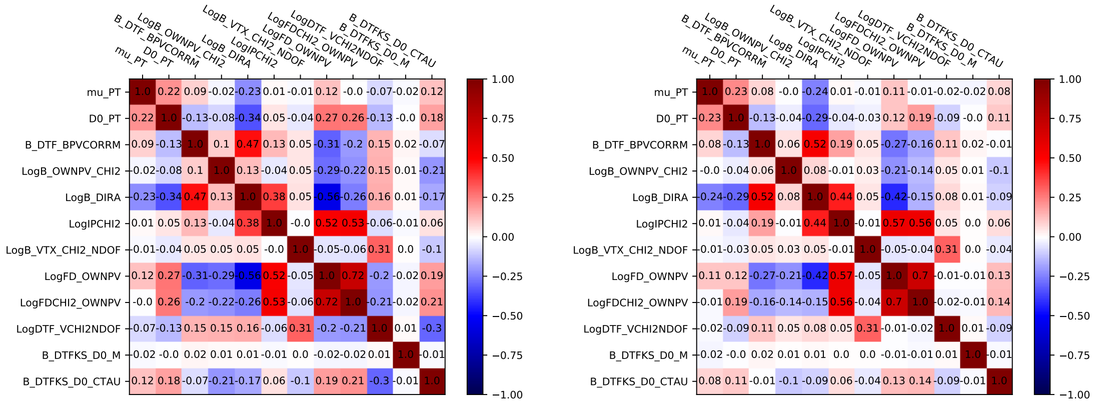

(a) K_S^0 (LL)

(b) K_S^0 (DD)

Figure 5.4: Correlations between the BDT input variables for the single-tagged 2018 samples.

A hyperparameter is a parameter whose value is used to control the learning process, such as number of trees, learning rate and maximum depth. The same kind of machine learning model can require different constraints, weights or learning rates to generalise different data patterns. These measures are called hyperparameters, and have to be tuned so that the model can optimally solve the machine learning problem. A range of hyperparameters for the uBoost BDT used in the event selection were investigated, and those which yield the optimal model were chosen.

One can check for overtraining of the classifier by comparing the BDT output distributions from the training sample and the test sample. Overtraining can occur when specific features caused by statistical fluctuations are used in the BDT training. The comparison of the two distributions can be quantified by the Kolmogorov-Smirnov (KS) test [55]. The KS statistic quantifies a distance between the empirical distribution functions of two samples. The null distribution of this statistic is calculated under the null hypothesis that the samples are drawn from the same distribution. The result of this test can be interpreted as the likelihood that the training sample distribution could have been obtained on the test sample distribution and vice versa. The BDT output distributions and overtraining check are shown in Figure 5.5.

A receiver operating characteristic (ROC) curve illustrates the diagnostic ability of a binary classifier system as its discrimination threshold is varied. The ROC curve

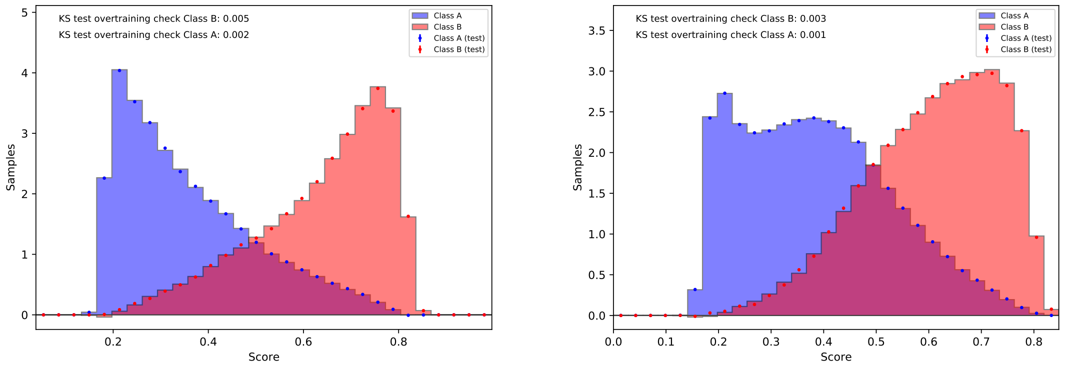

(a) K_S^0 (LL) 2018 even sample

(b) K_S^0 (DD) 2018 even sample

Figure 5.5: BDT output distributions and overtraining check for single-tagged K_S^0 (LL and DD) 2018 samples: the histograms show the test sample and the points show the training sample, the signal (Class A) distribution is in blue and background (Class B) is in red.

is created by plotting the True Positive Rate (TPR) against the False Positive Rate (FPR) at various cuts on the BDT response; where the TRP is the signal efficiency of the BDT cut and the FPR is equivalent to the background efficiency. The area under the ROC curve therefore gives a measure of the performance of the classifier, where a high number would represent a high signal efficiency and a high background rejection and a score of 0.5 would represent a random guess. The ROC curves along with the area under curve (AUC) are shown in Figure 5.6 for the single-tagged 2018 K_S^0 samples. In the hyperparameter optimisation, the optimal model can be chosen by the one which gives the highest ROC AUC score.

The cut on the BDT output is chosen to maximum the significance $S/\sqrt{S+B}$ where S and B are the number of signal and background events. The signal and background contributions are computed as the integral over the BDT response for a given cut value weighted by signal and background sWeights, respectively. The signal significance, signal efficiency and background efficiency for the single-tagged K_S^0 2018 samples are shown in Figure 5.7 along with the optimal cut. The optimal BDT cuts for all subsamples are shown in Table 5.5.

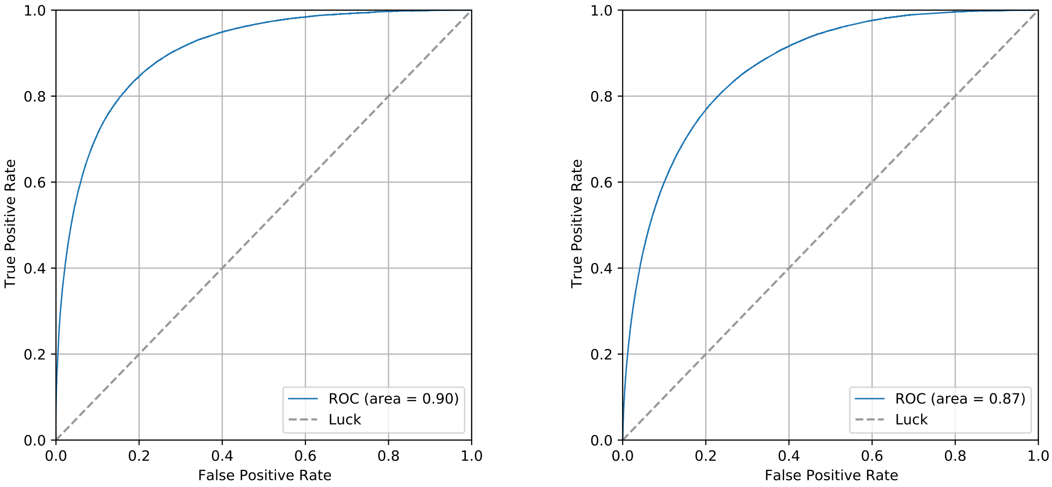

(a) K_S^0 (LL) 2018 even sample

(b) K_S^0 (DD) 2018 even sample

Figure 5.6: Receiver operating characteristic curves for the K_S^0 (LL and DD) single-tagged 2018 samples, showing True Positive Rate against False Positive Rate for the BDT output, the dashed line represents a random guess.

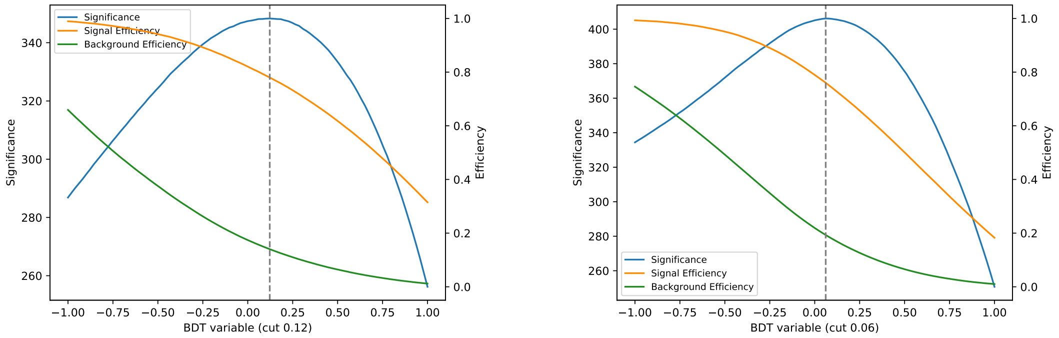

(a) K_S^0 (LL) 2018 even sample

(b) K_S^0 (DD) 2018 even sample

Figure 5.7: Signal significance $S/\sqrt{(S+B)}$ (blue line), signal efficiency (orange line) and background efficiency (green line) against the BDT response for single-tagged K_S^0 (LL and DD) 2018 samples.

	Cut on BDT response		Peak Significance	
	even	odd	even	odd
	Single-tagged			
K_S^0 (LL) 2016	0.04	0.02	285	284
K_S^0 (DD) 2016	0.10	0.04	343	344
K_S^0 (LL) 2017	-0.02	0.02	289	289
K_S^0 (DD) 2017	0.10	0.04	358	358
K_S^0 (LL) 2018	0.12	0.10	348	351
K_S^0 (DD) 2018	0.06	0.08	405	408
	Double-tagged			
K_S^0 (LL) 2016	-0.02	-0.02	118	117
K_S^0 (DD) 2016	-0.02	-0.02	169	168
K_S^0 (LL) 2017	-0.06	-0.10	119	120
K_S^0 (DD) 2017	0.00	0.04	176	176
K_S^0 (LL) 2018	0.10	0.12	144	144
K_S^0 (DD) 2018	-0.02	-0.04	202	203

Table 5.5: Optimal cuts on BDT response.

5.6 Multiple candidates

A common feature of many LHCb selections is that even after tight cuts several candidates per event remain. Depending on the kind of analysis this can bias the results and a special treatment is often needed. An event with multiple candidates is an event in which there are more than one candidates passing the final selection. There are several types of multiple candidates and analysts may chose to deal with them in different ways depending on their analysis needs. For example, one $D^0 \to K_S^0\pi^+\pi^-$ decay may combine with more than one muon to form several B meson candidates. Here one would have multiple entries with exactly the same D^0 properties, for example Dalitz coordinates and decay-time. These type of multiple candidates are double-counted in the Dalitz and decay-time distributions and therefore need to be removed. Multiple candidates can cause biases in the measurement of the observable of interest if their rate is correlated with this observable. For example more multiple candidates at low decay times may cause a bias in the measurement of the time-dependent mixing parameters.

Another type of multiple candidate is that where a single K_S^0 combines with different combinations of $\pi^+\pi^-$ to give several distinct D^0 candidates in the event (or several K^0 candidates combined with a single $\pi^+\pi^-$ combination). The phase-space and decay-time variables will be different in these cases so they are less harmful than the first case described and in principle they could be kept. However in this analysis we have decided to remove all multiple candidates for simplicity and since it represents a small fraction of the data. There are several ways of dealing with multiple candidates for example: keeping all of the candidates, rejecting all but one of the candidates, or rejecting all candidates from the given event [57]. In this analysis we have chosen to randomly reject all but one of the candidates with the same event number; this is about 2% for a single-tagged data sample.

In addition, due to the inclusive reconstruction in the preselection, we know that the double-tagged candidates are a subset of the single-tagged dataset. To avoid double-counting of candidates, double-tagged candidates have to be separated from the single-tagged sample. Candidates are removed from the single-tagged sample if they match a candidate in the double-tagged sample, where matching is defined by having the same event number and a difference in D^0 mass below 10^{-5} MeV.

After the optimal BDT cut is applied and the multiple candidates have been removed, a second unbinned extended maximum likelihood fit is performed to the D^0 mass distribution for the single-tagged samples and the δm distribution for the double-tagged samples. For the single-tagged samples, the signal model used is a Gaussian and a Johnson SU with a common mean and the background is a Chebychev polynomial. The PDF for the single-tagged samples is then given by:

$$F_{LL} = n_{sig} \times \left(c f_{SU}(m_{D^0}) + \frac{1}{\sqrt{2\pi\sigma}}(1-c) e^{-\frac{1}{2}\left(\frac{m_{D^0}-\mu}{\sigma}\right)^2} \right) + n_{bkg} \times (1 + a_1 m_{D^0}) \quad (5.10)$$

$$\begin{aligned} F_{DD} = n_{sig} \times \left(c f_{SU}(m_{D^0}) + \frac{1}{\sqrt{2\pi\sigma}}(1-c) e^{-\frac{1}{2}\left(\frac{m_{D^0}-\mu}{\sigma}\right)^2} \right) \\ + n_{bkg} \times \left(1 + a_1 m_{D^0} + a_2 \left(2m_{D^0}^2 - 1\right)\right) \end{aligned} \quad (5.11)$$

For the double-tagged samples, the signal model is a Johnson SU distribution and a Gaussian and the background is modelled by a polynomial as in Equation 5.8. The δ parameter in the Johnson SU distribution is set to 1. The per-event sWeights

	Single-tagged		Double-tagged	
	K_S^0 (LL)	K_S^0 (DD)	K_S^0 (LL)	K_S^0 (DD)
	2016			
Signal yield	434248	842698	77707	168604
Background yield	200468	788943	21886	56043
Signal purity	68.42%	51.65%	78.02%	75.05%
Signal efficiency	76.76%	70.98%	83.72%	83.04%
Background rejection	82.85%	81.20%	76.10%	75.05%
	2017			
Signal yield	440294	884392	81073	180110
Background yield	190815	876081	22408	55333
Signal purity	69.77%	50.24%	78.35%	76.50%
Signal efficiency	78.87%	69.83%	85.84%	82.30%
Background rejection	82.03%	79.82%	74.14%	76.74%
	2018			
Signal yield	674621	1181130	122435	239643
Background yield	359217	1083848	38723	76147
Signal purity	65.25%	52.15%	75.97%	75.89%
Signal efficiency	73.33%	71.59%	80.47%	83.91%
Background rejection	85.14%	81.39%	80.51%	75.87%

Table 5.6: Signal efficiency and yields and background rejection of the samples before and after the optimal cut on the BDT response.

and signal probabilities are extracted from the D^0 mass fit for the single-tagged samples and the δm distribution for the double-tagged samples. The sWeights are used to separated the signal and background distributions, in order to construct the background PDFs in decay-time and 2-dimensional Dalitz space to be used in the final mixing fits. The signal probabilities are used as a per-event quantity in the fit to assign the appropriate contribution of the signal and background PDFs. The signal probability is given by:

$$p_{sig} = \frac{PDF_{sig} \times n_{sig}}{PDF_{sig+bkg} \times (n_{sig} + n_{bkg})} \tag{5.12}$$

Plots of the $m(D^0)$ fits are shown in Figure 5.8 and the δm distributions for the double-tagged samples are shown in Figure 5.9. Table 5.6 shows the signal yields, signal efficiency and background rejection of the optimal BDT cut.

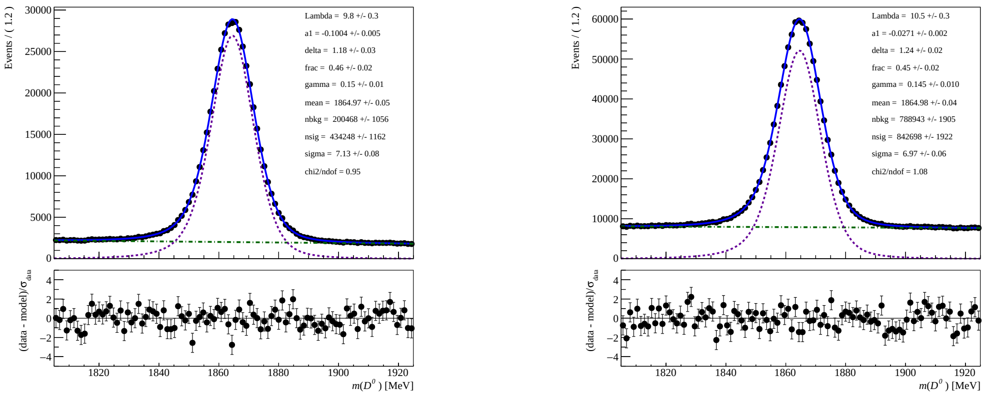

(a) K_S^0 (LL) 2016

(b) K_S^0 (DD) 2016

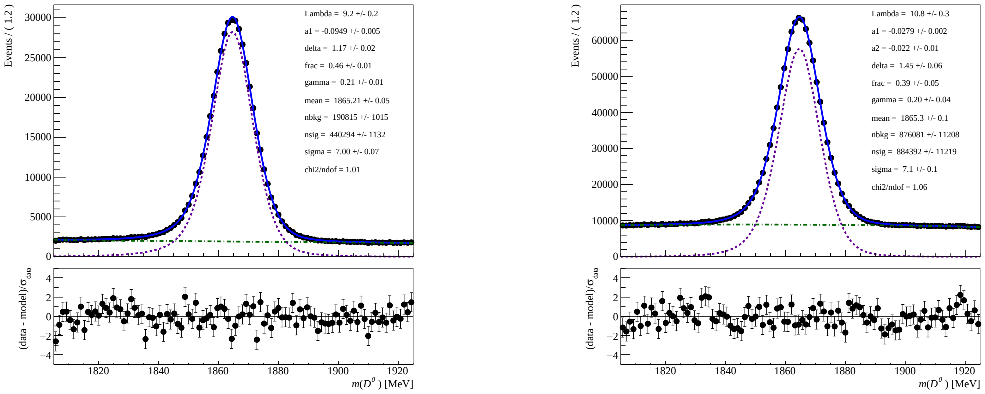

(c) K_S^0 (LL) 2017

(d) K_S^0 (DD) 2017

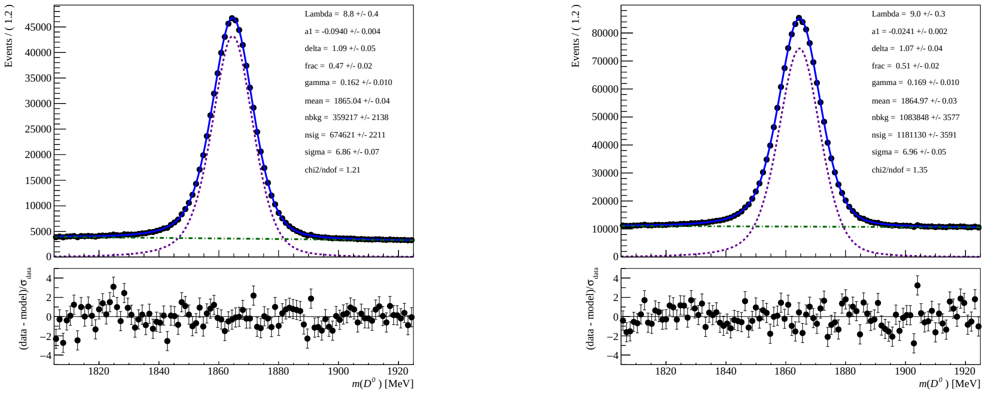

(e) K_S^0 (LL) 2018

(f) K_S^0 (DD) 2018

Figure 5.8: D^0 mass distributions for the single-tagged samples 2016-2018: data (black points), signal model (purple dashed line) background model (green dashed line), total model (blue line).

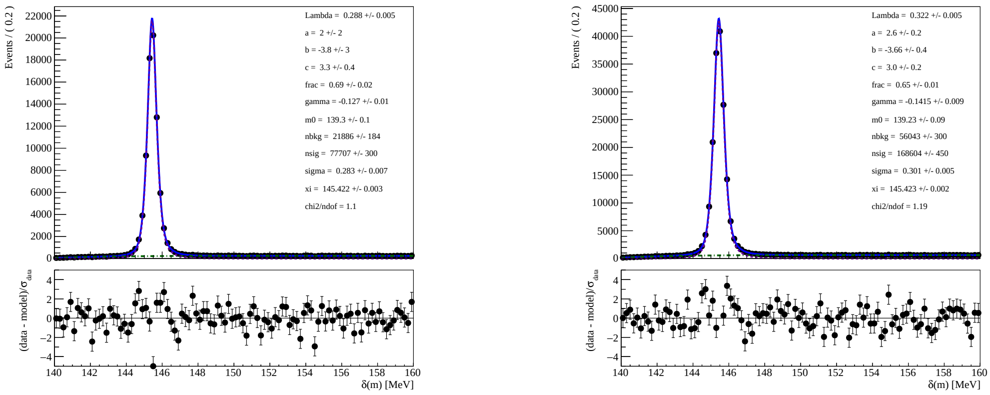

(a) K_S^0 (LL) 2016 (b) K_S^0 (DD) 2016

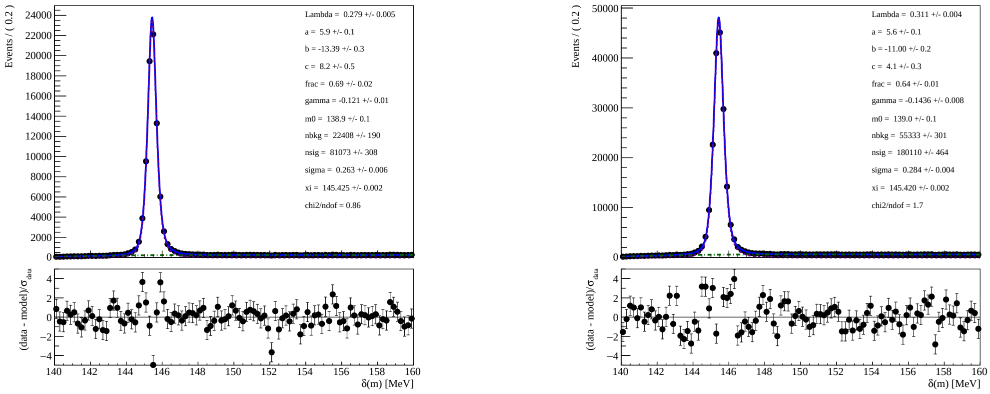

(c) K_S^0 (LL) 2017 (d) K_S^0 (DD) 2017

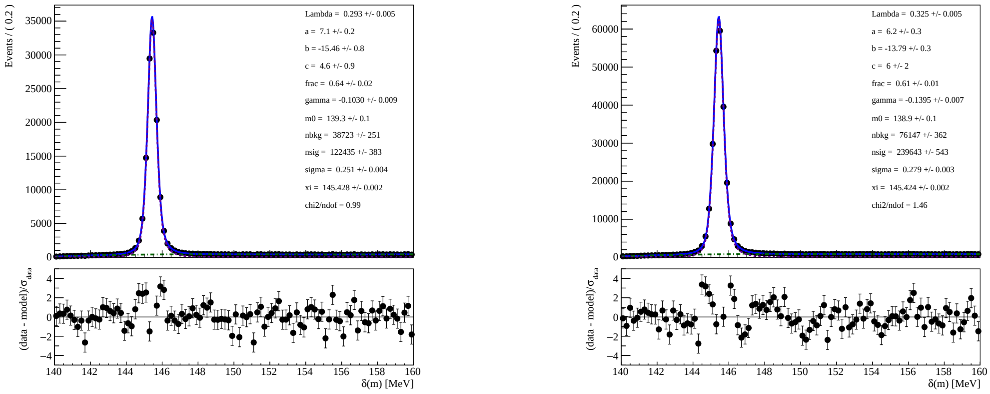

(e) K_S^0 (LL) 2018 (f) K_S^0 (DD) 2018

Figure 5.9: δm distributions for the double-tagged samples 2016-2018: data (black points), signal model (purple dashed line) background model (green dashed line), total model (blue line).

CHAPTER 6

Simulation

A common challenge in many measurements performed in high-energy physics is the necessity to understand the effects of the detector response on the physics parameters of interest. This response is driven by resolution effects that distort the true distribution of a quantity and by inefficiencies that are introduced by either an imperfect reconstruction in the detector or a deliberate event selection [66]. The solution is the generation of Monte Carlo (MC) events and the simulation of their detector response to study the evolution from the generated to the reconstructed and selected objects.

The LHCb simulation framework, Gauss [40], manages the creation of simulated events by interfacing to multiple external applications. The framework consists of a generation and simulation phase. A *pp* collision with the required signal particle is generated by Pythia [74] either by generating minimum bias events until a matching particle is found or by enforcing one to be produced in every event. The resulting event is comprised of a mixture of stable and unstable particles which can be decayed. The decay of the signal particle is modelled using EvtGen [58], all remaining unstable particles are decayed independently. Radiated photons are simulated by the Photos package [50]. The signal particle and its decay products may be required to pass generator level cuts in order to increase the fraction of the generated sample which passes subsequent reconstruction and selection requirements. The propagation of the particles through the detector is then performed in the simulation phase. The interactions of particles with the detector material are simulated by the Geant4 toolkit [22, 25]. A detailed description of the detector material is stored in an XML geometry database and data taking conditions, notably alignment and calibration constants, are contained in an XML conditions database, which is frequently updated to reflect the current state of the detector [71]. After the simulation of the detector response and the digitisation, the simulated data is passed through the same trigger and reconstruction chain as the collision data.

With the increase in data collected during Run 2 and that expected in Run 3, we require simulated data samples of significantly larger sizes in order to study the detector response in detail. The number of events that can be produced in full simulation is limited by CPU and storage requirements. The simulation of the detector response is the main contribution to the time needed to simulate full events, which accounts for 95-99% of the total time. The ReDecay package [66] exploits the fact that out of the many particles in the simulation, in general only the signal decay is of interest. In studies of heavy particles to exclusive final states, the event consists of particles that participate in the signal process and all remaining particles. The majority of the CPU time is used in the simulation of the remaining particles and not the signal decay of interest. ReDecay allows the signal particle to decay independently for every generated event, as usual, but the non-signal particles are reused multiple times saving a large factor of CPU time. This approach achieves an order of magnitude increase in speed and the same quality compared to the nominal simulation. This approach can introduce correlations between some parameters, in particular those corresponding to production properties of the signal particle (since each time an event is ReDecayed the signal particle retains the same four-vector). As such, care is needed when deciding which analyses can make use of this tool, including through the use of built-in tests to quantify the impact of any correlations in final reconstructed distributions. They will not bias or distort the distributions themselves provided that the overall number of candidates (typically $\mathcal{O}(10^6)$) is significantly greater than the number of so-called 'ReDecays' (typically $\mathcal{O}(100)$). For this analysis, the signal properties are independent to first order; i.e. the D^0 kinematics do not influence the decay dynamics, Dalitz distribution or decay-time. Also in the case of semi-leptonically produced D mesons, it is the B meson which is ReDecayed (the parent particle). Therefore the kinematics of the B meson are preserved between the events and not the D^0, making any residual correlations weaker. Therefore we conclude that ReDecay can safely be used in this analysis.

6.1 Monte Carlo data samples

The Monte Carlo simulation samples used in this analysis are of two different so-called 'event types' of neutral and charged B mesons. The event types are as follows:

- Event type 12875523: Charged B meson is required, the decay $D^{*+} \to D^0\pi^+$ is forced as is $D^0 \to K^0_S\pi^+\pi^-$, B meson can decay to the final state particles in a 'cocktail' of intermediate states, listed in Table 6.1.
- Event type 11876125: Neutral B meson is required, the decay $D^{*+} \to D^0\pi^+$ is forced as is $D^0 \to K^0_S\pi^+\pi^-$, B meson can decay to the final state particles in a 'cocktail' of intermediate states, listed in Table 6.2.

The number of events generated for each year is given in Table 6.3. In the decay model for the D^0, no intermediate resonances are included. Rather we generate uniformly over phase-space; this simplifies the extraction of the detector effects, as described in the next chapter. The Monte Carlo samples contain truth information at the generator level. The Monte Carlo is truth matched; whereby the reconstructed decays are required to match the known truth information about the generator level particle. This ensures that the Monte Carlo sample has very low background contamination.

The event type is an LHCb label for the different Decay Files in the database. The first number is a general flag which in this case requires events containing a b quark, extracted from a minimum bias sample. The second number is the selection flag which is 2 in the case of a charged B meson and 1 in the case of a neutral B meson. The third number is the decay flag which specifies that the selected particles are forced to decay into one of several exclusive final states (explicitly specified in a list) with different topologies, but the final states contain at least one particle which

Fraction [%]	B^- decay mode
2.2400	$D^0\mu^-\bar{\nu}_\mu$
5.6800	$D^*(2007)^0\mu^-\bar{\nu}_\mu$
0.2072	$D^*(2420)^0\mu^-\bar{\nu}_\mu$
0.1936	$D_1'(2430)^0\mu^-\bar{\nu}_\mu$
0.5244	$D_1(2420)^0\mu^-\bar{\nu}_\mu$
0.2792	$D_2^*(2460)^0\mu^-\bar{\nu}_\mu$
0.2451	$D^{*0}\pi^+\pi^-\mu^-\bar{\nu}_\mu$

Table 6.1: Decay modes listed in the 12875523 (charged B) event type. Fractions listed above 0.1%.

Fraction [%]	$\bar{B}^0$ decay mode
5.0100	$D^*(2010)^-\mu^-\bar{\nu}_\mu$
0.2451	$D^{*-}\pi^+\pi^-\mu^-\bar{\nu}_\mu$
0.1749	$D_1(2420)^-\mu^-\bar{\nu}_\mu$

Table 6.2: Decay modes listed in the 11876125 (neutral B) event type. Fractions listed above 0.1%.

Event Type	Year	Number of events	
		MagUp	MagDown
12875523 (charged B)	2016	832481	821690
	2017	2001031	2006471
	2018	2104890	2091375
11876125 (neutral B)	2016	1820108	1202273
	2017	2100163	2106046
	2018	2004089	2003099

Table 6.3: Number of Monte Carlo events generated for each event type, year and magnet polarity.

cannot be measured, in this case at least one neutrino. The fourth number is the charm/lepton content flag, in this case requires at least one open charm hadron and at least one muon. The fifth number is the track flag, which is the number of stable charged particles in the forced part of the decay chain of the selected particle; this is 5 for the charged B sample and 6 for the neutral B sample since this decay has an extra charged (soft) pion. The sixth number is the neutral decay flag which specifies $K_S^0 \to \pi^+\pi^-$. Finally the last two numbers are reserved for the user to distinguish between different event types. In this case they represent that they have different generator level cuts applied to those event types with the same first six numbers. Stripping filtered MC is used to reduce the number of events saved to disk and ensure that all saved events are useful; where the generated events are required to pass the same stripping requirements as data before being saved to disk.

Each MC sample has generator-level cuts applied to ensure daughter particles are in the detector acceptance and some kinematic cuts to ensure a higher number of generated candidates would pass the reconstruction or selection criteria applied before the samples are analysed. These generator level cuts are, in each case, looser than the offline preselection, in order that the Monte Carlo samples have the same selection as real data. The B flight distance along the z-axis of the B meson must be greater than 1.6 mm. The muon and the D^0 and K_S^0 daughter pions must satisfy $5 \leqslant \theta \leqslant 400$ mrad, where θ is the angle with respect to the forward proton beam in the LHCb frame as defined in Chapter 3. The z position of the K_S^0 decay vertex must fulfil $z < 2.4$ m. In addition momentum and transverse momentum requirements are applied on the pions, muon and D^0. The MC describes the decay $B \to D^0\mu X$ through intermediate resonances, where the decay $D^0 \to K_S^0\pi^+\pi^-$ is forced. The samples of charged and neutral B mesons are blended to best describe data, where the composition can be varied in order to assess a systematic uncertainty. A summary of the generator level cuts used in the MC generation can be seen in Table 6.4.

6.2 Monte Carlo Reweighting

Differences between simulated MC events and measured data can arise from limited knowledge of the underlying physics processes or detector mismodeling. To

Variable	Generator level cut
θ	$5 \leqslant \theta \leqslant 400$ mrad
z K_S^0 decay vertex	< 2.4 m
D^0 flight distance along B z	> 1.6 mm
$p(\mu)$	> 2.9 GeV
$p_T(\mu)$	> 700 MeV
K_S^0 daughter π momentum	> 2.5 GeV
D^0 daughter π momentum	> 1.9 GeV
$p(D^0)$	> 12 GeV
$p_T(D^0)$	> 1.9 GeV

Table 6.4: Generator level cuts applied to the Monte Carlo samples.

account for these differences a correction can be applied to MC samples. Reweighting is the procedure of finding weights for an original distribution, that make the original distribution identical to the target distribution for given variables. In this analysis the MC (original distribution) is reweighted to match the signal sWeighted data (target distribution). A multidimensional reweighter is used to calculate per-event weights using several kinematic variables, improving the agreement between MC and data across several kinematic distributions. In order to achieve this a multidimensional kinematic reweighting algorithm is used.

The Gradient Boosted Reweighter (GBReweighter) is a reweighting algorithm based on an ensemble of regression trees [64]. Several kinematic variables are used as input to the BDT, which are chosen for their discriminating power between MC and data. The approach of multidimensional reweighting has an advantage over reweighting in one dimension; which may bring disagreement in other distributions. Multidimensional reweighting also has the advantage that it takes into account correlations between the variables under consideration. This avoids the need for complicated and performance-limited iterative reweighting schemes when trying to match several correlated variables. The reweighting algorithm trains a BDT in which signal sWeighted data is used as Class A and MC is used as Class B. The BDT assigns a single output, as usual, to discriminate between MC and real (signal sWeighted) data. This output is transformed into an event weight which is used to reweight the MC to ensure it matches the data. K-folding is used to split the dataset into multiple training and testing samples in order to obtain unbiased weights for the entire dataset. The input variables are as follows:

- D^0 momentum
- μ momentum
- $\eta(D^0)$ psuedorapidity of D^0
- Corrected mass of the B meson
- $\eta(\mu)$ psuedorapidity of the muon
- B meson primary vertex χ^2
- D^0 transverse momentum
- μ transverse momentum

The performance of the reweighting strategy can be tested by training a second BDT to distinguish between the signal sWeighted data and reweighted MC. The input variables to this BDT include the IP χ^2, B meson flight distance, arccos($DIRA$) where $DIRA$ is the angle between the B meson's momentum and line of flight and the B meson decay vertex $\chi^2/ndof$. The area under the ROC cuve for this BDT can be used as a metric to assess the performance. A score of 0.5 would show that the BDT cannot distinguish between signal sWeighted data and reweighted MC, hence the reweighting algorithm is performing well. This metric is used to test the performance of the reweighter to optimise the hyperparameters of the BDT and the input variables. The ROC AUC (area under curve) score for each subsample before and after reweighting can be seen in Table 6.5. It can be seen that after reweighting the ROC AUC score reduces to closer to 0.5 for all subsamples; this shows that the signal sWeighted data and reweighted MC cannot be distinguished by a BDT and hence are in good agreement and the reweighter has good performance. The fact that the ROC AUC score is not perfectly 0.5 suggests some residual disagreement between data and MC. This can be assessed as a systematic uncertainty.

This ROC AUC score is used as a metric to test the optimal hyperparameters of the BDT. A scan can be performed over the hyperparameters, such as number of estimators, learning rate, max depth. The optimal values are found by the combination which produces the ROC AUC score closest to 0.5. The same can also be done for the input parameters, where different input parameters are tested and the optimal combination chosen as those which minimise the ROC AUC score.

	ROC AUC Score	
	original weights	GB weights
	Single-tagged	
K_S^0 (LL) 2016	0.607	0.510
K_S^0 (DD) 2016	0.607	0.513
K_S^0 (LL) 2017	0.598	0.523
K_S^0 (DD) 2017	0.601	0.533
K_S^0 (LL) 2018	0.605	0.525
K_S^0 (DD) 2018	0.607	0.513
	Double-tagged	
K_S^0 (LL) 2016	0.593	0.520
K_S^0 (DD) 2016	0.597	0.524
K_S^0 (LL) 2017	0.573	0.535
K_S^0 (DD) 2017	0.580	0.533
K_S^0 (LL) 2018	0.575	0.542
K_S^0 (DD) 2018	0.582	0.535

Table 6.5: Area under ROC curves for the BDT trained to distinguish between signal sWeighted data and MC; for original MC before reweighting and reweighted MC with the weights from GB Reweighter.

Note that the input parameters to the GBReweighter are changed whereas the input parameters to the second BDT are kept the same to test the performance of the different sets of input parameters. The number of estimators is the number of trees used in the ensemble. The learning rate is in the range [0,1]; a lesser learning rate requires more trees but makes the reweighting more stable. A lesser learning rate is also more likely to cause overtraining so an optimal learning rate is usually chosen based on these considerations. The maximum depth refers to the maximum depth of the trees. The distributions of the kinematic variables for sWeighted data and MC can be seen in Figure 6.1 and Figure 6.2; this shows the agreement between sWeighted data and MC significantly improves after the kinematic reweighting giving confidence that the reweighted simulation is an accurate description of reality. Unless otherwise stated, the MC samples used in this thesis include this reweighting.

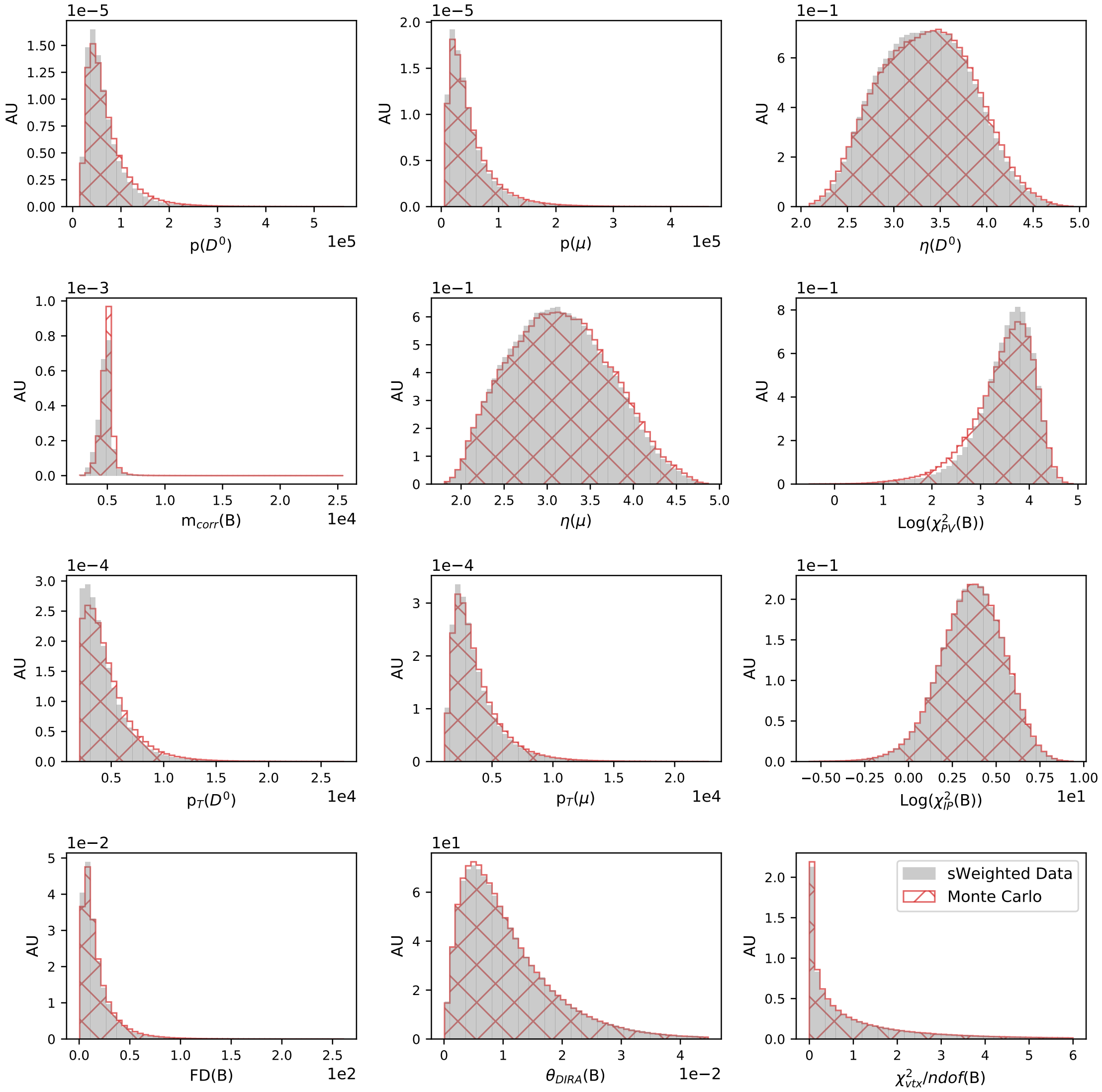

Figure 6.1: Distributions of kinematic variables for signal sWeighted data and Monte Carlo before reweighting for the single-tagged K_S^0 (LL) 2018 sample.

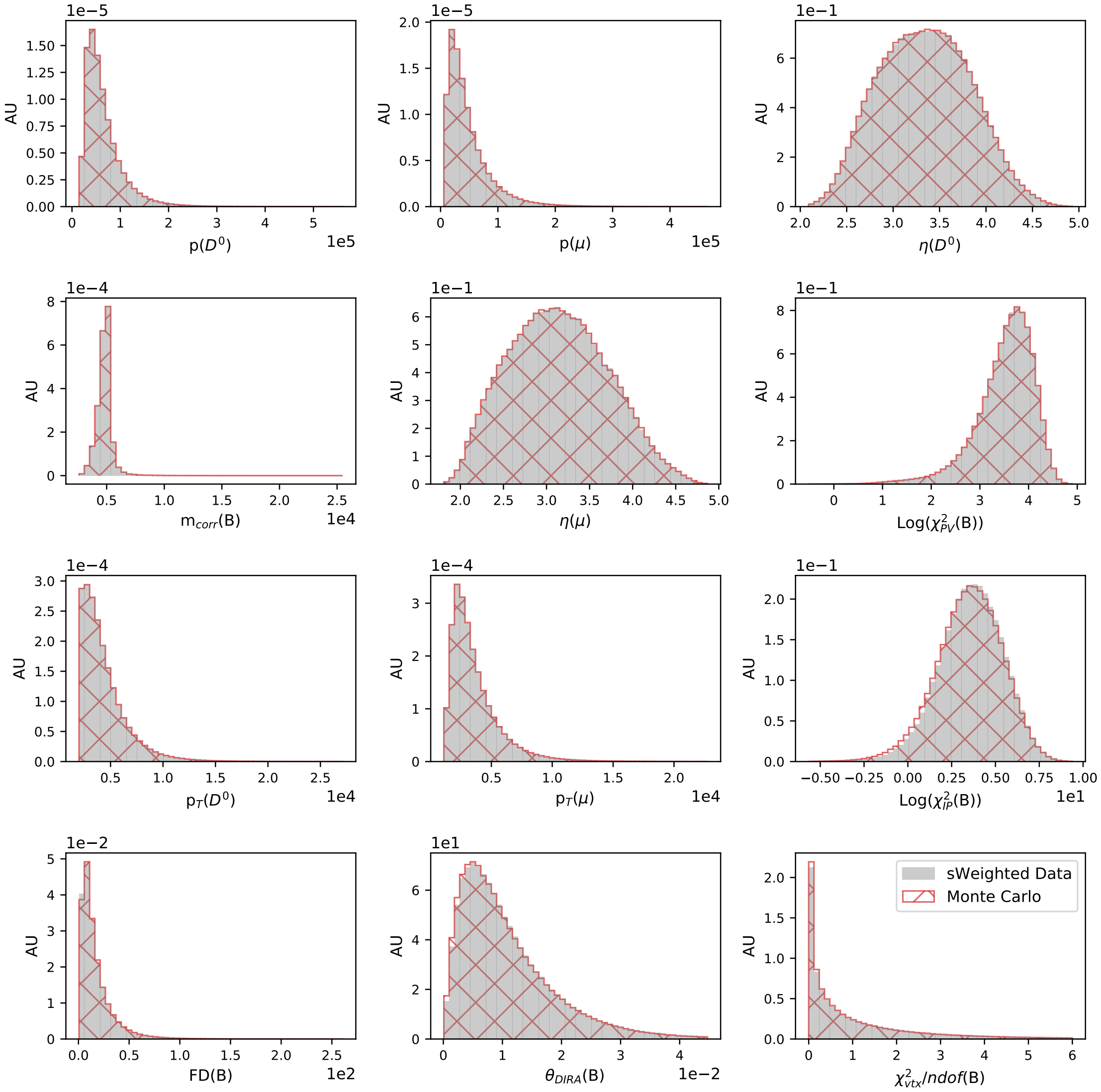

Figure 6.2: Distributions of kinematic variables for signal sWeighted data and Monte Carlo after reweighting for the single-tagged K^0_S (LL) 2018 sample.

CHAPTER 7

Detector effects

Due to the forward geometry of the LHCb detector, it covers a finite range in solid angle, leading to a limited geometrical acceptance. The reconstruction and event selection can distort the kinematic distributions of the final state particles, leading to a non-uniform acceptance across the Dalitz plane of the decay. This phase-space acceptance needs to be accounted for in the final amplitude fit. Similarly, there are variations in acceptance as a function of decay time. The detector also has some finite decay-time resolution, defined as the difference between the reconstructed decay-time and true decay-time. These effects are studied using simulation to provide accurate models to include in the final fit, with appropriate systematic uncertainties assigned in each case.

7.1 Phase-space acceptance

For this amplitude analysis it is crucial to model acceptance variations in D^0 decay-time $t(D^0)$ and across the Dalitz plane. The Dalitz efficiency is extracted using the reweighted Monte Carlo described in Chapter 6. The reweighting technique ensures that the efficiency derived from simulation is an accurate representation of reality. The aim of the acceptance study is not only to measure the acceptance but to find a mathematical parameterisation describing the variations as a function of position in the Dalitz plane, which will enter the amplitude fit. The efficiency in any particular region of parameter space is determined by measuring the number of generated events passing all reconstruction and selection requirements, with respect to an unbiased phase-space distribution. The parameterisation of the acceptance variations is chosen in the square Dalitz coordinates $m^2(\pi^+\pi^-)$ and $\cos\theta$ where θ is the decay angle between the π^- (π^+) and D^0 $(\bar{D}^0)$ in the $\pi^+\pi^-$ rest frame. In other words it has the form of the helicity angle. These variables are chosen as they provide a smooth parameterisation of the efficiency variation and they are correlated with the momenta of the daughter particles: $m^2(\pi^+\pi^-)$ depends on the K^0_S momentum and $\cos\theta$ depends on the bachelor pion momenta. The cosine of the decay angle is given by:

$$cos\theta = \frac{m^2(K^0_S\pi^+) - m^2(K^0_S\pi^-)}{4pq} \tag{7.1}$$

where

$$\begin{aligned} p &= \frac{\lambda^{1/2}(m^2(\pi^+\pi^-), m^2(D^0), m^2(K^0_S))}{2m^2(\pi^+\pi^-)}, \\ q &= \frac{\lambda^{1/2}(m^2(\pi^+\pi^-), m^2(\pi^+), m^2(\pi^-))}{2m^2(\pi^+\pi^-)} \end{aligned} \tag{7.2}$$

and

$$\lambda(x,y,z) = x^2 + y^2 + z^2 - 2xy - 2yz - 2xy \tag{7.3}$$

is the Kallen function.

The MC samples are passed through the same selection criteria as for data, as described in Chapter 5. The square Dalitz phase-space is split into bins of approximately equal number of MC events passing all selection requirements. The number of signal events in each bin is calculated as the sum of the weights, from the GBReweighter as discussed in Section 6.2. After truth matching and selection, the MC samples are assumed to be pure signal without background contamination. The denominator is generated by a uniform phase-space distribution where events are randomly generated and required to be in the allowed Dalitz phase-space due to momentum conservation. The efficiency in each two-dimensional $(\cos\theta, m^2(\pi^+\pi^-))$ bin is then determined by the ratio of the number of generated events passing all reconstruction and selection requirements, with respect to the uniform phase-space distribution:

$$\epsilon = \frac{n_{sig}}{n_{gen}} \tag{7.4}$$

where the denominator is equivalent to counting the total number of generated candidates, n_{gen}, prior to the application of any selection criteria. Note that we care only about the shape of the efficiency and not the absolute value which does not enter the analysis.

The measured acceptance and the bin centre of each two-dimensional bin in $(\cos\theta, m^2(\pi^+\pi^-))$ are taken as input for a two-dimensional fit to extract an analytic parameterisation, which describes the acceptance variations as a function of $\cos\theta$ and $m^2(\pi^+\pi^-)$. The parametrisation in square Dalitz coordinates is chosen to be a polynomial with up to quartic terms in $m^2(\pi^+\pi^-)$:

$$\begin{aligned}\epsilon(m^2(\pi^+\pi^-), cos(\theta)) = {} & c_0 m^4(\pi^+\pi^-) + c_1 m^2(\pi^+\pi^-) + c_2 m^2(\pi^+\pi^-) cos^2(\theta) \\ & + c_3 cos^2(\theta) + c_4 cos(\theta) + c_5 + c_6 m^8(\pi^+\pi^-) \\ & + c_7 m^6(\pi^+\pi^-)\end{aligned} \tag{7.5}$$

Different polynomial functions with up to quartic terms were tested and the final choice gives the best agreement with data. The efficiency is measured and parameterised separately for each sub-sample. Figure 7.1 shows the measured and parameterised efficiency and pulls [(measured efficiency - model)/uncertainty] for the single-tagged K_S^0 (LL) 2018 sample. The efficiency variation as a function of regular Dalitz coordinates m_{12}^2 and m_{13}^2 is shown in Figure 7.2. The uncertainties on the measured acceptance are calculated as binomial errors whereas the uncertainty on the parameterised acceptance results from a Gaussian error propagation of the fit uncertainties. Several source of systematic uncertainty are considered for the efficiency evaluation where correlations between the efficiency model parameters are taken into account.

The pulls of the two-dimensional fit can be collected into a histogram and then fitted with a Gaussian. This gives an estimate of how well the fit describes the measured efficiency; a good fit would produce pulls with a Gaussian mean of zero and a width of unity. Equivalently this means the model describes the measured

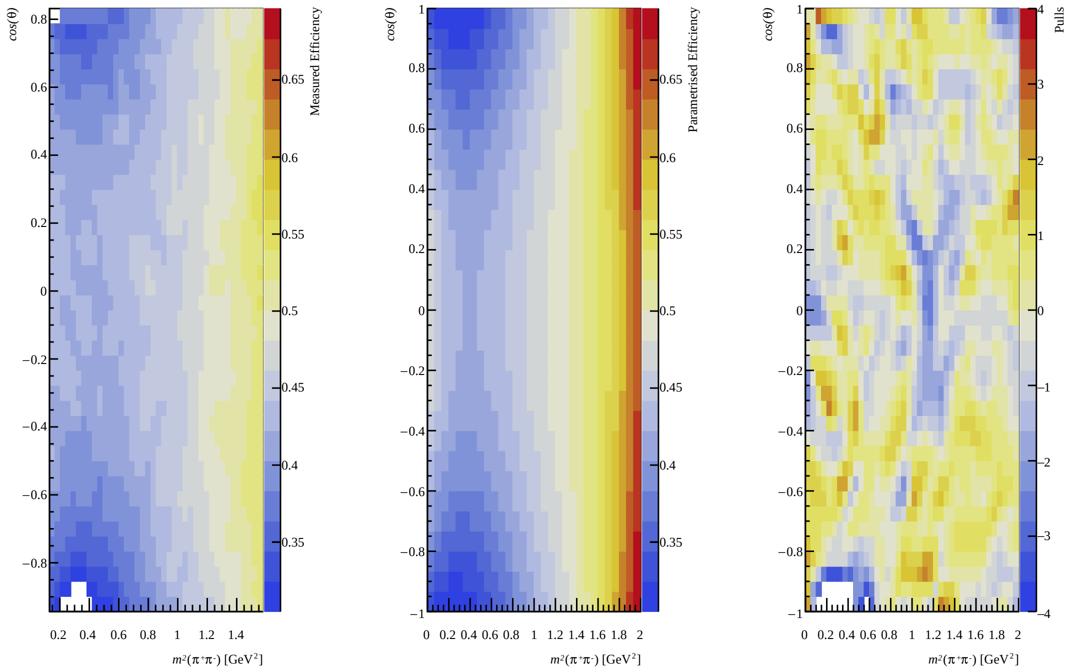

Figure 7.1: Measured (left) and parameterised (centre) phase-space acceptance for the single-tagged K_S^0(LL) 2018 sample. The pulls [(measured efficiency - model)/error] are shown on the right.

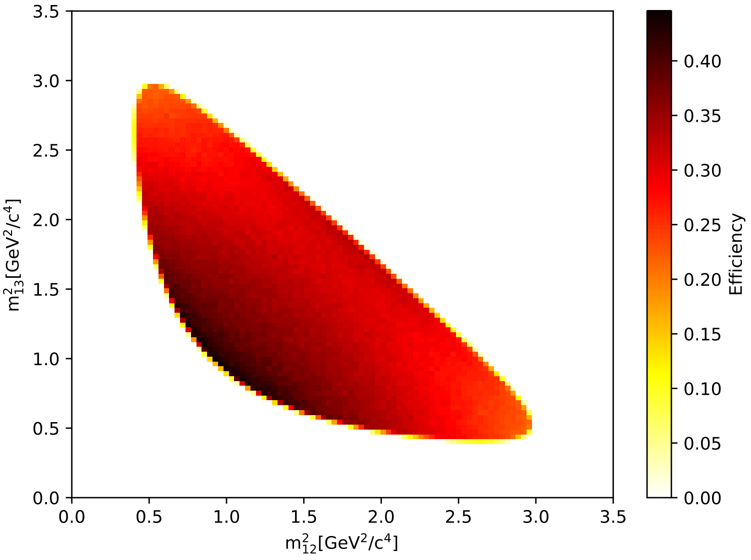

Figure 7.2: Efficiency variation in Dalitz coordinates m_{12}^2 and m_{13}^2 for the single-tagged K_S^0 (LL) 2018 sample.

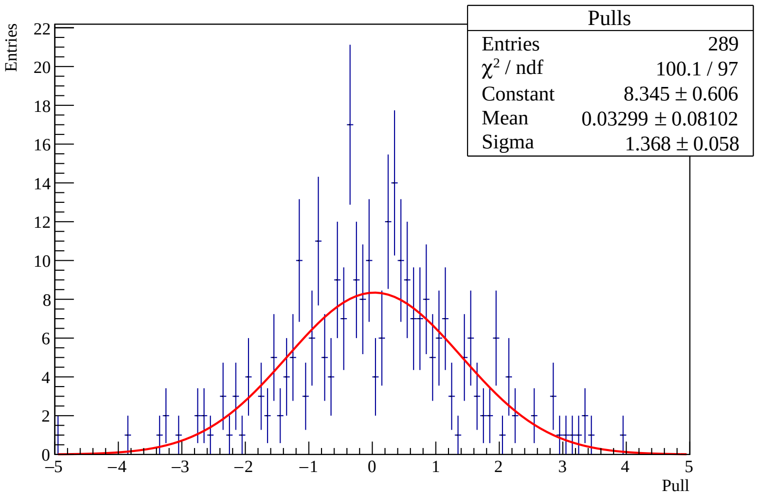

Figure 7.3: Pulls (Measured efficiency - parameterised efficiency)/Error fitted with a Gaussian (red line) for the single-tagged K_S^0 (LL) 2018 sample.

efficiency well within statistical fluctuations. The one-dimensional projection of the pulls can be seen in Figure 7.3, where each entry represents the pull for one of the two-dimensional bins shown in Figure 7.1. The mean of the Gaussian is consistent with zero but the width is larger than unity; this indicates that the uncertainties from the fit model do not cover the statistical fluctuations in data. This can be accounted for by inflating the uncertainties on the efficiency parameters such that the pull distribution is consistent with a unit Gaussian. However the χ^2/ndof is close to unity for the phase-space acceptance fits, so we do not need to inflate the errors for a systematic uncertainty. Figures 7.4 and 7.5 show the projection of the measured and parameterised acceptance onto the $m^2(\pi^+\pi^-)$ and $\cos\theta$ axes respectively. The overall agreement is good, with some indication of mismodelling at the edges of some individual bins; this can be taken into account when assigning a systematic uncertainty to the efficiency evaluation. The parameterised efficiency is determined and applied separately for each sample in the amplitude fit. Plots for additional sub-samples can be seen in Appendix C.1.

To account for possible systematic effects on the choice of model, the efficiency can be refitted with an additional term in the polynomial and the final amplitude fit repeated using the alternative efficiency parameterisation. In addition, the statistical uncertainty on the efficiency model parameters due to the limited MC statistics can be accounted for by rerunning the final mixing fit many times with the efficiency

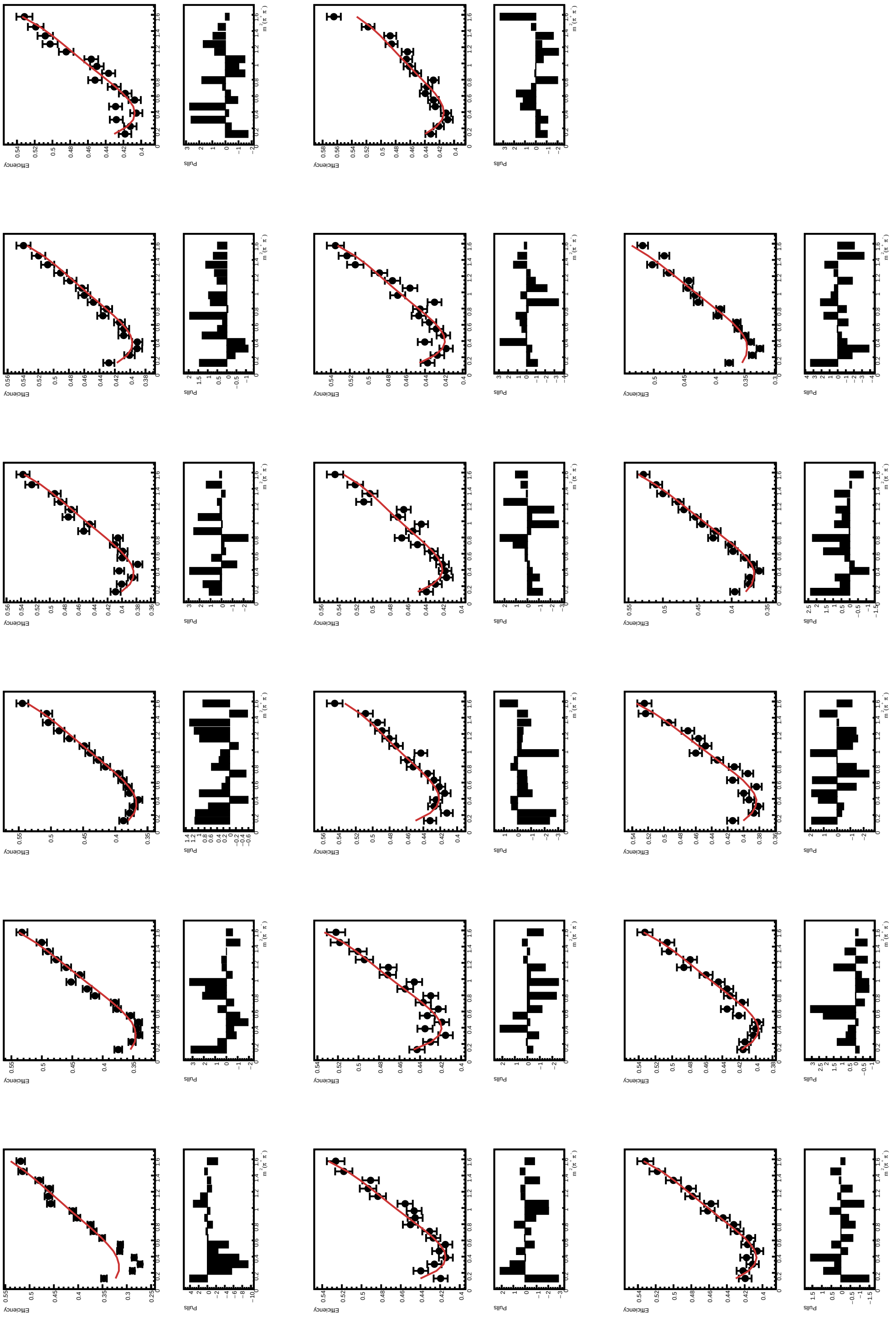

Figure 7.4: Phase-space acceptance projected onto the $m^2(\pi^+\pi^-)$ axis in bins of $\cos\theta$; measured efficiency (black points), parameterised efficiency (red line) and pulls are shown. Single-tagged K_S^0 (LL) 2018 sample.

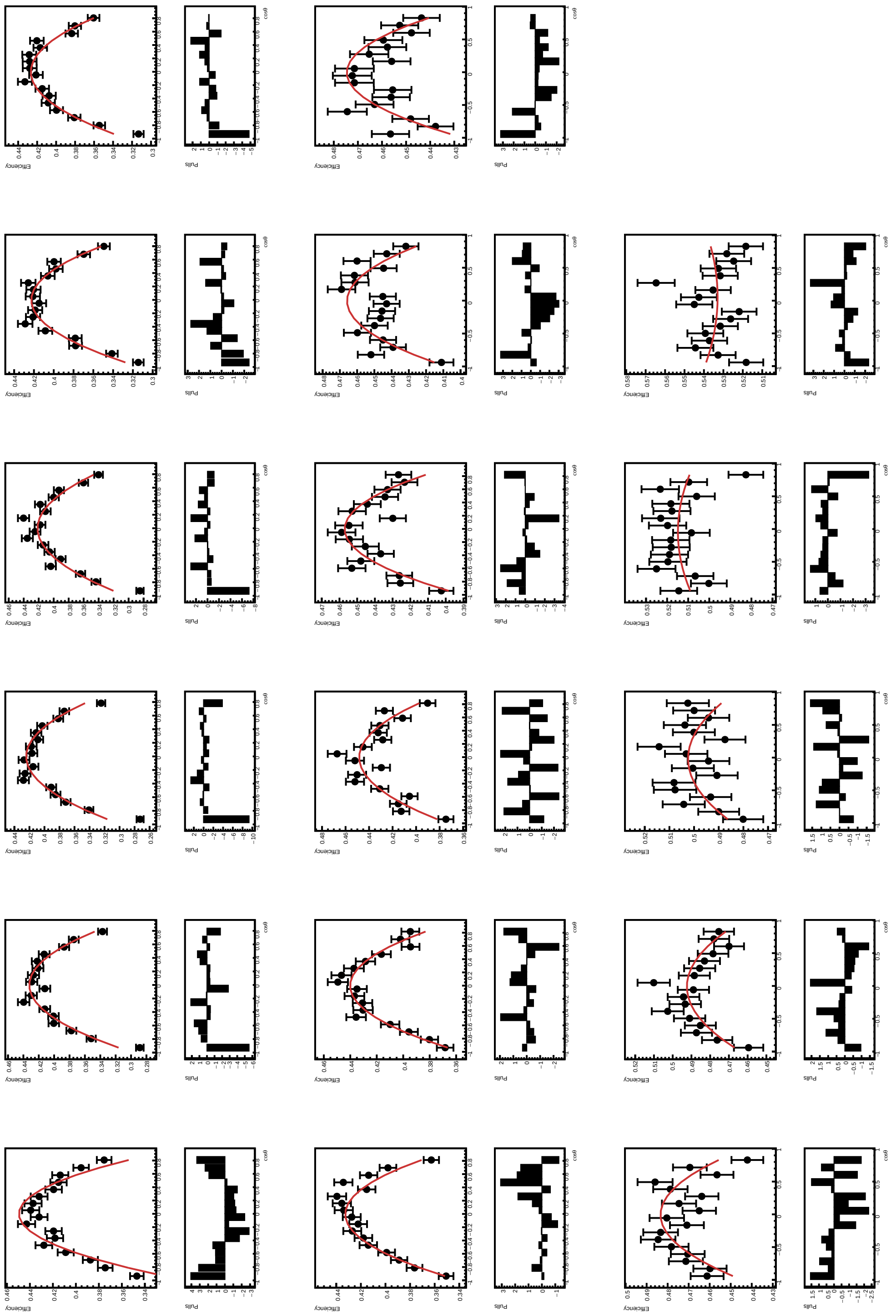

Figure 7.5: Phase-space acceptance projected onto the $\cos\theta$ axis in bins of $m^2(\pi^+\pi^-)$; measured efficiency (black points), parameterised efficiency (red line) and pulls are shown. Single-tagged K_S^0 (LL) 2018 sample.

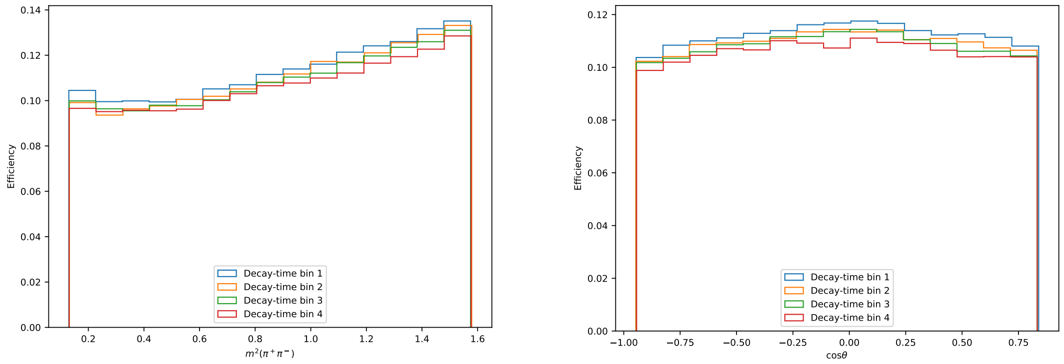

Figure 7.6: Measured efficiency variation in four bins of decay-time projected in bins of square Dalitz coordinates $m^2(\pi^+\pi^-)$ and $\cos\theta$ for the single-tagged K_S^0 (LL) 2018 sample.

parameters resampled for each fit, and assessing the corresponding variation in the mixing parameters. This resampling is performed using the known statistical uncertainties on the efficiency parameters, including correlations between them, and also for the uncertainty scaling required to ensure a unit Gaussian pull distribution as described above. The measured efficiencies are tested for consistency in different decay time bins, and no significant time-dependence is observed. As such, the nominal fit does not include a decay-time dependence on the phase-space efficiency variation. Figure 7.6 shows the measured efficiency variation in four bins of decay-time projected in bins of square Dalitz coordinates $m^2(\pi^+\pi^-)$ and $\cos\theta$. Figures 7.7 and 7.8 show the projections of the measured efficiency in the four bins of decay-time in slices of the phase-space variables $m^2(\pi^+\pi^-)$ and $\cos\theta$ for the different bins in the square Dalitz variables. A systematic uncertainty is estimated to account for a possible decay-time dependence below sensitivity.

7.2 Decay-time acceptance

There are also variations in acceptance as a function of decay-time, which need to be accounted for in the final amplitude fit. The decay-time acceptance is determined from the reweighted MC samples which are passed through the complete selection chain including stripping, preselection and multivariate analysis. The decay-time acceptance is evaluated as the ratio of the generated D^0 decay-time distribution after the complete selection and the true distribution in MC. As a proxy for the truth we use the MC samples with stripping selection applied but no others (trigger,

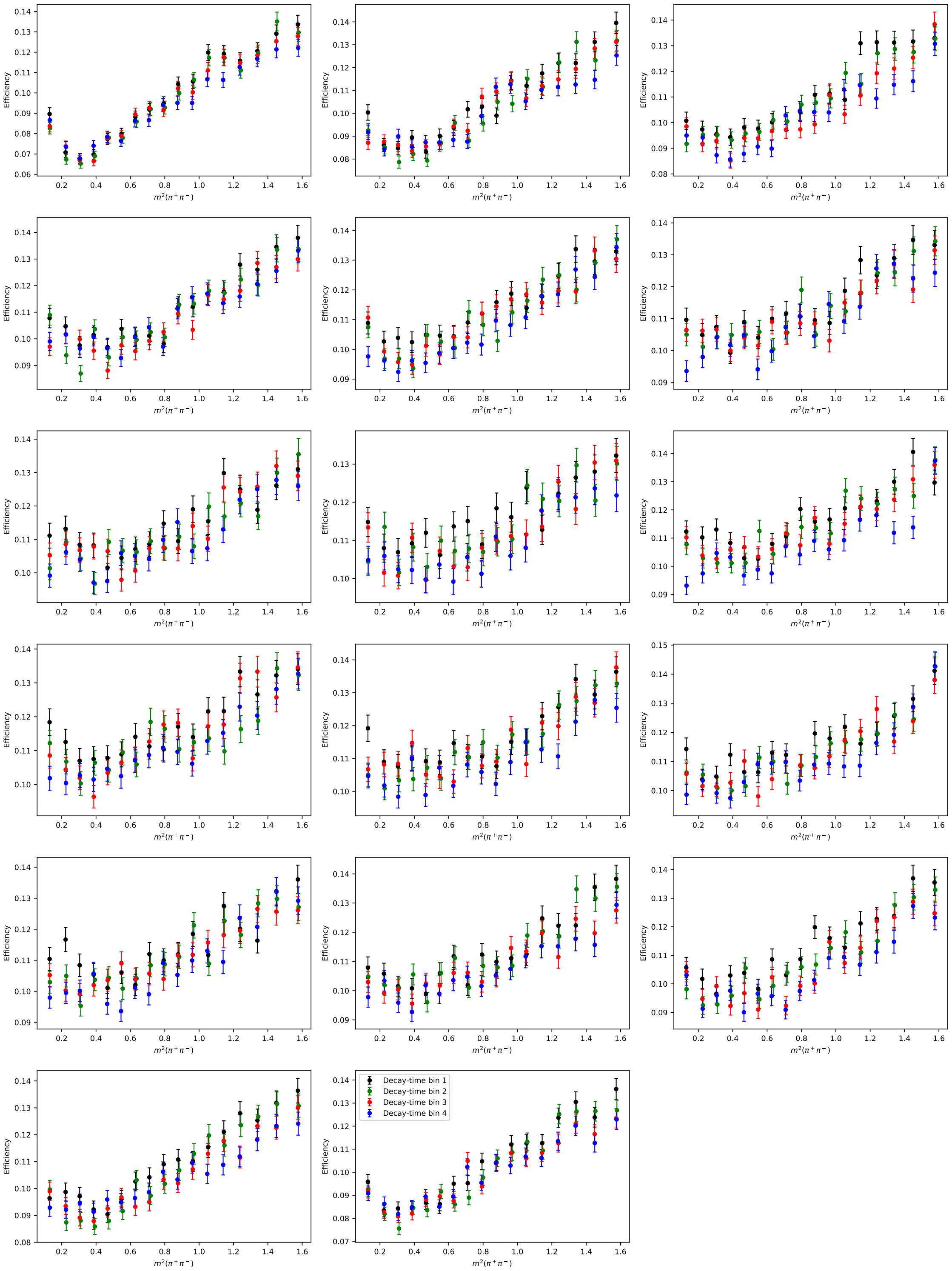

Figure 7.7: Projections of the measured efficiency in four bins of decay-time; projections in the $m^2(\pi^+\pi^-)$ variable in bins of $\cos\theta$ where the sub-plots are the different bins in $\cos\theta$. Single-tagged K_S^0 (LL) sample.

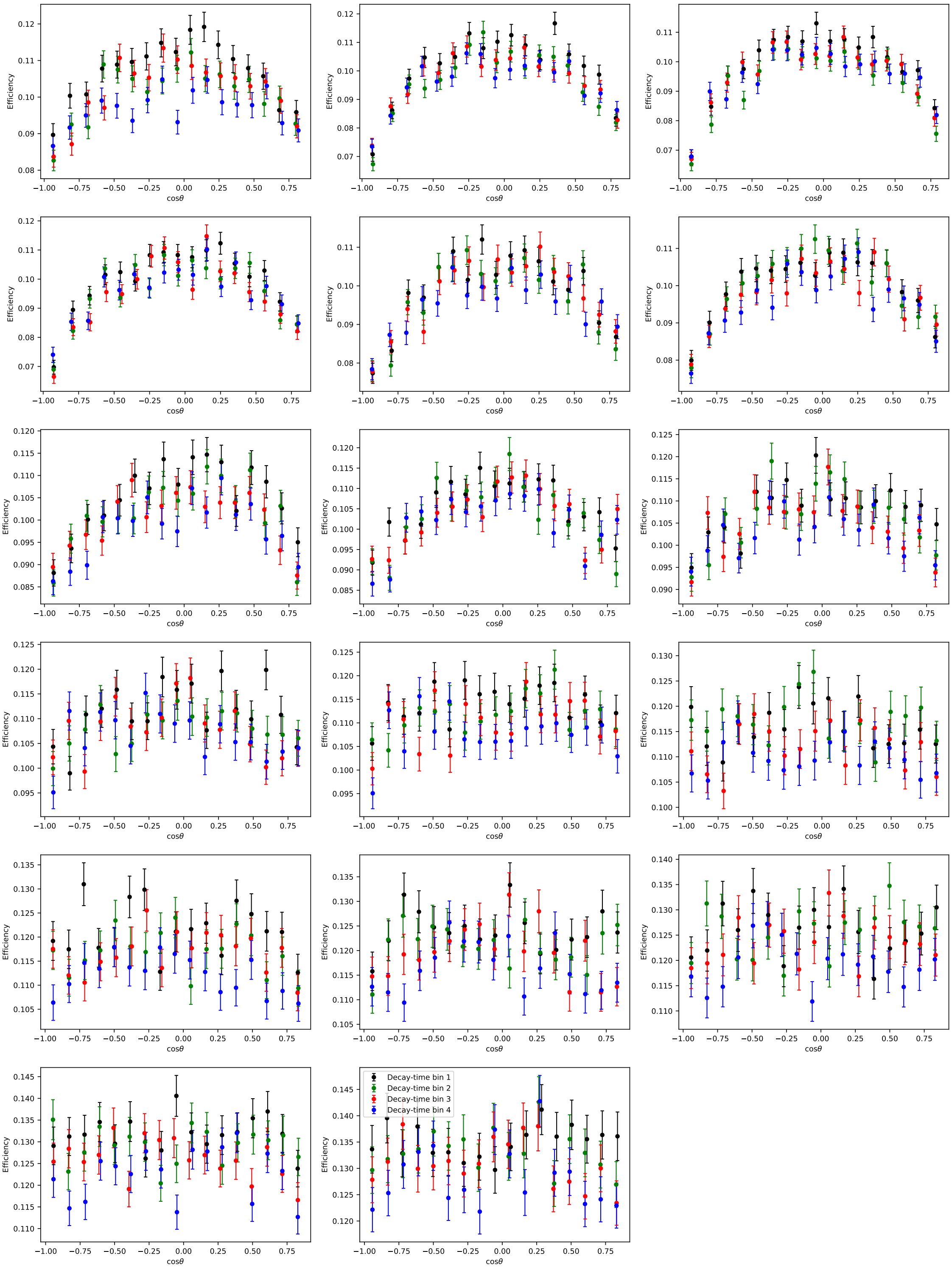

Figure 7.8: Projections of the measured efficiency in four bins of decay-time; projections in the $\cos\theta$ variable in bins of $m^2(\pi^+\pi^-)$ where the sub-plots are the different bins in $m^2(\pi^+\pi^-)$. Single-tagged K_S^0 (LL) sample.

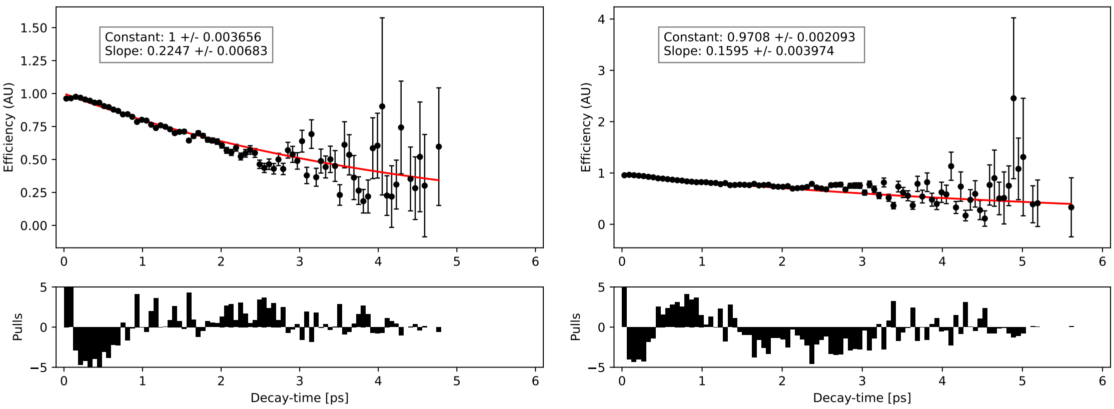

Figure 7.9: Measured decay-time acceptance (black points) fitted with an exponential function (red line) for single-tagged K_S^0 (LL left and DD right) 2018 samples.

preselection, or MVA). This has been checked against the expected exponential distribution and found to be consistent, in line with the fact that the cuts applied are independent of D^0 decay time. The decay-time acceptance is obtained by fitting the ratio distribution with an exponential function of the form $e^{b-at(D^0)}$, where b is a normalisation factor and the fit is in true decay-time. The correction factor $e^{-at(D^0)}$ is then included in the amplitude fit model. This is derived separately for all subsamples. Figure 7.9 shows the measured and parameterised decay-time acceptance for the single-tagged K_S^0 (LL and DD) 2018 samples. This shows some disagreement between the measured acceptance and the exponential fit model. This can be accounted for by including systematic uncertainties to account for the mismodelling of the acceptance by this exponential model. Currently the systematic does not include the effect of the fact that the exponential model is imperfect at describing the efficiency from MC, just the variations within the exponential model. This is described in Chapter 10. The results of the fit and the correction factors for all samples are shown in Table 7.1.

7.3 Decay-time resolution

The LHCb detector has a finite decay-time resolution which needs to be accounted for in the final amplitude fit model. The decay-time resolution is defined as the difference between the reconstructed decay-time and the true decay-time $t_{res} = t_{reco} - t_{true}$. The decay-time resolution is determined from simulation and is fitted

	Single-tagged		Double-tagged	
	K_S^0 (LL)	K_S^0 (DD)	K_S^0 (LL)	K_S^0 (DD)
	2016			
Constant	0.990 ± 0.003	0.940 ± 0.002	1.039 ± 0.004	1.008 ± 0.002
Slope [ps]	0.235 ± 0.006	0.134 ± 0.004	0.231 ± 0.008	0.132 ± 0.004
	2017			
Constant	1.013 ± 0.004	0.967 ± 0.002	1.071 ± 0.005	1.050 ± 0.003
Slope [ps]	0.229 ± 0.008	0.146 ± 0.004	0.214 ± 0.009	0.136 ± 0.005
	2018			
Constant	1.002 ± 0.004	0.971 ± 0.002	1.073 ± 0.005	1.062 ± 0.003
Slope [ps]	0.228 ± 0.007	0.161 ± 0.005	0.215 ± 0.009	0.153 ± 0.006

Table 7.1: Parameters of the exponential fit to the decay-time acceptance.

with a triple Gaussian function.

$$T_{res} = N\left(\frac{f}{\sqrt{2\pi}\sigma_1}e^{-\frac{1}{2}\left(\frac{t'-\mu}{\sigma_1}\right)^2} + \frac{g}{\sqrt{2\pi}\sigma_2}e^{-\frac{1}{2}\left(\frac{t'-\mu}{\sigma_2}\right)^2} + \frac{1-f-g}{\sqrt{2\pi}\sigma_3}e^{-\frac{1}{2}\left(\frac{t'-\mu}{\sigma_3}\right)^2}\right) \tag{7.6}$$

The scale of the decay-time smearing can then be expressed as an effective resolution:

$$\sigma_{eff} = \sqrt{f\sigma_1^2 + g\sigma_2^2 + (1-f-g)\sigma_3^2} \tag{7.7}$$

This is included in the final amplitude fit model by convoluting the decay-time PDF with the triple Gaussian resolution function. Plots of the decay-time resolution fitted with the triple Gaussian are shown in Figure 7.10. The fit parameters along with the effective resolution for each sub-sample is shown in Table 7.2 and additional plots for other sub-samples are shown in Appendix C.3. The sample-averaged effective resolution is found to be 107.9 fs for double-tagged and 113.2 fs for single-tagged samples, where the effective resolution of each sample is weighted by the fraction of events it contains.

7.4 Phase-space resolution

Similarly to decay-time, the Dalitz variables m_{12}^2 and m_{13}^2 also have some finite resolution due to the detector, defined as $m_{res}^2 = m_{reco}^2 - m_{true}^2$. Similarly to the treatment of the decay-time resolution, the phase-space resolution is derived from simulation. The resolutions of $m^2(K_S^0\pi^+)$ and $m^2(K_S^0\pi^-)$ are correlated through energy and momentum conservation, and hence the phase-space resolution is measured

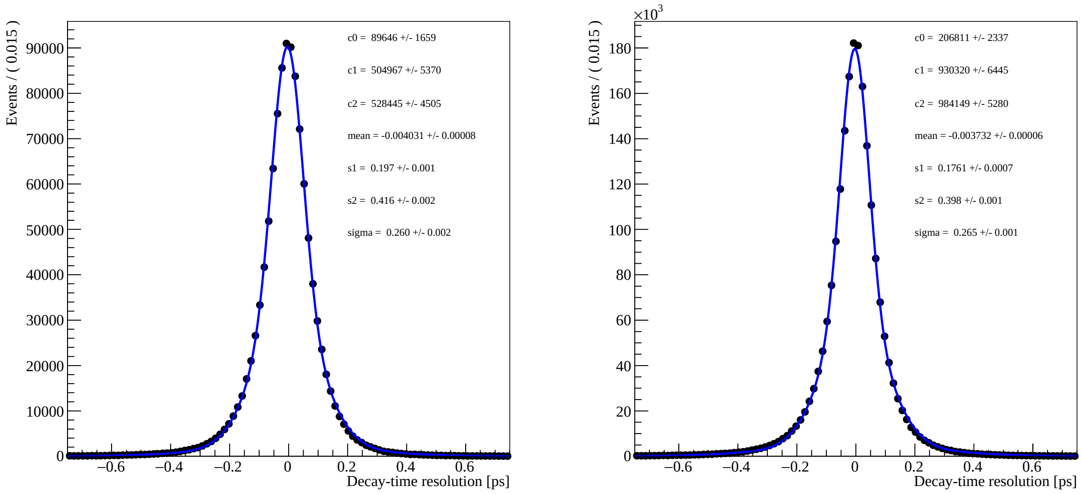

Figure 7.10: Decay-time resolution (black points) fitted with a triple Gaussian function (blue line) for the 2018 K_S^0 (LL left and DD right) samples. Fit parameters displayed.

in a set of uncorrelated variables. These uncorrelated variables are the sum and difference of $m^2(K_S^0\pi^+)$ and $m^2(K_S^0\pi^-)$, denoted by $u \equiv m^2(K_S^0\pi^+)+m^2(K_S^0\pi^-)$ and $v \equiv m^2(K_S^0\pi^+) - m^2(K_S^0\pi^-)$, respectively. The resolutions in u and v are computed as the difference between reconstructed and generated values, $u' - u$ and $v' - v$. The resolutions can also be fitted with a double Gaussian function:

$$F_{PS}(x;\mu,\sigma_1,\sigma_2,c) = N\left(\frac{c}{\sqrt{2\pi}\sigma_1}e^{-\left(\frac{x-\mu}{\sqrt{2}\sigma_1}\right)} + \frac{(1-c)}{\sqrt{2\pi}\sigma_2}e^{-\left(\frac{x-\mu}{\sqrt{2}\sigma_2}\right)}\right) \tag{7.8}$$

where the two Gaussians have a common mean μ and x is the given resolution of either the Dalitz variables m_{12}^2, m_{13}^2 or the uncorrelated variables u or v. Plots of the resolutions for the Dalitz variables and the uncorrelated variables can be seen in Figure 7.11. There is some mismodelling in the peak of the double Gaussian, however the phase-space resolution is small enough that this model is sufficient for the studies. The correlations between the Dalitz variables and the alternative variables u and v can be seen in the two-dimensional histograms in Figure 7.12. The Pearson correlation coefficient is a measure of the correlation between two variables and is given by:

$$r_{xy} = \frac{\sum_{i=1}^{n}(x_i-\bar{x})(y_i-\bar{y})}{\sqrt{\sum_{i=1}^{n}(x_i-\bar{x})^2}\sqrt{\sum_{i=1}^{n}(y_i-\bar{y})^2}} \tag{7.9}$$

	Single-tagged		Double-tagged	
	K_S^0 (LL)	K_S^0 (DD)	K_S^0 (LL)	K_S^0 (DD)
	2016			
μ [fs]	-3.57 ± 0.07	-3.54 ± 0.05	-3.00 ± 0.10	-2.89 ± 0.07
σ_1 [fs]	256 ± 1.51	268 ± 0.92	49.1 ± 0.37	254 ± 1.30
σ_2 [fs]	49.5 ± 0.25	107 ± 0.38	247 ± 2.25	47.2 ± 0.24
σ_3 [fs]	103 ± 0.53	47.7 ± 0.16	99.9 ± 0.78	104 ± 0.55
f	0.073 ± 0.001	0.105 ± 0.001	0.462 ± 0.008	0.099 ± 0.001
g	0.450 ± 0.005	0.471 ± 0.002	0.065 ± 0.002	0.424 ± 0.004
σ_{eff} [fs]	105	118	99	112
	2017			
μ [fs]	-3.81 ± 0.08	-3.81 ± 0.05	-3.16 ± 0.12	-3.06 ± 0.09
σ_1 [fs]	256 ± 1.89	266 ± 0.10	49.6 ± 0.47	252 ± 1.68
σ_2 [fs]	49.8 ± 0.28	107 ± 0.44	245 ± 2.96	105 ± 0.70
σ_3 [fs]	104 ± 0.65	47.9 ± 0.18	101 ± 1.08	47.6 ± 0.29
f	0.069 ± 0.001	0.10 ± 0.466	0.482 ± 0.011	0.095 ± 0.002
g	0.470 ± 0.006	0.466 ± 0.003	0.064 ± 0.002	0.466 ± 0.005
σ_{eff} [fs]	103	116	98	110
	2018			
μ [fs]	-4.15 ± 0.08	-3.93 ± 0.06	-3.32 ± 0.13	-3.17 ± 0.09
σ_1 [fs]	259 ± 1.76	266 ± 1.14	260 ± 3.11	253 ± 1.74
σ_2 [fs]	108 ± 0.65	106 ± 0.45	109 ± 1.04	104 ± 0.71
σ_3 [fs]	51.6 ± 0.28	47.2 ± 0.18	52.1 ± 0.42	46.8 ± 0.30
f	0.080 ± 0.002	0.099 ± 0.001	0.069 ± 0.002	0.095 ± 0.002
g	0.471 ± 0.005	0.463 ± 0.003	0.456 ± 0.007	0.471 ± 0.005
σ_{eff} [fs]	110	115	107	110

Table 7.2: Parameters for the decay-time resolution where μ and $\sigma_{1,2,3}$ are fit parameters of the triple Gaussian and σ_{eff} is the effective resolution.

for two variables x and y, where the sum is over the number of events in the dataset and x and y are the means of the distributions. It has a value in the range [-1,1] where a value of -1 would indicate perfect negative correlation, a value of zero would indicate no correlation and a value of 1 would indicate perfect positive correlation. The Pearson correlation coefficient for the resolution of the regular Dalitz variables m_{12}^2 and m_{13}^2 is -0.48 whereas for the uncorrelated variables u and v it is found to be 0.00 (to 2 decimal places) which confirms the assumption that we can safely neglect the correlation between these variables.

The phase-space resolution is small compared to the scale of resonances in the Dalitz plane. As such it should not affect the distributions being fitted and the mixing fit should not need to include a correction for the phase-space resolution.

	Single-tagged		Double-tagged	
	K_S^0 (LL)	K_S^0 (DD)	K_S^0 (LL)	K_S^0 (DD)
	2016			
$m^2(K_S^0\pi^+)$	6594	7792	6067	7160
$m^2(K_S^0\pi^-)$	6590	7805	6054	7175
$m_{12}^2 - m_{13}^2$	10500	12603	10317	12200
$m_{12}^2 + m_{13}^2$	5696	6894	5273	6403
	2017			
$m^2(K_S^0\pi^+)$	6615	7785	6057	7150
$m^2(K_S^0\pi^-)$	6609	7787	6057	7180
$m_{12}^2 - m_{13}^2$	10499	12575	10311	12171
$m_{12}^2 + m_{13}^2$	5737	6871	5278	6370
	2018			
$m^2(K_S^0\pi^+)$	6578	7833	5998	7193
$m^2(K_S^0\pi^-)$	6581	7840	5988	7204
$m_{12}^2 - m_{13}^2$	10408	12653	5284	12231
$m_{12}^2 + m_{13}^2$	5789	6945	10189	6452

Table 7.3: Effective resolutions for the phase-space variables: the Dalitz variables $m^2(K_S^0\pi^+)$ and $m^2(K_S^0\pi^-)$ and the uncorrelated variables u and v. Values are given in MeV^2.

The effect of not including the resolution on the mixing parameters can be studied with pseudo-experiments and an appropriate systematic uncertainty assigned. A resampling method is used to assign the systematic where the uncorrelated variables u and v are used since the correlations can be neglected in the resampling; this is discussed in more detail in Chapter 10. The phase-space resolution may also vary as a function of Dalitz space which can be included in the resampling study; this can be seen in the plots in Figure 7.13.

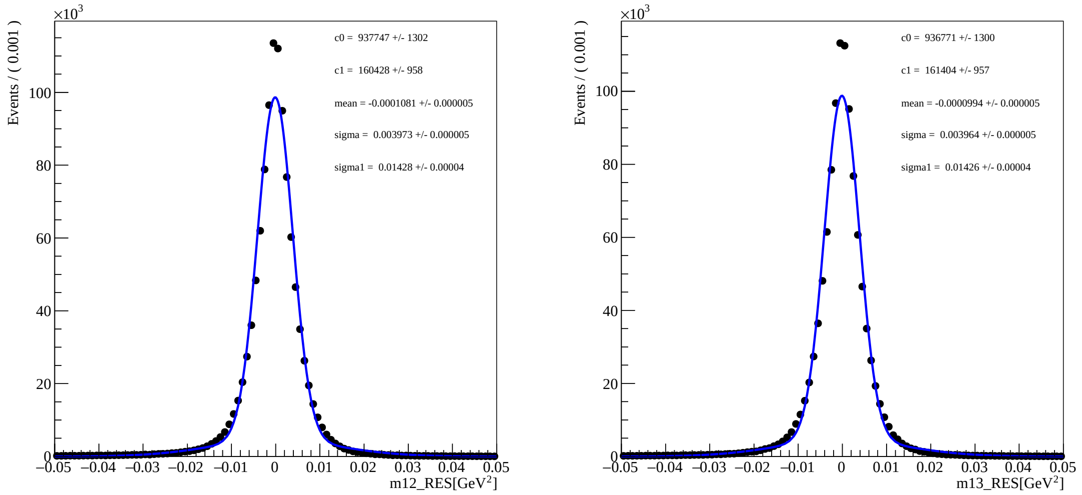

(a) m_{12}^2 resolution

(b) m_{13}^2 resolution

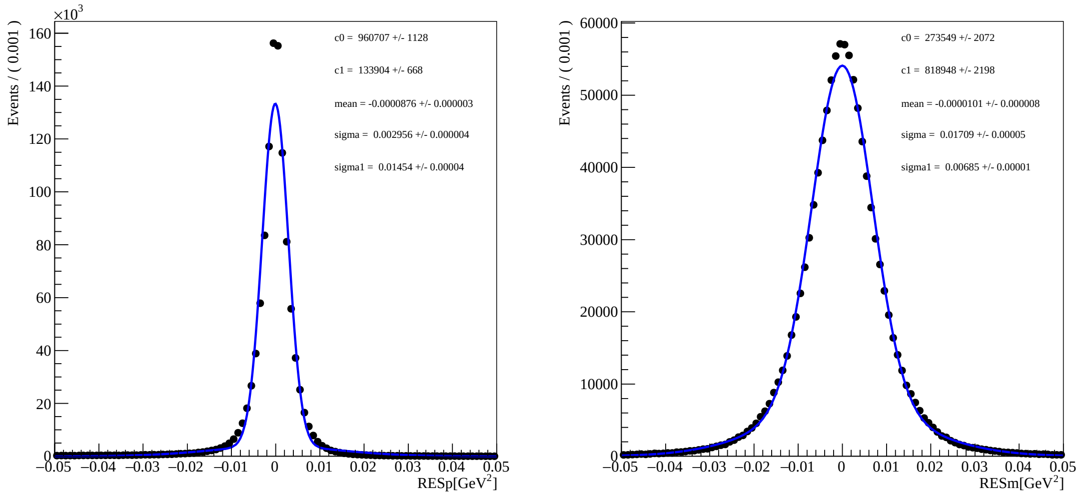

(c) $m_{12}^2 + m_{13}^2$ resolution

(d) $m_{12}^2 - m_{13}^2$ resolution

Figure 7.11: Phase-space resolutions of the Dalitz variables m_{12}^2 and m_{13}^2 and the uncorrelated variables u and v, derived from simulation (black points) and fitted with a double Gaussian (blue line) for the 2018 single-tagged K_S^0 (LL) sample.

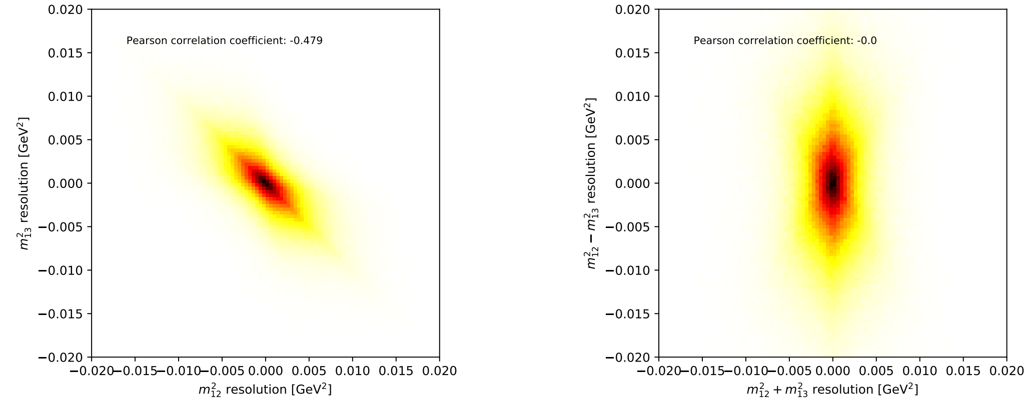

(a) Resolution in m_{12}^2 and m_{13}^2

(b) Resolution in u and v

Figure 7.12: Two-dimensional histograms of the phase-space resolutions in regular Dalitz coordinates (left) and the uncorrelated variables u and v (right) with the Pearson correlation coefficient shown for 2018 K_S^0 (LL) single-tagged sample.

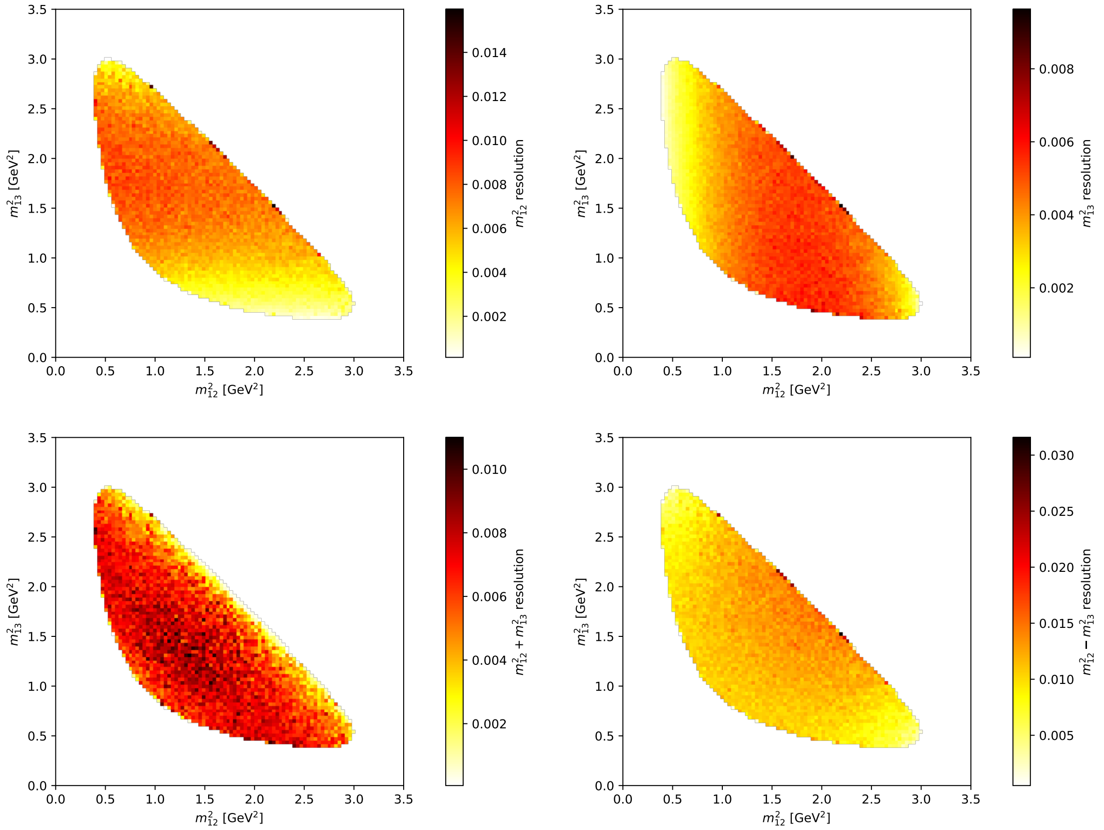

Figure 7.13: Phase-space resolution varies as a function of Dalitz coordinates.

In summary, the mixing fit is subject to detector acceptance and resolution effects, these need to be accounted for in the final time-dependent amplitude fit model. These are: the phase-space acceptance, decay-time acceptance and decay-time resolution which are included in the fit model, and the phase-space resolution which is neglected in the fit model and an appropriate systematic uncertainty assigned.

CHAPTER 8

Fit Model

The parameters of interest are extracted from an unbinned three-dimensional maximum likelihood fit of the model to data. The fit is performed simultaneously over the 12 sub-samples; by data taking year (2016, 2017, 2018), K_S^0 type (LL, DD) and decay origin (single-tagged, double-tagged). The overall PDF is given by:

$$\begin{aligned}\mathcal{P}(t, m_+^2, m_-^2, p_{sig}, tag, \vec{\alpha}) = p_{sig}\,\big[&(1-\omega_{muontag})\mathcal{P}_{sig}(t, m_+^2, m_-^2, tag, \vec{\alpha})\\ &+ \omega_{muontag}\mathcal{P}_{mt}(t, m_+^2, m_-^2, tag, \vec{\alpha})\big]\\ &+ (1-p_{sig})\mathcal{P}_{bkg}(t, m_+^2, m_-^2)\end{aligned} \tag{8.1}$$

where p_{sig} is the per-candidate signal probability which is extracted from a fit to $m(D^0)$ or δm, tag is the flavour tag and takes values of $+1$ (-1) for D^0 ($\bar{D}^0$), $\vec{\alpha}$ is a vector of the fit parameters, $\omega_{muontag}$ is the mistag fraction. The decay-time is given by t and the Dalitz variables are m_+^2 and m_-^2 (defined differently for D^0 and $\bar{D}^0$ to recover identical distributions under *CP*-symmetry). The signal PDF is given by:

$$\mathcal{P}_{sig}(t, m_+^2, m_-^2, tag, \vec{\alpha}) = \big[\big(\mid \mathcal{A}_f(t', m_+^2, m_-^2, tag) \mid^2 \epsilon(t')\big) \otimes R(t, t', \mu_t, \sigma_t)\big]\,\epsilon(m_+^2, m_-^2) \tag{8.2}$$

where $\mathcal{A}_f(t', m_+^2, m_-^2)$ is the time-dependent amplitude model, $\epsilon(t')$ and $\epsilon(m_+^2, m_-^2)$ are the decay-time and phase-space efficiencies and $R(t, t', \mu_t, \sigma_t)$ is the decay-time resolution and $\otimes$ represents the decay-time convolution.

The square of the time-dependent amplitude $\mathcal{A}_f(t)$ is given by:

$$\begin{aligned} \mid \mathcal{A}_f(t) \mid^2 = \frac{1}{2} e^{-\Gamma t} \Bigg[& \left(\mid A \mid^2 - \mid \frac{q}{p} B \mid^2 \right) \cos(x\Gamma t) - 2\,\mathrm{Im}\left(AB^* \left[\frac{q}{p}\right]^* \right) \sin(x\Gamma t) \\ & + \left(\mid A \mid^2 + \mid \frac{q}{p} B \mid^2 \right) \cosh(y\Gamma t) - 2\,\mathrm{Re}\left(AB^* \left[\frac{q}{p}\right]^* \right) \sinh(y\Gamma t) \Bigg] \end{aligned} \tag{8.3}$$

repeated from Equation 2.43 for convenience, as well as a similar equation for $\left|\bar{\mathcal{A}}_f(t)\right|^2$. The amplitudes A and B at a given point in phase-space are the amplitude of the $D^0 \to K^0_S \pi^+\pi^-$ process (direct) and the $\bar{D}^0 \to K^0_S \pi^+\pi^-$ process which proceeds via mixing. These can be expressed as the sum of component amplitudes multiplied by a complex coefficient:

$$A(m_+^2, m_-^2) = \sum_r a_r e^{i\phi_r} A_r(m_+^2, m_-^2) \tag{8.4}$$

$$B(m_+^2, m_-^2) = \sum_r \overline{a}_r e^{i\overline{\phi}_r} A_r(m_-^2, m_+^2) \tag{8.5}$$

where the Dalitz variables are defined as $m_+^2 = m^2(K^0_S\pi^+)$ and $m_-^2 = m^2(K^0_S\pi^-)$ for the D^0 case, and with reversed pion signs for the $\bar{D}^0$ case, $m_+^2 = m^2(K^0_S\pi^-)$ and $m_-^2 = m^2(K^0_S\pi^+)$.

The time-dependent amplitude is expressed as a sum of two-body intermediate resonances r with amplitudes A_r which depend on a point in phase-space. The amplitude model is built from a number of resonant and non-resonant components. The K-matrix formalism [38] is used for the $\pi\pi$ S-wave component and the LASS parametrisation [29] for the $K\pi$ S-wave. The model dependence of the analysis enters through the choice of resonances contributing to the sum in Equations 8.4 and 8.5 and the parameterisation of A_r.

The amplitude for a D^0 meson decaying to a three-body final state, $D \to abc$ through an intermediate resonance $r \to ab$ is given by:

$$A_r(m_+^2, m_-^2) = F_D^{(L)}(q, q_0) \times F_r^{(L)}(p, p_0) \times Z_L(\Omega) \times \mathcal{T}_r(m) \tag{8.6}$$

where the form factors $F_D^{(L)}$ and $F_r^{(L)}$ describe the decay $D \to rc$ and $r \to ab$ respectively, L is the orbital angular momentum between r and c, note that in this case the spin of c is zero so L is essentially the spin of the resonance r. p and q are the momenta of c and a in the resonance rest frame, $Z_L(\Omega)$ describes the angular distribution of the final state particles. $\mathcal{T}_r$ is the dynamical function describing the resonance r.

The angular momentum L is limited by the linear momentum q. Decay particles moving slowly may have difficulty generating sufficient angular momentum to conserve the spin of the resonance. The Blatt-Weisskopf factors [80] $F^{(L)}$ weight the amplitudes to account for this spin-dependent effect. The form factors are normalised to give $F^{(L)} = 1$ for $z = z_0 = (|q_0|d)^2$ where q_0 is the value of the momentum when $m_{ab} = m_r$. The Blatt-Weisskopf form factors are given in Table 8.1, this shows two common formulations, the second column is used here. The difference between the two columns is in the normalisation and should not effect the physics. This complicates comparisons between experiments; in this case we have used the same formulation as that in Ref. [20].

L	$B_L(q)$	$B'_L(q, q_0)$
0	1	1
1	$\sqrt{\frac{2z}{1+z}}$	$\sqrt{\frac{1+z_0}{1+z}}$
2	$\sqrt{\frac{13z^2}{(z-3)^2+9z}}$	$\sqrt{\frac{(z^0-3)^2+9z_0}{(z-3)^2+9z}}$

Table 8.1: Blatt-Weisskopf barrier factors: $z = (|q|d)^2$ and $z_0 = (|q_0|d)^2$; q is the momentum and q_0 is the value of q when the invariant mass equals the pole mass of the resonance, d is the meson radius or impact parameter of the decay particles.

This factor is evaluated for the decay $r \to ab$ where q is the momentum of a in the resonance rest frame and for $D \to rc$ where p is the momentum of c in the resonance rest frame. The centre-of-mass momentum of a in the two-body decay $r \to ab$ is given by:

$$q = \frac{1}{2M}\sqrt{\left[M^2 - (m_a^2 + m_b^2)^2\right]\left[M^2 - (m_a^2 - m_b^2)^2\right]} \tag{8.7}$$

The Zemach formalism [85] expresses the angular correlations among the final state particles by the function $Z_L(\Omega)$ where Ω represents the angular relations of the particles. Scalar resonances are not polarised and thus the angular distribution is

$Z_0 = 1$. For vector resonances:

$$Z_1 = m_{ac}^2 - m_{bc}^2 - \frac{(m_D^2 - m_c^2)(m_a^2 - m_b^2)}{m_{ab}^2} \tag{8.8}$$

For tensor resonances the angular distribution is:

$$\begin{aligned} Z_2 = &\left[m_{ac}^2 - m_{bc}^2 - \frac{(m_D^2 - m_c^2)(m_a^2 - m_b^2)}{m_{ab}^2} \right]^2 \\ &- \frac{1}{3}\left[m_{ab}^2 - 2(m_D^2 + m_c^2) + \frac{(m_D^2 + m_c^2)^2}{m_{ab}^2} \right] \left[m_{ab}^2 - 2(m_a^2 + m_b^2) + \frac{(m_a^2 + m_b^2)^2}{m_{ab}^2} \right] \end{aligned} \tag{8.9}$$

The spin of the resonance L has a characteristic appearance on the Dalitz plot with spin L corresponding to $L + 1$ distinctive lobes (ie. a spin 0 resonance will look like a straight line on the Dalitz plot, a spin 1 resonance will have 2 lobes).

The propagator $\mathcal{T}_r$ describes the dynamics of the resonance decay. Most resonances in this analysis are described using the relativistic Breit-Wigner propagator [34] given by:

$$\mathcal{T}_r(m) = \frac{1}{(m_0^2 - m^2) - i m_0 \Gamma(m)} \tag{8.10}$$

where m_0 is the mass of the pole and the width Γ is given by:

$$\Gamma(m) = \Gamma_0 \left(\frac{q}{q_0} \right)^{(2L+1)} \left(\frac{m_0}{m} \right) F_r^{(L)^2} \tag{8.11}$$

Differences in the parametrisations of $Z_L(\Omega)$, B_L, and $\mathcal{T}_r$, as well as in the set of resonances r are model-dependent, and may complicate the comparison of results from different experiments.

8.1 Gounaris-Sakurai propagator

The Gounaris-Sakurai propagator [51] has been shown shown to provide a better description of broad ρ resonances in $\pi\pi$ scattering data than the Breit-Wigner propagator. The Gounaris-Sakurai propagator is therefore used to describe the

$\rho(770)$ resonance in the amplitude model. The propagator is given by:

$$\mathcal{T}_r = \frac{1 - d\frac{\Gamma_r}{m_r}}{(m_r^2 - m_{ab}^2 + f) - im_r\Gamma(m_{ab})} \tag{8.12}$$

where

$$d = \frac{3}{\pi}\frac{m_\pi^2}{q_r^2}\log\left(\frac{m_r + 2q_r}{2m_\pi}\right) + \frac{m_r}{2\pi q_r} - \frac{m_\pi^2 m_r}{\pi q_r^3} \tag{8.13}$$

and $f = f(m_{ab}^2)$ is defined as:

$$\begin{aligned} f(m_{ab}^2) = \frac{\Gamma_r m_r^2}{q_r}&\left\{\frac{q^2}{q_r^2}\left[h(m_{ab}^2) - h(m_r^2)\right]\right. \\ &\left. + \, (m_r^2 - m_{ab}^2)\left[h(m_r^2)\left(\frac{1}{8q_r^2} - \frac{1}{2m_r^2}\right) + \frac{1}{2\pi m_r^2}\right]\right\} \end{aligned} \tag{8.14}$$

where q is the momentum of particle a in the rest frame of the resonant pair. The function $h(m^2)$ is given by:

$$h(m^2) = \frac{2q}{\pi m}\ln\left(\frac{m + 2q}{2m_\pi}\right) \tag{8.15}$$

8.2 K-matrix formalism

The Breit-Wigner amplitudes are known to provide a decent description of isolated resonances, but a poor description of overlapping resonances of the same partial wave and also does not preserve unitarity. Therefore in the case of broad overlapping resonances or for resonances located close to thresholds of additional decay channels, an alternative formalism is needed. The K-matrix formalism [38] preserves unitarity by construction as opposed to the Breit-Wigner amplitudes. The resonances contributing to the $\pi^+\pi^-$ S-wave are overlapping in mass and are better modelled by the K-matrix formalism.

The decay amplitude is defined by:

$$F_i(s) = \left[I - iK(s)\rho(s)\right]_{ij}^{-1} P_j(s) \tag{8.16}$$

where the indices i and j correspond to the (final and initial) channels contributing to the scattering process; $1 = \pi\pi$, $2 = K\bar{K}$, $3 = \pi\pi\pi\pi$, $4 = \eta\eta$, $5 = \eta\eta'$. The production vector is P where the term P_j represents the production of some state j, which then scatters into a final state i via the matrix term in the square brackets. I is the identity matrix and ρ is the phase-space matrix. In this analysis only the $\pi\pi$ final states need to be considered, meaning we only consider the $i = 1$ terms for the matrix, where i refers to the final state.

The K-matrix is given by:

$$K_{ij}(s) = \left(f_{ij}^{scatt} \frac{1 - s_0^{scatt}}{s - s_0^{scatt}} + \sum_{\alpha} \frac{g_i^{\alpha} g_j^{\alpha}}{m_{\alpha}^2 - s} \right) f_{A_0}(s) \tag{8.17}$$

The parameters m_α are the physical poles of the K-matrix and g_i^α are the coupling constants and are fixed from $\pi\pi$ scattering data [28]. The parameters f_{ij}^{scatt} and s_0^{scatt} are also fixed. The symbol f_{A_0} is defined as:

$$f_{A_0}(s) = \frac{1 - s_{A_0}}{s - s_{A_0}} \left(s - s_A \frac{m_\pi^2}{2} \right) \tag{8.18}$$

where s_{A_0} and s_A are also fixed parameters.

The production vector is defined as:

$$P_j(s) = f_{1j}^{prod} \frac{1 - s_0^{prod}}{s - s_0^{prod}} + \sum_{\alpha} \frac{\beta_\alpha g_j^\alpha}{m_\alpha^2 - s} \tag{8.19}$$

where β_α are the complex production couplings and f_{1j}^{prod} are some production parameters; these are not fixed from scattering data. The fixed parameters can be seen in Table 8.2. These are parameters which describe the scattering process, where dedicated measurements are used to fix the values [28], so are therefore fixed in the amplitude and mixing fits described in this thesis. The parameters relating to the production mechanism (β_α and f_{1j}^{prod}) can depend on the experiment. These parameters are fixed in the mixing fit based on initial time-integrated fits described in this chapter. We also do not consider the initial $j = 5 = \eta\eta'$ state since the mass of the η' is 957.78±0.06 MeV/c^2. The $\eta\eta'$ threshold and the pole mass are both beyond the kinematic range of the $\pi\pi$ production, hence there is little sensitivity to the associated parameters f_{15}^{prod} and β_5. This is therefore not included as a variation in

m_α	$g^\alpha_{\pi^+\pi^-}$	$g_{K\overline{K}}$	$g^\alpha_{4\pi}$	$g^\alpha_{\eta\eta}$	$g^\alpha_{\eta\eta'}$
0.65100	0.22889	-0.55377	0.00000	-0.39899	-0.34639
1.20360	0.94128	0.55095	0.00000	0.39065	0.31503
1.55817	0.36856	0.23888	0.55639	0.18340	0.18681
1.21000	0.33650	0.40907	0.85679	0.19906	-0.00984
1.82206	0.18171	-0.17558	-0.79658	-0.00355	0.22358
	f^{scatt}_{11}	f^{scatt}_{12}	f^{scatt}_{13}	f^{scatt}_{14}	f^{scatt}_{15}
	0.23399	0.15044	-0.20545	0.32825	0.35412
s^{scatt}_0	s_{A_0}	s_A			
-3.92637	-0.15	1			

Table 8.2: Fixed parameters used in the K-matrix formalism as inputs to the amplitude model. Taken from Ref. [28].

the fit when considering systematic uncertainties and alternative amplitude models, since it is nonphysical.

8.3 LASS parametrisation

The $K\pi$ S-wave systems are poorly understood and there is no clear theoretical guidance as to the correct description of these systems in the isobar model. Therefore the LASS parametrisation [29] is used to describe the $K\pi$ S-wave. The $K_0^*(1430)^+$ and $K_0^*(1430)^-$ contributions are described empirically based on scattering data from the LASS collaboration. The parametrisation is constructed from a Breit-Wigner term for the $K_0^*(1430)$ and a non-resonant component that has an effective range and introduces a phase shift:

$$\mathcal{A}_{K\pi_{L=0}}(s) = R\sin\delta_R e^{i\delta_R} e^{i2\delta_F} + F\sin\delta_F e^{i\delta_F} \tag{8.20}$$

where

$$\delta_R = \phi_R + \tan^{-1}\left[\frac{M\Gamma(m^2_{K\pi})}{M^2 - m^2_{K\pi}}\right] \tag{8.21}$$

and

$$\delta_F = \phi_F + \cot^{-1}\left[\frac{1}{aq} + \frac{rq}{2}\right] \tag{8.22}$$

The parameters R, ϕ_R, F, ϕ_F and the amplitudes and phases of the resonant and non-resonant components. The parameters a and r are the scattering length and effective interaction length; q is the momentum of the spectator particle in the $K\pi$ rest frame. M and Γ are the mass and width of the resonant term. Note that if the phase δ_F is set to zero, the relativistic Breit-Wigner propagator is recovered. The scatting length and effective range and the $K_0^*(1430)$ mass were measured at the LASS experiment.

The phases δ_R and δ_F depend on $m^2_{K\pi}$. The phase motion (δ_R and δ_F) as a function of the $K\pi$ invariant mass, is the same in elastic scattering and decay processes, in the absence of final state interactions (the isobar model) [62]. This motivates the LASS parametrisation. The studies of $K\pi$ scattering data at the LASS experiment show that the S-wave is elastic up to a threshold. The LASS parametrisation preserves the phase behaviour measured in $K\pi$ scattering.

8.4 Default Amplitude Model

In the default amplitude model, as mentioned, the decay is described through resonant and non-resonant components. Relativistic Breit-Wigner propagators are used for the parameterisation of $\mathcal{T}_r$ (from Equation 8.6), apart from the $\rho(770)$ which is described by the Gournaris-Sakurai. The $K\pi$ S-wave is described by the LASS amplitude and the $\pi\pi$ S-wave is described by the K-matrix formalism. These amplitudes are added coherently to the amplitudes of the resonant decays:

$$\mathcal{T}(D^0 \to K^0_S\pi^+\pi^-) = c_K\mathcal{T}_{\pi\pi} + c_L\mathcal{T}_{K\pi} + \sum_r c_r\mathcal{T}_r \tag{8.23}$$

where $\mathcal{T}_{K\pi}$ is the LASS amplitude, $\mathcal{T}_{\pi\pi}$ is the K-matrix amplitude and $\mathcal{T}_r$ are the amplitudes of the resonances, c_L, c_K and c_r are the complex coefficients. Note that the real and imaginary components of the $\rho(770)$ Gournaris-Sakurai amplitude are fixed to 1 and 0 respectively as a reference value.

The free parameters of the mixing fit are the D^0 lifetime $\tau(D^0)$, the mixing parameters x and y and the real and imaginary parts of the complex coefficients c_r. As discussed in Section 2.3, *CP*-violation can be added to the model by defining the mixing parameters differently for D^0 and $\bar{D}^0$ initial states by $x_{CP} \pm \Delta x$ and $y_{CP} \pm \Delta y$. The parameters Δx and Δy can be transformed into the physical parameters $|q/p|$ and ϕ mentioned previously in Section 2.3, which give a measurement of time-dependent *CP*-violation in mixing. The fit can be run with the assumption of *CP*-conservation (where $\Delta x = \Delta y = 0$ are fixed) or with *CP*-violation allowed where these parameters are allowed to float in the mixing fit.

In order to constrain the choice of amplitude model in the mixing fit, a time-independent fit is first performed; the time-integrated fits are limited to decay time $t < \tau(D^0)$ in this region mixing is negligible and will not affect the amplitude model. The initial base-line model is that reported by Belle and BaBar collaborations [20]. Resonances may be removed or added and the optimal amplitude model is chosen such that subsequent additions of resonances do not significantly improve the fit quality, defined at the negative log likelihood ($-2\log(\mathcal{L})$). These time-integrated fits can also be used to fix the S-wave shape parameters and some of the masses and widths of the resonances, which are fixed in the final mixing fit. These parameters are: the masses and widths of the resonances; the K-matrix shape parameters β, f^{prod} and s_0^{prod} and the LASS shape parameters R, ϕ_R, F, ϕ_F, a and r. Initially, the parameters are set to those from Belle and BaBar [20], and the masses and widths to the PDG values [78].

The initial time-integrated fit procedure is as follows:

1. Perform initial time-integrated fit with the complex coefficients of the Breit-Wigner amplitudes of the resonant components free to get reasonable agreement with data.
2. Fix coefficients of resonances and free the LASS shape parameters and complex coefficients.
3. Fix the LASS coefficients and parameters and free the K-matrix $f_{12...14}^{prod}$ and s_0^{prod} parameters and the K-matrix complex coefficient.
4. Fix the K-matrix f^{prod} parameters and free the K-matrix parameters $\beta^{1...4}$.

The final time-integrated fit shown in this section has the parameters fixed to those above and the Breit-Wigner coefficients free. The mixing fit has those parameters above fixed to the values from the time-integrated fit; the Breit-Wigner amplitudes and the mixing parameters and the D^0 lifetime are free. In the K-matrix formalism the parameters f_{11}^{prod} are fixed to the value from the Belle and BaBar model [20], f_{15}^{prod} is fixed to 0 and β_5 is 0. The choices made in the amplitude model development such as the values of the masses and widths and the S-wave shape parameters are varied when assessing systematic uncertainties. Some alternative models are listed in Chapter 10 (Table 10.1). There is a significant improvement in the fit quality when adding the $K^*(1680)^+$ resonance, hence this is added to the nominal model. Alternative models may be considered for systematic studies as discussed in Chapter 10.

Some of the masses and width do not converge close to the PDG value in the initial time-integrated fits and therefore cannot be released and are fixed to the PDG value. This is due to limitations in such cases where the resonances have very low fit fractions, the widths are wide and hence hard to separate from other contributions or particularly narrow and hence hard to normalise with the required precision. Others can be floated in the initial time-integrated fit and are fixed to those values in the mixing fit. The effect of fixing the masses and widths and the shape parameters on the mixing parameters is assessed by varying these parameters according to the limited knowledge of their true values, and assigning a systematic uncertainty. The masses and widths compared to the PDG values can be seen in Table 8.3. The S-wave shape parameters which are fixed from the initial time-integrated fits are shown in Table 8.4.

It can also be instructive to evaluate the fit fractions of the individual non-resonant and resonant contributions. The fit fraction is defined as the integral over the Dalitz plot of a single amplitude squared normalised by the integral over the Dalitz plot of the square of the coherent sum of all amplitudes:

$$FF_j = \frac{\int \left|a_j e^{i\phi_j}\mathcal{M}_j\right|^2 dm_{12}^2 dm_{13}^2}{\int \left|\sum_k a_k e^{i\phi_k}\mathcal{M}_k\right|^2 dm_{12}^2 dm_{13}^2} \tag{8.24}$$

where the amplitude $\mathcal{M}_j$ is defined in Equations 8.4 and 8.5, the complex coefficient is $a_j e^{i\phi_j}$ where a_j and ϕ_j are real. The complex coefficient is either defined in terms

Resonance	Mass	Width	Mass (PDG)	Width (PDG)
$\rho(770)$	777.67 ± 0.63	139.06 ± 1.49	775.26 ± 0.25	147.8 ± 0.9
$\omega(782)$	783.37 ± 0.21	8.49 (fixed)	782.65 ± 0.12	8.49 ± 0.08
$f_2(1270)$	1275.5 (fixed)	186.7 (fixed)	1275.5 ± 0.8	186.7 ± 2.5
$\rho(1450)$	1465 (fixed)	400 (fixed)	1465 ± 0.25	400 ± 60
$K^*(892)^\pm$	894.51 ± 0.08	47.63 ± 0.16	891.66 ± 0.26	50.8 ± 0.9
$K_2^*(1430)^\pm$	1427.3 (fixed)	100 (fixed)	1427.3 ± 1.5	100 ± 2.2
$K^*(1410)^\pm$	1414 (fixed)	232 (fixed)	1414 ± 15	232 ± 21
$K^*(1680)^\pm$	1684.61 (fixed)	322 (fixed)	1718 ± 18	322 ± 110
$K_0^*(1430)^\pm$	1469.87 ± 0.79	345.31 ± 7.65	1425 ± 50	270 ± 80

Table 8.3: Masses and widths of the resonances used in the amplitude model: values used in the mixing fit compared with the PDG values [78]. Units are in MeV and measured uncertainties are statistical only. The strategy for fixing and releasing parameters is described in the text.

of the real and imaginary components or the amplitude and phase. The sum of the fit fractions does not necessarily equal unity due to the possible constructive and destructive interference effects between the amplitudes. These constructed and destructive interferences are quantified by the interference fit fractions which are given in Chapter 11 for the time-dependent mixing fit.

The fit fraction for the interference term between two resonances is given by:

$$FF_{jl} = \frac{\int a_j a_l^* e^{i\phi_j} e^{-i\phi_l} \mathcal{M}_j \mathcal{M}_l^* dm_{12}^2 dm_{13}^2}{\int \left|\sum_k a_k e^{i\phi_k} \mathcal{M}_k\right|^2 dm_{12}^2 dm_{13}^2} \tag{8.25}$$

The fit fractions for the time-integrated fit are shown in Table 8.5. The largest contributions are the $K^*(892)^-$ resonance with a fit fraction of 56.1%, the $\rho(770)$ resonance (18.40%) and the $\pi\pi$ S-wave contribution (11.91%). The full list of resonances, and the values of the complex coefficients from the time-integrated fits, are used to generate the amplitude model for the toy studies discussed in the following chapter.

The fit projections for the time-integrated fit are shown in Figure 8.1. These show the projections of the individual components in the m_{12}^2, m_{13}^2 and m_{23}^2 systems. The left plots are on a linear scale and the right plots are on a log scale in order to increase the visibility of components with low fit fractions and other details of the model. Various features of the amplitude model can be observed such as the

System	Parameter	Real	Imaginary
$\pi\pi$ S-wave	β_1	-1.028 ± 0.070	3.466 ± 0.052
	β_2	14.799 ± 0.078	2.806 ± 0.084
	β_3	42.985 ± 1.054	-18.906 ± 0.619
	β_4	-1.859 ± 0.250	-7.059 ± 0.200
	f_{11}^{prod}	-4.702 (fixed)	-6.472 (fixed)
	f_{12}^{prod}	-14.288 ± 0.478	12.456 ± 0.181
	f_{13}^{prod}	-18.123 ± 0.425	-22.279 ± 0.804
	f_{14}^{prod}	-10.306 ± 0.329	-14.780 ± 0.068
$K\pi$ S-wave	F	0.817 ± 0.015	
	ϕ_F	0.077 ± 0.002	
	R	1 (fixed)	
	ϕ_R	-3.135 ± 0.022	
	a	0.224 ± 0.001	
	r	-21.286 ± 0.124	

Table 8.4: S-wave shape parameters of the K-matrix ($\pi\pi$) and LASS ($K\pi$) parameterisation from the initial time-integrated fit, to be fixed in the mixing fit. The strategy for fixing the parameters is described in the text.

Resonance	Fit Fraction (%)
$\rho(770)$	18.40
$\omega(782)$	0.44
$f_2(1270)$	0.87
$\rho(1450)$	0.15
$\pi^+\pi^-$ S-wave	11.91
$K^*(892)^-$	56.05
$K_2^*(1430)^-$	2.01
$K^*(1410)^-$	0.19
$K^*(1680)^-$	<0.1
$K_0^*(1430)^-$	8.21
$K^*(892)^+$	0.26
$K_2^*(1430)^+$	<0.1
$K^*(1410)^+$	0.26
$K_0^*(1430)^+$	<0.1

Table 8.5: Fit fractions for the time-integrated fit quantifying the contributions of individual amplitudes.

constructive and destructive interference of the components and the peak of the $\pi\pi$ S-wave in the m^2_{23} projection. The two-dimensional Dalitz distributions can be seen in Figure 8.2. In the time-integrated fits, all detector effects are accounted for as discussed in Chapter 7 and the background is modelled by the data-driven approach as discussed in the following section.

8.5 Combinatorial background model

The final time-dependent amplitude fit includes a single component to account for background contamination. The fit requires background distributions for the D^0 decay time and two-dimensional Dalitz plane; these are extracted using sWeighted data. The sPlot method is discussed in Chapter 5. The sWeights are extracted from a fit to the D^0 mass in the window 1805 MeV $< m(D^0) <$ 1925 MeV for the single-tagged samples and from a fit to the $\delta m(D^0)$ distribution with a cut of 1844 MeV $< m(D^0) <$ 1884 MeV for the double-tagged samples. The sWeights are extracted separately for each year, K^0_S type and by single and double-tagged samples. The D^0 mass is computed with the momenta refitted with the K^0_S mass constraint (see the further details on Decay Tree Fitter in Chapter 5). The Dalitz variables are computed with the momenta refitted with the K^0_S and D^0 mass constraints, and the D^0 decay-time is with the K^0_S mass constraint only. Note that while the sWeights are necessary to extract the background distributions, they are not used directly in the final amplitude fit.

An alternative method of extracting the background distributions would be to use the $m(D^0)$ sideband data, this assumes that the combination of lower and upper mass sidebands represents the distribution of the full mass range. The sWeight technique is preferable since is statistically disentangles the signal and background components for the full mass range. It is instructive to compare the resulting distributions from the lower and upper mass sidebands with those from the sWeight method, these can be seen in Figures 8.3 and 8.4. The sideband background distribution may be used to assess a systematic uncertainty since there are some differences in the background shape such as in the $K^*(892)^-$ peak. While some differences are observed, they are expected from the different kinematic regions in the lower and upper sidebands, and

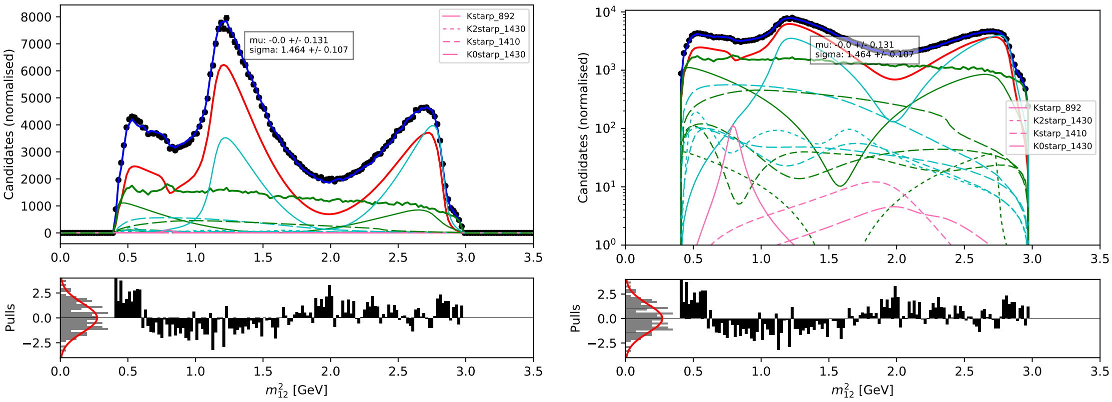

(a) m^2_{12} projection, linear scale.　　(b) m^2_{12} projection, log scale.

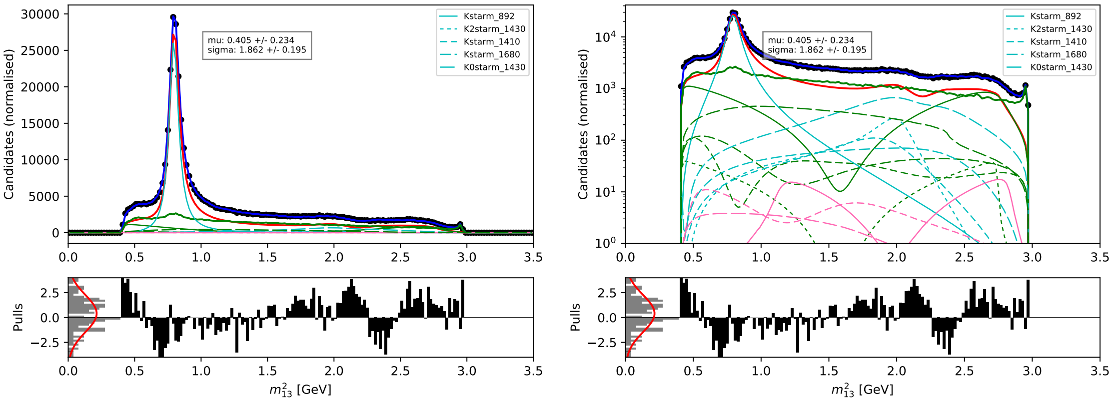

(c) m^2_{13} projection, linear scale.　　(d) m^2_{13} projection, log scale.

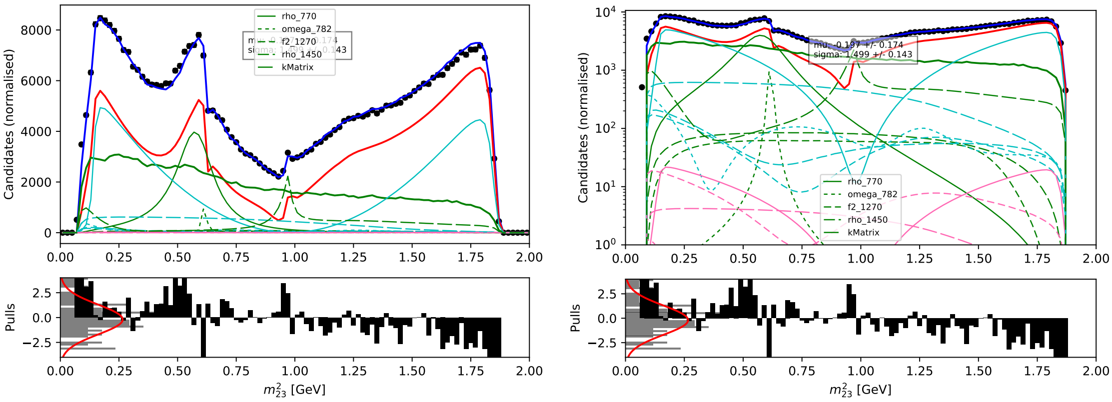

(e) m^2_{23} projection, linear scale.　　(f) m^2_{23} projection, log scale.

Figure 8.1: An initial time-integrated fit Dalitz coordinate projections: data (black points), the background PDF (green line), signal PDF (red line). The dotted and dashed lines show the projections of the individual components of the amplitude model: pink, blue and green lines show resonant components in the m^2_{12}, m^2_{13} and m^2_{23} systems respectively. The components are computed from the square of the amplitude of each contribution scaled by its fit fraction. Plots show the single-tagged K^0_S (LL) 2016 sample.

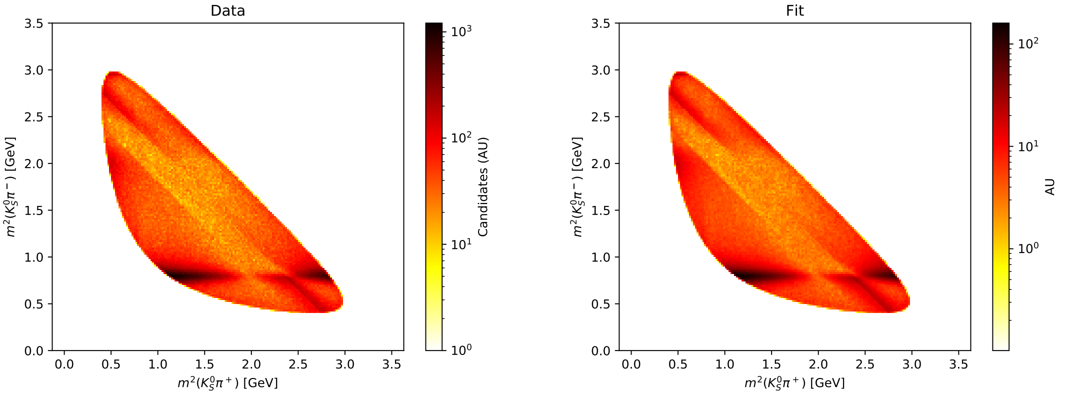

(a) Data (b) Fit model

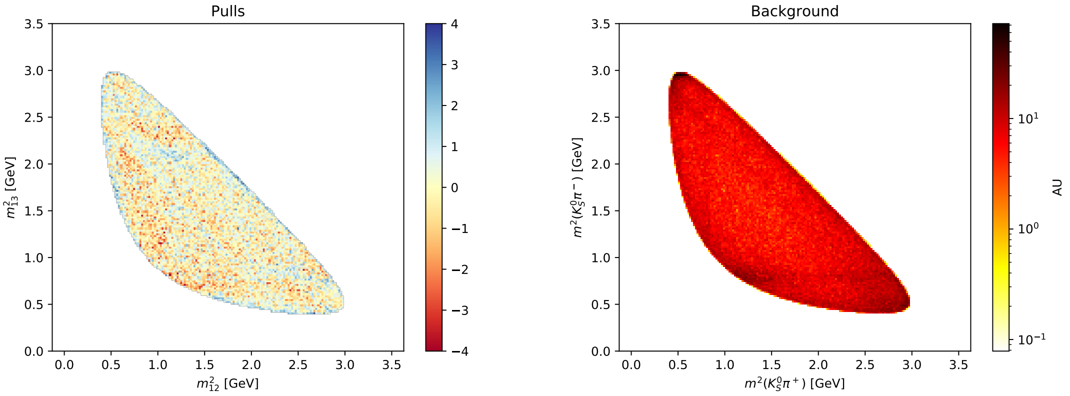

(c) Pulls (d) Background model

Figure 8.2: Two dimensional distributions of the Dalitz variables for the initial time-integrated fit: data, fit model, pulls ([fit - data]/error) and background model. Plots show the single-tagged K_S^0 (LL) 2016 sample.

in general the backgrounds are stable using these two different approaches.

The background distributions derived from the sWeight method are subject to statistical fluctuations from the limited size of the data sample. To suppress the effect of these fluctuations, the distributions of the Dalitz variables and decay-time are smoothed. The smoothing is achieved by taking a weighted average of the central bin and neighbouring bins. In the nominal model the neighbouring bins take 0.5 of the weight of the central bin, this is varied to assess a systematic uncertainty. In the two dimensional Dalitz histogram, the diagonal bins and the neighbouring bins are included in the average.

8.6 Mistag

The initial flavour of the D^0 ($\bar{D}^0$) is tagged by the charge of the muon in the single-tagged sample and the charge of the pion in the double-tagged sample. The single-tagged sample contains a fraction of events which have been reconstructed with a muon of the opposite charge, hence the initial flavour of the D^0 is assigned incorrectly. This is mainly due to cases where a genuine D^0 is paired with a random muon from another decay. A second possible source of mistagged candidates arised from poorly reconstructed muons which have the incorrect charge assignment. The mistag component therefore needs to be quantified and accounted for in the amplitude model. The mistag fraction is defined as the fraction of cases with random muons; half of which are assigned the wrong flavour since half have the correct flavour by chance.

A mistagged candidate differs from signal because the measured D^0 decay-time would not be correct since the D^0 is paired with a random muon, and for half of the mistagged candidates the flavour information would be incorrect. Therefore the mistag component $\mathcal{P}_{mt}$ (Equation 8.1) then consists of half with the Dalitz coordinates switched and half with them the same since for half the D^0 would be assigned the correct flavour by chance. For the total component $\mathcal{P}_{mt}$, the amplitude is calculated with the time-dependent and mixing parameters fixed since we do not know the correct decay-time of the D^0 and we neglect the contribution of this to the mixing.

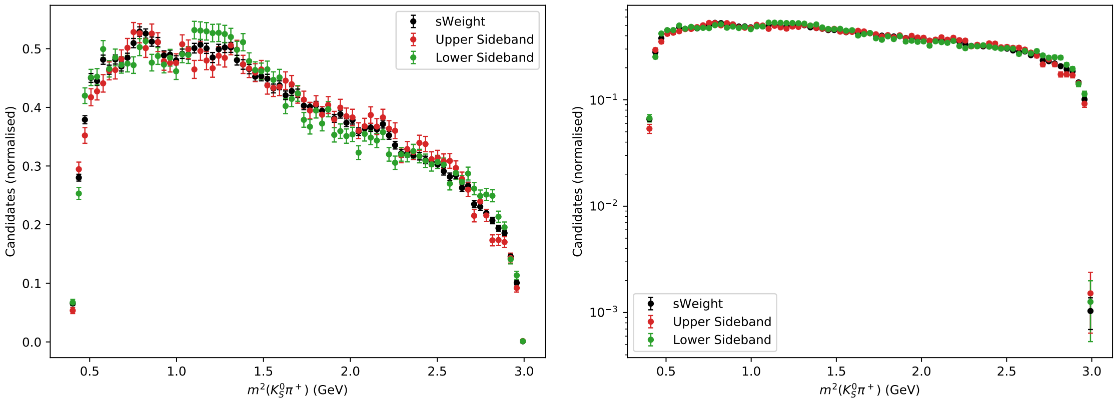

(a) m^2_{12} projection linear scale (b) m^2_{12} projection log scale

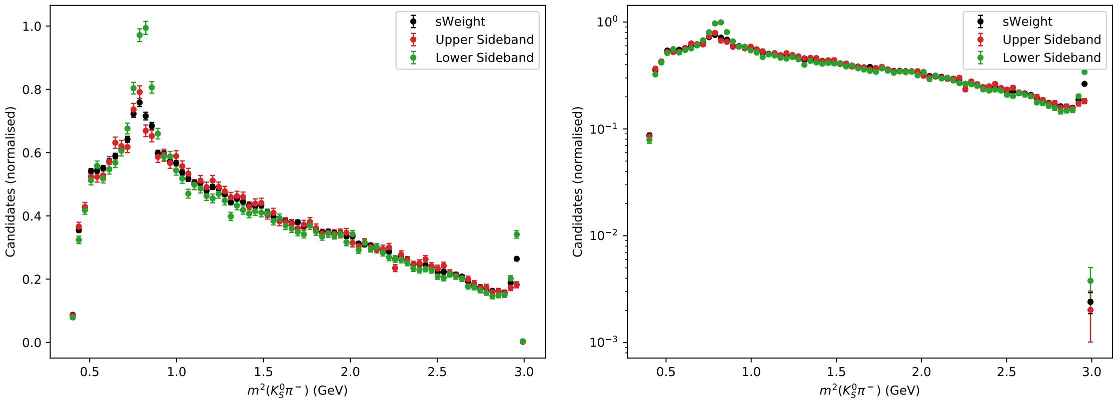

(c) m^2_{13} projection linear scale (d) m^2_{13} projection log scale

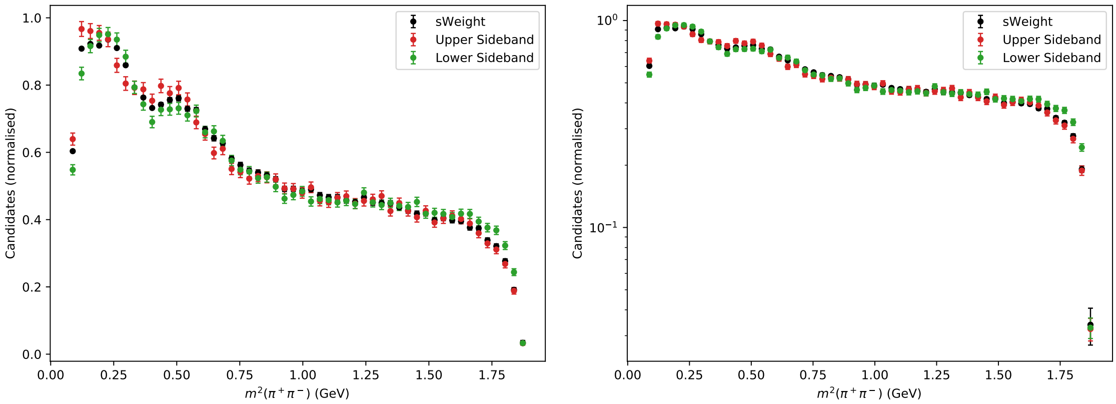

(e) m^2_{23} projection linear scale (f) m^2_{23} projection log scale

Figure 8.3: Comparison of the background distributions for, lower and upper $m(D^0)$ sidebands and background sWeighted data for the Dalitz variables m^2_{12}, m^2_{13} and m^2_{23}. Single-tagged K^0_S (LL) 2018 sample.

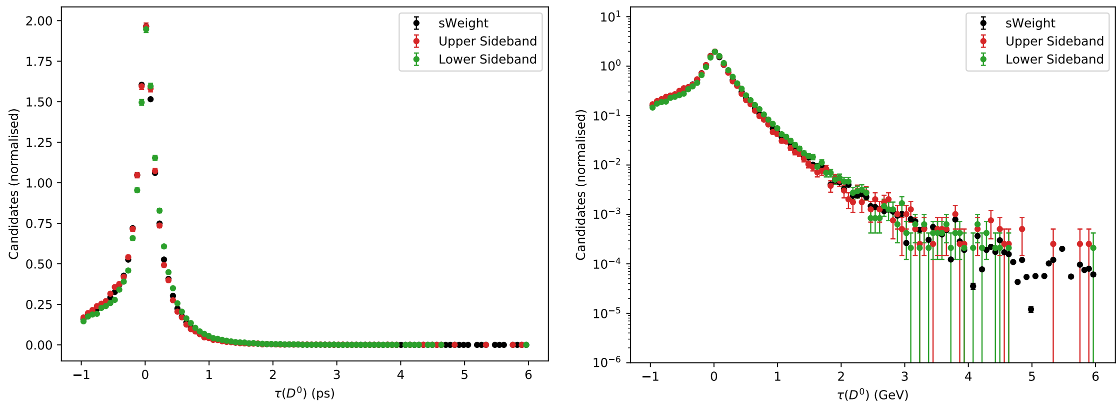

(a) $\tau(D^0)$ linear scale

(b) $\tau(D^0)$ log scale

Figure 8.4: Comparison of the background distributions for, lower and upper $m(D^0)$ sidebands and background sWeighted data for the D^0 decay-time. Single-tagged K^0_S (LL) 2018 sample.

In previous analyses [9, 71] the mistag probability was estimated using the double-tagged sample. The method is to compare the two tags - that from the pion (which we know to be correct as only genuine D^* candidates will peak in the δm distribution) and that from the muon. The fraction of candidates where the pion and muon tags disagree can be used to quantify the mistag fraction in general, which is then assumed to be the same for single and double-tagged cases. However we know that the mistag fraction as determined from the double-tagged sample may not be the same as that in the single-tagged sample. This is due to the mistag probability depending on the B meson decay vertex quality, which is different between the two modes due to the presence of the soft pion. In the double-tagged sample, the vertex fit is performed with the additional track from the soft pion which effects the vertex quality since we have more information from the additional track. The additional particle in the double-tagged case therefore lead to significantly more precise measurements of the D^0 production vertex than the single-tagged. This means that the single-tagged and double-tagged samples may not have the same fraction of candidates where a random muon passed the selection requirements to be combined with the D^0 (D^*) candidate.

As an alternative method, the two-body control channel $D^0 \to K^-\pi^+$ can be used where one can estimate the mistag both through the double-tagged sample as well as directly from the single-tagged by comparing the signs of the muon and kaon (after accounting for doubly-Cabibbo suppressed and mixing effects). The mistag probability can therefore be directly derived from the $D^0 \to K^-\pi^+$ channel, where the yields of right-sign ($D^0 \to K^-\pi^+$) and wrong-sign ($D^0 \to K^+\pi^-$) samples are calculated from $K\pi$ invariant mass fits. The mistag fraction is then defined as:

$$\text{Mistag} = \frac{n_{WS}}{n_{WS} + n_{RS}} \tag{8.26}$$

where n_{RS} and n_{WS} are the signal yields in the right-sign and wrong-sign samples respectively. This ratio is subtracted by the known values of mixing and doubly-Cabibbo suppressed decay as a function of D^0 decay-time [7].

In a previous LHCb analysis of semi-leptonic $D \to hh$ decays, it was found that the mistag probability was dependent on D^0 decay-time. However this has been shown to be as a result of some trigger (selection) requirements which were not used in this analysis, whereas using the selection requirements for this analysis means the mistag probability is reasonably flat as a function of decay-time. Figure 8.5 presents a comparison between different scenarios of trigger and preselections on this control channel in 2017 and 2018 data-taking years. With the trigger requirements from the A_Γ analysis, there is an enhanced dependency of the mistag fraction on decay-time (red points). However with the trigger and preselections used in this analysis, the time dependency is flattened (blue points). The trends are consistent among the data-taking years.

The $D^0 \to K\pi$ sample is processed with a similar selection to the one described in Chapter 5, with different MVAs used for K^0_S LL and DD samples. To confirm that the mistag probability in the $D^0 \to K\pi$ channel is representative of the $K^0_S\pi^+\pi^-$ channel, both double-tagged samples were analysed and compared. To match the kinematics of the two-body and three-body decays, the Gradient Boosted reweighter [77] is used. Kinematic variables including the B decay vertex χ^2, transverse momentum of the μ and D^0 and psuedorapidity of the D^0 are used as training variables. Figure 8.6 shows the mistag probability as a function of D^0 decay time separately for D^0 and $\bar{D}^0$. This mistag probability with the K^0_S (LL) MVA model is lower than that with the K^0_S (DD) model. The mistag fraction is derived separately for K^0_S LL and DD samples since the effect of the MVA is different. It is found to be 0.120 ± 0.013% for the LL sample and 0.291 ± 0.01% for DD. This shows good agreement between the

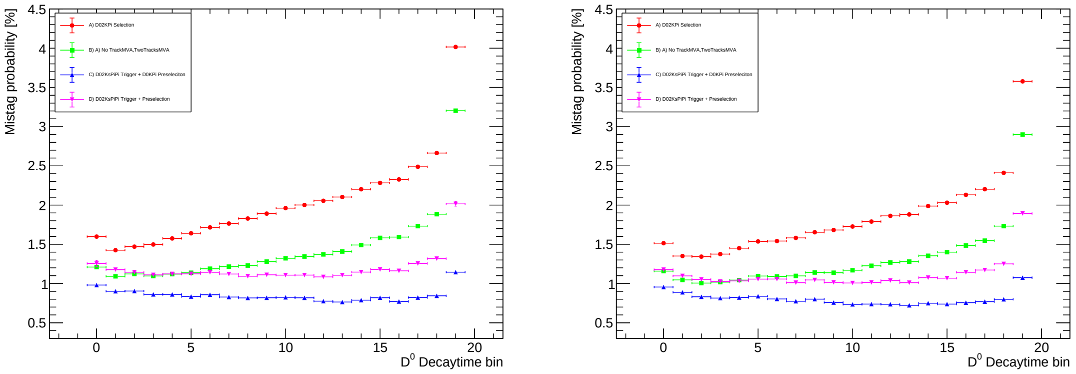

Figure 8.5: Comparison of the mistag probability in the single-tagged sample with different trigger requirements and preselections for 2017 (left), and 2018 (right). Plots taken from Ref. [36].

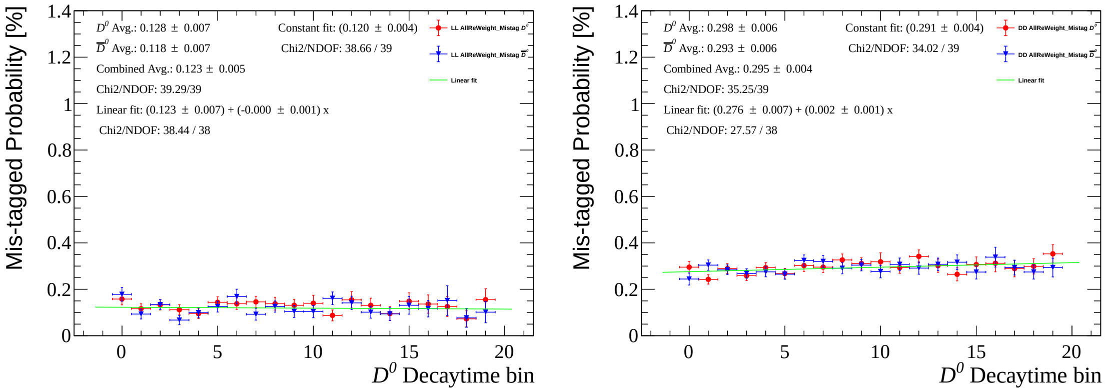

Figure 8.6: Mistag probability as a function of D^0 decay time separately for D^0 and $\bar{D}^0$ in the reweighted $D^0 \to K^-\pi^+$ sample. MVA selection is applied with the model trained on K_S^0 (DD) sample (left) and K_S^0 (LL) sample (right). Plots taken from Ref. [36].

red and blue points (D^0 and $\bar{D}^0$).

8.7 Fit model summary

In summary, the default amplitude model is described by the coherent sum of amplitudes of the D^0 decay through intermediate resonances and non-resonant components. The $\pi\pi$ S-wave is described by the K-matrix formalism and the $K\pi$ S-wave by the LASS amplitude. Relativistic Breit-Wigner propagators are used for the parameterisation of the resonant amplitudes, apart from the $\rho(770)$ which is described by the Gounaris-Sakurai model. The free parameters of the final mixing fit are the mixing parameters x and y, the D^0 lifetime $\tau(D^0)$ and the real and imaginary parts of the complex coefficients (c_r in Equation 8.23). Other model parameters are fixed based on preliminary time-integrated fits. These are the masses and widths of the resonances, the K-matrix shape parameters β, f^{prod} and s_0^{prod} as well as the LASS shape parameters, ϕ_R, F, ϕ_F, a and r. Fit stability and fit bias studies have been performed and are discussed in the following chapter. The background model is derived from a data-driven approach by taking the Dalitz and decay-time distributions from the sWeighted histograms and applying a smoothing factor. The choice of amplitude model has a number of associated systematic uncertainties on the measured values of x and y which will be discussed in detail in Chapter 10.

CHAPTER 9

Toy studies

One method to test the bias and stability of the mixing fit is the use of so-called ‘pseudo-experiments’ or toy data samples. This involves generating pseudo-data samples with realistic simulations of backgrounds and detector effects. By fitting ensembles of these ‘toy’ data samples, potential fit biases, expected statistical precision and several sources of systematic uncertainty can be assessed in a statistically sound manner. The toy data samples are generated using the signal model derived from the initial time-integrated fit, the detector effects derived from simulation and the backgrounds derived from the data-driven approach described in Chapters 7 and 8. When generating these pseudo-data samples the true values of the mixing (and other) parameters are exactly known. Hence, unlike in a fit to real data, we can directly compare the fit results with the truth, and thereby draw conclusions about potential fit biases, or issues with evaluating parameter uncertainties.

The process of generating the toy data samples is done within the GooFit [73] framework and proceeds as follows. The signal model is the time-dependent amplitude model described in Chapter 8, with the complex coefficients of the amplitudes and shape parameters of the amplitude model taken from the initial time-integrated fit. The phase-space acceptance is included in the amplitude model. The decay-time is defined within the mixing formalism discussed in Chapter 2, corrected for the decay-time acceptance and convoluted with the decay-time resolution.

Events are generated in a two-stage process. Events are first generated according to some simple PDF (uniform in phase-space, exponential in decay-time). Then we perform an accept/reject procedure to match the desired PDF, where events are randomly selected according to the distribution of the underlying PDF, taking into account the non-uniform acceptance and resolution. The background component is added by generating candidates with decay time and Dalitz variables randomly assigned using as a PDF the background distributions from sWeighted data.

The per-candidate signal probabilities are assigned, to mimic the case for real data. This is done by background and signal candidates being assigned a D^0 mass (according to some suitable PDF), the value of which can be translated into a signal/background probability. The D^0 mass is approximated as a uniform background and signal Gaussian distribution; from this the per-candidate signal probabilities are assigned to each event in the toy data sample.

The number of signal and background candidates is selected to match the yields in data. For the study in this section we consider one data sub-sample only, using the sample specific background and detector effects. The effect of mis-tagged initial D^0 flavour is also included, by randomly flipping the muon charge and exchanging the Dalitz coordinates m^2_{12} and m^2_{13} for the appropriate fraction of signal candidates. The outcome is a pseudo-dataset which mimics the real data in terms of detector effects and backgrounds, and can be used as an input sample for the fitter validation studies. Example fit projections for a single toy can be seen in Figure 9.1. The decay-time projections are in Figure 9.2 and the two-dimensional Dalitz plots are in Figure 9.3.

9.1 Fit bias studies

The fit validation procedure consists of generating and fitting an ensemble of $\mathcal{O}(100)$ toy data sets. The ensemble of fits leads to a corresponding ensemble of fit parameter values and uncertainties, which can be compared to the true (generated) values. This can be done either directly (by plotting the distribution of the fitted parameter for the ensemble of fits) or by inspecting the derived pull quantity (defined as [fit value - generated value]/uncertainty). The distribution of the fitted parameter

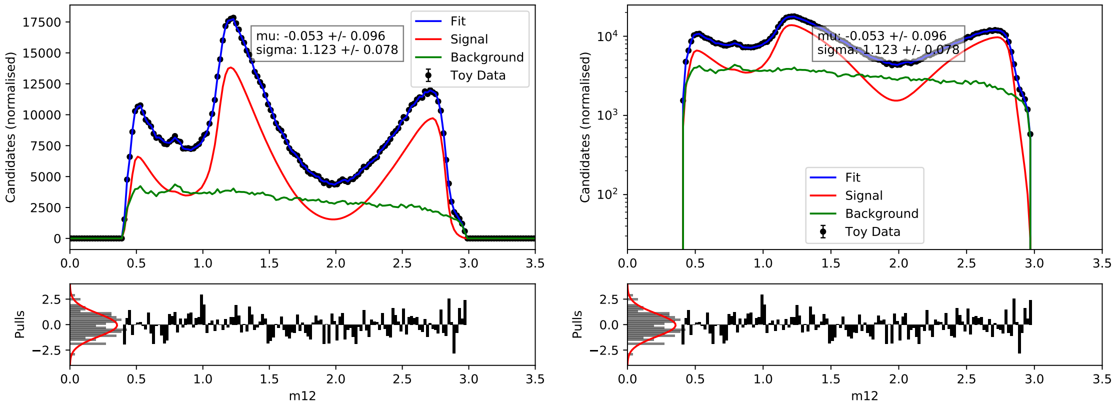

(a) m_{12}^2 projection, linear scale. (b) m_{12}^2 projection, log scale.

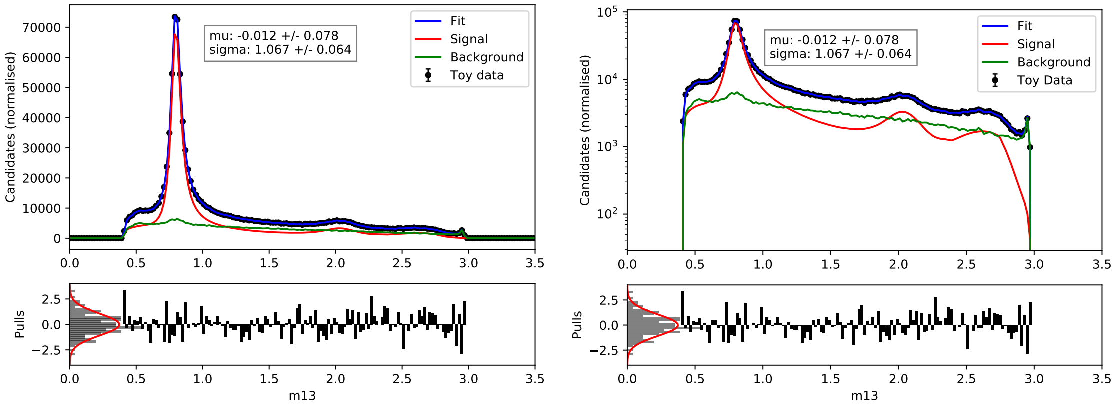

(c) m_{13}^2 projection, linear scale. (d) m_{13}^2 projection, log scale.

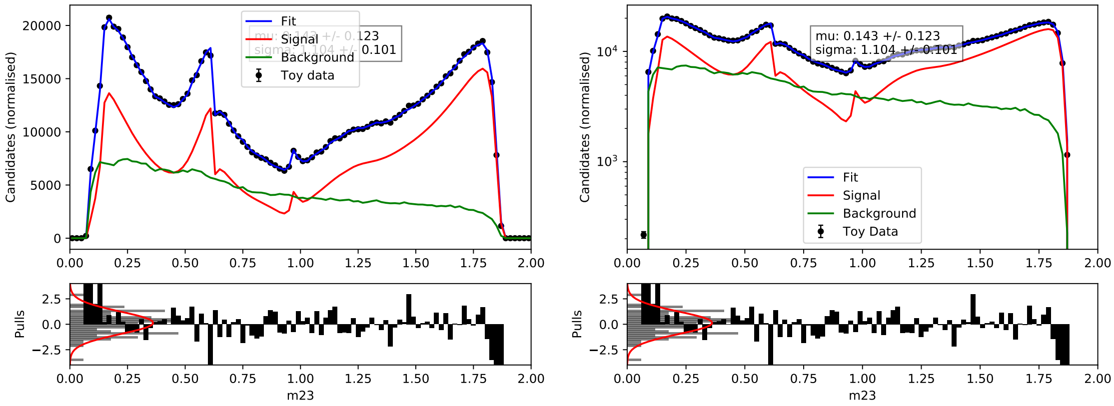

(e) m_{23}^2 projection, linear scale. (f) m_{23}^2 projection, log scale.

Figure 9.1: One-dimensional projections of the Dalitz coordinates for one example toy fit, linear scale on the left, and log scale on the right: toy data (black points), fit model (blue line), signal (red line) and background (green line).

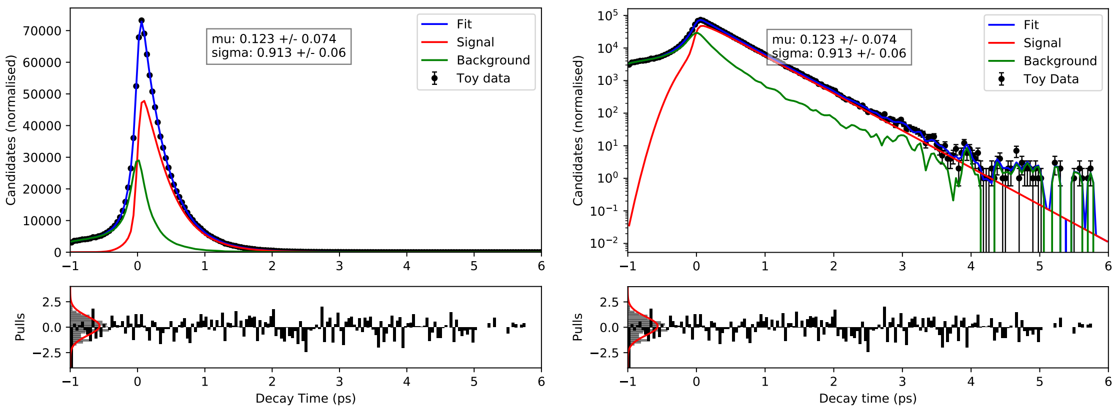

(a) $\tau(D^0)$ projection, linear scale.

(b) $\tau(D^0)$ projection, log scale.

Figure 9.2: Distribution of the decay-time for one example toy fit, linear scale on the left and log scale on the right: toy data (black points), fit model (blue line), signal (red line) and background (green line).

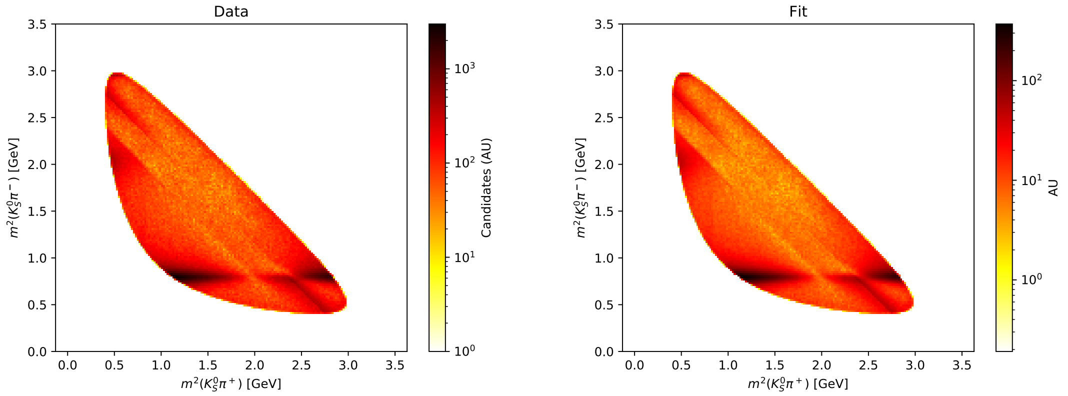

(a) Toy Data

(b) Fit model

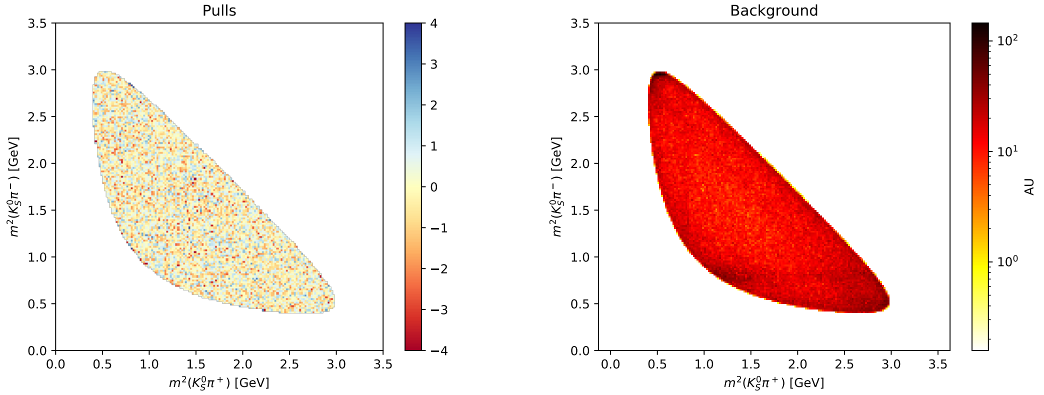

(c) Pulls

(d) Background model

Figure 9.3: Two dimensional distributions of the Dalitz variables for an example toy fit: data, fit model, pulls and background model.

(in particular x, y and $\tau(D^0)$ but also the complex coefficients of the amplitudes of the resonant and non-resonant components) or the pulls can then be fitted with a Gaussian. The mean of the pull distribution can be used to quantify potential fit biases, where an unbiased fit has a mean consistent with zero. The uncertainties reported in the fit are accurate if the width of the corresponding pull distribution is consistent with unity. Ensembles are generated with different values of the mixing parameters, corresponding to a grid of 9 (x, y) points. The grid is distributed as $[\mu - \sigma,\ \mu,\ \mu + \sigma]$ for x and y where μ and σ are the mean and uncertainty of the current world average values ($x = 0.51^{+0.12}_{-0.14}\%$ and $y = 0.63 \pm 0.07\%$ at the time of writing [27]). The generated D^0 lifetime is set to the PDG value of $\tau(D^0) = 0.4101$ ps.

9.1.1 Results

The largest ensemble is generated with the world average values of the mixing parameters and has ∼250 pseudo-experiments. The distributions of x, y and $\tau(D^0)$ are shown in Figure 9.4. The fitted value of x is 0.540 ± 0.014% with a spread (width of the Gaussian) of 0.216 ± 0.012%. For y the fitted value is 0.649 ± 0.009% with a spread of 0.141 ± 0.007%. One can also examine the distribution of parameter errors reported by the fit: these are $\sigma(x) = 0.1998 \pm 0.0001\%$ and $\sigma(y) = 0.1694 \pm 0.0001\%$. These are evaluated from the fits in Figure 9.5. The results for the D^0 lifetime are: $\tau(D^0) = 0.41 \pm 0.00$ ps and $\sigma(\tau) = 0.0005691 \pm 0.0000001$ ps. The sensitivities can then be estimated as 0.22% for x and 0.14% for y, these are consistent with the blinded fits to data reported in the following chapters.

The pulls of the parameters of interest x, y and $\tau(D^0)$ are shown in Figure 9.6. The pulls are fitted with a Gaussian, the mean of which is consistent with zero which gives confidence that the fitter is unbiased. The width is equal to unity within uncertainties for x and $\tau(D^0)$ and is below unity for y; this gives confidence that the fitter is not underestimating the uncertainties. Figure 9.7 shows the pulls of all the free parameters of the fit including the magnitude and phases of the resonant and non-resonant components of the amplitude model. This shows there may be some biases in the measurement of the amplitude model. We assess the affect of the amplitude model on the final measured values of x and y and assign a corresponding systematic uncertainty as discussed in more detail in Chapter 10.

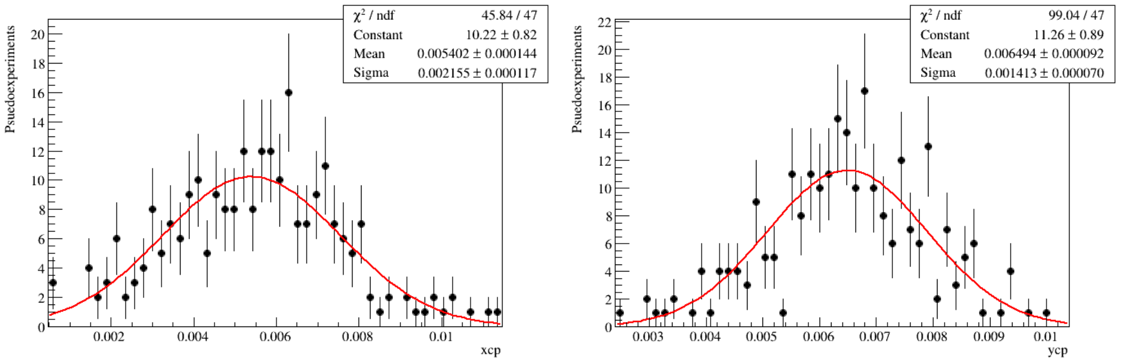

Figure 9.4: Distributions of the fitted values of x and y from the ensemble of pseudo-experiments, fitted with a Gaussian. The mean is consistent with the generated value, the width is consistent with the uncertainties given in the text.

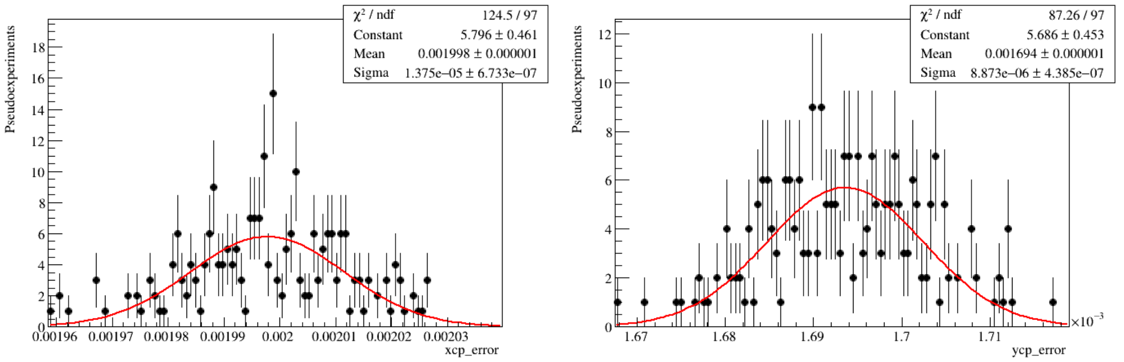

(a) Fit uncertainties x

(b) Fit uncertainties y

Figure 9.5: Distribution of the fit uncertainties for x and y for an ensemble of pseudo-experiments fitted with a Gaussian (red line) mean and width are shown in the stats box.

9.1.2 Alternative values of mixing parameters

The procedure described in the previous section is repeated for the nine combinations of x and y mentioned previously. The results are summarised in Table 9.1. In this case the toy samples are representative of one data sub-sample only (single-tagged K^0_S (LL) 2016). The bias is expressed as the mean of the distribution of the pulls of the given parameter and, as can be seen from the results in the table, there are no significant biases in x and y. Figure 9.8 visualises the results in Table 9.1, where the mean and the width of the Gaussian are shown as the black bars, the corresponding uncertainties are shown by the blue and orange bars. Again, the width is slightly larger than unity which may suggest that the uncertainties are

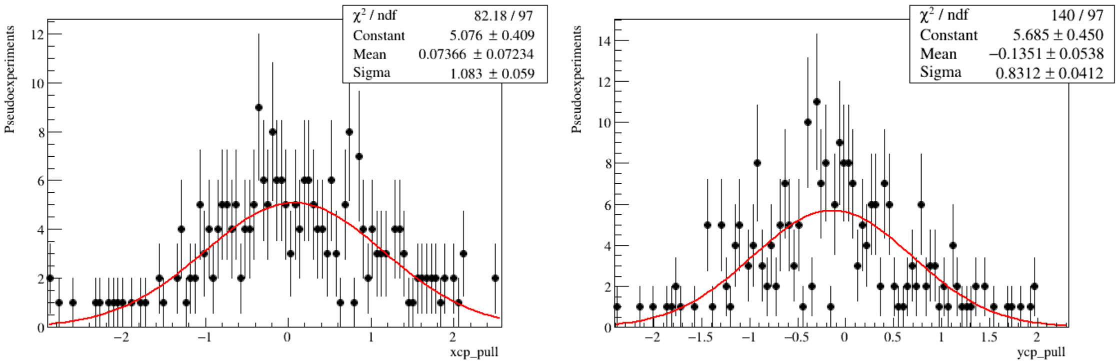

(a) Pull of x (b) Pull of y

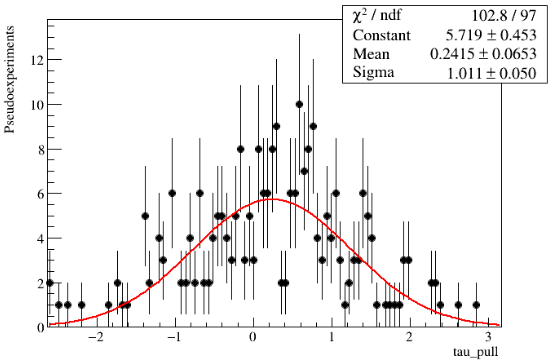

(c) Pull of $\tau(D^0)$

Figure 9.6: Distribution of the pulls of x, y and $\tau(D^0)$ for an ensemble of pseudo-experiments fitted with a Gaussian (red line) mean and width are shown in the stats box.

underestimated in the fit. This can be accounted for with a systematic uncertainty which will be discussed in the following chapter.

9.2 Toy fits with *CP*-violation allowed

As mentioned in Chapter 8, the mixing fit can be run with the assumption of no *CP*-violation or with *CP*-violation allowed. *CP*-violation may be included in the mixing fit by allowing different values of the mixing parameters for D^0 and $\bar{D}^0$ by $x_{CP} \pm \Delta x$ and $y_{CP} \pm \Delta y$. These are related to the *CP*-violation parameters $|q/p|$ and ϕ as follows (repeated from Equations 2.51-2.54 for convenience):

$$x_{CP} = \frac{1}{2}\left[x\cos\phi\left(\left|\frac{q}{p}\right| + \left|\frac{p}{q}\right|\right) + y\sin\phi\left(\left|\frac{q}{p}\right| - \left|\frac{p}{q}\right|\right)\right] \tag{9.1}$$

$$\Delta x = \frac{1}{2}\left[x\cos\phi\left(\left|\frac{q}{p}\right| - \left|\frac{p}{q}\right|\right) + y\sin\phi\left(\left|\frac{q}{p}\right| + \left|\frac{p}{q}\right|\right)\right] \tag{9.2}$$

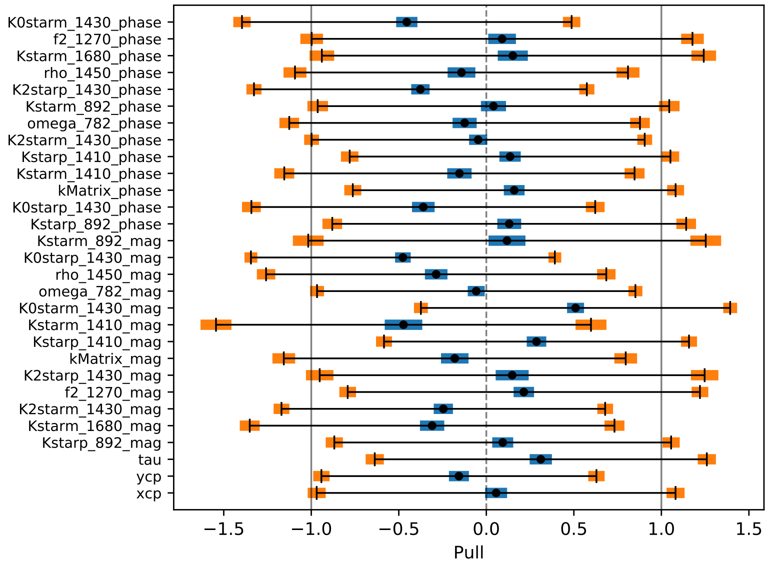

Figure 9.7: Plot showing the pulls of the free parameters of the fit, x, y and $\tau(D^0)$ and the magnitude and phases of the amplitudes of the resonant and non-resonant components. The pulls are fitted with a Gaussian, the back bars are the mean and width of the Gaussian, the uncertainties on the mean and width are the blue and orange bars respectively. The toys are generated with world average values of the mixing parameters.

$$y_{CP} = \frac{1}{2}\left[y\cos\phi\left(\left|\frac{q}{p}\right| + \left|\frac{p}{q}\right|\right) - x\sin\phi\left(\left|\frac{q}{p}\right| - \left|\frac{p}{q}\right|\right)\right] \tag{9.3}$$

$$\Delta x = \frac{1}{2}\left[y\cos\phi\left(\left|\frac{q}{p}\right| - \left|\frac{p}{q}\right|\right) - x\sin\phi\left(\left|\frac{q}{p}\right| + \left|\frac{p}{q}\right|\right)\right] \tag{9.4}$$

In fits with *CP*-violation in mixing allowed, the parameters Δx and Δy are allowed to float, as opposed to the nominal no *CP*-violation case in which these are fixed to zero. For this study, toy datasets are generated with no *CP*-violation ($\Delta x = \Delta y = 0$) but the *CP*-violation parameters Δx and Δy are allowed to float in the mixing fit. Similarly to the previous toy studies, the pulls of the parameters of interest are fitted with a Gaussian, the mean of width is consistent with zero and the width is consistent with unity within uncertainties. The distribution of the pulls is shown in Figure 9.9 and the fitted parameters in Figure 9.10. This gives confidence that this method of measuring time-dependent *CP*-violation in mixing is valid and unbiased.

In summary, pseudo-experiments are used to validate the fitter, assess fit biases and give confidence in the evaluation of the errors reported in the fit. While we use

Generated		Bias	
x (%)	y (%)	$\Delta x/\sigma(x)$	$\Delta y/\sigma(y)$
0.51	0.63	-0.131 ± 0.141	0.226 ± 0.131
0.51	0.56	-0.204 ± 0.156	0.189 ± 0.152
0.51	0.70	-0.204 ± 0.156	0.189 ± 0.152
0.37	0.63	0.129 ± 0.083	-0.245 ± 0.068
0.37	0.56	-0.013 ± 0.126	0.004 ± 0.144
0.37	0.70	0.045 ± 0.100	-0.330 ± 0.114
0.63	0.63	-0.040 ± 0.171	-0.122 ± 0.084
0.63	0.56	0.058 ± 0.076	-0.060 ± 0.083
0.63	0.70	0.059 ± 0.207	-0.042 ± 0.139

Table 9.1: Summary of the results of running fits over ensembles of toy pseudo-experiments, generated at a range of different mixing parameter values covering the world average values $\pm 1\sigma$. The bias is expressed as the shift in the parameter divided by the statistical uncertainty $\sigma(x, y)$.

toys for this purpose, one can also assess sources of systematic uncertainties through the use of dedicated toys. For example, one can inject some effect into the toy generation and then fit with the regular mixing fit model which has been developed. This will give an idea whether injecting some effect into the toy data biases the results of the parameters of interest. For example, we neglect the phase-space resolution in the fit model when in reality this is non-zero. One can assess the effect of neglecting the phase-space resolution by generating toy datasets with the phase-space resolution included and then fitting with a model in which it is not. This shows the effect of neglecting it in the fit. This will be discussed in more detail in Chapter 10.

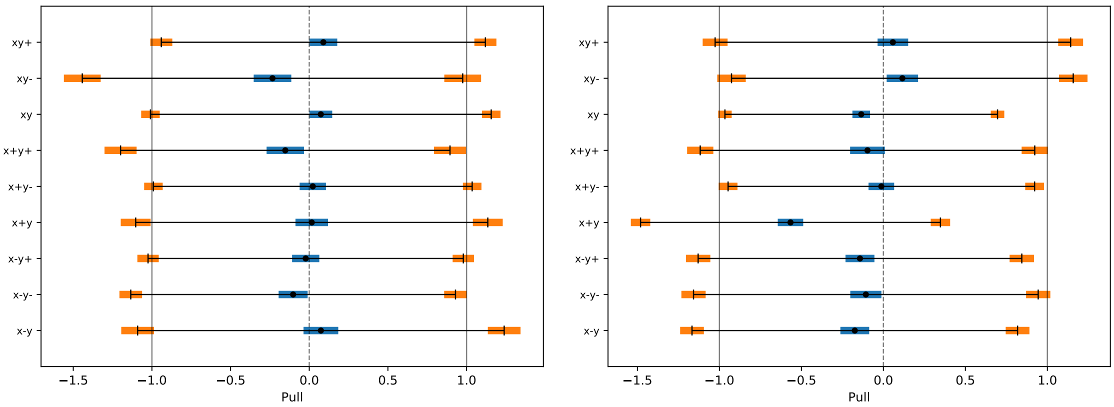

(a) Pull of x

(b) Pull of y

Figure 9.8: Visualisation of the results of ensembles of pseudo-experiments for different values of the mixing parameters. The black bars show the mean and width of the Gaussian fitted to the pulls of x (left) and y (right), the blue and orange bars are the corresponding uncertainties from the Gaussian fit.

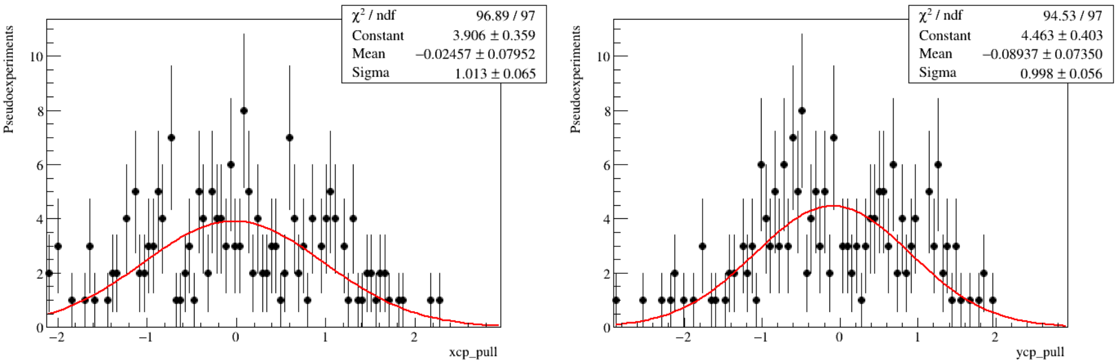

(a) Pull of x_{CP}

(b) Pull of y_{CP}

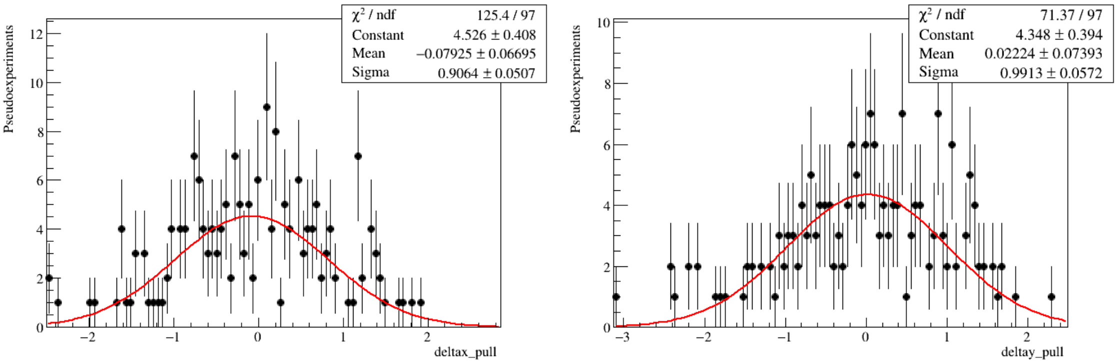

(c) Pull of Δx

(d) Pull of Δy

Figure 9.9: Distribution of the pulls of the parameters x_{CP} and y_{CP} and Δx, Δy for an ensemble of pseudo-experiments where CP-violation is allowed.

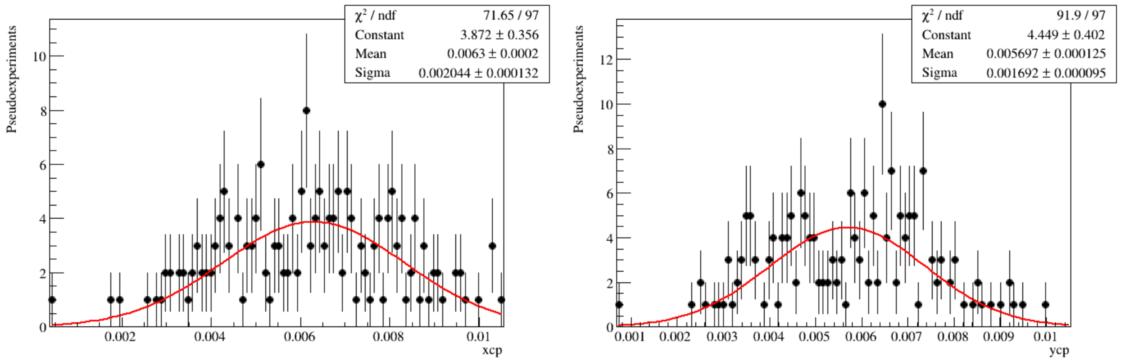

(a) Distribution of x_{CP} (b) Distribution of y_{CP}

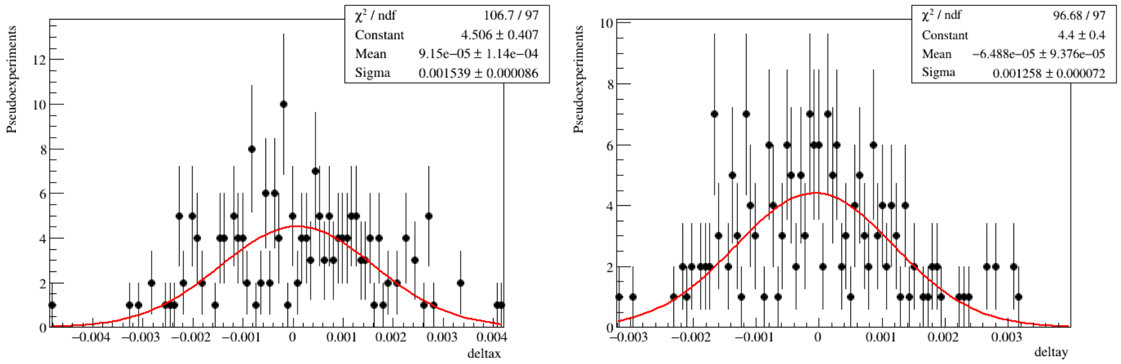

(c) Distribution of Δx (d) Distribution of Δy

Figure 9.10: Distribution of the parameters x_{CP} and y_{CP} and Δx, Δy for an ensemble of pseudo-experiments where CP-violation is allowed.

CHAPTER 10

Systematic Uncertainties

This analysis relies on several inputs and assumptions including: detector effects from simulation, contributions from background and mistagged candidates, and the amplitude model. These have an impact on the measured values of the mixing parameters which must be quantified through systematic uncertainties. These can be evaluated in different ways and are discussed in detail in this chapter. One method is to make some variation to the analysis inputs or method and rerun the fit to data, any shift in the parameters of interest can be considered a systematic uncertainty. This is typically evaluated by a resampling technique in which any fixed parameters or inputs can be randomly resampled (assuming a Gaussian distribution) taking into account their uncertainties and correlations. The fit to data is rerun $\mathcal{O}(100)$ times and the shift on the measured value of the mixing parameters is fitted with a Gaussian - this can be used to quantify the spread or shift on the measured parameter. Alternatively one can use dedicated toys to evaluate certain systematic uncertainties. Realistic toy data can be generated with some variation to the inputs and the fit run, any shift in the measured value of x and y can be quantified as a systematic uncertainty. Systematic uncertainties on the mixing parameters are extracted from various sources including the fit model used in the amplitude fit and the detector and resolution effects which are derived from simulation.

10.1 Fit model

The measurement of the mixing parameters in the model-dependent analysis relies on a choice of amplitude model. The amplitude model is necessary to associate particular candidates with particular decay processes (eg. Cabibbo-favoured, doubly-Cabibbo-suppressed followed by mixing), based on their Dalitz coordinates. The measurement is therefore sensitive to the details of this model, such as the set of intermediate resonances considered, and their specific amplitude descriptions. For example, the choice of intermediate resonances is based on that from Belle and BaBar [20] and verified by adding alternative resonances until there is not a significant improvement in the fit quality. In addition some of the model parameters are fixed from the initial time-integrated fits described in Chapter 8. The limited knowledge of these parameter values must be propagated to the final measurement in the form of a systematic uncertainty. Therefore we consider several modifications to the amplitude model and evaluate the effect of these on the measured value of the mixing parameters.

The amplitude of the $D^0 \to K^0_S\pi^+\pi^-$ decay is given in Equation 8.6 and is repeated here for convenience:

$$A_r(m_+^2, m_-^2) = F_D^{(L)}(q, q_0) \times F_r^{(L)}(p, p_0) \times Z_L(\Omega) \times \mathcal{T}_r(m) \tag{10.1}$$

The factor $Z_L(\Omega)$, describing the angular dependence, is given in the Zemach formalism. The form factors $F_D^{(L)}$ and $F_r^{(L)}$ describe the decay $D \to rc$ and $r \to ab$ respectively and are parameterised by the Blatt-Weisskopf form factors in which the Blatt-Weisskopf meson radius enters the amplitude formalism as described in Chapter 8. The dynamical function $\mathcal{T}_r$ relies on different resonance lineshapes; the choice of resonances which enter the model and of the lineshape used to describe the resonance are the model-dependence of this analysis. In this analysis an initial list of resonances is selected based on previous investigations of this channel [20, 71]. The model is refined through an initial investigation with time-integrated fits to the data. The goal is to achieve as good a fit quality as possible while excluding resonances without significant fit fractions which favours a simpler model. Therefore it is possible that alternative models can be found which have similarly good agreement with data. The amplitude fit can be repeated with several different models by adding resonances, and corresponding systematic uncertainties assigned to account for the corresponding variation in the mixing parameters. Systematic uncertainties are also evaluated to account for the fact that the masses and widths of the resonances as well as the S-wave shape parameters are fixed based on those values from the PDG and from initial time-integrated fits.

10.1.1 Blatt-Weisskopf radii

Since there is no strong consensus on the values of the Blatt-Weisskopf meson radii, we use a data-driven approach to select the fixed values used in the default fit, and to determine a reasonable range of variation for systematic studies. As a first step, we repeat the (blinded) mixing fit several hundred times with the values of the two Blatt-Weisskopf radii randomly resampled for each fit, according to a uniform 2D distribution. From this we pick a nominal value around the minimum of the FCN$= -2\log(\mathcal{L})$ and a suitable width to vary for the systematic uncertainty; this is chosen to be 1.0 GeV^{-1} for the meson radii for the intermediate resonance and 2.25 GeV^{-1} for the D^0 meson. We repeat the fit $\mathcal{O}(100)$ times with the meson radii resampled with a Gaussian distribution of this mean. The width is chosen to be 0.25 GeV^{-1} which is assumed from the first step to be a reasonable variation. This ensures that the variation of FCN in the resampled fits is reasonable, and therefore that the corresponding variations observed in the mixing parameters can be interpreted as the systematic uncertainties on these quantities. The variations of the mixing parameters is estimated as the mean of the Gaussian when fitting the shifts for the individual fits. Using this method the variations in the mixing parameters are 4.216×10^{-5} for x and 9.434×10^{-5} for y. This corresponds to 1.92% of the statistical uncertainty for x and 5.05% of the statistical uncertainty for y.

10.1.2 Choice of resonances

The initial amplitude model is chosen based on previous studies such as Ref. [20] and [71]. It is then fixed based on the initial time-integrated fits described in Chapter 8. The default model is chosen by adding components until subsequent

	$\Delta x(\%)$	$\Delta x/\sigma(x)$	$\Delta y(\%)$	$\Delta y/\sigma(y)$	$\Delta(-2\log(\mathcal{L}))$
Remove $K^*(1410)^+$	-0.007	-0.037	-0.086	-0.550	+219
Add $K^*(1680)^+$	0.086	0.442	0.038	0.247	-40.4
Both above	0.014	0.074	-0.096	-0.616	+147
Remove f_{14}^{prod}	0.098	0.505	-0.159	1.022	+12,262

Table 10.1: Alternative amplitude models. The significance of the shift is expressed by dividing by the statistical uncertainty. The last column is defined such that a negative value corresponds to an improved fit quality.

additions do not strongly affect the fit quality, defined as the minimum negative log likelihood $-2\log(\mathcal{L})$. As such, there may be a number of alternative models with extra components that have comparable fit quality to the default fit. Therefore adding resonances will provide a reasonable measure of the stability of the mixing parameters versus the model choice. The model-dependence of this analysis enters through this choice of amplitude model. Alternative models are investigated by repeating the mixing fit by adding and removing terms in the S-wave parameterisation, and by adding or removing resonances. As seen in Table 10.1, when $K^*(1410)^+$ and f_{14}^{prod} are removed, the fit quality ($-2\log(\mathcal{L})$) is significantly worsened. By construction, the default model has the minimum reasonable resonance content, so only variations with additional resonances are considered. In addition the β_5 and f_{15}^{prod} correspond to $\pi\pi$ scattering terms which are not physical in this case. The metric used to determine the reasonable variation in fit quality is the negative log likelihood. Using this metric we added the $K^*(1680)^+$ resonance as discussed in Chapter 8 and choose not to include the other variations as a systematic since they result in a significant degradation of the fit quality - this can be seen by the positive numbers corresponding to an increase in the negative log likelihood. We may choose to consider other variations, however previous studies (Refs. [20, 71, 78] show no other viable options. Therefore we chose not to assign a systematic uncertainty to the model choice, and propose that the variations of the shape parameters and masses and widths discussed in the subsequent sections account for any discrepancies between the amplitude model and the data.

10.1.3 Masses and widths of resonances

As mentioned in Chapter 8, the masses and widths of the resonances in the amplitude model are fixed from initial time-integrated fits or to the values from the PDG, and summarised in Table 8.3. The fit is run $\mathcal{O}(100)$ times with the parameters resampled assuming a Gaussian distribution with the mean and the width taken from the central value and uncertainty from the time-integrated fit (or PDG). For those parameters floated in the initial time-integrated fit, the correlations are taken into account. The values fixed from the PDG are assumed to be uncorrelated. This gives a value for the systematic uncertainty on x as 2.014×10^{-4} and 1.692×10^{-4} for y which corresponds to 23.3% of the statistical uncertainty for x and 22.2% of the statistical uncertainty for y.

10.1.4 S-wave shape parameters

Similarly, the shape parameters of the LASS $K\pi$ S-wave and the K-matrix parametrisation for the $\pi\pi$ S-wave are fixed in the mixing fit to those values from initial time-integrated fits. To account for the uncertainties on these parameters the mixing fit is repeated $\mathcal{O}(100)$ times with the parameters resampled according to the fit values from the time-integrated fits and the uncertainties. The correlations are taken into account separately for the K-matrix and LASS parameters since these are fixed in separate time-integrated fits. Those parameters fixed in separate time-integrated fits are assumed to be uncorrelated. The corresponding shifts in x and y are found by fitting the difference in the measured values of x and y in the (blinded) nominal fit and those with the S-wave parameters resampled. Those from the K-matrix and LASS are added in quadrature to obtain a systematic uncertainty to account for the uncertainties in the fixed S-wave shape parameters. This gives a value of 5.66×10^{-5} for x and 8.87×10^{-5} for y. This corresponds to a 6.62% of the statistical uncertainty for x and 11.77% of the statistical uncertainty for y.

10.1.5 Total fit model uncertainty

In summary the contributions to the total fit model systematic uncertainty are: the fixed value of the Blatt-Weisskopf meson radii which enter in the form factors

Source	Systematic uncertainty x [10^{-5}]	y [10^{-5}]
Blatt-Weisskopf radii	5	11
Masses and widths	23	22
S-wave parameters	6	9
Total	24.4	26.2
Statistical	85.5	75.4

Table 10.2: Contributions to the total fit model systematic uncertainty.

described in the amplitude model; uncertainties due to the limited knowledge of the masses and widths and the S-wave shape parameters which are fixed from initial time-integrated fits. These are listed in Table 10.2. The contributions are added in quadrature to obtain the total fit model uncertainty. Alternative amplitude models which give comparable fit quality by adding resonances and S-wave parameters are neglected as a systematic uncertainty since the model is by construction minimal, and there are no obvious remaining candidates for additional resonances to be included.

10.2 Signal and background mass models

As mentioned previously (chapters 4 and 8), there are inputs to the mixing fit which are derived from a fit to the D^0 invariant mass (δm) for the single-tagged (double-tagged) samples. These are: the per-candidate signal probabilities, used to set appropriate fractions of signal and background PDFs for each event; and the background PDF which is derived using a data driven approach using the sWeights from the mass fits. As shown in Chapter 5, the fits are of good quality with no obvious missing or mismodelled components. However there is still an associated systematic uncertainty on the choice of parameterisation in the mass fit. This is evaluated by repeating the mixing fit with new signal and background probabilities and sWeights derived using alternative functions for the signal and background components in the $m(D^0)$ and δm fits.

For the $m(D^0)$ signal PDF a Gaussian and a Crystal Ball function is used instead of the nominal model of a Gaussian and a Johnson SU. A Crystal Ball is a PDF which consists of a Gaussian core and a power-law low end tail. This is commonly used in high energy physics to model processes which take into account non-Gaussian tails such as radiative effects. For the alternative background distribution, an exponential function is used instead of a Chebychev polynomial. These alternative $m(D^0)$ fits are found to give comparable fit quality (χ^2/ndof) compared to the nominal model.

New inputs of signal probabilities and background PDFs are produced using the alternative models discussed above. The mixing fit is repeated with the new sets of signal probabilities and background distributions. For the signal $m(D^0)$ model, the mixing parameters are shifted by $\Delta x = -7.96 \times 10^{-6}$ and $\Delta y = -2.21 \times 10^{-4}$; this corresponds to 0.41% of the statistical uncertainty for x and 14% for y. For the alternative background model, the shift in x is $\Delta x = 4.99 \times 10^{-4}$ and $\Delta y = 4.73 \times 10^{-4}$ for y; this corresponds to 25.7% of the statistical uncertainty for x and 30.4% of the statistical uncertainty for y. These shifts can be assigned as symmetric systematic uncertainties for the mixing parameters.

There is also a finite statistical precision associated with the mass fits; even with a perfect fit model we only have limited ability to statistically disentangle the signal and background components. This will give some uncertainty on the shape of the background PDF which uses the sWeights and which is accounted for and described in the next section. However there is also some uncertainty associated with the per-event signal probabilities which are used in the final mixing fit. The statistical precision associated with the mass fit is much smaller than the corresponding systematic from alternative models, hence it is neglected.

10.3 Background PDF

As mentioned in Chapter 8, the PDFs used to model the decay-time and Dalitz distributions in the mixing fit are derived from a data-driven approach. sWeights are derived from the $m(D^0)$ and δm fits as described in previous chapters (5 and 8) and are used to statistically disentangle the signal and background distributions. The histograms in Dalitz variables and decay-time are weighted with the background sWeights. The background PDFs used in the mixing fit therefore have limited statistical precision due to the limited statistics used to construct the histograms. To assess the effect this has on the final measurement, the fit is repeated 100 times with each bin (in the histograms in Dalitz variables and decay-time) randomly resampled assuming Poisson statistics using a Gaussian of mean N (number of events in each bin) and width $\sqrt{N}$. The resulting shift in the mixing parameters x and y can be assigned as a systematic uncertainty. The corresponding systematic uncertainties are 3.526×10^{-4} for x (16% of the statistical uncertainty), and 4.921×10^{-4} for y (26% of the statistical uncertainty).

For the nominal fit, the histograms are smoothed with a smoothing factor which averages over neighbouring bins of the histogram. The smoothing factor corresponds to the weight assigned to the neighbouring bins in the averaging: ie. a smoothing factor of 0 would mean the neighbouring bins are not included, 1 would mean they are assigned equal weight in the averaging and 0.5 would mean they are assigned half the weight of the central bin in the averaging. For the default fit the smoothing factor is 0.5. The background histograms are a two-dimensional histogram in Dalitz coordinates and a one-dimensional histogram in decay-time. For the two-dimensional histogram, the diagonal neighbouring bins are included in the average. To account for the possible effect on the smoothing on the measured value of the mixing parameters, the fit is repeated with reasonable variations of the smoothing parameter from 0.1 to 0.9. The shifts in the measured value of x and y can then be assigned as a systematic uncertainty. The systematic uncertainties are found to be 4.96×10^{-5} for x (2.25% of the statistical uncertainty) and 1.42×10^{-4} for y (7.59% of the statistical uncertainty).

An additional check to assess the effect of the background histogram PDF is to use sidebands for the histogram as opposed to the nominal method of background sWeights. Comparisons between the lower and upper sidebands and the sWeights have been done and are shown in Chapter 8, these are found to be in reasonable agreement.

10.4 Mistag

The mistag fraction is derived as described in Section 8.6 and accounts for the small fraction of $D^0 \to K^0_S\pi^+\pi^-$ decays which have been assigned the wrong flavour given they were reconstructed with a muon of the wrong charge. The affect of using this fixed fraction needs to be accounted for as a systematic uncertainty. This is done by repeating the mixing fit with variations of the mistag fraction of $\pm 1\sigma$. The shifts caused by the two fits are added in quadrature and assigned as a systematic uncertainty. They are found to be 0.746×10^{-5} for x and 8.11×10^{-5} for y, corresponding to 0.87% of the statistical uncertainty for x and 10.8% for y.

10.5 Phase-space acceptance

Variations in acceptance over the two-dimensional Dalitz plane are modelled using a parametrisation derived from Monte Carlo, as described in Section 7.1. A common model is used for all data samples with parameters extracted independently for each one. The resulting parameters have an uncertainty due to the finite statistics of the Monte Carlo sample, these must be accounted for when assigning a systematic uncertainty to the mixing parameters. In addition there is a potential systematic uncertainty associated with the limited agreement of the Monte Carlo with data, largely mitigated against by the reweighting procedure described in Chapter 6. Finally, we need to take into account the quality of fit of the parametrisation used to model the efficiency variation from MC.

The limited MC statistics is taken into account by repeating the mixing fit 100 times with the phase-space efficiency parameters resampled assuming Gaussian behaviour and taking into account the uncertainties and correlations between the parameters. The shift in x and y with respect to the nominal (blinded) fit is fitted with a Gaussian, the width can be assigned as a systematic uncertainty. The shift in x is 1.607×10^{-4} and for y it is 9.749×10^{-5}. These correspond to 7.30% of the statistical uncertainty for x and 5.22% for y. The fit quality of the efficiency parametrisation is assessed by inspecting the χ^2/ndof; this is close to 1 for all samples so we can neglect this as it is smaller than the effect from the MC statistics. For any fits with $\chi^2/\mathrm{ndof} > 1$ we may inflate the uncertainties on the parameters when resampling; however in this case we neglect this since the fits have χ^2/ndof close to unity.

10.6 Decay-time acceptance

The procedure of including the decay-time acceptance in the mixing fit is described in Section 7.2. This is through a correction factor which is derived from Monte Carlo simulation. A systematic uncertainty is assigned associated to the limited Monte Carlo statistics. As with the other MC inputs, the effect of this statistical uncertainty is determined by running an ensemble of mixing fits with the decay time correction parameters resampled based on their central values and uncertainties. The associated systematic uncertainties are 1.475×10^{-5} for x (0.67% of the statistical uncertainty) and 3.39×10^{-5} for y (1.81% of the statistical uncertainty).

There is, in addition, a known disagreement seen in the decay-time acceptance description as shown in Section 7.2. This can be accounted for through the use of dedicated toys where we generate data with a more realistic decay-time acceptance model and then fit with the nominal fit model. This will be assessed either as a systematic or by improving the description of the decay-time acceptance in GooFit.

10.7 Decay-time resolution

The decay-time resolution is derived from simulation and is described by a set of parameters of a triple Gaussian as described in Section 7.3. Similarly these parameters have corresponding uncertainties caused by the limited size of the Monte Carlo samples. In order to assess this, the mixing fit is repeated 100 times with the parameters resampled according to their central values, uncertainties and correlations. The spread of the measured values of the mixing parameters is assigned as a systematic uncertainty. This is evaluated as between 0.2 - 0.8% of the statistical precision for x and y.

10.8 Phase-space resolution

As discussed in Chapter 7, there is a finite phase-space resolution which smears the measured values of the Dalitz coordinates and this is not accounted for in the GooFit amplitude model. Therefore we need to assess the effect of neglecting this resolution on the measured values of x and y. This is done through the use of toys: an ensemble of pseudo-datasets are generated from a single underlying toy sample. The phase-space coordinates are re-smeared several times in order to generate an ensemble of pseudo-datasets. As such any variation in the measured values of the mixing parameters within this ensemble must be as a consequence of the phase-space resolution. The Dalitz coordinates are smeared according to the known phase-space resolution as derived from simulation and discussed in Chapter 7. The coordinates $m_{12}^2 \pm m_{13}^2$ are used to smear the toy dataset since these are uncorrelated and the correlations do not need to be taken into account when smearing. This method can result in candidates being pushed out of the physically-allowed region, which can't happen in real data due to the kinematic constraints used when calculating the phase space variables. To ensure realistic pseudo-datasets, for candidates where this happens we simply repeat the smearing until the post-smeared candidate lies in the allowed phase space. This is found to accurately reproduce the impact of resolution on real data. The pseudo-datasets are then fitted with the nominal fit model (without phase-space resolution). Any shift between the generated and measured values of x and y can be assigned as a systematic. This is found by plotting the shifts from the ensemble of pseudo-experiments and fitting with a Gaussian, the shift can be quantified as the mean or width of the Gaussian. This is found to be 2.40×10^{-4} for x and 1.46×10^{-4} for y, corresponding to 28% and 19% of the statistical uncertainties respectively.

10.9 Numerical integration of PDFs

As part of the maximum likelihood fitting framework, the PDFs must be normalised and the functions comprising them must be integrated. The decay-time PDF used in the mixing fit model is analytically integrable, however the PDF is not analytically integrable over the two-dimensional Dalitz plane. Instead, a numerical integration is used where the PDFs are evaluated at points on a two-dimensional grid. The grid covers the physically allowed Dalitz region (the value of the PDF outside this region will be zero) and the separation of the grid points is uniform. The grid spacing must be carefully chosen such that it is fine enough to ensure precise integration and to resolve narrow resonances, but coarse enough to allow the fit to converge within the available computing and time resources. The nominal grid spacing is chosen in this case to be a separation of 0.0025 $\mathrm{GeV}^2/\mathrm{c}^4$ corresponding to 1400 bins in the Dalitz variable's range 0 - 3.5 $\mathrm{GeV}^2/\mathrm{c}^4$. A further reduction in the grid spacing gives changes to the measured values of the mixing parameters significantly smaller than the statistical uncertainties reported in the fit.

In order to assess the effect of the grid spacing in the normalisation on the measured value of the mixing parameters, we vary the grid spacing to ±50% of the nominal value, the changes in the mixing parameters can be assigned as a systematic uncertainty. The systematic uncertainty can be conservatively chosen to be the largest shift in each mixing parameter; this occurs in both cases when increasing the grid spacing. For x the shift is 3.79×10^{-5}, for y it is 1.34×10^{-5}. In both cases of finer and coarser grids, the changes in the measured value of the mixing parameters are at the level of 0.5 - 2% of the statistical precision.

10.10 Systematic uncertainties summary

A summary of all the systematic uncertainties is given in Table 10.3. One of the largest contribution is of the uncertainties associated with the amplitude model. This is followed by also the background mass models which are used for the signal probabilities and the background PDFs in the mixing fit, as well as the background PDF. The total systematic uncertainties are calculated by adding in quadrature the individual contributions. This assumes that there are no correlations between the systematic uncertainties and may be conservative if some have significant correlations. For example the background PDF is considered as a systematic uncertainty in the background mass model and the background PDF in Table 10.3; these therefore may be correlated and overestimating the contribution of the background PDF to the total systematic uncertainty. However since it is not dominant and is less than the statistical uncertainty we decide to quantify as such at this time.

Source	Systematic uncertainty	
	$x[10^{-5}]$	$y[10^{-5}]$
Fit biases	0	10
Signal mass model	2	5
Background mass model	2	5
Background PDF	35	49
Background smoothing	5	14
Mistag	1	8
Phase-space acceptance	16	10
Decay-time acceptance	1	3
Decay-time resolution	1	1
Phase-space resolution	24	15
Numerical integration	0	0
Total experimental	39.3	54.2
Total fit model	24.4	26.2
Total	46.2	60.2
Statistical	85.5	75.4

Table 10.3: Summary of the systematic uncertainties, the fit model systematic is detailed in Table 10.2.

CHAPTER 11

Results and Crosschecks

This thesis presents the measurement of the mixing parameters of the D^0 meson using a time-dependent amplitude analysis of $D^0 \to K^0_S\pi^+\pi^-$ decays at the LHCb detector. The mixing parameters x and y (and the *CP*-violation parameters Δx and Δy) are extracted from a fit of a time-dependent amplitude model to the Dalitz coordinates and decay-time of this decay. The amplitude model is discussed in Chapter 8, we use the isobar model where the $D^0 \to K^0_S\pi^+\pi^-$ decay amplitude is modelled as a linear superposition of resonant (Breit-Wigner and Gounaris-Sakurai) and non-resonant amplitudes. The amplitude model uses the K-matrix formalism to describe the S-wave component in the $\pi^+\pi^-$ channel and the LASS model for the $K\pi$ S-wave. Some aspects of the amplitude model are determined in an initial time-integrated fit to the same data sample. This includes the shape parameters of the S-wave components (fixed in the mixing fit), some masses and widths of resonances, and the starting values for the complex coefficients multiplying each amplitude. In the time-integrated fit, we fit to a dataset of D^0 decay times below one D^0 lifetime where there are negligible effects from mixing. The isobar model reported by Belle and BaBar collaborations [20] is used as the starting point when developing the model. This is then varied by adding or removing resonances and the nominal model is chosen based on adding resonances until subsequent additions do not significantly improve the fit quality, defined as the negative log likelihood

$-2\log(\mathcal{L})$. The time-integrated fit is used to fix some some aspects of the amplitude model, and also as the starting values of the complex coefficients multiplying each component amplitude for the time-dependent mixing fit.

The fit can be run with the assumption of no *CP*-violation, where the parameters Δx and Δy are fixed to zero, or with *CP*-violation allowed in which case the *CP*-violation parameters are allowed to float in the fit. In the time-dependent amplitude fit the free parameters are the Breit-Wigner complex coefficients as well as the mixing parameters and the D^0 lifetime. The other parameters such as the masses and widths of the resonances and the S-wave shape parameters are fixed based on the initial time-integrated fits described in Chapter 8 or to world averages of experimental measurements [78] in the case of some of the masses and widths. The results of the mixing parameters are currently blind, pending approval to unblind by the LHCb collaboration, as part of the internal review process. The fit is performed for the LHCb Run 2 (2016-2018) data-taking period. We use D^0 mesons originating from semi-leptonic B meson decays: $B \to D^0\mu^-\bar{\nu}X$ for the single-tagged sample and $B \to D^{*+}(\to D^0\pi^+)\mu^-\bar{\nu}X$ for the double-tagged sample with the simultaneous fit of 12 subsamples differentiated by data-taking year, K^0_S type, and single and double-tagged. We perform a time and phase-space dependent fit to data, the data coordinates are:

- Decay-time and Dalitz (m^2_{12}, m^2_{13}) coordinates,
- Flavour tag (defined as +1 for D^0 and -1 for $\bar{D}^0$) from the charge of the muon for the single-tagged sample and the charge of the pion in the double-tagged sample,
- Per-candidate signal probability derived from fits to $m(D^0)$ for single-tagged samples and $\delta(m)$ for double-tagged.

The inputs to the final mixing fit are:

- Phase-space efficiency parameterisation derived from simulation (Section 7.1),
- Decay-time acceptance parameterisation derived from simulation (Section 7.2),
- Decay-time resolution parameterisation derived from simulation (Section 7.3),
- Background histograms for Dalitz variables and decay time derived from

sWeighted data,

- Mistag fraction of wrongly tagged muons for the single-tagged sample.

The results of the time-dependent amplitude fit are shown in Figure 11.1 for one single-tagged K_S^0 (LL) 2018 subsample, which shows the projections of the Dalitz variables and in Figure 11.2 which shows the decay-time projections. The Dalitz plots can be seen in Figure 11.3. The quality of the fit can be assessed by the pulls which is the difference between data and value of the PDF in each bin divided by the uncertainty on the data. These are shown in the one-dimensional projections in Figures 11.1 and 11.2. The observed inaccuracies in the model are considered reasonable and are taken into account in the systematic uncertainties as discussed in detail in Chapter 10. These could be partly to do with plotting at the threshold regions which can also be seen in the toy fits in Chapter 9 and also to the imperfect description of the efficiency at the threshold regions. Fit projections for other data sub-samples can be seen in Appendix D. These are fit projections of one sample for the simultaneous fit rather than for fits to individual samples. The fit quality over the Dalitz plane corresponds to a χ^2 value 8947 for 7946 degrees of freedom, χ^2/dof = 1.13.

The blinded mixing parameters are:

$$x = (x.xx \pm 0.086_{\text{stat}} \pm 0.039_{\text{syst}} \pm 0.024_{\text{model}})\% \tag{11.1}$$

$$y = (y.yy \pm 0.076_{\text{stat}} \pm 0.054_{\text{syst}} \pm 0.026_{\text{model}})\% \tag{11.2}$$

The result for the D^0 lifetime is:

$$\tau(D^0) = 0.4019 \pm 0.0002\,\text{ps} \tag{11.3}$$

This is not blind and is slightly below the world average value of 0.4101 ± 0.015 ps which could be to do with the description of the decay-time acceptance. The correlations between x, y and $\tau(D^0)$ for the mixing fit with no CP-violation is shown in Table 11.1.

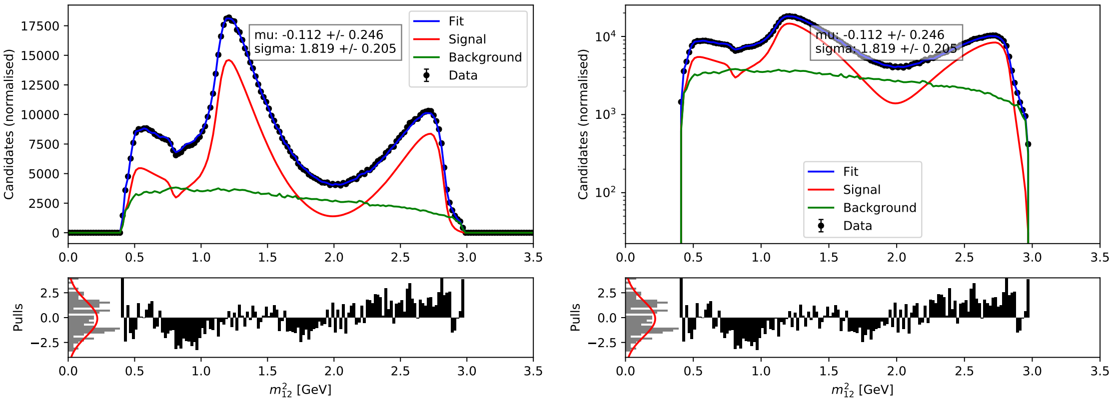

(a) m_{12}^2 linear scale

(b) m_{12}^2 log scale

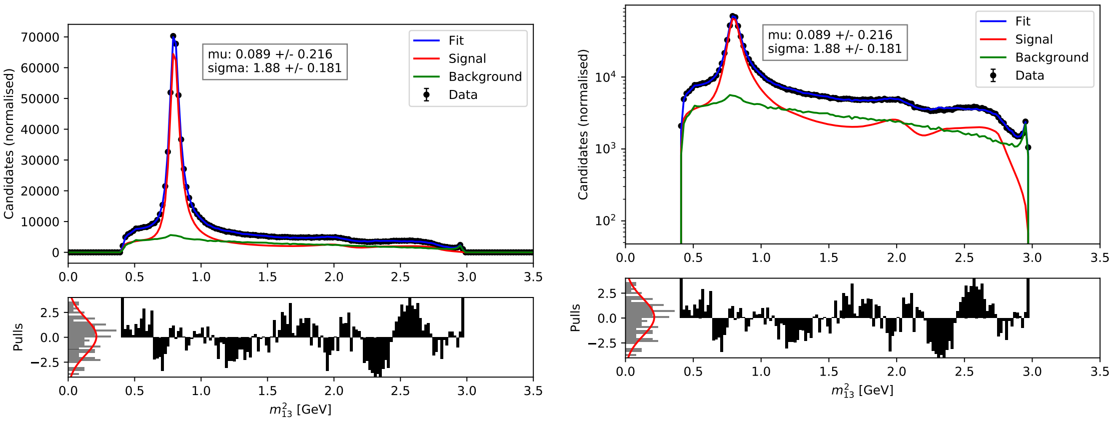

(c) m_{13}^2 linear scale

(d) m_{13}^2 log scale

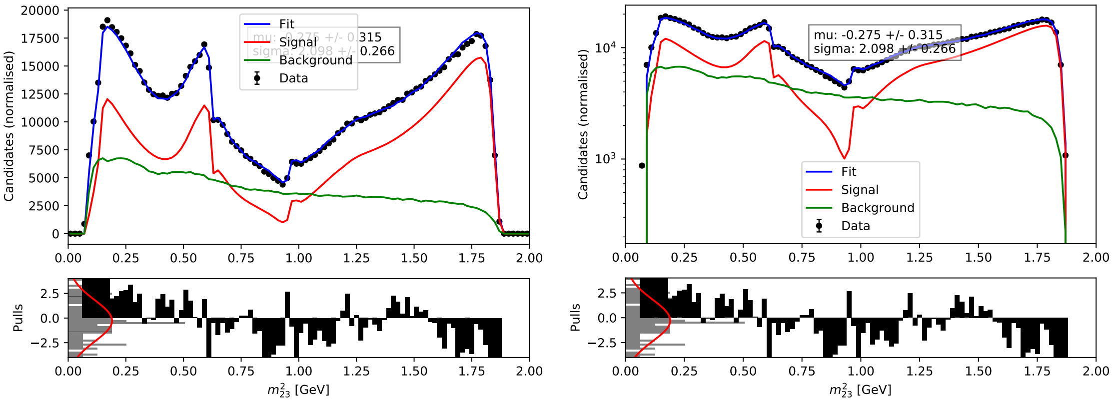

(e) m_{23}^2 linear scale

(f) m_{23}^2 log scale

Figure 11.1: Fit projections of the Dalitz variables for the time-dependent amplitude fit. Single-tag K_S^0 (LL) 2018 sample. Linear and log scales. Plots show signal component in red and background in green.

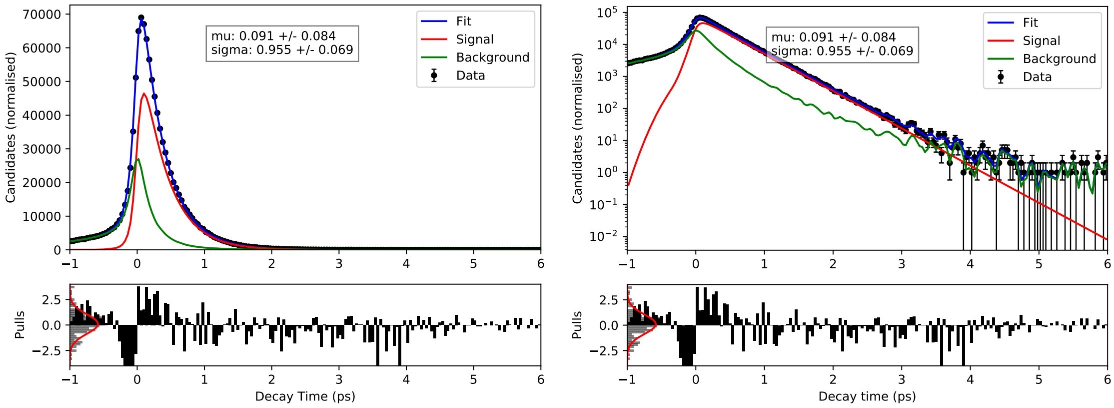

Figure 11.2: Decay-time projections for the time-dependent amplitude fit. Single-tag K_S^0 (LL) 2018 sample. Linear and log scales. Plots show signal component in red and background in green.

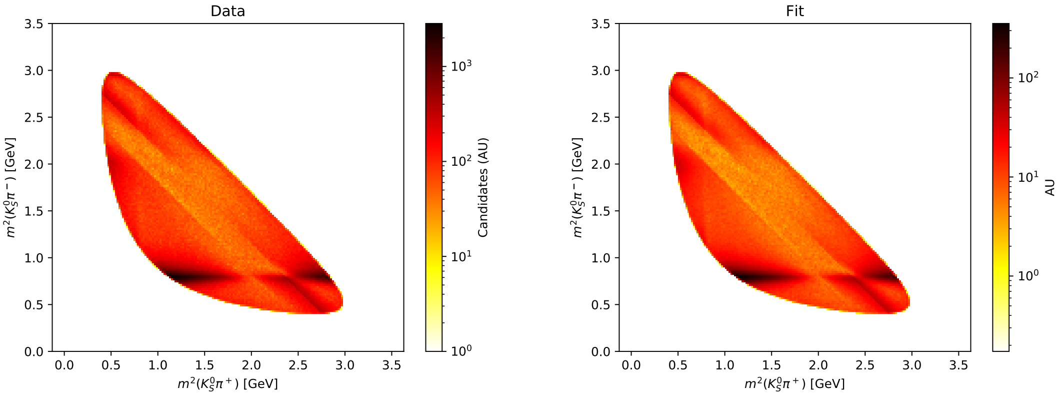

(a) Data

(b) Fit model

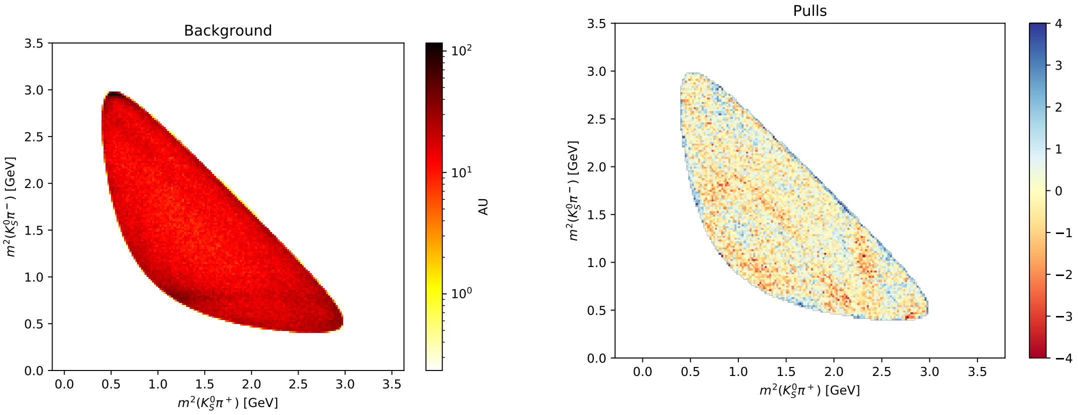

(c) Background model

(d) Pulls

Figure 11.3: Two-dimensional distributions of the Dalitz variables for the time-dependent amplitude fit: data, total fit model, background model and pulls.

	x	y	$\tau(D^0)$
x	1.0	0.006	-0.002
y		1.0	0.081
$\tau(D^0)$			1.0

Table 11.1: Correlations between x, y and $\tau(D^0)$ in the mixing fit.

	x_{CP}	y_{CP}	Δx	Δy	$\tau(D^0)$
x_{CP}	1.0	0.006	-0.0	0.006	-0.002
y_{CP}		1.0	0.007	-0.005	0.081
Δx			1.0	0.006	0.001
Δy				1.0	-0.003
$\tau(D^0)$					1.0

Table 11.2: Correlations between x_{CP}, y_{CP}, Δx, Δy and $\tau(D^0)$ in the mixing fit with *CP*-violation allowed.

The world average values at the time of writing are, for the no *CP*-violation allowed case:

$$\begin{aligned} x\,(\%) &= 0.51^{+0.12}_{-0.14} \\ y\,(\%) &= 0.63 \pm 0.07 \end{aligned} \tag{11.4}$$

For the *CP*-violation allowed fit the blinded results are:

$$\begin{aligned} x &= (x.xx \pm 0.086)\% \\ y &= (y.yy \pm 0.076)\% \\ \Delta x &= (0.00 \pm 0.059)\% \\ \Delta y &= (0.00 \pm 0.051)\% \end{aligned} \tag{11.5}$$

where the uncertainties quoted here are statistical only. These can also be converted to the *CP*-violation parameters with the ± 1σ uncertainties using the Equation 2.54:

$$\begin{aligned} |q/p| &= 0.996 \pm 0.093 \\ \phi(^\circ) &= -0.055 \pm 0.089 \end{aligned} \tag{11.6}$$

where the central values are blind and are assumed to be the world average values in the fit. Table 11.2 shows the correlations for the *CP*-violation allowed fit. These are also visualised in Figure 11.4.

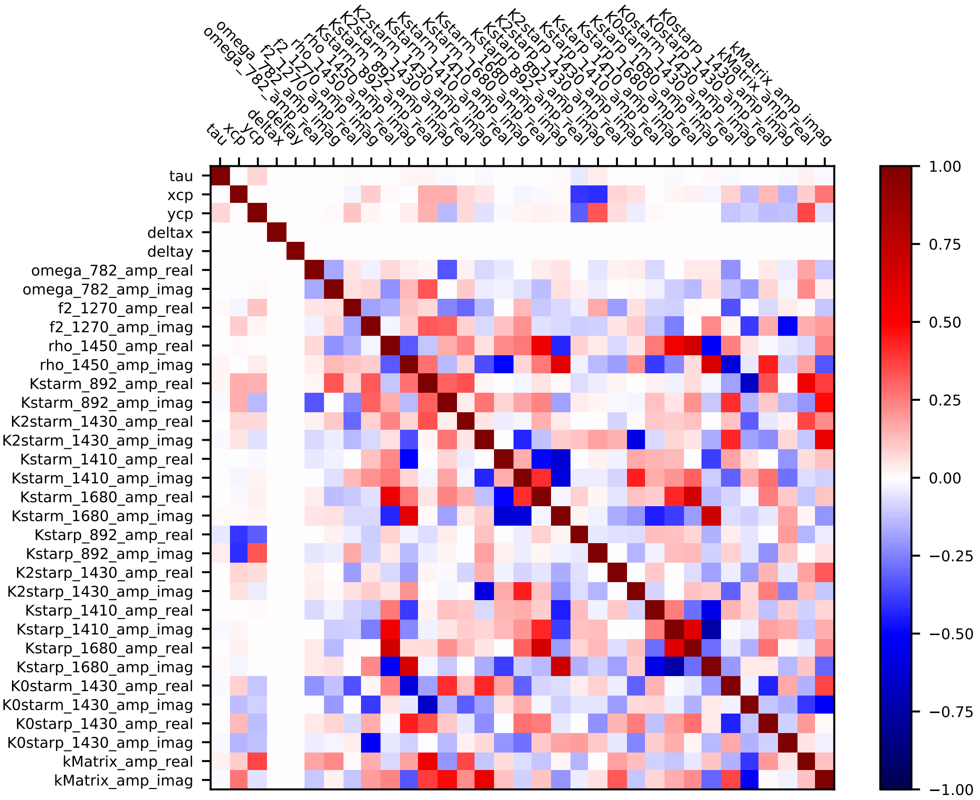

Figure 11.4: Correlations between the parameters of the mixing fit with *CP*-violation allowed, $\tau(D^0)$, x, y, Δx, Δy, and the real and imaginary complex coefficients of the amplitudes.

The current world averages on the mixing and *CP*-violation parameters in the *CP*-violation allowed global fit are:

$$\begin{aligned} x\,(\%) &= 0.37 \pm 0.12 \\ y\,(\%) &= 0.68^{+0.06}_{-0.07} \\ |q/p| &= 0.951^{+0.053}_{-0.042} \\ \phi\,(^\circ) &= -5.3^{+4.9}_{-4.5} \end{aligned} \tag{11.7}$$

The effect of this measurement on the world average values can be assessed by performing the global fit and assuming no correlation with the other measurements since this is an independent dataset. When performing the combination the central values are assumed to be the same as the results from Ref. [13] (the 2021 prompt model-independent result) since the result of this measurement is still blind. This is visualised in Figure 11.5 which shows: the current world average in purple, the world

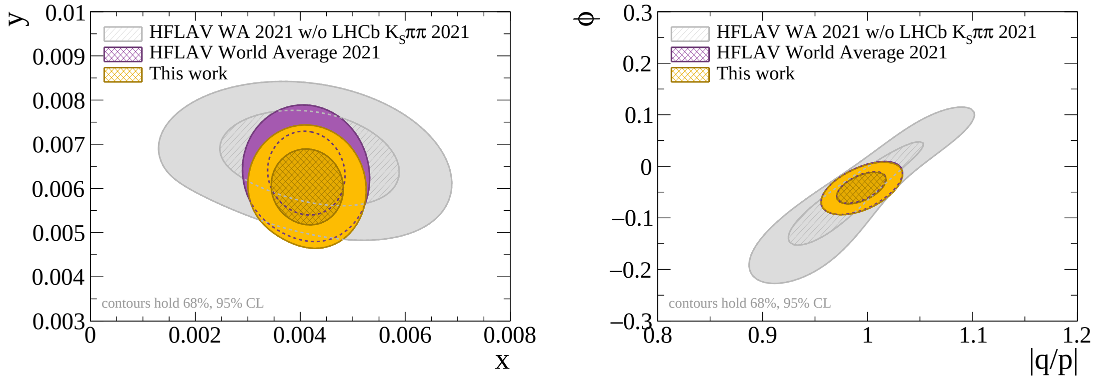

Figure 11.5: This figure shows world average not including the bin-flip result [13] (grey), current world averages on the mixing and CP-violation parameters (purple) including the bin-flip result, and the world average including this work (yellow).

average without the bin-flip result [13] in grey and the effect of including this result in the world average in yellow. This demonstrates how the current world average is dominated by the prompt bin-flip result [13].

Since the world average values are dominated by the model-independent bin-flip result from the LHCb collaboration [13], it is also instructive to compare the results with this analysis. The results are (repeated from Equation 1.6):

$$\begin{aligned} y_{CP} &= [0.459 \pm 0.120_{\text{stat}} \pm 0.085_{\text{syst}}]\% \\ \Delta y &= [0.020 \pm 0.036_{\text{stat}} \pm 0.013_{\text{syst}}]\% \\ x_{CP} &= [0.397 \pm 0.046_{\text{stat}} \pm 0.029_{\text{syst}}]\% \\ \Delta x &= [-0.027 \pm 0.018_{\text{stat}} \pm 0.001_{\text{syst}}]\% \end{aligned} \tag{11.8}$$

The bin-flip result is more precise in the measurement of x by over a factor of 2, since is it specifically designed for precision on the measurement of x. However the model-dependent result is more precise in the measurement of y. In addition it is important to note that the bin-flip analysis uses the prompt dataset which corresponds to a total of 30.6 million $D^0 \to K^0_S\pi^+\pi^-$ decays, whereas this result has a smaller signal yield of 5.3 million events. This demonstrates the power of the model-dependent method and the importance of both complimentary methods within the LHCb collaboration. Figure 11.6 shows a similar plot but with this work in yellow, the bin-flip 2021 result [13] in purple and the current world average in grey. This directly compares this work to the bin-flip result which demonstrates the power

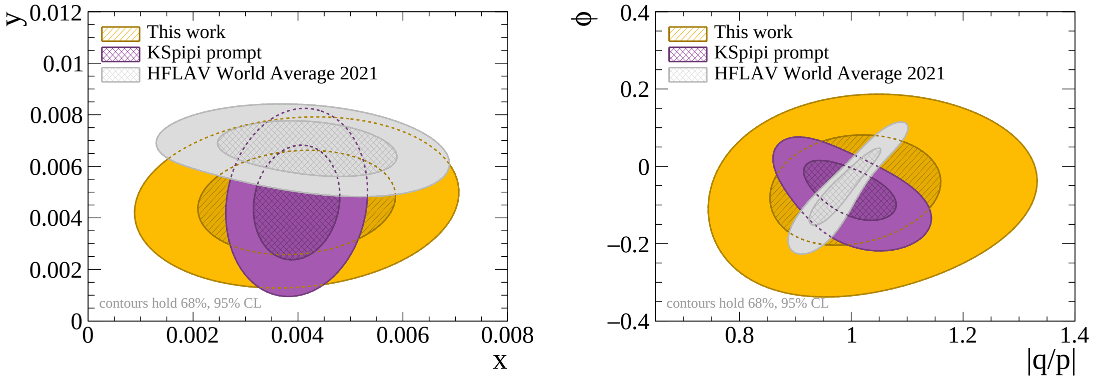

Figure 11.6: This shows the world averages without the bin-flip result on the mixing and *CP*-violation parameters (grey), the 2021 bin-flip result [13] (purple) and this work (yellow).

of this method compared to the bin-flip method which has ~ 6 times more data.

One should not compare the amplitudes between experiments because there may be differences in the Blatt-Weisskopf form-factors and in the production parameters in the K-matrix parametrisation. However we can compare the fit fractions which are more physically meaningful, as defined in Equation 8.24. The results for the final mixing fit are shown in Table 11.3 along with the fit fractions. These can be compared to the most recent result from the Belle and BaBar collaborations in Ref. [20]. For components with the highest fit fraction excellent agreement is observed. The $K^*(892)^-$ resonance has 56% fit fraction for this analysis (60% for Ref. [20]), the $\rho(770)$ resonance has 16% (20%) and the $\pi\pi$ S-wave has 11% (10%). The interference fit fractions can be seen in Table 11.4 for the three main components of the amplitude model: the $K^*(892)^-$, $\rho(770)$ and the $\pi\pi$ S-wave. These show the constructive and destructive interferences between the resonances denoted by the positive and negative signs of the interference fit fractions. The fit fractions in Table 8.5 do not necessarily equal unity due to the constructive and destructive interference effects.

System	Resonance	Real	Imaginary	Fit Fraction (%)
	$\rho(770)$	1.0 (fixed)	0.0 (fixed)	15.67
	$\omega(782)$	-0.017 ± 0.000	0.037 ± 0.000	0.40
	$f_2(1270)$	0.747 ± 0.005	0.094 ± 0.006	0.78
	$\rho(1450)$	-1.353 ± 0.017	0.539 ± 0.021	0.76
	$K^*(892)^-$	1.372 ± 0.003	-1.343 ± 0.003	56.18
	$K_2^*(1430)^-$	0.912 ± 0.006	-0.869 ± 0.007	1.63
	$K^*(1410)^-$	-0.707 ± 0.011	-0.455 ± 0.013	0.84
	$K^*(1680)^-$	0.207 ± 0.025	1.931 ± 0.028	2.01
	$K_0^*(1430)^-$	-3.381 ± 0.014	-2.797 ± 0.012	8.07
	$K^*(892)^+$	0.112 ± 0.001	-0.099 ± 0.001	0.34
	$K_2^*(1430)^+$	-0.009 ± 0.005	0.047 ± 0.006	<0.1
	$K^*(1410)^+$	-0.470 ± 0.011	-0.474 ± 0.012	0.53
	$K^*(1680)^+$	-0.487 ± 0.025	0.940 ± 0.030	0.60
	$K_0^*(1430)^+$	-0.144 ± 0.009	-0.124 ± 0.010	<0.1
$\pi\pi$ S-wave	β_1	-1.028 ± 0.070	3.466 ± 0.052	11.07
	β_2	14.799 ± 0.078	2.806 ± 0.084	
	β_3	42.985 ± 1.054	-18.906 ± 0.619	
	β_4	-1.859 ± 0.250	-7.059 ± 0.200	
	f_{11}^{prod}	-4.702 (fixed)	-6.472 (fixed)	
	f_{12}^{prod}	-14.288 ± 0.478	12.456 ± 0.181	
	f_{13}^{prod}	-18.123 ± 0.425	-22.279 ± 0.804	
	f_{14}^{prod}	-10.306 ± 0.329	-14.780 ± 0.068	
$K\pi$ S-wave	F	0.817 ± 0.015		
	ϕ_F	0.077 ± 0.002		
	R	1 (fixed)		
	ϕ_R	-3.135 ± 0.022		
	a	0.224 ± 0.001		
	r	-21.286 ± 0.124		
Sum of fit fractions		98.90		

Table 11.3: Results of the parameters of the amplitude model obtained from the final mixing fit, including complex amplitudes of resonant components, $\pi\pi$ and $K\pi$ S-wave parameters and fit fractions for each component. The errors are statistical. The S-wave parameters are fixed from the initial time integrated fit as described in the text.

Resonance 1	Resonance 2	Fit Fraction (%)
$\rho(770)$	$\omega(782)$	-0.317
	$f_2(1270)$	-0.002
	$\rho(1450)$	-0.020
	$K^*(892)^-$	-3.329
	$K_2^*(1430)^-$	0.644
	$K^*(1410)^-$	0.765
	$K^*(1680)^-$	-1.112
	$K_0^*(1430)^-$	1.301
	$K^*(892)^+$	-0.262
	$K_2^*(1430)^+$	0.013
	$K^*(1410)^+$	0.607
	$K^*(1680)^+$	-0.314
	$K_0^*(1430)^+$	-0.057
	$\pi\pi$ S-wave	-0.008
$K^*(892)^-$	$f_2(1270)$	-0.732
	$\rho(1450)$	-0.324
	$K_2^*(1430)^-$	-0.059
	$K^*(1410)^-$	-1.687
	$K^*(1680)^-$	3.107
	$K_0^*(1430)^-$	0.369
	$K^*(892)^+$	-0.225
	$K_2^*(1430)^+$	-0.004
	$K^*(1410)^+$	0.889
	$K^*(1680)^+$	-0.380
	$K_0^*(1430)^+$	0.123
	$\pi\pi$ S-wave	2.734
$\pi\pi$ S-wave	$\rho(1450)$	0.001
	$K_2^*(1430)^-$	-0.788
	$K^*(1410)^-$	-0.883
	$K^*(1680)^-$	1.875
	$K_0^*(1430)^-$	1.446
	$K^*(892)^+$	-0.224
	$K_2^*(1430)^+$	-0.016
	$K^*(1410)^+$	0.742
	$K^*(1680)^+$	-0.695
	$K_0^*(1430)^+$	0.063

Table 11.4: Interference fit fractions for the $\rho(770)$, $K^*(892)^-$ and $\pi\pi$ S-wave terms in the Dalitz fit including the sign of the term where a negative sign denotes destructive interference.

11.1 Crosschecks

11.1.1 Fits to individual samples

The mixing fit is performed on several disjoint samples of the dataset. The parameters of interest are extracted separately for data-taking year, K_S^0 type as well as for single and double-tagged decays. The results of the mixing parameters for the fits to individual samples can be seen in Figure 11.7. The data subsamples are labelled by numbers, these are in the following order: by year 2016, 2017, 2018 (ie. the first four entries are for 2016) then single-tagged K_S^0 (LL), K_S^0 (DD), double-tagged K_S^0 (LL), K_S^0 (DD). The χ^2 per number of degrees of freedom of the points with respect to the red line is calculated, a value of 1.00 suggests that the mixing parameters are stable across all subsamples. Figure 11.7 shows the excellent agreement in the parameter x with a χ^2/ndof value of 1.00. However there is poor agreement in y, this could be to the decay-time acceptance description which there is ongoing work to resolve. We aim to include an improved model of the decay-time acceptance in GooFit, which currently uses the exponential model as seen in Section 7.2. The exponential model is clearly a poor description of the acceptance. This may affect the measured value of $\tau(D^0)$ and y since these two parameters are correlated (Table 11.1).

This is a strong test of the method because the different K_S^0 types and tags are subject to different detector effects and background levels and shapes. The statistical uncertainties for the fits to individual samples are reported in Table 11.5. Adding these using the rule for combining variances suggests that the combination is approximately as sensitive as the simultaneous fit. Although for the final result the simultaneous fit is used since it simplifies the measurement and the systematic uncertainties.

11.1.2 Fits in disjoint subsamples of D^0 p and η

We also perform the mixing fit in disjoint subsamples in kinematics of the D^0, namely momentum $p(D^0)$ and pseudorapidity $\eta(D^0)$. These can be seen in Figure 11.8. These also show reasonable agreement in x and not such good agreement in y,

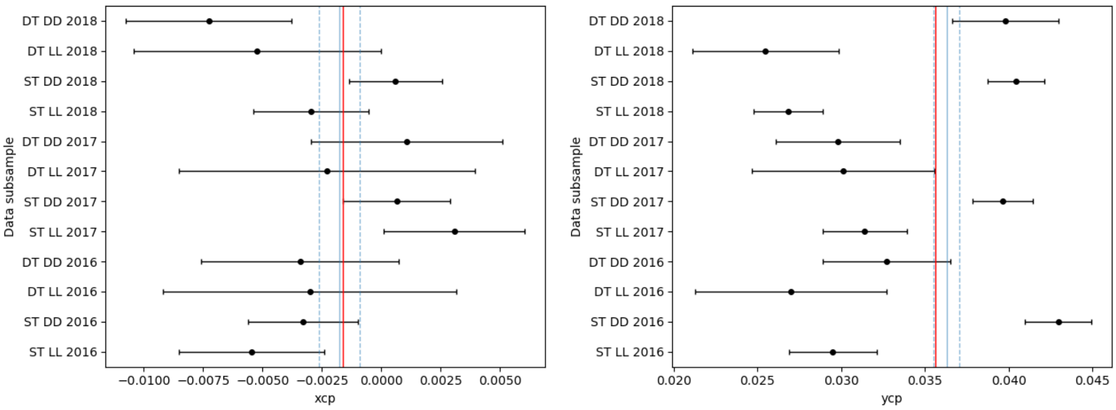

(a) χ^2/ndof = 1.00 (b) χ^2/ndof = 6.06

Figure 11.7: Comparison of the results of the mixing parameters for fits to individual samples: red line is the weighted average of the individual fits, and the blue line is the simultaneous fit result to all samples combined, with statistical errors.

Sample	Statistical uncertainty	
	x [%]	y [%]
Single-tagged		
2016 K_S^0 (LL)	0.311	0.264
2016 K_S^0 (DD)	0.229	0.199
2017 K_S^0 (LL)	0.304	0.256
2017 K_S^0 (DD)	0.223	0.195
2018 K_S^0 (LL)	0.247	0.211
2018 K_S^0 (DD)	0.194	0.170
Double-tagged		
2016 K_S^0 (LL)	0.684	0.576
2016 K_S^0 (DD)	0.441	0.395
2017 K_S^0 (LL)	0.656	0.567
2017 K_S^0 (DD)	0.426	0.379
2018 K_S^0 (LL)	0.536	0.451
2018 K_S^0 (DD)	0.371	0.324

Table 11.5: Statistical uncertainties of fits to individual samples.

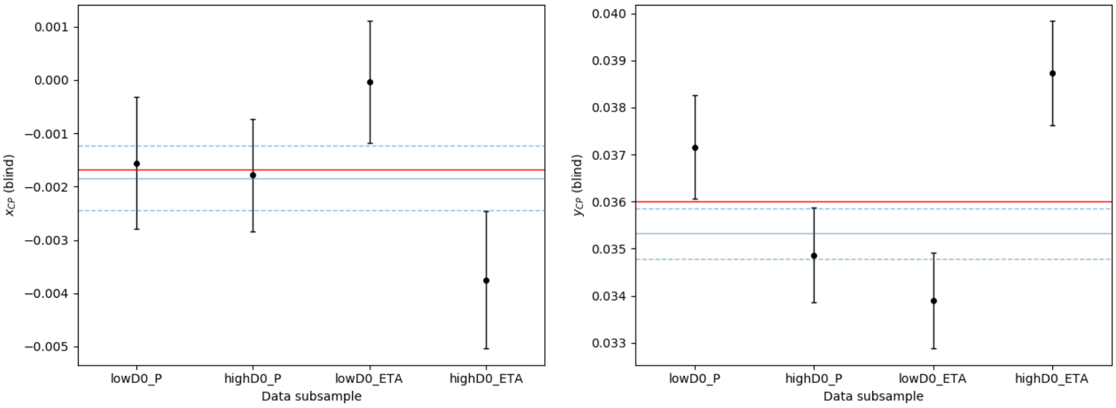

(a) χ^2/ndof = 1.57 (b) χ^2/ndof = 4.23

Figure 11.8: Comparison of the results of the mixing parameters for low and high D^0 momentum and η: red line is the weighted average of the individual fits, and the blue line is the simultaneous fit result to all samples combined, with errors.

again potentially due to the decay-time acceptance since y is correlated with the D^0 lifetime in the fit.

CHAPTER 12

Conclusion

This thesis reports a measurement of the mixing parameters of the D^0 meson using semi-leptonic $D^0 \to K_S^0\pi^+\pi^-$ decays with 6 fb^{-1} of data collected at the LHCb detector in the Run 2 data-taking period. The work undertaken in this thesis includes the search for indirect *CP*-violation - the results reported are both for the no *CP*-violation and the *CP*-violation allowed case. The mixing and *CP*-violation parameters are extracted from a time and phase-space dependent amplitude fit to the D^0 decay-time and the Dalitz variables of this decay $m^2(K_S^0\pi^+)$ and $m^2(K_S^0\pi^-)$.

The blinded mixing parameters are measured to be:

$$x = (x.xx \pm 0.86_{\text{stat}} \pm 0.39_{\text{syst}} \pm 0.24_{\text{model}}) \times 10^{-3} \tag{12.1}$$

$$y = (y.yy \pm 0.76_{\text{stat}} \pm 0.59_{\text{syst}} \pm 0.26_{\text{model}}) \times 10^{-3} \tag{12.2}$$

This measurement has been compared to the current world average and previous results in Chapter 11 (Figures 11.6 and 11.5). This measurement has a precision exceeding the world average of all existing measurements, with the exception of the result bin-flip analysis on the prompt LHCb data sample [13]. The world average values are quoted in Equation 11.4 and 11.7.

Ongoing work includes improving the description of the decay-time acceptance

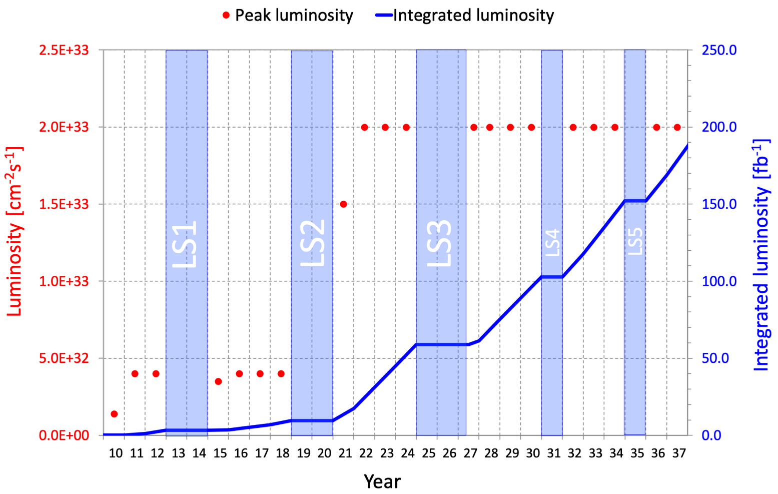

Figure 12.1: LHCb peak luminosity and integrated luminosity projections for Run 3 and beyond. Figure from Ref. [41].

in the model. This should reduce the discrepancies in the measurements in disjoint subsamples and also the measurement of the D^0 lifetime. The estimation of the systematic uncertainties for the CP-violation parameters will be performed but based on previous analyses is expected to be small [13]. The Run 1 dataset has also been prepared for this measurement, including the data selection in Chapter 5 and the evaluation of the detector acceptance and resolution effects with MC described in Chapter 7. For example the Run 1 selection is shown in Appendix A and B.4.

The systematic uncertainties for the mixing parameters have been estimated. The systematic uncertainties are comparable with the statistical, which will shrink with more data being collected in Run 3 and beyond. However some of the systematics will become smaller with more data, such as the limited knowledge of the fixed parameters in the fit and the limited Monte Carlo statistics. There are ongoing efforts within the LHCb collaboration to improve and speed up the generation of Monte Carlo simulation since our needs will increase significantly in Run 3. Figure 12.1 shows the projected peak luminosity and integrated luminosity for LHCb for Run 3 and the successive upgrades. This is a new era in flavour physics with precision measurements in the flavour sector being at the forefront of searches for new physics.

12.1 Future prospects in $D^0 \to K^0_S\pi^+\pi^-$ decays

This thesis reports the measurement of the mixing parameters of neutral charm mesons, and a search for indirect *CP*-violation, parameterised by the parameters Δx and Δy. The systematic uncertainties have been evaluated and estimated for the mixing parameters. Future analysis will have reduced statistical uncertainties due to the increase in data. However some of the systematic uncertainties are expected to decrease in the future. For example, the fixed parameters of the fit are resampled within their uncertainties derived from a fit to data - the corresponding systematic uncertainty will also decrease with more data. In addition, those systematic uncertainties originating from the inputs from simulation will decrease with increased Monte Carlo statistics expected in Run 3 with improved fast simulation within LHCb. We also hope to benefit from improved description of the amplitude model and any developments in the fitting framework and software used in this analysis.

Complimentary model-independent analyses are being undertaken at LHCb including the model-independent bin-flip analysis of the semi-leptonic tagged $D^0 \to K^0_S\pi^+\pi^-$ decays. The combination of this model-dependent measurement with the semi-leptonic and prompt bin-flip measurements will lead to a higher precision, in particular due to the bin-flip method being particularly sensitive to x as well as the high signal yield of the prompt dataset. The model-dependent and model-independent methods are complimentary with different techniques and systematic uncertainties. The bin-flip method has small systematic uncertainties due to the method of using ratios in which some of the uncertainties cancel. The model-dependent method relies on the understanding of the amplitude model and detector resolution and acceptance effects.

It is also possible to combine the full Run 1 and Run 2 datasets for a legacy measurement of the mixing parameters. The LHC Run 3 is expected to start in 2022 and the LHCb aims to collect at least 50 fb^{-1} by the end of Run 4. The increased data will improve the statistical precision of measurements of charm mixing and *CP*-violation, with searches for *CP*-violation in charm expected to reach a precision precision of 10^{-4}. With the flavour anomalies in the B sector at around the 3 σ level, Run 3 will be needed to confirm these hints of new physics. The LHCb detector will be almost fully upgraded for the start of Run 3 including an upgraded detector hardware as well as moving to a fully online software trigger. In order to cope with the increased luminosity and pile up, data challenges are being faced by running a fully software-based trigger and readout of all detectors at 40 MHz. The HLT1 will also be run on GPUs in Run 3. The detector is being upgraded with a new VELO and tracking systems, new particle ID detector and electronics and new calorimeter and muon electronics.

This measurement will be complimented by the model-independent bin-flip method, which will have more precise and updated results in Run 3. In addition the charm program at LHCb will be complimented by the new upgraded Belle II detector [17]. These precision flavour physics measurements are important in answering some of the open questions of the Standard Model and help us to understand the universe at the most fundamental level.

APPENDIX A

Selection

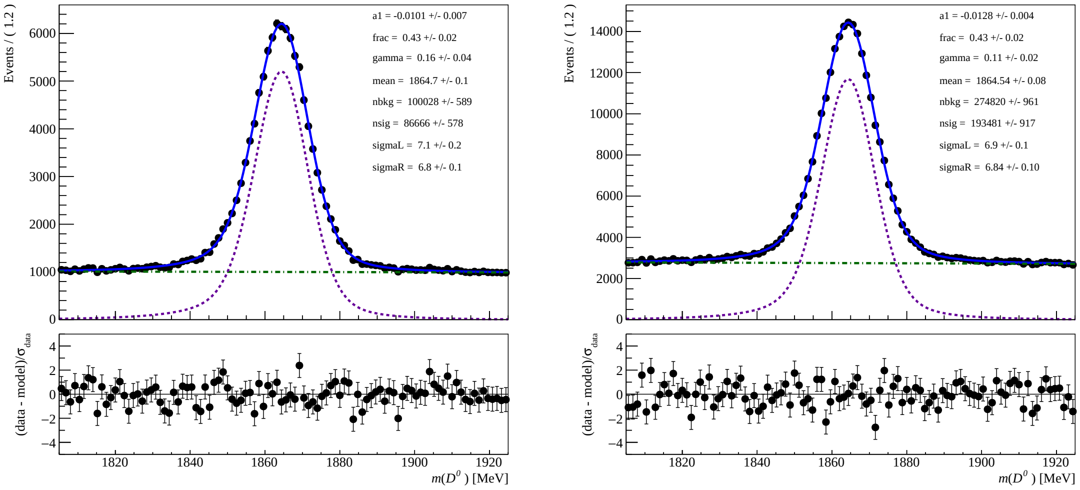

(a) K_S^0 (LL) 2011

(b) K_S^0 (LL) 2012

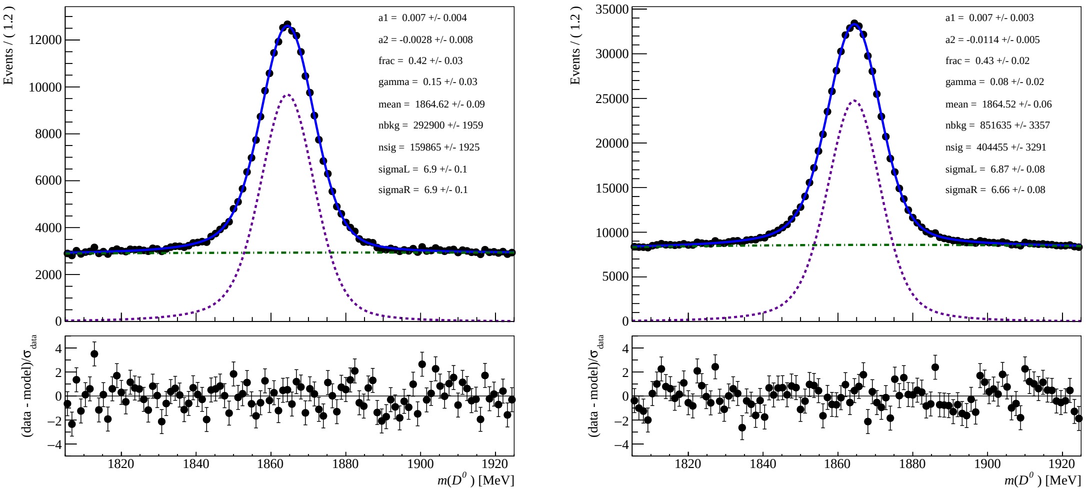

(c) K_S^0 (DD) 2011

(d) K_S^0 (DD) 2012

Figure A.1: D^0 mass fits after preselection for the Run 1 (2011-2012) single-tagged datasets.

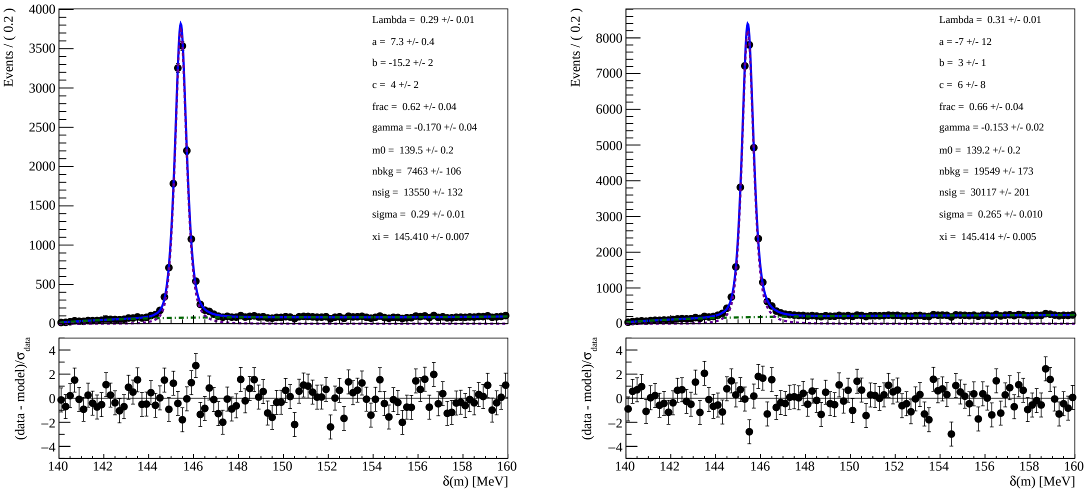

(a) K_S^0 (LL) 2011

(b) K_S^0 (LL) 2012

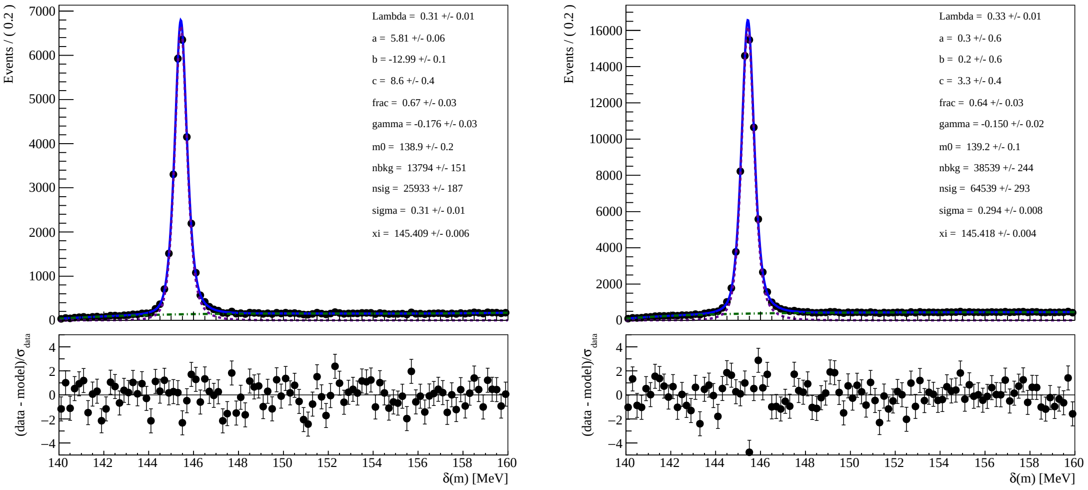

(c) K_S^0 (DD) 2011

(d) K_S^0 (DD) 2012

Figure A.2: Fits to the δm distribution after preselection for the Run 1 (2011-2012) double-tagged datasets.

APPENDIX B

Multivariate analysis

B.1 BDT output and overtraining check

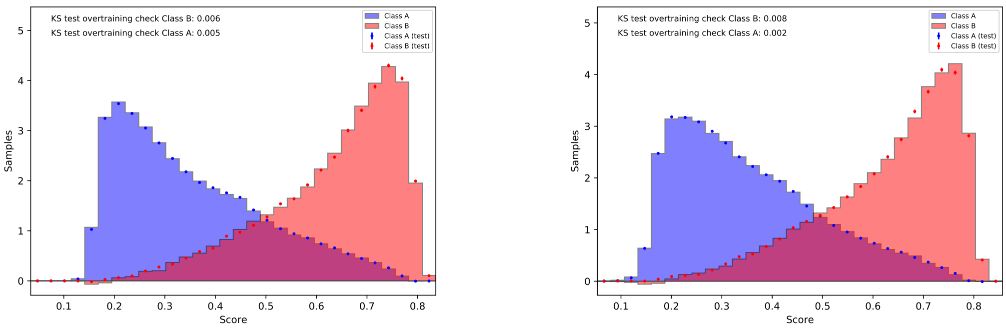

(a) K_S^0 (LL) 2016 even sample

(b) K_S^0 (LL) 2016 odd sample

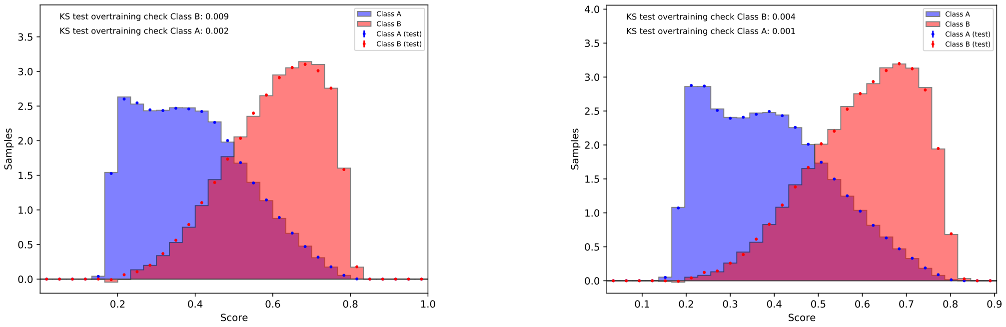

(c) K_S^0 (DD) 2016 even sample

(d) K_S^0 (DD) 2016 odd sample

Figure B.1: BDT output distributions and overtraining check for single-tagged 2016 samples.

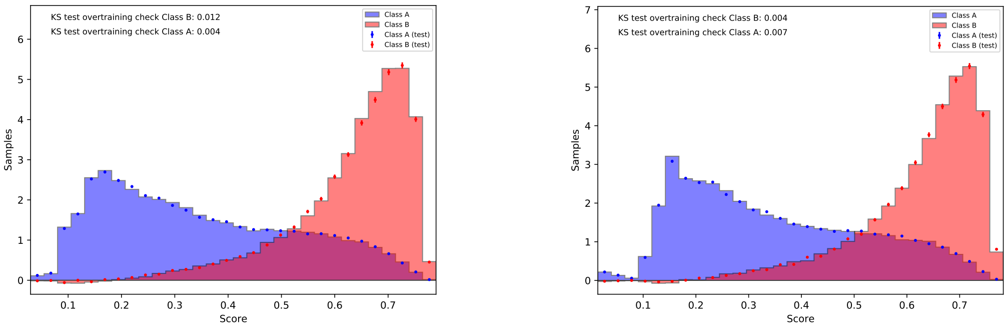

(a) K_S^0 (LL) 2018 even sample

(b) K_S^0 (LL) 2018 odd sample

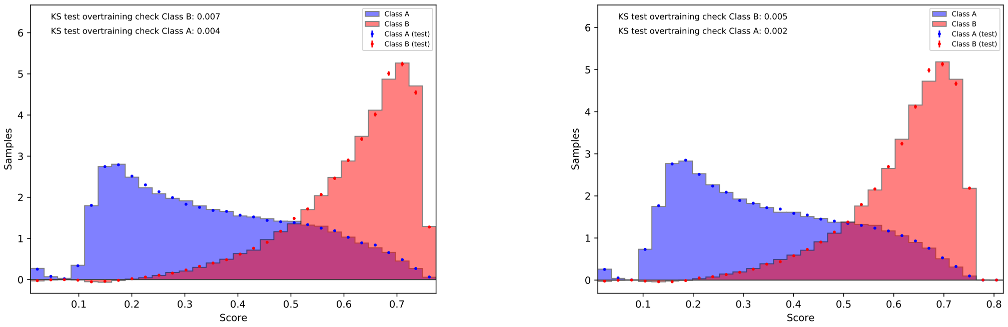

(c) K_S^0 (DD) 2018 even sample

(d) K_S^0 (DD) 2018 odd sample

Figure B.2: BDT output distributions and overtraining check for double-tagged 2018 samples.

B.2 Receiver operator characteristic curves

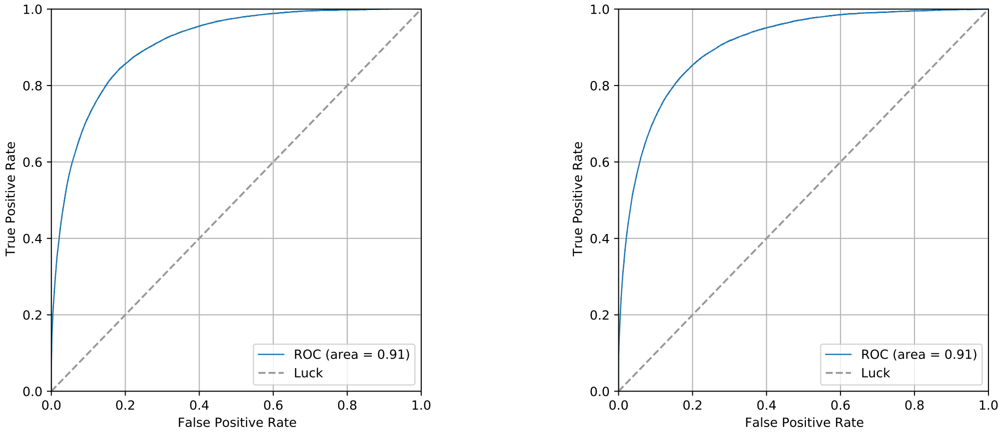

(a) K_S^0(LL) even (b) K_S^0(LL) odd

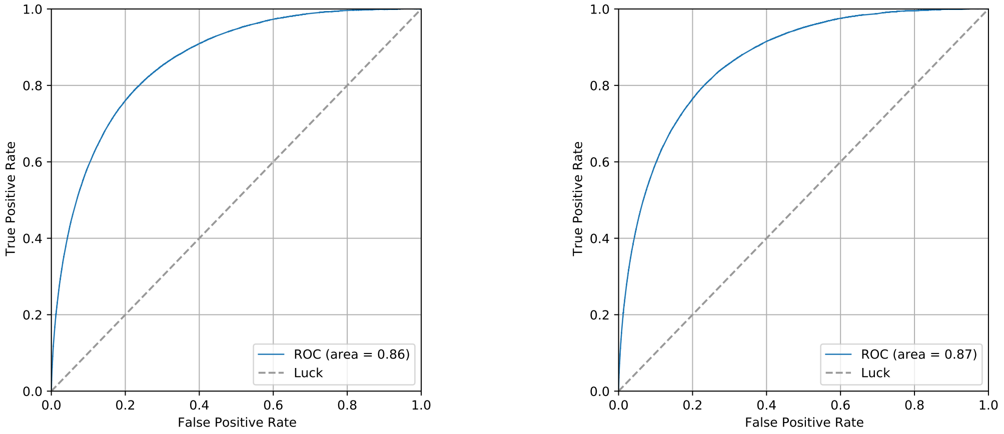

(c) K_S^0(DD) even (d) K_S^0(DD) odd

Figure B.3: ROC curves for single-tagged 2016 samples.

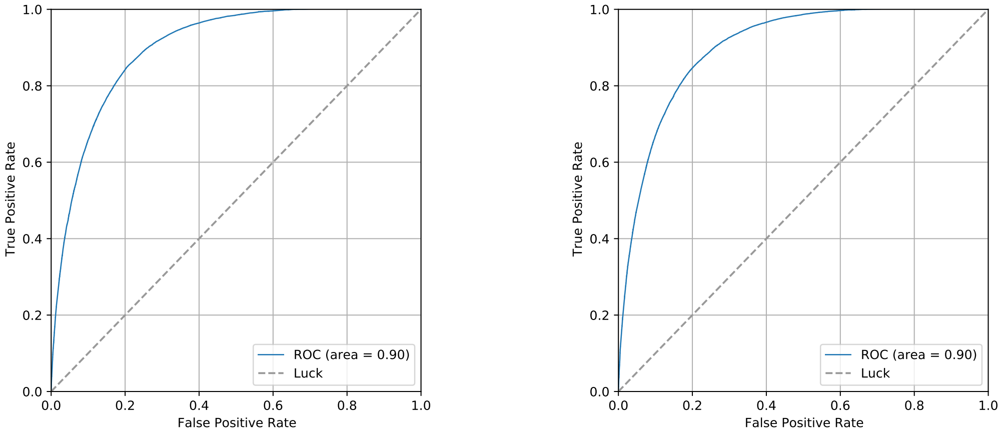

(a) K_S^0(LL) even (b) K_S^0(LL) odd

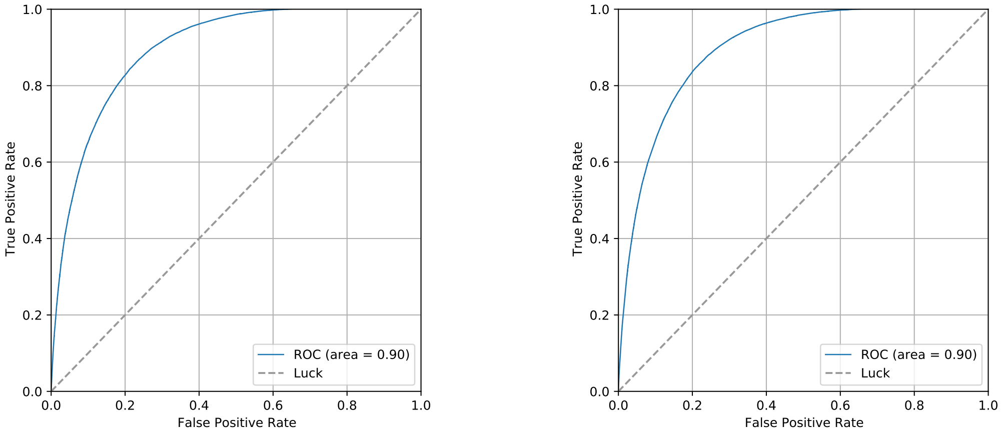

(c) K_S^0(DD) even (d) K_S^0(DD) odd

Figure B.4: ROC curves for double-tagged 2018 samples.

B.3 Significance and optimal BDT cut

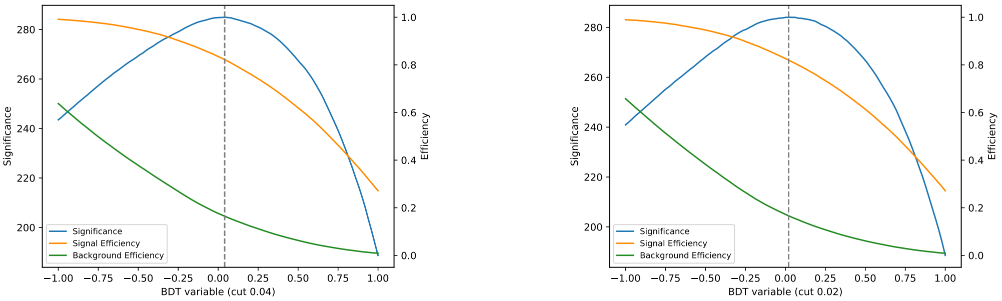

(a) K_S^0(LL) 2016 even

(b) K_S^0(LL) 2016 odd

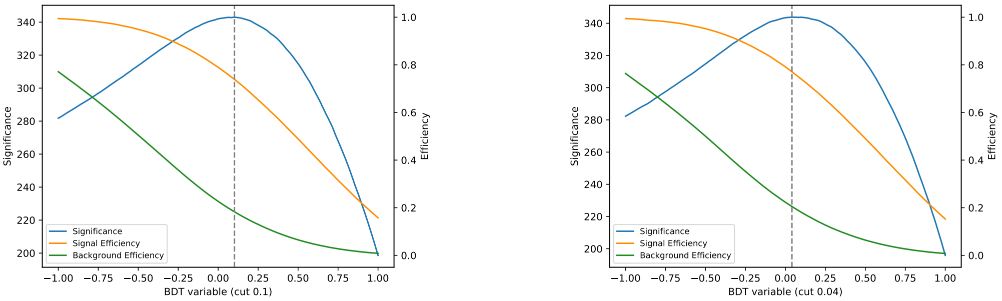

(c) K_S^0(DD) 2016 even

(d) K_S^0(DD) 2016 odd

Figure B.5: Significance versus BDT response for single-tagged 2016 samples.

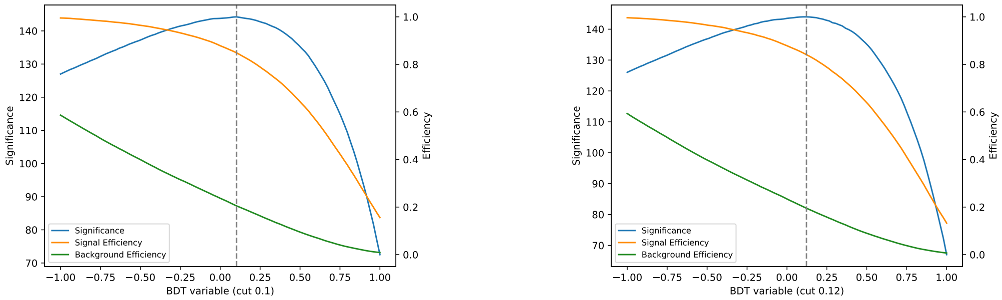

(a) K_S^0(LL) 2018 even (b) K_S^0(LL) 2018 odd

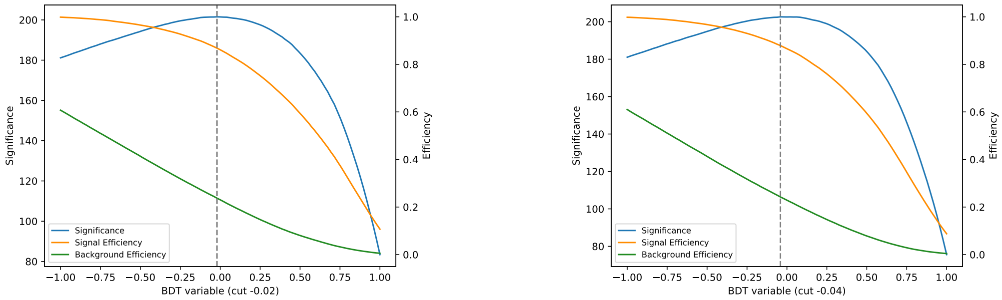

(c) K_S^0(DD) 2018 even (d) K_S^0(DD) 2018 odd

Figure B.6: Significance versus BDT response for double-tagged 2018 samples.

B.4 D^0 mass and δm fits

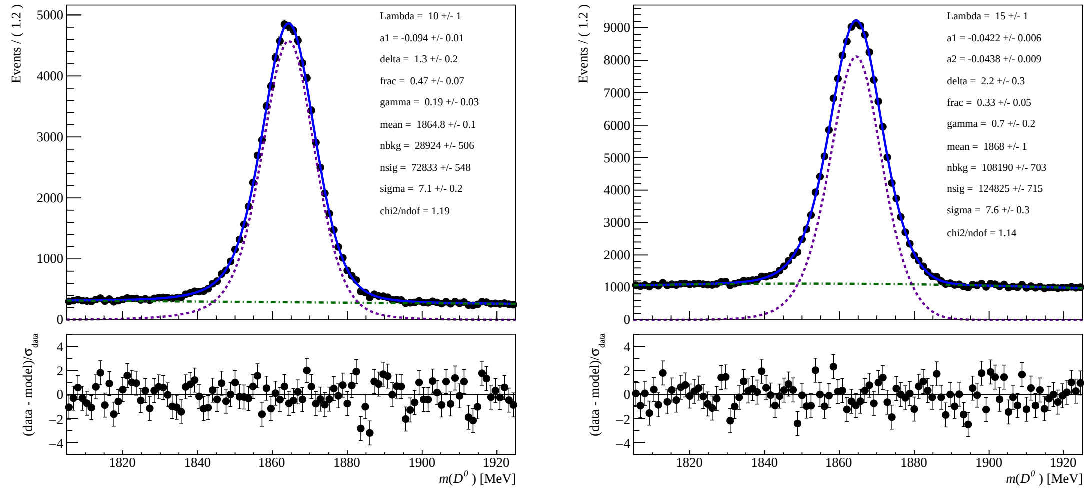

(a) K^0 (LL) 2011 (b) K^0 (DD) 2011

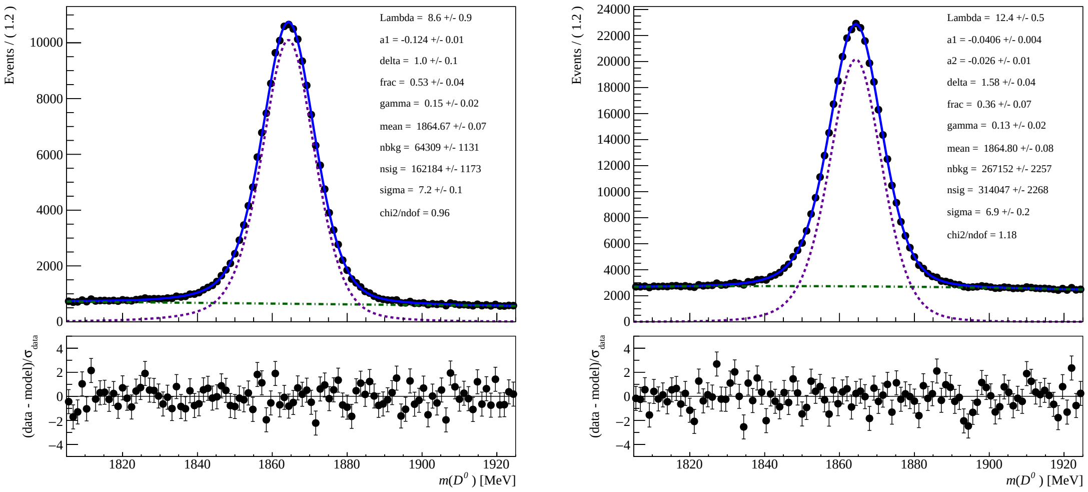

(c) K^0 (LL) 2012 (d) K^0 (DD) 2012

Figure B.7: D^0 mass fits for the single-tagged 2011 and 2012 samples: signal model (purple dashed), background (green dashed), total model (blue line).

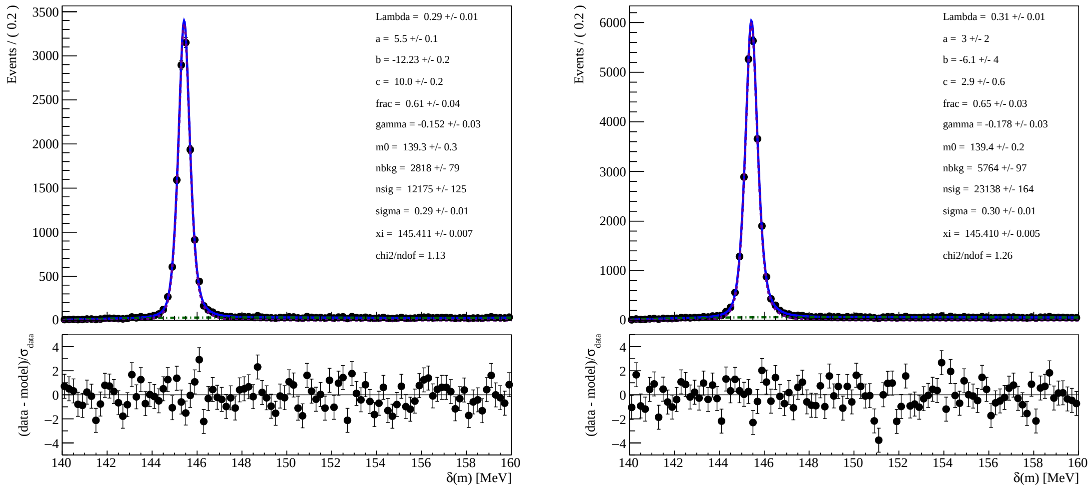

(a) K^0 (LL) 2011 (b) K^0 (DD) 2011

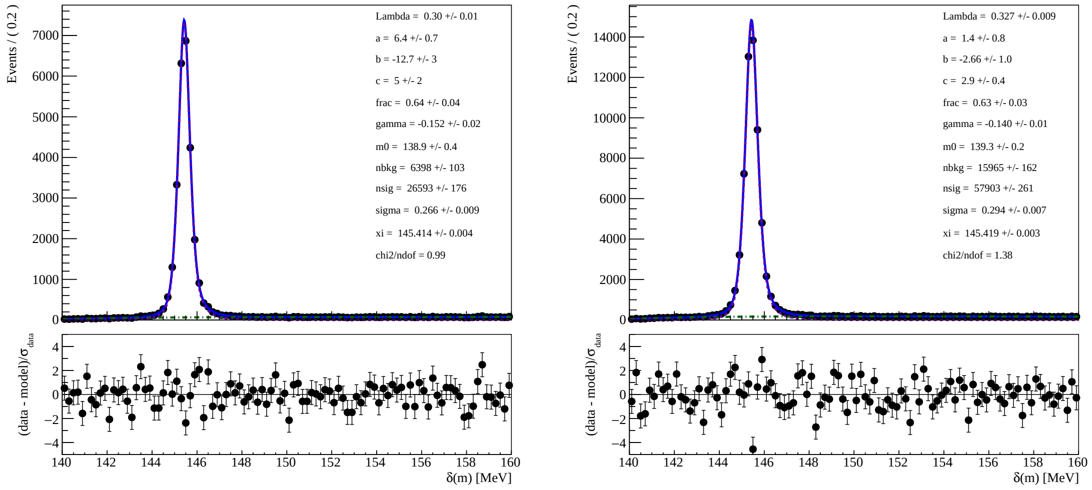

(c) K^0 (LL) 2012 (d) K^0 (DD) 2012

Figure B.8: δm fits for the double-tagged 2011 and 2012 samples: signal model (purple dashed), background (green dashed), total model (blue line).

APPENDIX C

Detector Effects

C.1 Phase-space acceptance

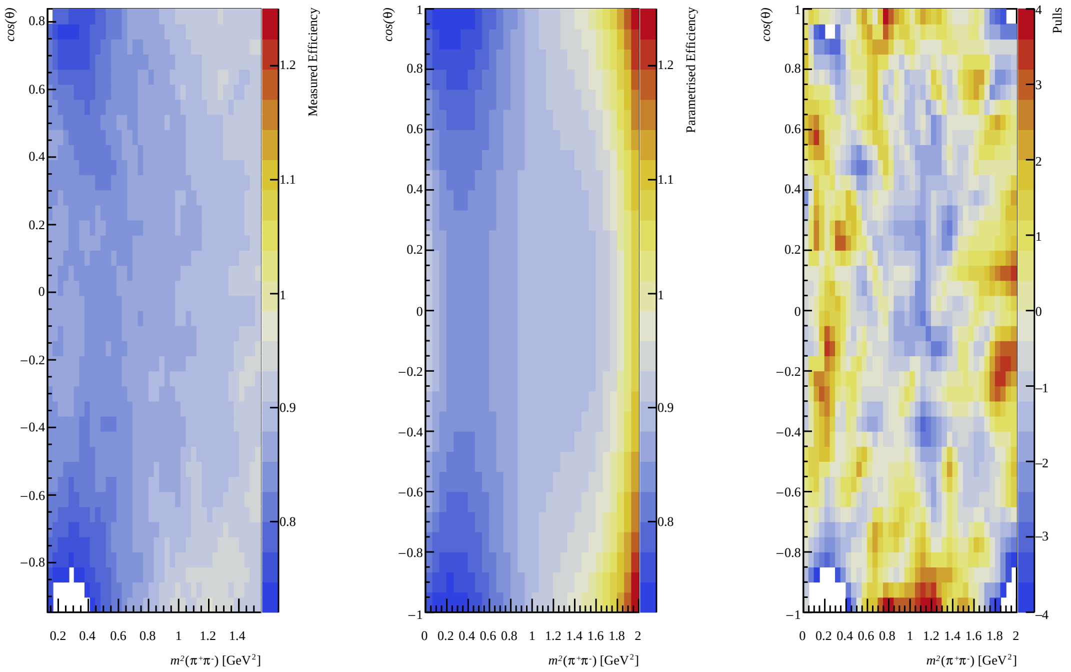

(a) Single-tagged K_S^0 (DD)

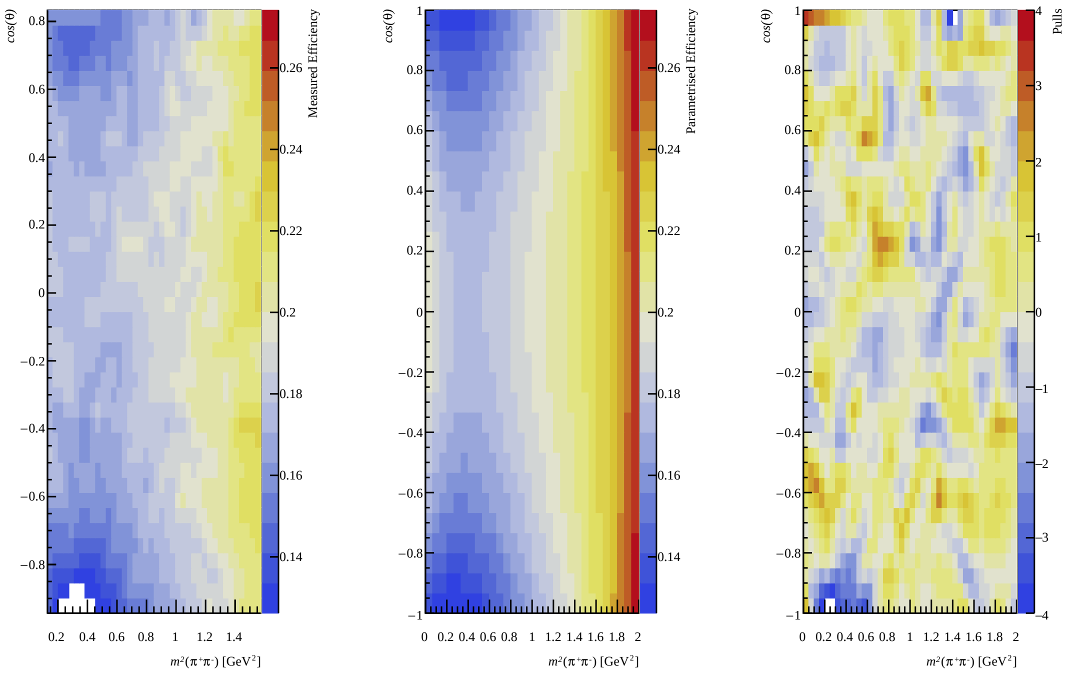

(b) Double-tagged K_S^0 (LL)

Figure C.1: Phase-space acceptance for 2018 subsamples.

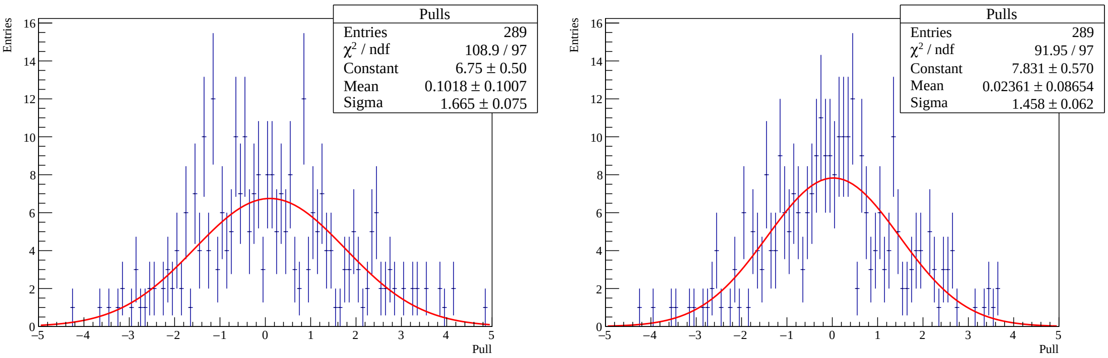

(a) Single-tagged K_S^0 (DD)

(b) Double-tagged K_S^0 (DD)

Figure C.2: Distribution of pulls of the efficiency fit, fitted with a Gaussian for 2018 samples.

C.2 Decay-time acceptance

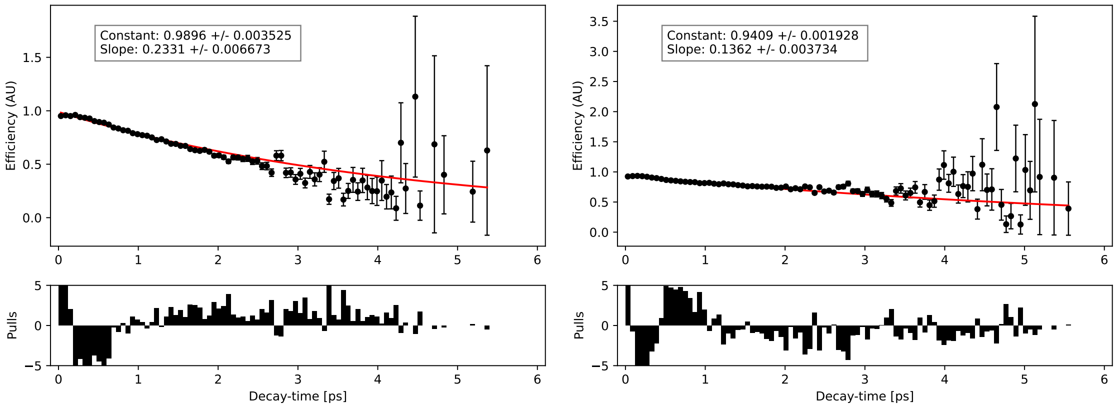

(a) Single-tagged K_S^0 (LL) (b) Single-tagged K_S^0 (DD)

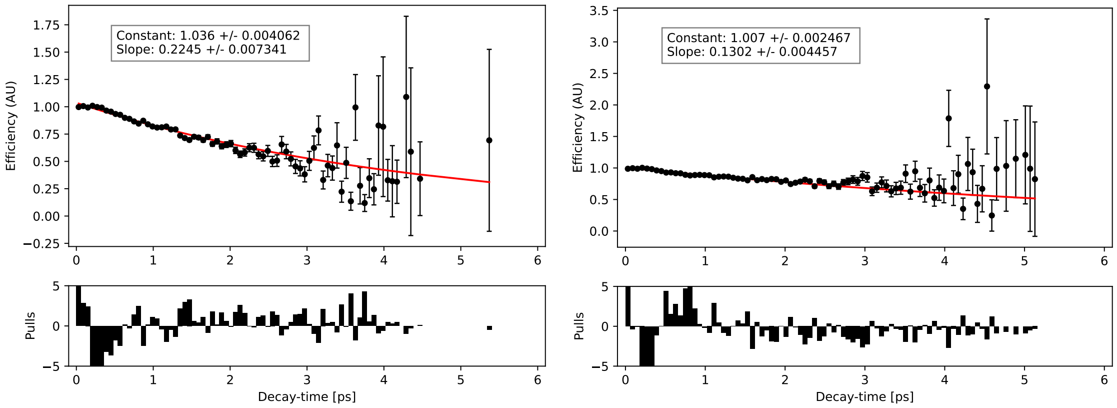

(c) Double-tagged K_S^0 (LL) (d) Double-tagged K_S^0 (DD)

Figure C.3: Decay-time acceptance (black points) fitted with an exponential function (red line) derived from simulation for the 2016 samples.

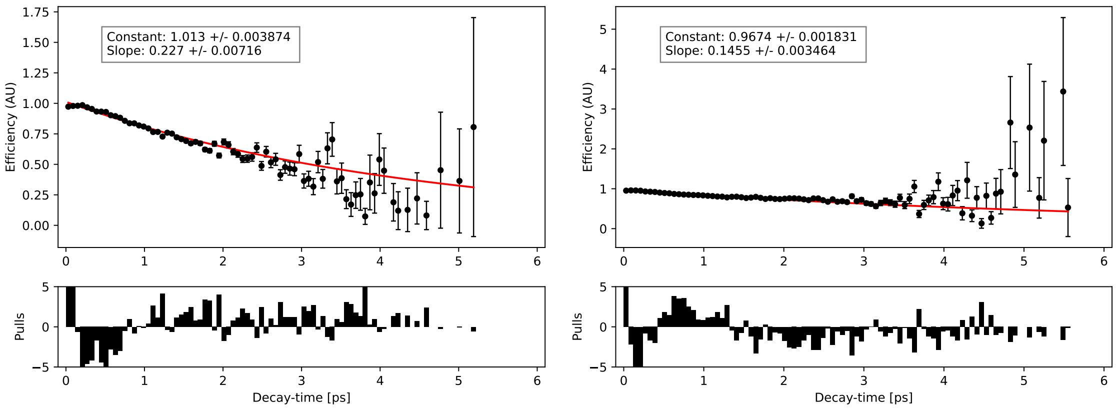

(a) Single-tagged K_S^0 (LL)

(b) Single-tagged K_S^0 (DD)

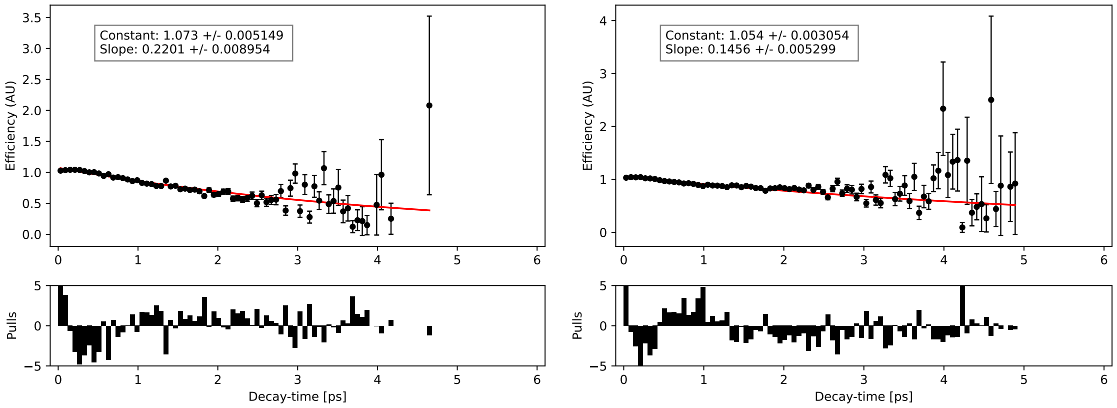

(c) Double-tagged K_S^0 (LL)

(d) Double-tagged K_S^0 (DD)

Figure C.4: Decay-time acceptance (black points) fitted with an exponential function (red line) derived from simulation for the 2017 samples.

C.3 Decay-time resolution

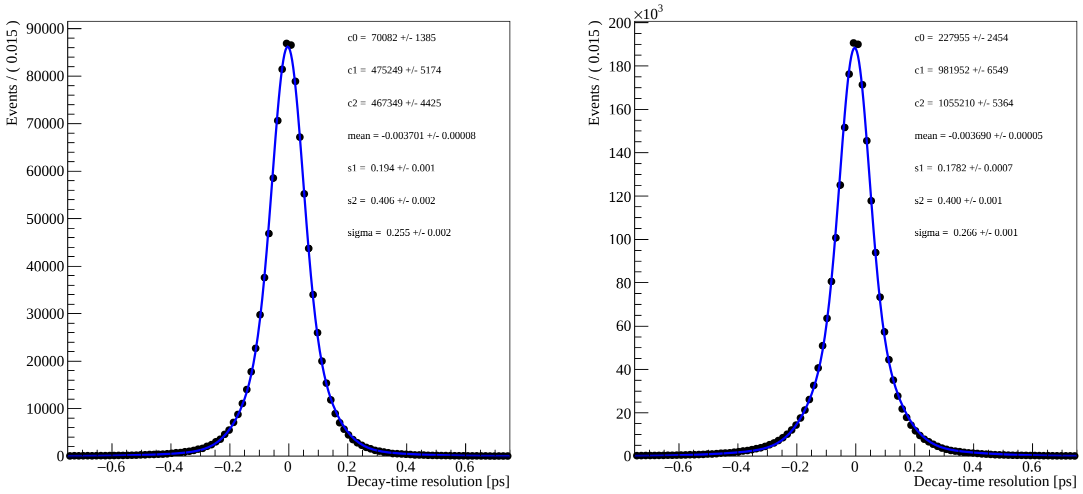

(a) Single-tag K_S^0 (LL) (b) Single-tag K_S^0 (DD)

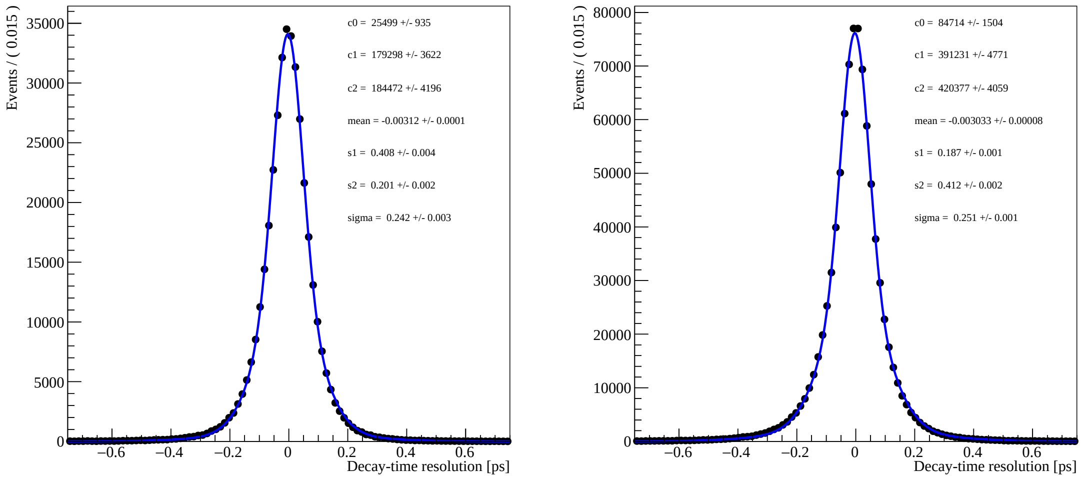

(c) Double-tag K_S^0 (LL) (d) Double-tag K_S^0 (DD)

Figure C.5: Decay-time resolution (black points) fitted with a triple Gaussian function (blue line) for the 2017 samples. Fit parameters displayed.

APPENDIX D

Fit projections for other sub-samples

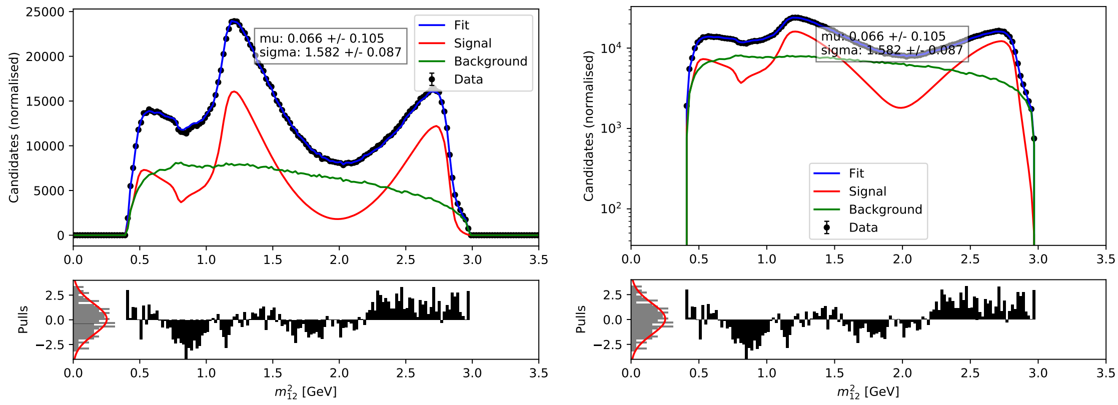

(a) m_{12}^2 linear scale

(b) m_{12}^2 log scale

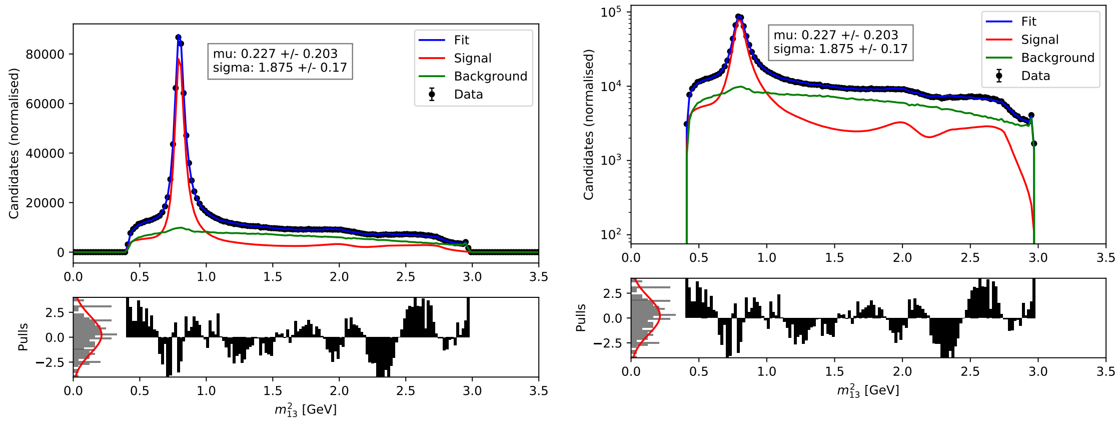

(c) m_{13}^2 linear scale

(d) m_{13}^2 log scale

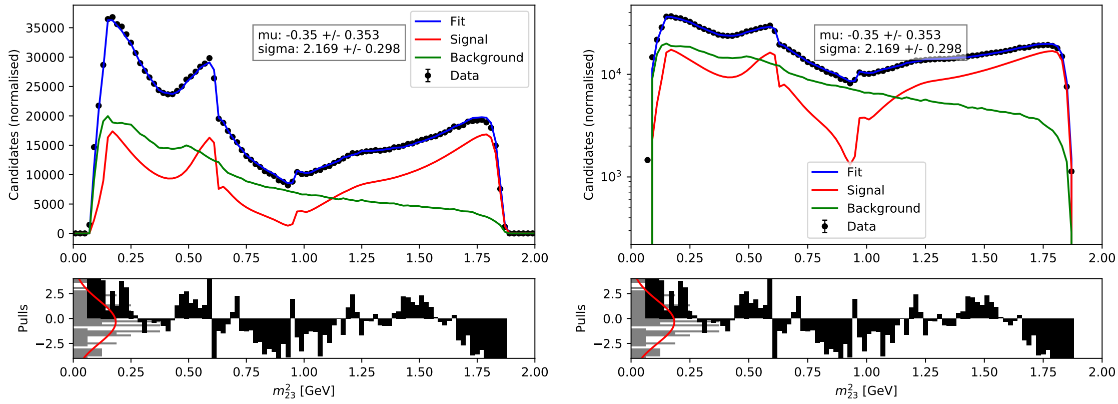

(e) m_{23}^2 linear scale

(f) m_{23}^2 log scale

Figure D.1: Fit projections of the Dalitz variables for the time-dependent amplitude fit. Single-tag K_S^0 (DD) 2016 sample. Linear and log scales. Plots show signal component in red and background in green.

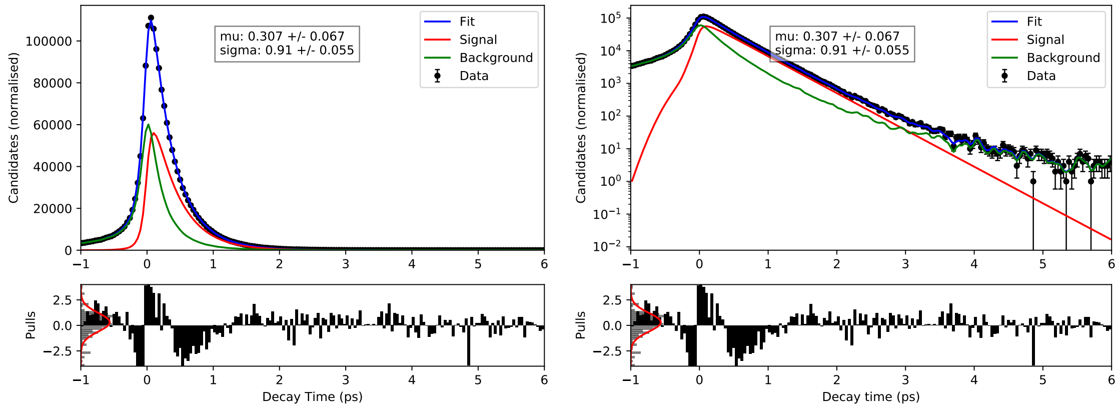

Figure D.2: Decay-time projections for the time-dependent amplitude fit. Single-tag K_S^0 (DD) 2016 sample. Linear and log scales. Plots show signal component in red and background in green.

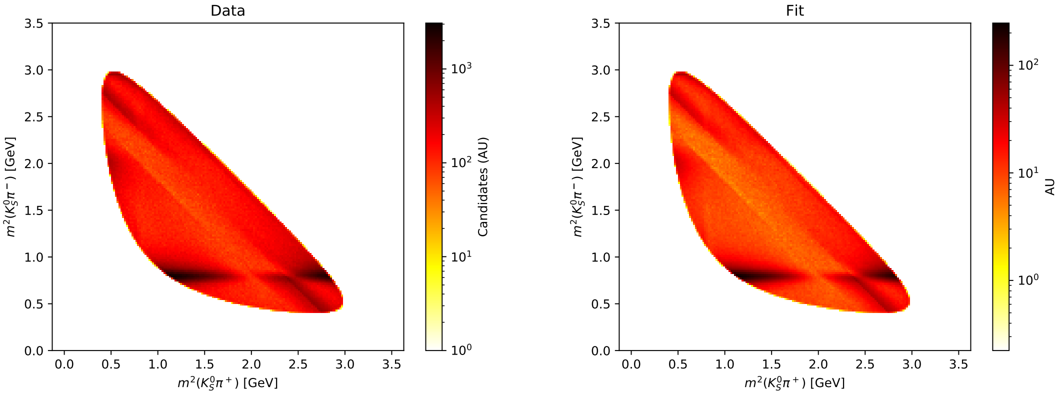

(a) Data (b) Fit model

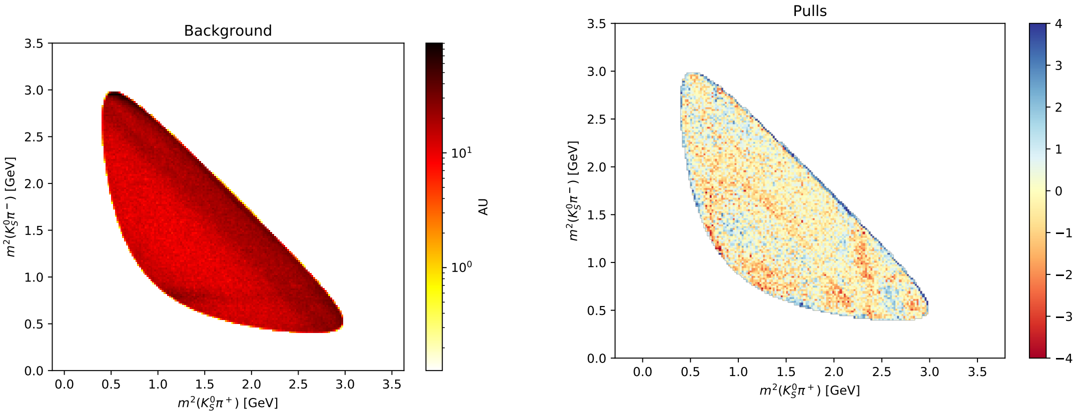

(c) Background model (d) Pulls

Figure D.3: Two-dimensional distributions of the Dalitz variables for the time-dependent amplitude fit: data, total fit model, background model and pulls. Single-tagged K_S^0 (DD) 2016 sample.

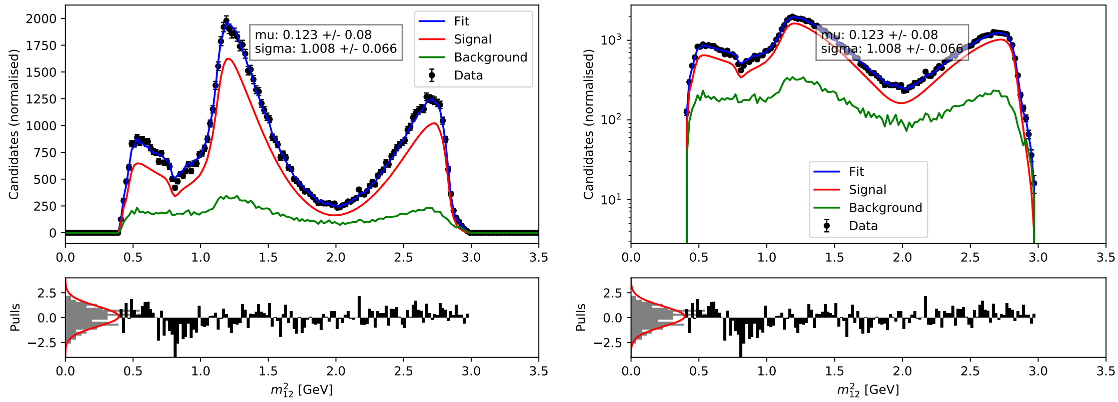

(a) m_{12}^2 linear scale

(b) m_{12}^2 log scale

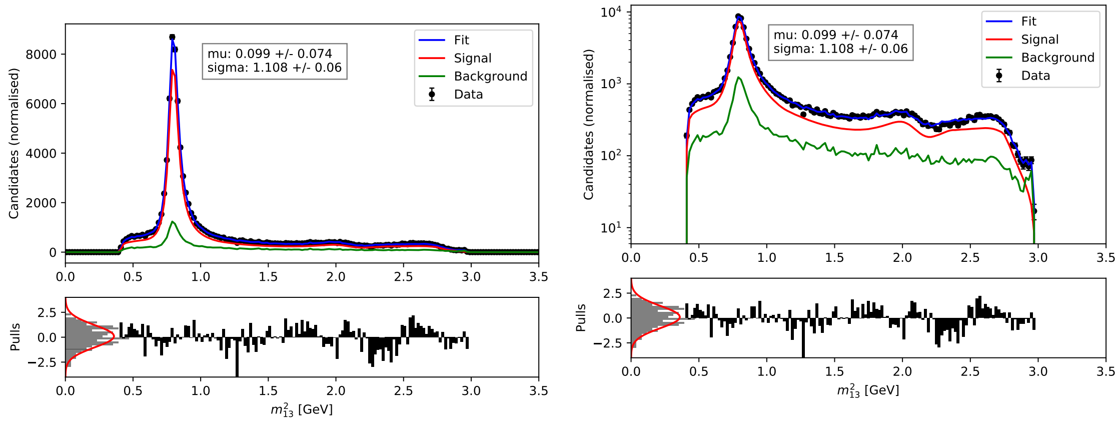

(c) m_{13}^2 linear scale

(d) m_{13}^2 log scale

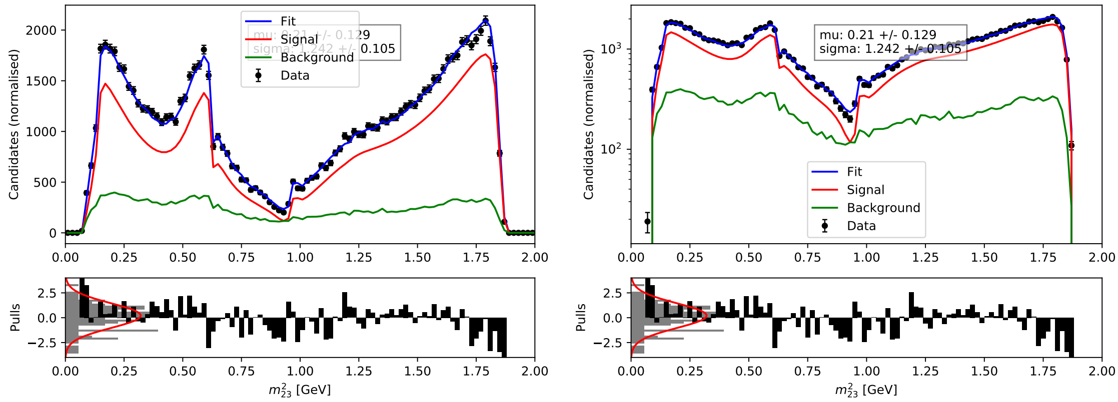

(e) m_{23}^2 linear scale

(f) m_{23}^2 log scale

Figure D.4: Fit projections of the Dalitz variables for the time-dependent amplitude fit. Double-tag K_S^0 (LL) 2016 sample. Linear and log scales. Plots show signal component in red and background in green.

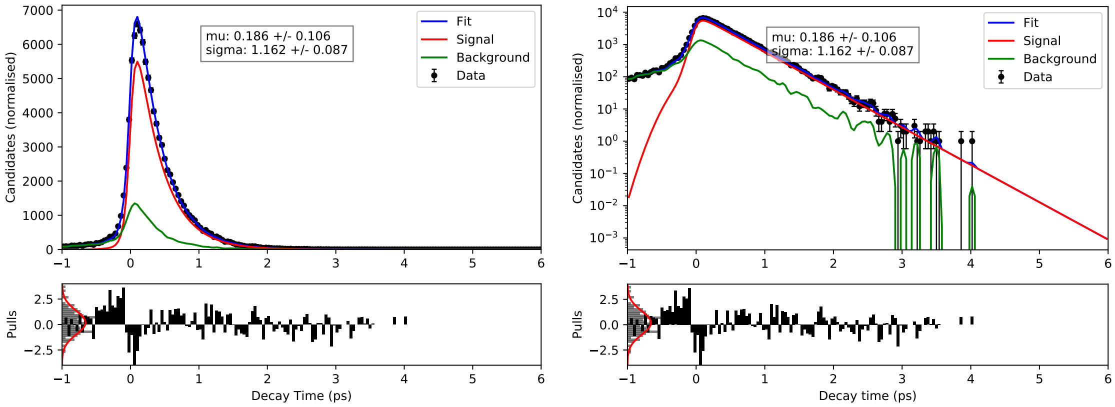

Figure D.5: Decay-time projections for the time-dependent amplitude fit. Double-tag K_S^0 (LL) 2016 sample. Linear and log scales. Plots show signal component in red and background in green.

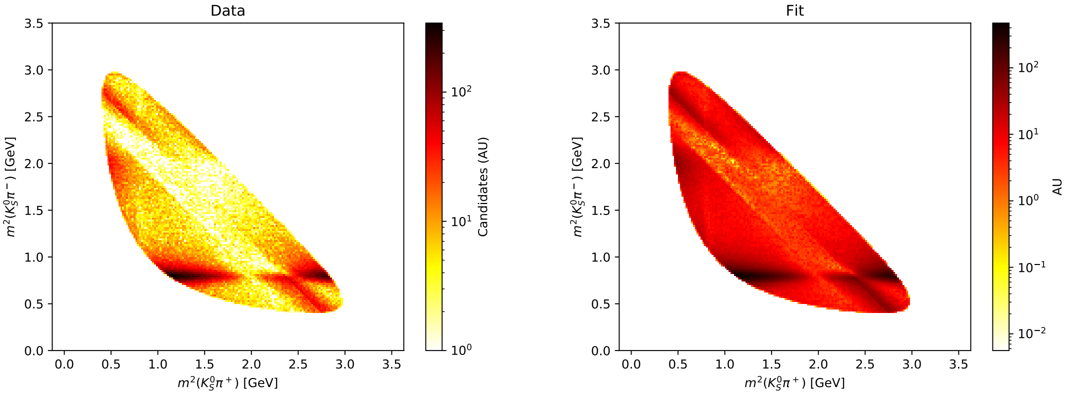

(a) Data

(b) Fit model

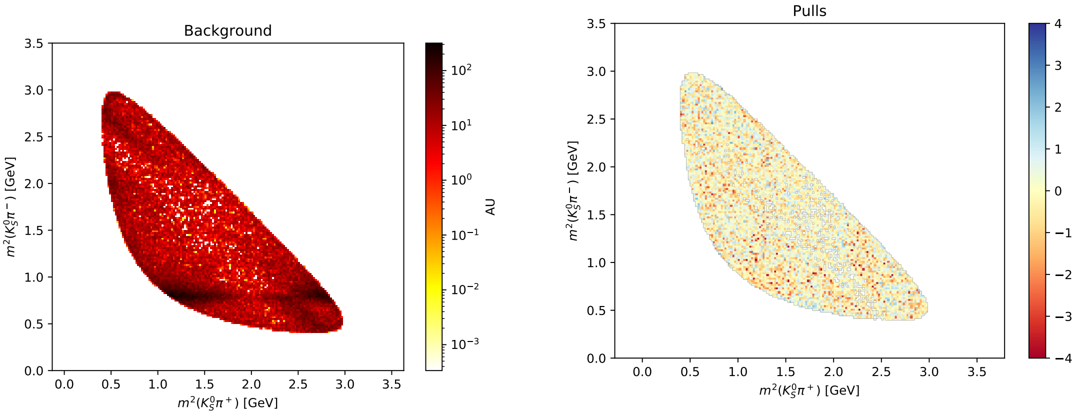

(c) Background model

(d) Pulls

Figure D.6: Two-dimensional distributions of the Dalitz variables for the time-dependent amplitude fit: data, total fit model, background model and pulls. Double-tagged K_S^0 (LL) 2016 sample.

APPENDIX E

Interference fit fractions

Resonance 1	Resonance 2	Fit Fraction (%)
$\omega(782)$	$f_2(1270)$	0.000
	$\rho(1450)$	0.069
	$K_2^*(1430)^-$	-0.029
	$K^*(1410)^-$	-0.021
	$K^*(1680)^-$	0.001
	$K_0^*(1430)^-$	-0.068
	$K^*(892)^+$	0.006
	$K_2^*(1430)^+$	-0.001
	$K^*(1410)^+$	-0.011
	$K^*(1680)^+$	-0.018
	$K_0^*(1430)^+$	0.003
$f_2(1270)$	$\rho(1450)$	0.002
	$K_2^*(1430)^-$	0.222
	$K^*(1410)^-$	0.027
	$K^*(1680)^-$	-0.100
	$K_0^*(1430)^-$	-0.750
	$K^*(892)^+$	0.056
	$K_2^*(1430)^+$	-0.003
	$K^*(1410)^+$	-0.051
	$K^*(1680)^+$	0.120
	$K_0^*(1430)^+$	-0.032
$\rho(1450)$	$K_2^*(1430)^-$	0.051
	$K^*(1410)^-$	-0.039
	$K^*(1680)^-$	-0.172
	$K_0^*(1430)^-$	-0.607
	$K^*(892)^+$	-0.029
	$K_2^*(1430)^+$	0.000
	$K^*(1410)^+$	0.012
	$K^*(1680)^+$	-0.192
	$K_0^*(1430)^+$	0.026
$K_2^*(1430)^-$	$K^*(1410)^-$	-0.001
	$K^*(1680)^-$	-0.059
	$K_0^*(1430)^-$	-0.039
	$K^*(892)^+$	-0.059
	$K_2^*(1430)^+$	-0.019
	$K^*(1410)^+$	0.140
	$K^*(1680)^+$	-0.004
	$K_0^*(1430)^+$	-0.002

Table E.1: Interference fit fractions for the terms in the Dalitz fit including the sign of the term where a negative sign denotes destructive interference.

Resonance 1	Resonance 2	Fit Fraction (%)
$K^*(1410)^-$	$K^*(1680)^-$	-1.004
	$K_0^*(1430)^-$	-0.127
	$K^*(892)^+$	0.093
	$K_2^*(1430)^+$	0.005
	$K^*(1410)^+$	-0.293
	$K^*(1680)^+$	0.140
	$K_0^*(1430)^+$	-0.013
$K^*(1680)^-$	$K_0^*(1430)^-$	0.153
	$K^*(892)^+$	-0.147
	$K_2^*(1430)^+$	0.000
	$K^*(1410)^+$	0.526
	$K^*(1680)^+$	-0.619
	$K_0^*(1430)^+$	0.005
$K_0^*(1430)^-$	$K^*(892)^+$	-0.222
	$K_2^*(1430)^+$	-0.007
	$K^*(1410)^+$	0.212
	$K^*(1680)^+$	0.167
	$K_0^*(1430)^+$	0.130
$K^*(892)^+$	$K_2^*(1430)^+$	-0.001
	$K^*(1410)^+$	-0.113
	$K^*(1680)^+$	0.087
	$K_0^*(1430)^+$	-0.001
$K_2^*(1430)^+$	$K^*(1410)^+$	0.001
	$K^*(1680)^+$	-0.002
	$K_0^*(1430)^+$	0.000
$K^*(1410)^+$	$K^*(1680)^+$	-0.313
	$K_0^*(1430)^+$	0.004
$K^*(1680)^+$	$K_0^*(1430)^+$	-0.001

Table E.2: Interference fit fractions for the terms in the Dalitz fit including the sign of the term where a negative sign denotes destructive interference.

Bibliography

[1] R. Aaij et al. Observation of J/ψp resonances consistent with pentaquark states in $\Lambda_b^0 \rightarrow$ J/ψpK^- decays. *Phys. Rev. Lett.*, 115:072001, 2015.

[2] R. Aaij et al. Measurement of the forward Z boson production cross-section in pp collisions at $\sqrt{s}$ =13 TeV. *JHEP*, 09:136, 2016.

[3] R. Aaij et al. Measurements of prompt charm production cross-sections in pp collisions at $\sqrt{s}$ =13 TeV. *JHEP*, 03:159, 2016.

[4] R. Aaij et al. Measurement of the $B_s^0 \rightarrow \mu^+\mu^-$ branching fraction and effective lifetime and search for $B^0 \rightarrow \mu^+\mu^-$ decays. *Phys. Rev. Lett.*, 118:191801, 2017.

[5] R. Aaij et al. Test of lepton universality with $B^0 \rightarrow K^{*0}\ell^+\ell^-$ decays. *JHEP*, 08:055, 2017.

[6] R. Aaij et al. Search for dark photons produced in 13 TeV *pp* collisions. *Phys. Rev. Lett.*, 120:061801, 2018.

[7] R. Aaij et al. Updated determination of $D^0 - \overline{D}^0$ mixing and CP violation parameters with $D^0 \rightarrow K^+\pi^-$ decays. *Phys. Rev. D*, 97:031101, Feb 2018.

[8] R. Aaij et al. Measurement of the Charm-Mixing Parameter y_{CP}. *Phys. Rev. Lett.*, 122:011802, Jan 2019.

[9] R. Aaij et al. Measurement of the mass difference between neutral charm-meson eigenstates. *Phys. Rev. Lett.*, 122:231802, 2019.

[10] R. Aaij et al. Observation of *CP* violation in charm decays. *Phys. Rev. Lett.*, 122:211803, 2019.

[11] R. Aaij et al. Performance of the LHCb trigger and full real-time reconstruction in Run 2 of the LHC. *JINST*, 14(LHCb-DP-2019-001):P04013, 2019.

[12] R. Aaij et al. Search for lepton-universality violation in $\mathrm{B}^+ \rightarrow K^+\ell^+\ell^-$ decays. *Phys. Rev. Lett.*, 122:191801, 2019.

[13] R. Aaij et al. Observation of the mass difference between neutral charm-meson eigenstates. Technical report, CERN, Geneva, Jun 2021.

[14] T. Aaltonen et al. Measurement of CP-violation asymmetries in $D^0 \rightarrow K_S\pi^+\pi^-$. *Phys. Rev. D*, 86:032007, 2012.

[15] A. Abashian et al. The Belle Detector. *Nucl. Instrum. Meth. A*, 479:117–232, 2002.

[16] K. Abe et al. Observation of Large *CP* Violation in the Neutral *B* Meson System. *Phys. Rev. Lett.*, 87:091802, Aug 2001.

[17] T. Abe et al. Belle II Technical Design Report, 2010.

[18] Carlos Abellán Beteta et al. Calibration and performance of the LHCb calorimeters in Run 1 and 2 at the LHC. Technical report, CERN, Aug 2020. (LHCb public pages).

[19] M. Ablikim, M. N. Achasov, P. Adlarson, S. Ahmed, M. Albrecht, M. Alekseev, D. Ambrose, A. Amoroso, F. F. An, Q. An, Anita, Y. Bai, O. Bakina, R. Baldini Ferroli, I. Balossino, Y. Ban, K. Begzsuren, J. V. Bennett, N. Berger, M. Bertani, D. Bettoni, F. Bianchi, J. Biernat, J. Bloms, I. Boyko, R. A. Briere, H. Cai, X. Cai, A. Calcaterra, G. F. Cao, N. Cao, S. A. Cetin, J. Chai, J. F. Chang, W. L. Chang, G. Chelkov, D. Y. Chen, G. Chen, H. S. Chen, J. Chen, J. C. Chen, M. L. Chen, S. J. Chen, Y. B. Chen, W. Cheng, G. Cibinetto, F. Cossio, X. F. Cui, H. L. Dai, J. P. Dai, X. C. Dai, A. Dbeyssi, D. Dedovich, Z. Y. Deng, A. Denig, I. Denysenko, M. Destefanis, F. De Mori, Y. Ding, C. Dong, J. Dong, L. Y. Dong, M. Y. Dong, Z. L. Dou, S. X. Du, J. Z. Fan, J. Fang, S. S. Fang, Y. Fang, R. Farinelli, L. Fava, F. Feldbauer, G. Felici, C. Q. Feng, M. Fritsch, C. D. Fu, Y. Fu, Q. Gao, X. L. Gao, Y. Gao, Y. Gao, Y. G. Gao, Z. Gao, B. Garillon, I. Garzia, E. M. Gersabeck, A. Gilman, K. Goetzen, L. Gong, W. X. Gong,

W. Gradl, M. Greco, L. M. Gu, M. H. Gu, S. Gu, Y. T. Gu, A. Q. Guo, L. B. Guo, R. P. Guo, Y. P. Guo, A. Guskov, S. Han, X. Q. Hao, F. A. Harris, K. L. He, F. H. Heinsius, T. Held, Y. K. Heng, M. Himmelreich, Y. R. Hou, Z. L. Hou, H. M. Hu, J. F. Hu, T. Hu, Y. Hu, G. S. Huang, J. S. Huang, X. T. Huang, X. Z. Huang, N. Huesken, T. Hussain, W. Ikegami Andersson, W. Imoehl, M. Irshad, Q. Ji, Q. P. Ji, X. B. Ji, X. L. Ji, H. L. Jiang, X. S. Jiang, X. Y. Jiang, J. B. Jiao, Z. Jiao, D. P. Jin, S. Jin, Y. Jin, T. Johansson, N. Kalantar-Nayestanaki, X. S. Kang, R. Kappert, M. Kavatsyuk, B. C. Ke, I. K. Keshk, A. Khoukaz, P. Kiese, R. Kiuchi, R. Kliemt, L. Koch, O. B. Kolcu, B. Kopf, M. Kuemmel, M. Kuessner, A. Kupsc, M. Kurth, M. G. Kurth, W. Kühn, J. S. Lange, P. Larin, L. Lavezzi, H. Leithoff, T. Lenz, C. Li, Cheng Li, D. M. Li, F. Li, F. Y. Li, G. Li, H. B. Li, H. J. Li, J. C. Li, J. W. Li, Ke Li, L. K. Li, Lei Li, P. L. Li, P. R. Li, Q. Y. Li, W. D. Li, W. G. Li, X. H. Li, X. L. Li, X. N. Li, Z. B. Li, Z. Y. Li, H. Liang, H. Liang, Y. F. Liang, Y. T. Liang, G. R. Liao, L. Z. Liao, J. Libby, C. X. Lin, D. X. Lin, Y. J. Lin, B. Liu, B. J. Liu, C. X. Liu, D. Liu, D. Y. Liu, F. H. Liu, Fang Liu, Feng Liu, H. B. Liu, H. M. Liu, Huanhuan Liu, Huihui Liu, J. B. Liu, J. Y. Liu, K. Liu, K. Y. Liu, Ke Liu, L. Y. Liu, Q. Liu, S. B. Liu, T. Liu, X. Liu, X. Y. Liu, Y. B. Liu, Z. A. Liu, Zhiqing Liu, Y. F. Long, X. C. Lou, H. J. Lu, J. D. Lu, J. G. Lu, Y. Lu, Y. P. Lu, C. L. Luo, M. X. Luo, P. W. Luo, T. Luo, X. L. Luo, S. Lusso, X. R. Lyu, F. C. Ma, H. L. Ma, L. L. Ma, M. M. Ma, Q. M. Ma, X. N. Ma, X. X. Ma, X. Y. Ma, Y. M. Ma, F. E. Maas, M. Maggiora, S. Maldaner, S. Malde, Q. A. Malik, A. Mangoni, Y. J. Mao, Z. P. Mao, S. Marcello, Z. X. Meng, J. G. Messchendorp, G. Mezzadri, J. Min, T. J. Min, R. E. Mitchell, X. H. Mo, Y. J. Mo, C. Morales Morales, N. Yu. Muchnoi, H. Muramatsu, A. Mustafa, S. Nakhoul, Y. Nefedov, F. Nerling, I. B. Nikolaev, Z. Ning, S. Nisar, S. L. Niu, S. L. Olsen, Q. Ouyang, S. Pacetti, Y. Pan, M. Papenbrock, P. Patteri, M. Pelizaeus, H. P. Peng, K. Peters, J. Pettersson, J. L. Ping, R. G. Ping, A. Pitka, R. Poling, V. Prasad, H. R. Qi, M. Qi, T. Y. Qi, S. Qian, C. F. Qiao, N. Qin, X. P. Qin, X. S. Qin, Z. H. Qin, J. F. Qiu, S. Q. Qu, K. H. Rashid, K. Ravindran, C. F. Redmer, M. Richter, A. Rivetti, V. Rodin, M. Rolo, G. Rong, Ch. Rosner, M. Rump, A. Sarantsev, M. Savrié, Y. Schelhaas, K. Schoenning, W. Shan, X. Y. Shan, M. Shao, C. P. Shen, P. X.

Shen, X. Y. Shen, H. Y. Sheng, X. Shi, X. D. Shi, J. J. Song, Q. Q. Song, X. Y. Song, S. Sosio, C. Sowa, S. Spataro, F. F. Sui, G. X. Sun, J. F. Sun, L. Sun, S. S. Sun, X. H. Sun, Y. J. Sun, Y. K. Sun, Y. Z. Sun, Z. J. Sun, Z. T. Sun, Y. T. Tan, C. J. Tang, G. Y. Tang, X. Tang, V. Thoren, B. Tsednee, I. Uman, B. Wang, B. L. Wang, C. W. Wang, D. Y. Wang, K. Wang, L. L. Wang, L. S. Wang, M. Wang, M. Z. Wang, Meng Wang, P. L. Wang, R. M. Wang, W. P. Wang, X. Wang, X. F. Wang, X. L. Wang, Y. Wang, Y. Wang, Y. F. Wang, Y. Q. Wang, Z. Wang, Z. G. Wang, Z. Y. Wang, Zongyuan Wang, T. Weber, D. H. Wei, P. Weidenkaff, H. W. Wen, S. P. Wen, U. Wiedner, G. Wilkinson, M. Wolke, L. H. Wu, L. J. Wu, Z. Wu, L. Xia, Y. Xia, S. Y. Xiao, Y. J. Xiao, Z. J. Xiao, Y. G. Xie, Y. H. Xie, T. Y. Xing, X. A. Xiong, Q. L. Xiu, G. F. Xu, J. J. Xu, L. Xu, Q. J. Xu, W. Xu, X. P. Xu, F. Yan, L. Yan, W. B. Yan, W. C. Yan, Y. H. Yan, H. J. Yang, H. X. Yang, L. Yang, R. X. Yang, S. L. Yang, Y. H. Yang, Y. X. Yang, Yifan Yang, Z. Q. Yang, M. Ye, M. H. Ye, J. H. Yin, Z. Y. You, B. X. Yu, C. X. Yu, J. S. Yu, T. Yu, C. Z. Yuan, X. Q. Yuan, Y. Yuan, A. Yuncu, A. A. Zafar, Y. Zeng, B. X. Zhang, B. Y. Zhang, C. C. Zhang, D. H. Zhang, H. H. Zhang, H. Y. Zhang, J. Zhang, J. L. Zhang, J. Q. Zhang, J. W. Zhang, J. Y. Zhang, J. Z. Zhang, K. Zhang, L. Zhang, L. Zhang, S. F. Zhang, T. J. Zhang, X. Y. Zhang, Y. Zhang, Y. H. Zhang, Y. T. Zhang, Yang Zhang, Yao Zhang, Yi Zhang, Yu Zhang, Z. H. Zhang, Z. P. Zhang, Z. Y. Zhang, G. Zhao, J. W. Zhao, J. Y. Zhao, J. Z. Zhao, Lei Zhao, Ling Zhao, M. G. Zhao, Q. Zhao, S. J. Zhao, T. C. Zhao, Y. B. Zhao, Z. G. Zhao, A. Zhemchugov, B. Zheng, J. P. Zheng, Y. Zheng, Y. H. Zheng, B. Zhong, L. Zhou, L. P. Zhou, Q. Zhou, X. Zhou, X. K. Zhou, X. R. Zhou, Xiaoyu Zhou, Xu Zhou, A. N. Zhu, J. Zhu, J. Zhu, K. Zhu, K. J. Zhu, S. H. Zhu, W. J. Zhu, X. L. Zhu, Y. C. Zhu, Y. S. Zhu, Z. A. Zhu, J. Zhuang, B. S. Zou, and J. H. Zou. Model-independent determination of the relative strong-phase difference between D^0 and $\overline{d}^0 \to K^0_{S,L}\pi^+\pi^-$ and its impact on the measurement of the ckm angle γ/ϕ_3. *Phys. Rev. D*, 101:112002, Jun 2020.

[20] I. Adachi et al. Measurement of $\cos 2\beta$ in $B^0 \to D^{(*)}h^0$ with $D \to K^0_S\pi^+\pi^-$ decays by a combined time-dependent Dalitz plot analysis of BaBar and Belle data. *Phys. Rev.*, D98(11):112012, 2018.

[21] P. A. R. Ade et al. Planck2015 results. *Astronomy & Astrophysics*, 594:A13, Sep 2016.

[22] S. Agostinelli et al. Geant4: A simulation toolkit. *Nucl. Instrum. Meth.*, A506:250, 2003.

[23] H. Albrecht et al. Observation of $B^0 - \bar{B}^0$ Mixing. *Phys. Lett. B*, 192:245–252, 1987.

[24] M. Alexander et al. Mapping the material in the LHCb vertex locator using secondary hadronic interactions. *JINST*, 13:P06008. 11 p, Mar 2018.

[25] John Allison, K. Amako, J. Apostolakis, H. Araujo, P.A. Dubois, et al. Geant4 developments and applications. *IEEE Trans.Nucl.Sci.*, 53:270, 2006.

[26] A. A. Alves Jr. et al. The LHCb detector at the LHC. *JINST*, 3(LHCb-DP-2008-001):S08005, 2008.

[27] Y. Amhis et al. Averages of b-hadron, c-hadron, and τ-lepton properties as of 2018. In *Averages of b-hadron, c-hadron, and τ-lepton properties as of 2018*, 2016. updated results and plots available at `https://hflav.web.cern.ch`.

[28] V.V. Anisovich and A.V. Sarantsev. K-matrix analysis of the (ijpc = 00++)-wave in the mass region below 1900 mev. *The European Physical Journal A*, 16(2):229–258, Feb 2003.

[29] D. Aston et al. A Study of $K^-\pi^+$ Scattering in the Reaction $K^-p \to K^-\pi^+n$ at 11 GeV/c. *Nucl. Phys.*, B296:493–526, 1988.

[30] B. Aubert et al. Measurement of *CP*-Violating Asymmetries in B^0 Decays to *CP* Eigenstates. *Phys. Rev. Lett.*, 86:2515–2522, Mar 2001.

[31] B. Aubert et al. Observation of *CP* Violation in the B^0 Meson System. *Phys. Rev. Lett.*, 87:091801, 2001.

[32] B. Aubert et al. Evidence for $D^0 - \overline{D}^0$ Mixing. *Phys. Rev. Lett.*, 98:211802, May 2007.

[33] Federico Betti. A Review of *CP* Violation Measurements in Charm at LHCb, 7 2021.

[34] G. Breit and E. Wigner. Capture of Slow Neutrons. *Phys. Rev.*, 49:519–531, Apr 1936.

[35] Nicola Cabibbo. Unitary symmetry and leptonic decays. *Phys. Rev. Lett.*, 10:531–533, 1963.

[36] A. Di Canto et al. LHCb-ANA-2020-038, 2020. LHCb internal Analysis Note document, plots shared by private correspondence.

[37] J. H. Christenson, J. W. Cronin, V. L. Fitch, and R. Turlay. Evidence for the 2π decay of the K_2^0 Meson. *Phys. Rev. Lett.*, 13:138–140, 1964.

[38] S. U. Chung, J. Brose, R. Hackmann, E. Klempt, S. Spanier, and C. Strassburger. Partial wave analysis in K matrix formalism. *Annalen Phys.*, 4:404–430, 1995.

[39] X. Cid Vidal. Muon Identification in the LHCb experiment. Technical report, CERN, May 2010. Comments: Proceedings for the Moriond 2010 EW.

[40] M Clemencic et al. The LHCb simulation application, Gauss: Design, evolution and experience. *J. Phys. Conf. Ser.*, 331:032023, 2011.

[41] LHC Commissioning. LHC Commissioning Schedules and Luminosity forecasts. `https://lhc-commissioning.web.cern.ch/schedule/HL-LHC-plots.htm`, Last accessed 30-07-2021.

[42] Edvige Corbelli and Paolo Salucci. The extended rotation curve and the dark matter halo of M33. *Monthly Notices of the Royal Astronomical Society*, 311(2):441–447, 01 2000.

[43] Michel De Cian, Stephen Farry, Paul Seyfert, and Sascha Stahl. Fast neural-net based fake track rejection in the LHCb reconstruction. Technical Report LHCb-PUB-2017-011. CERN-LHCb-PUB-2017-011, CERN, Geneva, Mar 2017.

[44] A. Di Canto, J. Garra Ticó, T. Gershon, N. Jurik, M. Martinelli, T. Pilař, S. Stahl, and D. Tonelli. Novel method for measuring charm-mixing parameters using multibody decays. *Phys. Rev. D*, 99:012007, Jan 2019.

[45] Emmy Pauline Maria Gabriel. *Observation of new* Ξ_c^0 *states decaying to* $\Lambda_c^+ K^-$*, and development of the TORCH time-of-flight detector.* PhD thesis, University of Edinburgh, 2020. Presented 24 Apr 2020.

[46] Richard L. Garwin, Leon M. Lederman, and Marcel Weinrich. Observations of the Failure of Conservation of Parity and Charge Conjugation in Meson Decays: the Magnetic Moment of the Free Muon. *Phys. Rev.*, 105:1415–1417, Feb 1957.

[47] M. Gell-Mann and A. Pais. Behavior of Neutral Particles under Charge Conjugation. *Phys. Rev.*, 97:1387–1389, Mar 1955.

[48] S. L. Glashow, J. Iliopoulos, and L. Maiani. Weak Interactions with Lepton-Hadron Symmetry. *Phys. Rev. D*, 2:1285–1292, Oct 1970.

[49] S.L. Glashow. Partial Symmetries of Weak Interactions. *Nucl. Phys.*, 22:579–588, 1961.

[50] Piotr Golonka and Zbigniew Was. PHOTOS Monte Carlo: A precision tool for QED corrections in Z and W decays. *Eur. Phys. J.*, C45:97–107, 2006.

[51] G. J. Gounaris and J. J. Sakurai. Finite-Width Corrections to the Vector-Meson-Dominance Prediction for $\rho \to e^+e^-$. *Phys. Rev. Lett.*, 21:244–247, Jul 1968.

[52] Yuval Grossman, Alexander L. Kagan, and Yosef Nir. New physics and CP violation in singly Cabibbo suppressed D decays. *Phys. Rev. D*, 75:036008, Feb 2007.

[53] Wouter D. Hulsbergen. Decay chain fitting with a Kalman filter. *Nucl. Instrum. Meth.*, A552:566–575, 2005.

[54] N. L. Johnson. Systems of frequency curves generated by methods of translation. *Biometrika*, 36(1/2):149–176, 1949.

[55] Ana Justel, Daniel Peña, and Rubén Zamar. A multivariate Kolmogorov-Smirnov test of goodness of fit. *Statistics & Probability Letters*, 35(3):251–259, October 1997.

[56] Makoto Kobayashi and Toshihide Maskawa. *CP*-violation in the renormalizable theory of weak interaction. *Prog. Theor. Phys.*, 49:652–657, 1973.

[57] Patrick Koppenburg. Dealing with multiple candidates - an update. Technical Report LHCb-INT-2016-045. CERN-LHCb-INT-2016-045, CERN, Geneva, Nov 2016.

[58] D. J. Lange. The EvtGen particle decay simulation package. *Nucl. Instrum. Meth.*, A462:152–155, 2001.

[59] LHCb. Trigger schemes. `http://lhcb.web.cern.ch/lhcb/speakersbureau/html/TriggerScheme.html`, Last accessed on 07-06-2021.

[60] LHCb. Tracking System, 2008. `https://lhcb-public.web.cern.ch/en/Detector/Trackers2-en.html`, Last accessed on 07-06-2021.

[61] J. Libby, M. Kornicer, R. E. Mitchell, M. R. Shepherd, C. M. Tarbert, D. Besson, T. K. Pedlar, J. Xavier, D. Cronin-Hennessy, J. Hietala, P. Zweber, S. Dobbs, Z. Metreveli, K. K. Seth, A. Tomaradze, T. Xiao, S. Brisbane, S. Malde, L. Martin, A. Powell, P. Spradlin, G. Wilkinson, H. Mendez, J. Y. Ge, D. H. Miller, I. P. J. Shipsey, B. Xin, G. S. Adams, D. Hu, B. Moziak, J. Napolitano, K. M. Ecklund, J. Insler, H. Muramatsu, C. S. Park, L. J. Pearson, E. H. Thorndike, F. Yang, S. Ricciardi, C. Thomas, M. Artuso, S. Blusk, N. Horwitz, R. Mountain, T. Skwarnicki, S. Stone, J. C. Wang, L. M. Zhang, T. Gershon, G. Bonvicini, D. Cinabro, A. Lincoln, M. J. Smith, P. Zhou, J. Zhu, P. Naik, J. Rademacker, D. M. Asner, K. W. Edwards, K. Randrianarivony, G. Tatishvili, R. A. Briere, H. Vogel, P. U. E. Onyisi, J. L. Rosner, J. P. Alexander, D. G. Cassel, S. Das, R. Ehrlich, L. Fields, L. Gibbons, S. W. Gray, D. L. Hartill, B. K. Heltsley, D. L. Kreinick, V. E. Kuznetsov, J. R. Patterson, D. Peterson, D. Riley, A. Ryd, A. J. Sadoff, X. Shi, W. M. Sun, J. Yelton, P. Rubin, N. Lowrey, S. Mehrabyan, M. Selen, and J. Wiss. Model-independent determination of the strong-phase difference between D^0 and $\overline{d}^0 \to K^0_{S,L}h^+h^-$ $(h = \pi,\ k)$ and its impact on the measurement of the ckm angle γ/ϕ_3. *Phys. Rev. D*, 82:112006, Dec 2010.

[62] Oliver Lupton. *Studies of* $\mathrm{D^0 \to K^0_S h^+ h'^-}$ *decays at the LHCb experiment.* PhD thesis, University of Oxford, Jul 2016. Presented 14 Sep 2016.

[63] Ziro Maki, Masami Nakagawa, and Shoichi Sakata. Remarks on the Unified Model of Elementary Particles. *Progress of Theoretical Physics*, 28(5):870–880, 11 1962.

[64] D Martschei, M Feindt, S Honc, and J Wagner-Kuhr. Advanced event reweighting using multivariate analysis. *Journal of Physics: Conference Series*, 368:012028, jun 2012.

[65] Esma Mobs. The CERN accelerator complex - 2019. Complexe des accélérateurs du CERN - 2019, Jul 2019. General Photo.

[66] D. Muller, M. Clemencic, G. Corti, and M. Gersabeck. ReDecay: A novel approach to speed up the simulation at LHCb. *Eur. Phys. J. C*, 78(arXiv:1810.10362. 12):1009. 9 p, Oct 2018.

[67] Antonis Papanestis and Carmelo D'Ambrosio. Performance of the LHCb RICH detectors during the LHC Run II. Technical Report LHCB-PUB-2017-012. CERN-LHCb-PUB-2017-012, CERN, Geneva, Mar 2017. Updated authors' details and DOI.

[68] Alexey A Petrov. Long-distance effects in charm mixing. In *6th International Workshop on Charm Physics*, 12 2013.

[69] Muriel Pivk and Francois R. Le Diberder. sPlot: A statistical tool to unfold data distributions. *Nucl. Instrum. Meth.*, A555:356–369, 2005.

[70] B. Pontecorvo. Inverse beta processes and nonconservation of lepton charge. *Sov. Phys. JETP*, 7:172–173, 1958.

[71] Stefanie Reichert. *Measurement of the mixing parameters of neutral charm mesons and search for indirect CP violation with* $D^0 \to K^0_S\pi^+\pi^-$ *decays at LHCb.* PhD thesis, University of Manchester, Dec 2015. Presented 18 Feb 2016.

[72] Andrei D Sakharov. Violation of *CP*-invariance, C asymmetry, and baryon asymmetry of the universe. *Soviet Physics Uspekhi*, 34(5):392–393, May 1991.

[73] Henry Schreiner, Christoph Hasse, Brad Hittle, Himadri Pandey, Robert Lupton, Liang Sun, Martha Hilton, Christoph Deil, Juan Leite, Daniel Vieira, and Brian Forrest Maddock. GooFit/GooFit: Version 2.2.3: Python builds, January 2020.

[74] Torbjörn Sjöstrand, Stephen Mrenna, and Peter Skands. A brief introduction to PYTHIA 8.1. *Comput. Phys. Commun.*, 178:852–867, 2008.

[75] Marian Stahl. Machine learning and parallelism in the reconstruction of LHCb and its upgrade. *Journal of Physics: Conference Series*, 898:042042, Oct 2017.

[76] M. Starič et al. Evidence for $D^0-\overline{D}^0$ Mixing. *Phys. Rev. Lett.*, 98:211803, May 2007.

[77] J Stevens and M Williams. uBoost: a boosting method for producing uniform selection efficiencies from multivariate classifiers. *Journal of Instrumentation*, 8(12):P12013–P12013, Dec 2013.

[78] M. Tanabashi et al. Review of particle physics. *Phys. Rev.*, D98:030001, 2018.

[79] A. N. Taylor, S. Dye, T. J. Broadhurst, N. Benitez, and E. van Kampen. Gravitational Lens Magnification and the Mass of Abell 1689. *The Astrophysical Journal*, 501(2):539–553, Jul 1998.

[80] Frank von Hippel and C. Quigg. Centrifugal-Barrier Effects in Resonance Partial Decay Widths, Shapes, and Production Amplitudes. *Phys. Rev. D*, 5:624–638, Feb 1972.

[81] Steven Weinberg. A Model of Leptons. *Phys. Rev. Lett.*, 19:1264–1266, Nov 1967.

[82] Wikipedia. Wikipedia: Cross validation (statistics).

[83] Wikipedia. Wikipedia: Standard model.

[84] Lincoln Wolfenstein. Parametrization of the Kobayashi-Maskawa Matrix. *Phys. Rev. Lett.*, 51:1945–1947, Nov 1983.

[85] Charles Zemach. Three-Pion Decays of Unstable Particles. *Phys. Rev.*, 133:B1201–B1220, Mar 1964.